FACULTY OF ENGINEERING
AND ARCHITECTURE

A Robust Wireless Backhaul Solution for Optical Attocell Networks

Yuhui Wu

Doctoral dissertation submitted to obtain the academic degree of
Doctor of Electrical Engineering

Supervisors
Prof. Didier Colle, PhD - Prof. Mario Pickavet, PhD

Department of Information Technology
Faculty of Engineering and Architecture, Ghent University

January 2022

GHENT
UNIVERSITY

ISBN 978-94-6355-565-4
NUR 964
Wettelijk depot: D/2022/10.500/6

Members of the Examination Board

Chair

Prof. Em. Hendrik Van Landeghem, PhD, Ghent University

Other members entitled to vote

Prof. Steinar Bjornstad, PhD, Norwegian University of Science and Technology, Norway
Prof. Kristiaan Neyts, PhD, Ghent University
Prof. Kris Steenhaut, PhD, Vrije Universiteit Brussel
Prof. Wouter Tavernier, PhD, Ghent University

Supervisors

Prof. Didier Colle, PhD, Ghent University
Prof. Mario Pickavet, PhD, Ghent University

Dankwoord

I would like to thank all the people who have greatly inspired and supported me throughout both my personal life and the PhD research.

First and foremost, I would like to thank my supervisors, Prof. Didier Colle and Prof. Mario Pickavet for offering me the opportunity to do the PhD research at Ghent University. I am extremely grateful for their invaluable advice, continuous support, encouragement, and guidance during my PhD. The methodology of doing research and the rigorous scientific attitude I learned from them will guide me in my future career. I also appreciate the valuable advice from Prof. Pieter Audenaert.

I would like to thank Prof. Hendrik Van Landeghem for accepting my request to chair my PhD examination board. I would also like to thank Prof. Steinar Bjornstad, Prof. Kristiaan Neyts, Prof. Kris Steenhaut, and Prof. Wouter Tavenier for being jury members of my PhD examination board and for providing valuable feedback to improve the quality of my PhD dissertation.

I would like to thank my colleagues, Sander, Thomas, Steven, Pieter, Askhad, Chong, and Gourav. They gave me warm advice and help for my research and introduced me to the Belgian culture. I would like to thank my friends and my roommates for their company in my personal life, especially during the Corona pandemic.

I am also thankful to the technical and administrative staff of IDLAB and the department of personnel and organization for helping me carry out the administrative formalities during my stay in Ghent.

I also give my special thanks to my husband who has encouraged and helped me throughout both my personal life and professional career. I am grateful for the unwavering support from my parents and all my family.

Ghent, December 2021
Yuhui Wu

Table of Contents

Dankwoord **i**

Nederlandse samenvatting **xxi**

English summary **xxv**

1 Introduction **1-1**
1.1 A brief introduction of VLC 1-3
1.1.1 VLC transmitters 1-6
1.1.2 VLC receivers 1-13
1.1.3 The VLC channel 1-16
1.2 VLC-based optical attocell networks 1-19
1.2.1 Cellular networks 1-21
1.2.2 The structure of optical attocell networks 1-22
1.2.3 Challenges of optical attocell networks 1-25
1.3 The new backhaul solution 1-27
1.4 Outline and research contributions 1-28
1.5 Publications 1-33
1.5.1 Publications in international journals (listed in the Science Citation Index) 1-33
1.5.2 Publications in international conferences (listed in the Science Citation Index) 1-33

2 Mirror-Aided Non-LOS VLC Channel Characterizations with A Time-Efficient Simulation Model **2-1**
2.1 Introduction 2-2
2.2 Theoretical approaches 2-5
2.2.1 Modeling of the environment 2-5
2.2.2 VLC channel impulse response 2-7
2.2.3 Lambert's cosine law and line-of-sight (LOS) path 2-9
2.2.4 Modeling of diffuse reflections 2-12
2.2.5 Modeling of specular reflections 2-14
2.3 Implementation 2-15
2.3.1 Environment initialization 2-15
2.3.2 Iterative calculations and impulse responses 2-17

2.4 Simulation results 2-17
2.4.1 Multipath effect on non-LOS VLC links 2-21
2.4.2 Wavelength dependency of VLC links 2-24
2.4.3 Mirror-aided non-LOS VLC channel characterizations . . 2-25
2.5 Conclusion 2-31

3 Analysis of Interference on Backhaul Data Transmission in VLC Attocell Networks 3-1
3.1 Introduction 3-2
3.2 Physical layer channel model 3-4
3.2.1 Light propagation model 3-5
3.2.2 Optical OFDM 3-6
3.3 Optical Attocell Network Based on VLC Backhaul 3-7
3.3.1 Cellular system 3-8
3.3.2 VLC backhaul configuration 3-8
3.4 Performance Analysis 3-11
3.4.1 Illuminance requirements 3-12
3.4.2 SINR analysis of VLC backhaul 3-13
3.4.2.1 Ma-nLOS (single) backhaul 3-13
3.4.2.2 Ma-nLOS (multi) backhaul 3-16
3.4.2.3 LOS (multi) backhaul 3-17
3.4.3 Channel performance 3-17
3.5 Conclusion 3-23

4 Performance Analysis of Optimization Algorithms for RASP Shadowing Recover Scheme 4-1
4.1 Introduction 4-2
4.2 Optical Attocell Networks 4-5
4.2.1 Network Model 4-5
4.2.2 Visible Light Communication Channel 4-7
4.3 Resilience Scheme 4-9
4.3.1 Control Variables 4-9
4.3.2 RASP Method 4-11
4.3.2.1 Routing Policy (R) 4-11
4.3.2.2 Load Assignment Policy (A) 4-12
4.3.2.3 Subcarrier Allocation Policy (S) 4-12
4.3.2.4 Power Allocation Policy (P) 4-14
4.3.3 Simulations of Performance of RASP Scheme 4-14
4.4 Optimization Methods And Simulations 4-17
4.4.1 Neighbor-Searching Algorithms 4-17
4.4.2 Comparison of Optimization Methods 4-19
4.4.3 An Improved TS Algorithm 4-23
4.5 Conclusion 4-25

5 Misalignment Effect of Wireless Backhaul Links on Downlink Transmission in Optical Attocell Networks 5-1
5.1 Introduction . . . 5-2
5.2 Optical Attocell Networks . . . 5-4
5.2.1 Cellular network . . . 5-4
5.2.2 Illumination requirements . . . 5-6
5.2.3 Resource allocation . . . 5-6
5.3 Misalignment in Cellular Networks . . . 5-9
5.3.1 Impact caused by misalignment . . . 5-9
5.3.2 Misalignment detection . . . 5-11
5.4 Mitigation Strategies for Different Misaligned Scenarios . . . 5-14
5.4.1 Redundant transmission strategy . . . 5-14
5.4.2 Adaptive strategy . . . 5-17
5.5 Conclusions . . . 5-18

6 Conclusion 6-1
6.1 Summary of the major contributions . . . 6-1
6.2 Future research . . . 6-4
6.2.1 Further applications of the simulation model . . . 6-4
6.2.2 Universal standardization of VLC-based backhaul links . . . 6-5
6.2.3 Implementation and testing of recovery schemes . . . 6-5
6.2.4 Cooperative research with SDN . . . 6-6

A Analysis of the Impact of Misaligned Wireless Backhaul Links on Optical Attocell Networks A-1
A.1 Introduction . . . A-2
A.2 System Model . . . A-2
A.2.1 Visible Light Communication . . . A-2
A.2.2 Optical Attocell Network . . . A-4
A.2.3 Frequency Reuse Schemes . . . A-5
A.3 Numeric Analysis . . . A-6
A.3.1 Illumination And Eye Safety . . . A-7
A.3.2 Bandwidth Allocation . . . A-7
A.4 Simulations and Results . . . A-8
A.4.1 Average Spectral Efficiency . . . A-8
A.4.2 Cumulative Distribution Function of ASE . . . A-11
A.5 Conclusions . . . A-15

B Physical Quantities and Units of Light B-1

List of Figures

1.1 Illustration of electromagnetic spectrum including: (a) RF spectrum with illustration of frequency allocation from 30 GHz to 300 GHz provided in [1], texts in the allocation figure denote the usage of the allocated band; (b) IR spectrum; (c) visible light spectrum; (d) UV spectrum 1-2

1.2 The first industrialized LiFi solution co-developed by pureLiFi and Lucibel [2] 1-4

1.3 A typical VLC communication system 1-5

1.4 Working principle of a semiconductor light source [3] 1-6

1.5 Spectral power distribution of two LEDs; spectral data obtained from LSPDD database [4] 1-8

1.6 Lambertian emission patterns (blue and red curves) of two light sources with semi-angles of 60° and 30°; gray contour lines indicate the radiant intensity relative to the central intensity 1-9

1.7 A typical LED output power and input current (P-I) curve 1-9

1.8 Example of information bits modulated with (a) OOK; (b) 4-PPM; (c) general OFDM and two optical OFDM schemes 1-11

1.9 Responsivity of silicon-based PDs in visible light range 1-14

1.10 Circuit diagram of a typical TIA 1-15

1.11 Typical configurations of VLC links 1-17

1.12 CIRs of non-directed-LOS and non-directed non-LOS (diffuse) infrared communication links. Measurements were performed in a 5.5 m$\times$7.5 m room having a 3.5-m-high ceiling. Shadowing was effected by a person standing next to receiver. Detector area was 1 cm^2 [5] 1-17

1.13 MAC topologies supported for VPAN in IEEE 15.7 standardization [6] 1-20

1.14 Network topologies: (a) single-cell-per-user; (b) single-cell-per-room; (c) cellular; darkness of the color indicates the quality of the signal 1-21

1.15 Illustration of the structure of optical attocell networks 1-22

1.16 Wired backhaul network solutions for optical attocell networks: (a) power-line communication (PLC); (b) power-over-Ethernet (PoE); (c) optical fiber; BSs are modular light bulbs (modBulb) for VLC [7]1-24

1.17 Characteristic of wireless transmission: transmission range, detection range, interference range [8] 1-26
1.18 Outline of this doctoral dissertation 1-29

2.1 Backhaul configurations: (a) Wired backhaul links with PoE or PLC; (b) LOS-based wireless backhaul links; (c) Mirror-aided non-LOS wireless backhaul links 2-3
2.2 (a) Geometry of an L-shaped room modeled with a room (B_1), a wall-box (B_2), and an object-box (B_3); (b) A path between two points denoted by $\vec{\mathbf{r_1}}$ and $\vec{\mathbf{r_2}}$ obstructed by a plane at the point $\vec{\mathbf{r}}$. 2-6
2.3 SPD of LED, responsivity of PD and reflectivity of (a) pine wood at incident angle $10°$, (b) white rubberized coating at incident angle $10°$, (c) aluminum at normal incidence angle $0°$ 2-8
2.4 Geometry of (a) a LOS path from a point light source s to a receiver r, (b) a diffusely reflected path from s to r which is reflected off a Lambertian surface with $m = 1$ at a point ε, (c) a specularly reflected path from s to r which is reflected off an ideal mirror at a point ε; blue dash lines denote LOS paths while red vectors denote possible directions and lengths of the vectors denote radiant intensity of light rays 2-10
2.5 (a) Geometry of a specularly reflected path (*mirror-obstructed* LOS path) from s to r; s' denotes the mirror image of s, ε denotes the reflecting point; (b) Multi-bounce specular reflections caused by multiple mirror images of s 2-13
2.6 (a) Differential elements aligned on a Cartesian grid; (b) Elements on two surfaces having opposite orientations; (c) Elements on two intersecting surfaces having perpendicular orientations 2-16
2.7 Multipath impulse responses of one link with configuration A (both senders and receivers are oriented directly downwards) in Environment 1 (purely diffuse); $\Phi_{1/2} = 60°$, $\Theta = 70°$, $\Delta d = 0.2m$, $\Delta\lambda = 20nm$, $K = 7$ 2-22
2.8 Multipath impulse responses of one link with configuration A (both senders and receivers are oriented directly downwards) in Environment 2 (mirror-aided, small); $\Phi_{1/2} = 60°$, $\Theta = 70°$, $\Delta d = 0.2m$, $\Delta\lambda = 20nm$, $K = 7$ 2-22
2.9 Multipath impulse responses of one link with configuration A (both senders and receivers are oriented directly downwards) in Environment 3 (mirror-aided, large); $\Phi_{1/2} = 60°$, $\Theta = 70°$, $\Delta d = 0.2m$, $\Delta\lambda = 20nm$, $K = 7$, ... 2-23
2.10 Mean values and confidence intervals of (a) the calculation error ratio of the DC gain $\xi_{H0^{(K)}}$ and (b) the calculation error ratio of the RMS delay spread $\xi_{\tau^{(K)}_{RMS}}$ 2-26

2.11 SNR of non-LOS VLC channels with different link configurations normalized to the required SNR using uncoded 4-QAM and 64-QAM with the BER requirement of 10^{-6}; (a) S and R oriented directly downwards; (b) S oriented downwards, R oriented towards the mirror. 2-29

2.11 (continued) SNR of non-LOS VLC channels with different link configurations normalized to the required SNR using uncoded 4-QAM and 64-QAM with the BER requirement of 10^{-6}; (c) S oriented towards the mirror, R oriented downwards; (d) S and R oriented towards the mirror. 2-30

3.1 (a) Mirror-aided non-LOS VLC link-based backhaul network; (b)Illumination design with embedded ceiling lamps; (c) Illumination design with diffuse lighting system 3-3

3.2 Geometry of (a) a LOS path from a Lambertian sender s to a receiver r, $\vec{n}_s$ and $\vec{n}_r$ represent orientations of the sender and the receiver, respectively, the red lobe represents the emission pattern of the sender; (b) a mirror-obstructed LOS path from a virtual sender s' (the mirror image of a sender s) to a receiver r 3-5

3.3 (a) Layout of the optical attocell network with cell radius $R = 2\,\mathrm{m}$ and horizontal orientation of auxiliary transceivers; (b) LOS (multi) configuration; (c) ma-nLOS (single) configuration; (d) ma-nLOS (multi) configuration 3-7

3.4 Examples of misalignment of (a) LOS (multi) backhaul configuration and (b) ma-nLOS (multi) backhaul configuration 3-11

3.5 Contour lines of the average illuminance requirement ($750\,\mathrm{lx}$) and the vertical illuminance threshold ($2000\,\mathrm{lx}$) for (a) LOS (multi) backhaul and (b) ma-nLOS (multi) backhaul; shadowed areas are admission regions of power ratio k and semi-angle Φ^b 3-14

3.6 Bandwidth allocation ratio δ of three backhaul configurations with different backhaul semi-angle Φ^b; horizontal misalignment angle $\Delta\theta = 0°$; heights of UEs are $1.15\,\mathrm{m}$ 3-18

3.7 Aggregate data rates of optical attocell networks using different backhaul configurations; horizontal misalignment angle $\Delta\theta = 0°$; heights of UEs are $1.15\,\mathrm{m}$ 3-19

3.8 Data rate ratio $R_{mis}(\Delta\theta)/R(0)$of networks using two backhaul configurations when rotating auxiliary transceivers of (a) BS_0 (gateway) and (b) BS_1 ($\mathcal{T}_1$) against the vertical axis; Φ^b=5°; heights of UEs are $1.15\,\mathrm{m}$. 3-21

3.8 (continued) Data rate ratio $R_{mis}(\Delta\theta)/R(0)$of networks using two backhaul configurations when rotating auxiliary transceivers of (c) BS_7 ($\mathcal{T}_{2^a}$) and (d) BS_{14} ($\mathcal{T}_{2^b}$) against the vertical axis; Φ^b=5°; heights of UEs are $1.15\,\mathrm{m}$. 3-22

4.1 (a) Optical attocell network and (b) wireless backhaul link configurations (hexagons represent cells) 4-3
4.2 Layout of a two-tier optical attocell network 4-6
4.3 Vertical geometry of (a) a LOS link and (b) a mirror-aided non-LOS link; FOV is the filed-of-view of PDs 4-8
4.4 Illustration of (a) blockwise subcarrier allocation and (b) interleaved subcarrier allocation schemes for a BS with seven active LED transmitters, each link from a LED transmitter is represented by a different color 4-13
4.5 Performance of RASP scheme of (a) one-tier network and (b) two-tier network; left axis shows loss of aggregate throughput of unshadowed, shadowed and recovered networks; right axis shows the percentage of throughput loss recovered by RASP 4-15
4.6 Loss of aggregate throughput versus aggregate throughput of one-tier optical attocell networks; PE$-$TS(all) and HC(all)$-$TS(all) denote the difference of ΔT of PE and TS(all) and that of HC(all) and TS(all), respectively; maximum iteration is 20 4-21
4.7 Solutions found by each iteration with HC and TS in a one-tier network with data request with 1.8 Mbps/UE, maximum iteration is 20 4-23
4.8 CDF of loss of aggregate throughput in (a) one-tier networks and (b) two-tier networks with one random shadowed link; each cell has one central UE continuously requesting data rates of 4 Mbps; maximum number of visited solutions are shown in insets 4-26

5.1 VLC backhaul link using (a) LOS link configuration; (b) mirror-aided non-LOS link configuration 5-3
5.2 (a)Horizontal view of a two-tier cellular network; (b)Fixed shortest-path routing 5-5
5.3 Illustration of bandwidth allocation of frequency reuse scheme (a) FR; (b) IB mode 1; (c) IB mode 2; (d) IB mode 3; B is the electrical bandwidth available for one BS 5-7
5.4 Examples of misalignment of ma-nLOS (multi) backhaul configuration; horizontal misalignment angle $\Delta\theta_{max} = 30^\circ$ 5-10
5.5 SINR of link BS0 to BS1 with different horizontal misalignment angles 5-11
5.6 Frequency domain of HELLO messages and ACK messages in OMACK-based detection process with IB mode 2 5-12
5.7 An example of redundant transmission using IB mode 2 5-15
5.8 Aggregate data rate of networks using FDM and redundant transmission; $R = 2\,\mathrm{m}$; heights of UEs and BSs are $1.15\,\mathrm{m}$ and $2.85\,\mathrm{m}$, respectively 5-16
5.9 CDF of aggregate data rates of two-tier ring-type optical attocell network with random misalignment angles; $R = 2\,\mathrm{m}$; heights of UEs and BSs are $1.15\,\mathrm{m}$ and $2.85\,\mathrm{m}$, respectively 5-17

A.1 (a) LOS link configuration; (b) Mirror-aided non-LOS link configuration; (c) Two-tier optical attocell network with central gateway A-3
A.2 Illustration of spectrum allocation of frequency reuse scheme (a) FR; (b) IB mode 1; (c) IB mode 2; B is the electrical bandwidth available for one BS A-5
A.3 Average spectral efficiency of networks using (a) LOS backhaul configuration with $\Delta\theta = 0^\circ$; (b) LOS backhaul configuration with $\Delta\theta = 27^\circ$. A-9
A.3 (continued) Average spectral efficiency of networks using (c) Mirror-aided non-LOS backhaul configuration with $\Delta\theta = 0^\circ$; (d) Mirror-aided non-LOS backhaul configuration with $\Delta\theta = 27^\circ$. A-10
A.4 CDF of maximum ASE of networks using (a) LOS backhaul configuration in the noise-limited regime; (b) LOS backhaul configuration in the interference-limited regime; (c) Mirror-aided non-LOS backhaul configuration in the interference-limited regime . . A-12

List of Tables

2.1 Simulation environments 2-19
2.2 Materials and reflectivity of surfaces 2-19
2.3 Link configurations 2-20
2.4 Channel parameters 2-28

3.1 Simulation parameters 3-19

4.1 Simulation parameters 4-17
4.2 Maximum number of visited solutions 4-23

5.1 Simulation parameters 5-11
5.2 Time slot allocation for HELLO/ACK processes 5-12
5.3 Transition angle 5-16

A.1 Best auxiliary semi-angle to achieve the maximum of expected value of ASE A-14

B.1 Radiometric quantities and units B-2
B.2 Photometric quantities and units B-2

List of Acronyms

A

AC	Alternating Current
ACK	ACKnowledgment
ACO	Asymmetrically Clipped Optical
ADC	Analog-to-Digital Converter
AM	Amplitude Modulation
AGC	Automatic Gain Control
AP	Access Point
ASE	Area Spectral Efficiency
AWGN	Additive White Gaussian Noise

B

BER	Bit Error Rate
BS	Base Station

C

CCD	Charge Coupled Device
CCI	Co-Channel Interference
CDF	Cumulative Distribution Function
CIR	Channel Impulse Response
CMOS	Complimentary Metal Oxide Semiconductor
CP	Cyclic Prefix
CPU	Central Processing Unit
CRI	Color Rendering Index

D

DAC	Digital-to-Analog Converter
DCO	Direct Current biased Optical
DD	Direct Detection
DF	Decode and Forward
DSP	Digital Signal Processor

F

FCC	Federal Communication Commission
FDMA	Frequency Division Multiple Access
FEC	Forward Error Correction
FFT	Fast Fourier Transformation
FM	Frequency Modulation
FOV	Field Of View
FPGA	Field Programmable Gate Arrays
FR	Fully Reused
FSO	Free Space Optical

G

GaN	Gallium Nitride
GPS	Global Positioning System

H

HC	Hill Climbing

I

IB	In Band
IFFT	Inverse Fast Fourier Transformation
IM	Intensity Modulation
INR	Interference-to-Noise Ratio

IoT	Internet of Things
IR	Infrared
ISI	Inter-Symbol Interference

L

LaaS	Light-as-a-Service
LD	Laser Diode
LED	Light Emitting Diode
LOS	Line Of Sight
Li-Fi	Light Fidelity

M

MAC	Medium Access Control
ma-nLOS	mirror-aided non Line Of Sight
MIMO	Multiple-Input Multiple-Output
mmWave	millimeter Wave
MOSFET	Metal Oxide Semiconductor Field Effect Transistor
MSD	Multi-spot Diffuse

O

OCC	Optical Camera Communication
OOK	On Off Keying
op-amp	operational amplifier
OFDM	Orthogonal Frequency Division Multiplexing
OWC	Optical Wireless Communication

P

PD	Photo Diode
PE	Partial Enumeration
PHY	Physical
PLC	Power Line Communication
PM	Phase Modulation

PoE	Power over Ethernet
PPM	Pulse Position Modulation
PSD	Power Spectral Density
PSE	Power Sourcing Equipment
PWM	Pulse Width Modulation

Q

QAM	Quadrature Amplitude Modulation

R

RGB	Red, Green, Blue
RHR	Radius Height Ratio
RMS	Root Mean Square
RF	Radio Frequency
RSS	Rceived Signal Strength

S

SDN	Software Defined Networking
SIFS	Short Inter-Frame Space
SINR	Signal-to-Interference-plus-Noise Ratio
SNR	Signal-to-Noise Ratio
SPD	Spectral Power Distribution
SSL	Solid State Lighting

T

TED	Technology, Entertainment, Design
TIA	Trans-Impedance Amplifier
TS	Tabu Search

U

UE	User Equipment
UV	Ultra Violet

V

VLC	Visible Light Communication
VPAN	Visible Light Communication Personal Area Network

W

WDMA	Wavelength Division Multiple Access
Wi-Fi	Wireless Fidelity
WLAN	Wireless Local Area Network
WPAN	Wireless Personal Area Network

Nederlandse samenvatting –Summary in Dutch–

In ons dagelijks leven vervullen indoor draadloze netwerken een belangrijke rol. Als gevolg van de Covid-19 pandemie blijven de mensen dikwijls thuis om fysieke contacten te vermijden. De nood aan communicatie via het Internet, zowel voor professionele als vrijetijdsdoelen, is dan ook sterk toegenomen in 2020. Het aantal mobiele applicaties kent in de huidige tijden een spectaculaire groei. Vele mobiele applicaties hebben een betrouwbare Internetconnectie nodig. Sommige applicaties vereisen hoge bandbreedte voor draadloze communicatie. Het radiofrequentie (RF) spectrum, dat gebruikt wordt voor de huidige draadloze lokale netwerken (WLANs), kent een beperkte bandbreedte. Vanwege de explosief groeiende vraag naar indoor draadloos verkeer, wordt het RF spectrum drukker en drukker.

Vele onderzoekers stelden voor om hogere frequenties in het elektromagnetisch spectrum aan te boren. Meer recent heeft communicatie via zichtbaar licht (VLC) aanzienlijke wetenschappelijke aandacht gekregen. VLC gebruikt commercieel verkrijgbare licht-emitterende diodes (LEDs) en fotodiodes (PDs) om gegevens via zichtbaar licht over te brengen. Indoor draadloze netwerken gebaseerd op zichtbaar licht voor gegevenscommunicatie, dikwijls optische attocel netwerken genoemd, worden vooropgesteld als aanvulling op RF-gebaseerde netwerken. In dergelijke optische draadloze netwerken, worden LED lampen gebruikt als basisstations (BSs) die communiceren met gebruikersapparatuur (UEs) via zichtbaar licht. Deze communicatielinks vormen een toegangsnetwerk. Dit toegangsnetwerk is verbonden met het Internet via een backhaul netwerk bestaande uit communicatielinks tussen BSs en een gateway. Bedrade backhaul netwerken versturen gegevens door kabels. Hierbij zijn hoge kosten en complexiteit bij installatie en onderhoud onvermijdelijk. Gebruik van VLC voor backhaul communicatie is dan ook voor de hand liggend, omdat een dergelijk netwerk kost-efficiënt is en geen extra kabels of controle-eenheden vereist. Er zijn evenwel vele uitdagingen bij VLC-gebaseerde backhaul netwerken. Ten eerste, alhoewel een directe lichtstraal (LOS: line-of-sight) communicatie met hoge bandbreedte toelaat, is de LOS voorwaarde niet altijd vervuld bij indoor toepassingen. Niet-LOS VLC verbindingen zijn onderhevig aan multipad-effecten en en zullen weinig betrouwbare backhaul verbindingen realiseren. Bovendien worden VLC verbindingen afgeblokt door menselijke lichamen of meubels, aangezien zichtbaar licht niet doorheen opake objecten kan dringen. Dit schaduweffect degradeert niet alleen de prestaties van het backhaul netwerk maar ook van het toegangsnetwerk. Tenslotte hangt de pres-

tatie van VLC-gebaseerde backhaul verbindingen ook af van de goede alignering van LEDs en PDs.

Om deze uitdagingen aan te pakken, wordt in dit proefschrift een nieuw VLC-gebaseerd backhaul netwerk voorgesteld, gebaseerd op niet-LOS signalen met behulp van spiegels. Het doel van dit proefschrift is om een robuust backhaul netwerk te bouwen gebaseerd op deze principes. Deze configuratie kan gebruikt worden bij vele indoor toepassingen waarbij de LOS voorwaarde niet kan verzekerd worden.

De eerste helft van het proefschrift focust op de prestatie-analyse. In hoofdstuk 2 wordt de prestatie van een enkelvoudige VLC link geanalyseerd. De kanaalprestatie wordt ingeschat a.d.h.v. een simulatiemodel voorgesteld in dit hoofdstuk. Dit model simuleert accurate kanaalimpulsantwoorden van VLC links bij diverse configuraties. Hierbij wordt rekening gehouden met de spectrale informatie van VLC links. Zowel spiegelende als diffuze weerkaatsingen worden gesimuleerd. Dit model is accurater en sneller dan bestaande modellen. Gebruik makend van dit model hebben we in kaart gebracht dat eerste-orde spiegelende weerkaatsingen het multipad-effect van niet-LOS links significant kan verminderen. Deze eerste-orde spiegelende weerkaatsingen kan men realiseren door kleine spiegels of glimmende tegels op de vloer of op tafels.

In hoofdstuk 3 gaan we verder in op de prestatie van spiegelgebaseerde niet-LOS links in een backhaul netwerk. Aangezien de backhaul hulpLEDs in dat geval naar de vloer gericht zijn, kan interferentie tussen toegangs- en backhaul links niet vermeden worden. We beoordelen de netwerkprestatie a.d.h.v. de geaggregeerde datastroom, dit is de som van de eind-tot-eind datastromen naar alle gebruikers (UEs) in het netwerk. Deze geaggregeerde datastroom wordt bepaald door de signaal-tot-interferentie-plus-ruis verhouding (SINR) van de links. We vergelijken de netwerkprestaties bij verschillende gezichtswijdtes van LEDs en PDs. Om een eerlijke vergelijking toe te laten, wordt de signaalsterkte telkens ingesteld conform de verlichtings- een oogveiligheidsvoorschriften. Een directe LOS link en 2 spiegelgebaseerde niet-LOS links (hybride en directe) worden gesimuleerd en vergeleken. De resultaten tonen aan dat de spiegelgebaseerde niet-LOS links geen goede prestaties kunnen bereiken, vanwege de hoge interferentie tussen toegangs- en backhaul links. Een eenvoudige, vaste frequentieplanning wordt voorgesteld, om die interferentie te omzeilen. Simulaties tonen aan dat de prestatie van de directe spiegel-gebaseerde niet-LOS backhaul links kan verbeterd worden via deze frequentieplanning.

In de tweede helft van het proefschrift, stellen we strategieën voor om twee uitdagingen van spiegelgebaseerde niet-LOS backhaul links aan te pakken: het schaduweffect en uitlijningsfouten. Het schaduweffect is een grote uitdaging bij algemene optische attocel netwerken. Dit is a fortiori het geval bij spiegelgebaseerde niet-LOS backhaul links, omdat de LEDs voor toegangs- en backhaullinks beide naar de vloer gericht zijn en zo dikwijls gehinderd worden door mensen die zich bewegen in de ruimte. Om dit probleem aan te pakken, stellen we meerlaags herstelschema RASP voor in hoofdstuk 4. RASP verbetert de prestatie van netwerken onderhevig aan schaduweffecten, via optimale of bijna-optimale controlemechanismen zoals routeeralgoritmen en frequentieschema's. Onze simulaties

tonen aan dat zo meer dan 90% van de verliezen kunnen hersteld worden, in het geval van netwerken met lage bandbreedtevereisten. Om de zoektocht naar (bijna-)optimale controlemechanismen te versnellen, vergeleken we verschillende optimalisatietechnieken en stellen we Tabu Search met gesplitste burenverzamelingen voor. Deze methode beperkt de zoektijd aanzienlijk, en levert bij schaduweffecten meer kans op geen verliezen.

Uitlijningsfouten bij de backhaul links veroorzaken prestatiedegradatie bij optische attocel netwerken. De SINR van de backhaul links wordt aanzienlijk slechter als zender of ontvanger slecht uitgelijnd zijn. Om dit probleem aan te pakken, stellen we twee strategieën voor in hoofdstuk 5. De eerste strategie gebruikt naburige backhaul zenders om extra (redundante) informatie te versturen. Via een goede frequentieplanning wordt interferentie vermeden. Deze strategie bewijst haar nut vooral als de uitlijningsfout groter wordt dan een bepaalde drempelhoek. Aangezien de prestatie van deze redundante strategie pover is bij kleine uitlijningsfouten (in vergelijking met de vaste frequentieplanning), stellen we een tweede strategie voor die de methode aanpast op basis van de grootte van de uitlijningsfout. Deze adaptieve strategie kan hoge datastromen realiseren in netwerk met randomgegenereerde uitlijningsfouten. Om de uitlijningsfout in te schatten, wordt een protocol opgesteld in dit hoofdstuk.

Het proefschrift eindigt met een conclusie-hoofdstuk. Hierbij worden voornaamste bijdragen van dit doctoraat opgesomd en wordt een overzicht gegeven van mogelijke toekomstige onderzoekspistes.

English summary

Indoor wireless networks have been playing an important role in our everyday lives. Due to the Covid-19 pandemic, people have to stay at home to avoid physical contact. The need for communication through the Internet, for both work and entertainment purposes, has been increasing since the year 2020. Nowadays, the number of mobile applications dramatically grows. Many mobile applications need a reliable Internet connection, some of them require a large amount of bandwidth for wireless communication. Radio frequency (RF) spectrum used for current wireless local area networks (WLANs) is a limited resource. Due to the booming demand for indoor wireless traffic, the RF spectrum becomes more and more crowded.

Many researchers proposed to use resources with higher frequencies in the electromagnetic spectrum. Recently, visible light communication (VLC) has attracted considerable scientific interests. VLC uses off-the-shelf light-emitting-diodes (LEDs) and photodiodes (PDs) to transmit data via visible light. Indoor wireless networks using VLC for data communication, typically called optical attocell networks, have been proposed to complement the RF-based WLANs. In optical wireless networks, LED lamps are base stations (BSs) which communicate with user equipment (UEs) using VLC. These communication links form an access network. The access network is connected to the Internet through a backhaul network which consists of communication links between BSs and a gateway. Wired backhaul networks send data through cables. High cost and complexity for installation and maintenance are inevitable. Using VLC for backhaul data transmission is straightforward, as the VLC-based backhaul network is cost-efficient and does not require extra cables or control units. However, there are many open issues for VLC-based backhaul networks. First, although the line-of-sight (LOS) VLC link can achieve high data rates, the LOS condition may not be fulfilled in many indoor applications. Non-LOS VLC links suffer from multipath effects and cannot provide reliable backhaul data transmission. Moreover, VLC links are blocked by human bodies or furniture as the visible light cannot pass through opaque objects. This shadowing effect degrades the performance of not only VLC backhaul links, but also access links. Finally, the performance of VLC-based backhaul links depends on the alignment of auxiliary LEDs and PDs which are used for backhaul communication.

To address these issues, a novel VLC-based backhaul network using the mirror-aided non-LOS configuration is presented in this dissertation. This backhaul link configuration can be used in many indoor applications when the LOS condition

cannot be ensured. The purpose of this dissertation is to design a robust mirror-aided non-LOS VLC link-based backhaul network.

The first half of this dissertation focuses on the performance analysis. In Chapter 2, the performance of a single VLC link is analyzed. The channel performance is assessed by a simulation model proposed in this chapter. The model is developed to simulate accurate channel impulse responses of VLC links with different configurations. The spectral information of VLC links is taken into account. In addition, both specular and diffuse reflections can be simulated. This model is more accurate and time-efficient than existing models. By using this model, we simulate VLC links with different configurations and find out that adding the first-order specular reflection can significantly reduce the multipath effect of non-LOS links. The first-order specular reflection can be obtained by placing small mirrors or glossy tiles on the floor or tables.

In Chapter 3, we further analyze the performance of mirror-aided non-LOS backhaul links in a network. As auxiliary LEDs of mirror-aided non-LOS backhaul links are oriented towards the floor, interference between VLC access links and backhaul links cannot be avoided. We assess the performance of networks using mirror-aided non-LOS backhaul links in terms of the aggregate data rate, which is the sum of the end-to-end data rates of all UEs in the network. The end-to-end data rate is determined by the signal-to-interference-plus-noise ratio (SINR) of the link. We compare the network performance when applying different viewing angles of LEDs and PDs. To ensure fair comparison, the transmitted power is configured according to the illumination and eye-safety requirements. A directed LOS link and two mirror-aided non-LOS links (hybrid and directed) are simulated and compared. Results show that mirror-aided non-LOS backhaul links cannot achieve good performance due to large interference between access and backhaul links. A simple static frequency planning is proposed to mitigate the interference between access and backhaul links. Simulation results reveal that the performance of the directed mirror-aided non-LOS backhaul links can be improved by the static frequency planning method.

In the second half of the dissertation, we present strategies to address two challenges faced by mirror-aided non-LOS backhaul links: the shadowing effect and the misalignment effect. The shadowing effect is a major challenge of general optical attocell networks. The performance degradation caused by the shadowing effect is much more significant for networks using mirror-aided non-LOS backhaul links, as LEDs used for access and backhaul communication are both oriented towards the floor and will be blocked by people roaming in the room. To address this issue, we propose a cross-layer resilience scheme RASP in Chapter 4. The RASP improves the performance of shadowed networks by finding the optimal or near-optimal control policies such as routing algorithms and frequency allocation schemes. Simulation results show that more than 90% of throughput losses can be recovered in networks with low throughput requirements. To reduce the time for searching the (near-)optimal control policies, we compare different optimization algorithms and propose to use Tabu search with decomposed neighbor sets. This method significantly reduces the searching time and has larger probability to get

zero throughput loss when shadowing occurs.

Misaligned backhaul links will cause performance degradation in optical attocell networks. The SINR of the backhaul link is decreased when the transmitter or the receiver is misaligned. In order to mitigate the misalignment effect, we propose two strategies in Chapter 5. The first strategy, a redundant transmission strategy, uses neighboring backhaul transmitters to send redundant data. Interference is avoided by using a proper frequency planning. This strategy becomes beneficial when the misalignment angle becomes larger than a certain threshold. As the performance of the redundant transmission strategy is not comparable to a static frequency division multiplexing when the misalignment angle is small, we propose an adaptive strategy which chooses proper methods for different misalignment angles. The adaptive strategy can achieve higher aggregate data rates in networks with random misalignment angles. To detect the misalignment angle, a protocol is also proposed and presented in this chapter.

At the end of the dissertation, a concluding chapter is presented. A summary of major contributions of this dissertation and an overview of possibilities of future research are presented.

1 Introduction

In the last decade, we have experienced a more and more digital world. The rapid growth of mobile devices, e.g. smartphones and tablets, have benefited from improved hardware technologies. A rich number and a variety of application software available on both desktop and mobile devices have changed our lifestyle and work style. For example, streaming media and real-time video games are welcoming leisure and entertainment activities. Video conferencing has been widely used as it is highly convenient for users in different locations. Due to the demand for huge volumes of real-time data transmission, the quality of these applications depends on the capacity of the network.

The network access of mobile devices is mostly wireless. The well-known indoor wireless technology, Wireless-Fidelity (Wi-Fi), has been deployed in many private and public spaces. With the development of generations, Wi-Fi exploits radio-frequency (RF) resources up to $6\,\mathrm{GHz}$. One drawback of using the RF spectrum is that the transmission power of RF devices is strictly regulated to a certain level to avoid causing health risks to human bodies. In addition, RF is a costly resource for every network service provider. Many governments use an auction system to sell licenses of the specific bands in order to efficiently allocate the RF spectrum to network service providers. Since 1994, Federal Communication Commission (FCC) has conducted more than 100 spectrum auctions. The illustration of the electromagnetic spectrum from $3\,\mathrm{Hz}$ to $30\,\mathrm{PHz}$ is shown in Fig.1.1. A fraction of the RF spectrum allocated by FCC (from $30\,\mathrm{GHz}$ to $300\,\mathrm{GHz}$) is also shown in the figure. It can be seen that the RF spectrum ranging from $3\,\mathrm{Hz}$ to $300\,\mathrm{GHz}$ (Fig.1.1(a)) is crowded. In contrast, the optical spectrum starting from $300\,\mathrm{GHz}$

(1 mm wavelength) to 30 PHz (10 nm wavelength) is an unregulated license-free resource. Therefore, optical wireless communication (OWC) using the license-free optical spectrum has been proposed to complement indoor RF-based technologies without interfering with currently used Wi-Fi devices.

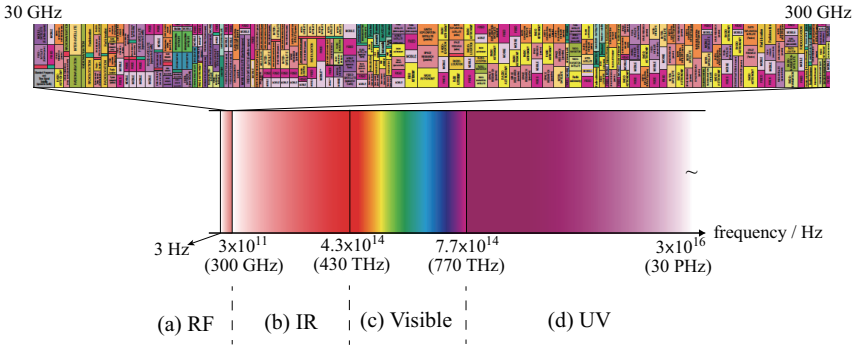

Figure 1.1: Illustration of electromagnetic spectrum including: (a) RF spectrum with illustration of frequency allocation from 30 GHz *to* 300 GHz *provided in [1], texts in the allocation figure denote the usage of the allocated band; (b) IR spectrum; (c) visible light spectrum; (d) UV spectrum*

The optical spectrum includes the infrared (IR) spectrum (300 GHz-430 THz), the visible light(VL) spectrum (430-750 THz), and the ultra-violet (UV) spectrum (750 THz-30 PHz) as shown in Fig.1.1(b)-(d), respectively. The OWC system operating in the VL spectrum is referred to as visible light communication (VLC). VLC systems use existing light-emitting-diode (LED) lamps for simultaneous illumination and data transmission. Low-cost and off-the-shelf photo-diodes (PDs) can be used to detect the signal transmitted by LED lamps. Unlike the other two spectra, communication systems based on the VL spectrum do not cause health hazards [9]. Although VLC systems do not cause severe health problems, there still exist eye-safety regulations. The eye-safety regulations mitigate the flicker of light which can cause noticeable, negative/harmful physiological changes in human eyes [10].

An optical attocell network is based on VLC and uses LED lamps as base stations (BSs). Mobile devices, which are normally called user equipment (UE), communicate with BSs via an access network. The communication links between BSs form a backhaul network. The backhaul network can be wired or wireless. Wired backhaul network technologies send data transmission through cables. Some wired backhaul technologies can simultaneously provide data and power supply via the same cable. Wireless backhaul networks use RF or VLC for data transmission. Among these backhaul solutions, the VLC-based backhaul network is a natural choice for optical attocell networks as the VLC control units have been already embedded in BSs for access data transmission.

In this doctoral dissertation, we investigated the performance of a VLC-based backhaul network with a link configuration based on mirror reflections. We presented a novel time-efficient simulation model for conducting simulations of arbitrary VLC links including the proposed mirror-based link configuration. Research on strategies for addressing current issues of the VLC-based backhaul network was performed. To better understand the necessity and research challenges of the robust VLC-based backhaul network, we introduce the concept of VLC technologies and optical attocell networks as well as the related challenges further in the next sections. In section 1.1, the basic concept and technologies used for VLC are introduced. Next, section 1.2 explains the motivation and illustrates the structure of VLC-based optical attocell networks. Finally, in section 1.3, state-of-the-art and challenges of optical attocell networks are clarified.

1.1 A brief introduction of VLC

Data transmission using OWC has been proposed for many years. Optical communication was first proposed in the early 60s. Free space optical (FSO) communication using laser diodes (LDs) was mainly used for air-to-air, satellite-to-submarine, air-to-submarine, air-to-satellite, and satellite-to-satellite applications [11]. With the development of optical components including light sources and detectors, indoor OWC systems have drawn scientific interests over the past decades. A pioneering work showed the potential of a low-cost indoor OWC system for low to medium speed data transmission [12]. The OWC system was based on LEDs operating in the IR spectrum. In recent years, visible LEDs operating in the range $400\,\mathrm{THz}$-$790\,\mathrm{THz}$ have been well developed and widely used for indoor lighting systems. Tanaka *et al.* first proposed a VLC system using white colored LEDs [13, 14]. In 2011, a point-to-point VLC system was demonstrated in Technology, Entertainment, Design (TED) Global Talk, and the term light-fidelity (Li-Fi) was first used to refer to a subset of VLC technology which exhibits high-speed, bidirectional, and fully networked communications. In 2016, LiFi solutions provided by pureLiFi and Lucibel are available in the market (Fig.1.2). The Li-Fi, as well as the VLC technology, have gained scientific interest as they complement current RF-based indoor communication networks, i.e. Wi-Fi, without interference.

The potential of the VLC market is also boosted by the popularity of indoor LED lighting. Residential LEDs use less energy and last longer than incandescent lighting. The United States Department of Energy estimates that faster adoption rate of LED lighting in the United States (US) over the next 20 years can deliver energy savings of about US dollar (USD) 265 billion and reduce the demand for lighting electricity by 33% in 2027 [15]. The inevitable growth of LED lighting systems reveals the potential of the VLC market. The overall VLC market is ex-

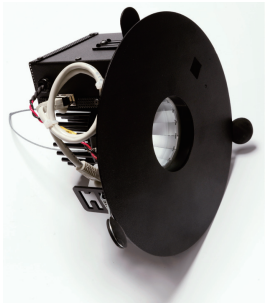

Figure 1.2: The first industrialized LiFi solution co-developed by pureLiFi and Lucibel [2]

pected to grow from USD 6.8 billion in 2020 to USD 200.1 billion by 2025. The Asia-Pacific region is expected to be the fastest-growing market for VLC and Li-Fi technology [16]. An associate member of the European 5G public-private partnership (PPP), the company OpticWise, also proposed LiFi as a candidate technology for the fifth-generation (5G) network [17].

A typical VLC communication system consists of three components: the **transmitter**, the **receiver** and the **VLC channel**. A simple illustration of the VLC system is shown in Fig.1.3. The transmitter and the receiver convert an electrical signal to and from an optical signal. The **modulator** constructs the input data (normally represented in bits) to the signal which is carried by the visible light emitted by the **light source**. An **optical system** can be used to further shape the light beam. At the receiver side, the **optical system** is used to filter the light such that the ambient light and noises/interference at unwanted wavelength are removed. The **light detector** converts the optical signal back to the electrical current and the **demodulator** reconstructs the information bits. The **VLC channel** is the most important and complicated component in the VLC system. The optical signal travels unguided in the free space. Light rays arrive at the receiver via multiple paths. The intensity and the delay of the received light rays depend on the lengths of the paths and the reflectivity of all possible reflecting surfaces. The quality of the VLC channel highly depends on the environment and the configuration of the transmitter and the receiver. In this section, we explain each component of the VLC system separately. The mechanism of the LED emission and modulation schemes are explained in subsection 1.1.1. In subsection 1.1.2, we introduce the technology used for optical-electrical conversion at the optical receiver. The signal is carried by the visible light illuminating an indoor environment. In order to ensure high-quality indoor illumination while transmitting high-speed signals, VLC uses intensity modulation and direct detection (IM/DD) technology which will be introduced in the next subsection 1.1.3. Different configurations of transmitters and receivers and their performance will also be discussed in 1.1.3.

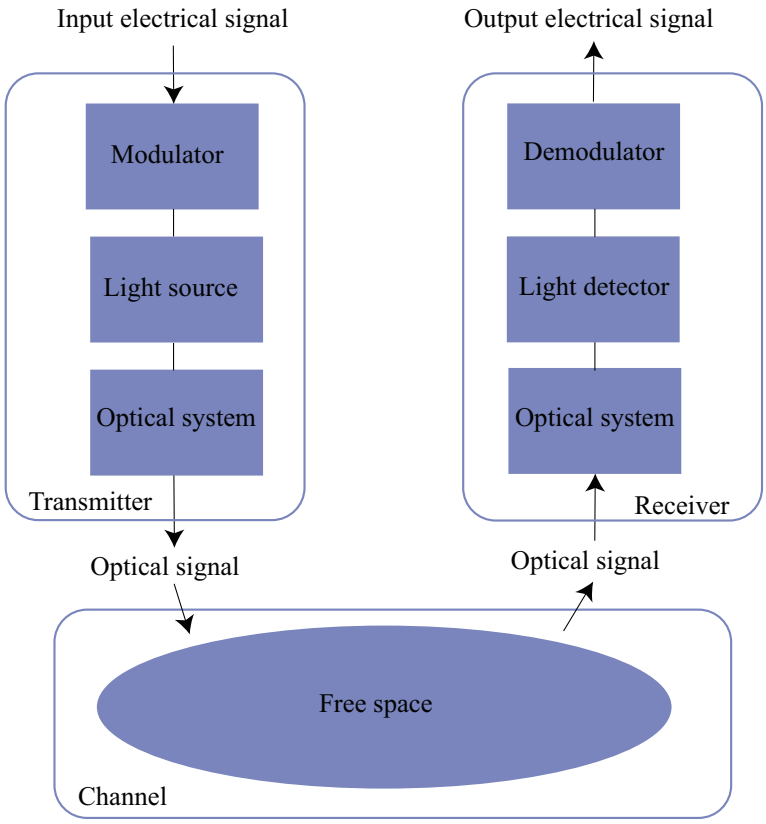

Figure 1.3: A typical VLC communication system

1.1.1 VLC transmitters

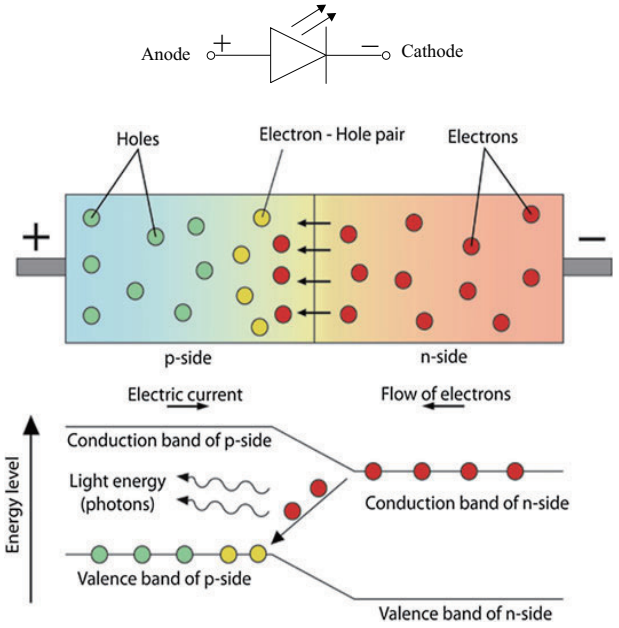

Figure 1.4: Working principle of a semiconductor light source [3]

The main component of a VLC transmitter is the **light source**. Nowadays, solid-state lighting (SSL) like laser diodes (LDs) and light-emitting-diodes (LEDs) have been commercialized and widely used. With the continuous improvement of the performance and the reduction of the cost, SSL has emerged to be a realistic replacement of traditional light sources like incandescent and fluorescent lamps for indoor usages [18]. Compared to traditional light sources, SSL has a longer lifetime (about three times the lifetime of fluorescent and 50 times that of incandescent sources [19]) and higher energy efficiency (50% the energy consumption compared to that of fluorescent lamps [20]). Thus, SSL is considered the most viable light source for low-cost VLC systems.

The working principle of an SSL is based on the *p*-*n* junction of the solid-state semiconductor. The illustration of the principle of a semiconductor light source is shown in Fig.1.4. The *p*-*n* junction is a fusion of *p*-type- and *n*-type-doped semiconductor crystals. The *p*-type dopant has a high number of empty slots or so-called "holes", while the *n*-type dopant has a high number of valence electrons. When a forward bias voltage is applied to the *p*-*n* junction (the voltage applied to the *p*-side is higher than that to the *n*-side), the electrons residing in the *n*-side are forced to move towards the *p*-side. These electrons recombine with the holes in the *p*-side. From the point of view of the energy level, the electrons pass from

the conduction band to the valence band. This means that the electrons have to release excessive energy. The magnitude of the excessive energy is determined by the materials (the type of the *p*- and *n*-type dopants). This energy is released as photon energy which induces electromagnetic radiation with a certain wavelength. The equation

$$E = hf = \frac{hc}{\lambda} \tag{1.1}$$

can be used to describe the relationship between the energy and the wavelength, where $h = 6.626 \times 10^{-34}\ \mathrm{J \cdot Hz^{-1}}$ is the Planck's constant, $c = 3 \times 10^{8}\ \mathrm{m \cdot s^{-1}}$ is the speed of the light, E is the photon energy and λ is the wavelength of the emitted photon.

The purpose of a light source is to convert electricity to visible light. An efficient light source uses less electrical power to produce artificial light. At the IR spectrum, LDs are known as the most efficient converters with electrical-to-optical efficiency of 76%. However, the extremely high efficiency demonstrated in the near IR has not been achieved in the VL spectrum [21]. The efficiency of LDs in the VL spectrum depends on the wavelength, i.e. the color of LDs. The emission spectrum of LDs is extremely narrow ($< 1\ \mathrm{nm}$). A light source with three or four discrete laser lines (red-green-blue or red-yellow-green-blue) far from fills the visible spectrum [22]. In addition, the low internal quantum efficiency in the green makes achieving a laser at green and yellow wavelengths extremely challenging. As LDs need to mix colors to produce white light, a lot of efforts have to be made in order to efficiently use LDs for the emission of white artificial light.

LEDs are a simple and low-cost alternative to LDs. The efficiency of white LEDs at $30\ ^{\circ}\mathrm{C}$ is 42% and the efficiencies may be around 20% for a wide range of elevated temperatures [23]. Commercial available LEDs generate white light by using two methods: blue LEDs coated with phosphor or mixing red, green, and blue (RGB) colors [10]. Phosphor is a type of wavelength-converter material. The photon from the blue light emitted by the LED has high energy. When this photon passes through the phosphor layer, it is absorbed in the phosphor and excites the electron in the phosphor to higher energy. This excited electron wanders through the crystal lattice. After losing some energy, it falls back to its ground state energy level and emits a photon of lower energy. From Eq.(1.1) we can know that the photon with lower energy has a longer wavelength, normally yellow or red. Not all photos from the blue light are absorbed by the phosphor. Photons leaking through the phosphor layer will not change color. As a result, the light emits light with two different wavelengths: the yellow or red light emitted from the phosphor and the remaining blue light leaking through the phosphor layer. The combination of the light with different wavelengths is perceived as white by human eyes [24]. RGB LEDs combine three single-color LEDs (red, green, and blue) and configure the power emitted by each LED. The radiant flux, which is also called optical

power, of the LED emitted at different wavelengths is adjusted by an eye sensitivity function in order to produce white light. The spectral power distribution (SPD) of a phosphor-based LED and a RGB LED is shown in Fig.1.5.

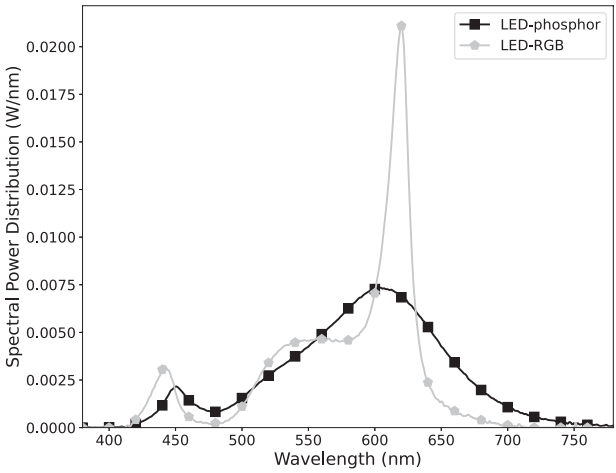

Figure 1.5: Spectral power distribution of two LEDs; spectral data obtained from LSPDD database [4]

The radiant light of LEDs is not in a single direction. The radiation pattern of LEDs is generally modeled as a Lambertian emission pattern. The Lambertian emission pattern is described by the Lambertian cosine law. The Lambertian cosine law is normally described by the radiant intensity of a light source, which is the radiant optical power in a given direction per unit solid angle. One unit solid angle corresponds to one unit of area on the unit sphere surrounding the light source. A light source that obeys the Lambertian cosine law radiates light in all directions. The radiant intensity of a light ray emitted from the source is directly proportional to the cosine of the angle between the direction of the ray and the surface normal (orientation):

$$I = I_0 \cos\theta, \tag{1.2}$$

where I_0 is the maximum radiant intensity at the surface normal, and θ is the angle between the emission direction and the surface normal. An important parameter of LEDs is the semi-angle $\Phi_{1/2}$ of half intensity. The radiant intensity at the angle $\Phi_{1/2}$ is half of the central radiant intensity I_0. Thus, this parameter can be used to describe how concentrated the emitted light is. An example of Lambertian emission patterns of two light sources with semi-angles of 60° and 30° are shown in Fig.1.6. A light source with a smaller semi-angle (the red pattern) has a more concentrated light beam. It is also clearly shown that a Lambertian light source does not emit light with angles greater than 90° as the light intensity cannot be negative.

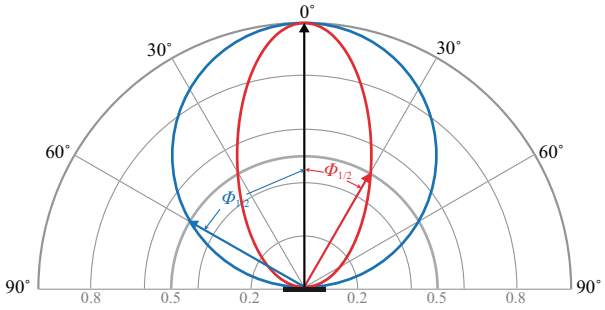

Figure 1.6: Lambertian emission patterns (blue and red curves) of two light sources with semi-angles of 60° *and* 30°*; gray contour lines indicate the radiant intensity relative to the central intensity*

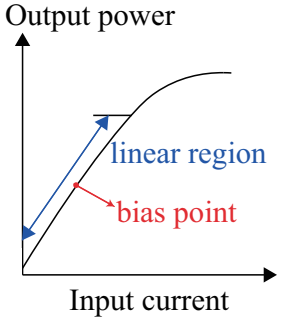

Figure 1.7: A typical LED output power and input current (P-I) curve

LEDs are solid-state semiconductors which are driven by the forward current. The forward current is generated by putting a voltage across the diode in the direction that allows the current to flow easily. Such a condition is called forward bias. The voltage must be large enough to generate an electrical current. When the voltage is below a threshold voltage, no current flows through the LED. When the LED is forward biased to the threshold voltage, the electrical current flows and increases rapidly. Within a certain range, the output optical power is linearly proportional to the electrical current. This range is normally referred to as the linear region of LEDs. The light emission saturates when the electrical current exceeds a certain level. The modulation characteristic of an LED is described with optical power and electrical current (P-I curve) as shown in Fig.1.7. LEDs normally work in the linear region to ensure linearity. In order to send data via visible light, LEDs use intensity modulation (IM) which represents the envelope of the signal by the instantaneous optical power of the light. IM requires rapid changes of the output optical power in time. When a bias point is determined, the output optical power is changed by tuning the electrical current around the bias current within the linear region. Modulation bandwidth is used to describe how fast an LED can change its output optical power. Typically, the modulation bandwidth is defined as the frequency of the drive current for which the amplitude of the modulated optical output has decreased by a factor of 2 compared to the case of a low-frequency drive current. This is also called the 3-dB electrical modulation bandwidth of LEDs. The modulation bandwidth depends on the semiconductor materials and varies with the type of LEDs. The theoretical maximum bandwidth of LEDs is $2\,\mathrm{GHz}$ [25]. Commercial-available LEDs normally have very small modulation bandwidths. Phosphor-based LEDs have a modulation bandwidth of a few MHz as the frequency response of the phosphor is limited. RGB LEDs have larger bandwidth ($\sim 20\,\mathrm{MHz}$) than phosphor-based LEDs. Recently, many researchers propose to use different materials and structures for LEDs in order to approach the theoretical maximum bandwidth. For example, several hundreds of MHz bandwidth using gallium nitride (GaN)-based micro-LEDs has been demonstrated in [26] and [27].

In order to drive LEDs with information-carried current, the **modulator** converts the digital signals to electrical signals. This is normally done by a digital signal processor (DSP) together with a digital-to-analog converter (DAC). The digital signals, i.e. the information bits, are converted to electrical signals using single-carrier or multi-carrier modulation schemes. On-off-keying (OOK) and pulse-position-modulation (PPM) shown in Fig.1.8 (a) and (b) are the most widely used schemes [28]. The usage of OOK is straightforward, as we can simply use the "ON" and "OFF" status of the light to represent the digital "0" and "1". In real VLC applications, the "OFF" status can be represented by a low-intensity level which can be clearly distinguished from the "ON" status. This setting ensures that

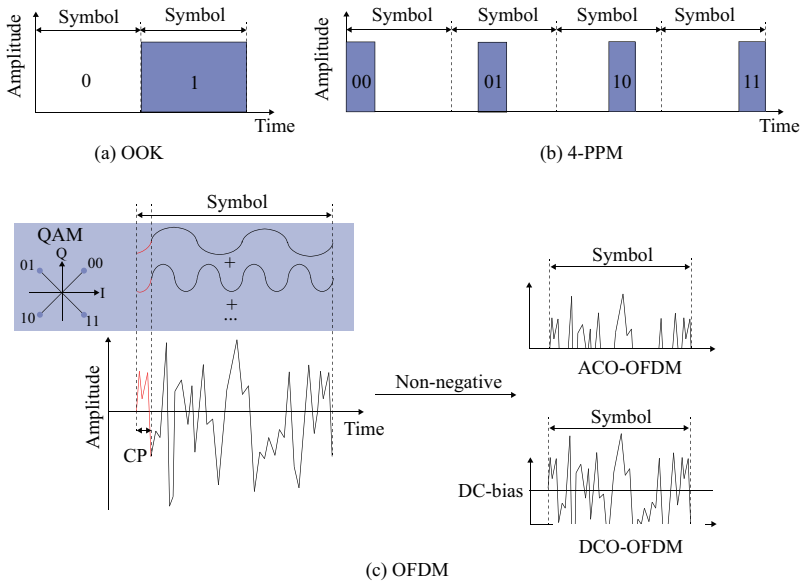

Figure 1.8: Example of information bits modulated with (a) OOK; (b) 4-PPM; (c) general OFDM and two optical OFDM schemes

the average output optical power can still meet illumination requirements. The electrical signal consists of multiple symbols, which could be digital "0"s and "1"s as shown in Fig.1.8 (a) and (b) or a continous waveform (Fig.1.8 (c)). A symbol presents in the communication channel for a fixed period of time, which is also called symbol time or symbol duration. The reciprocal of a symbol duration is the symbol rate, which is the number of symbols per second. In general, a higher symbol rate requires higher electrical bandwidth. However, the total electrical bandwidth used by the channel is limited due to the modulation bandwidth of LED. Thus, the number of bits represented by one symbol, which is also called spectral efficiency, is of importance. As only one bit is transmitted in one symbol time, OOK is not very spectral efficient. The PPM uses pulse positions in a symbol time to represent the information bits, which improves spectral efficiency. M bits are presented in one symbol in a 2^M-PPM scheme. OOK and PPM are single-carrier modulation schemes, as they exploit only one signal frequency to transmit data symbols [29]. These single-carrier modulation schemes are easy to realize. However, they require complex technologies to remove inter-symbol interference (ISI). ISI is the effect caused by unwanted copies of symbols traversed from multiple paths. One symbol is affected by subsequent symbols such that the detection of the symbol is not reliable. Multi-carrier modulation schemes can be used to mitigate ISI [30]. Orthogonal frequency division multiplexing (OFDM) is

a multi-carrier modulation scheme which has been widely used in the 4th generation (4G) and the 5G mobile communication technologies. OFDM has larger data rates than single-carrier modulation schemes. Fig.1.8 (c) illustrates the principle of OFDM modulation scheme. OFDM divides the total electrical bandwidth into multiple subcarriers which are sinusoidal waves with different frequencies. These subcarriers are orthogonal to each other, i.e. subcarriers can be demodulated without interference. This property is based on the orthogonality of sinusoidal waves:

$$\frac{1}{T}\int_{-T}^{T}\sin(\frac{n\pi}{T}t)\sin(\frac{m\pi}{T}t)dt=\begin{cases}1, n=m\neq 0\\ 0, n\neq m\end{cases} \tag{1.3}$$

and

$$\frac{1}{T}\int_{-T}^{T}\cos(\frac{n\pi}{T}t)\sin(\frac{m\pi}{T}t)dt=0 \tag{1.4}$$

In order to transmit more bits in one symbol, the information bits are first mapped to complex numbers using quadrature amplitude modulation (QAM). QAM is a digital modulation method which sends two carrier waves (sinusoidal and cosinusoidal) with different amplitudes. These two carrier waves have the same frequency. Based on Eq.(1.4) these two carrier waves are also orthogonal. QAM maps the information bits to complex numbers using a modulation constellation. The complex numbers are translated to the phase and the amplitude of the carrier waves using inverse fast-Fourier transformation (IFFT). Orthogonal waves can be added together and sent via the channel. The receiver can easily separate these waves due to their orthogonality property. The ISI effect can be simply mitigated by adding a cyclic prefix (CP) which is the repetition of the end of the signal. Traditional OFDM signals have negative values. As LEDs are driven by an electrical current which must be positive, OFDM used for VLC systems, which is normally called optical OFDM (O-OFDM), has to be modified in order to remove negative values. Two non-negative strategies, asymmetrically clipped O-OFDM (ACO-OFDM) and direct-current biased O-OFDM (DCO-OFDM), have been proposed. ACO-OFDM clips all negative values and uses an intelligent data allocation strategy to ensure that data-carrying subcarriers are not impaired [31]. DCO-OFDM adds DC-bias to the OFDM signal and clips the remaining negative values. Both strategies managed to remove negative values of OFDM signals without loss of information or adding new noises. An important effect which should be noticed by all modulation schemes is the flickering of the light. Flicker is caused by the fluctuation of the brightness of the light. Human eyes cannot perceive the flicker if the frequency is greater than $200\,\mathrm{Hz}$. Thus, the modulator must not introduce any noticeable flicker either during data frame or between data frames [10].

The **optical system** in the transmitter is used to further control the emission of the light. Optical amplifiers can be used to increase the level of the transmitted optical signal. Collimators or diffusers can be employed to concentrate or broaden

the beam [32]. The light pattern can be reshaped to fulfill the illumination requirements and to ensure eye safety.

1.1.2 VLC receivers

A VLC receiver handles the optical signal received from the free space optical channel. The most important device is the **light detector** which converts the optical signal to electrical current or voltage. Most light detectors are based on the photoelectric effect which is the emission of electrons when photons hit a material. Depending on the requirement of the communication, photodiode (PDs) or image sensors can be used for detecting received optical signals. Charge-coupled devices (CCD) and complementary metal-oxide-semiconductor (CMOS) are mostly used as image sensors. As CCD and CMOS are commonly used for cameras, communication systems using image sensors are normally called optical camera communication (OCC) systems. Image sensors are composed of an array of MOS capacitors or MOS field-effect transistor (MOSFET) amplifiers. The advantage of using image sensors is that they are able to spatially separate different light sources according to different directions of projection [33]. Optical signals are captured by frames and each activated pixel in the frame generates a voltage proportional to the number of impinging photons [34]. The challenge of using image sensors is that the frame rate of many consumer-grade image sensors is about 30–60 fps. Thus, OCC is normally considered for low-rate applications, for instance, car-to-car communication. PDs are simple and low-cost photon-detecting devices. Electrical current flow is triggered by absorbed photons. PDs made by different materials have different responsivities. The responsivity is the ratio of the electrical current to the incident optical power. Silicon-based and germanium-based PDs can be used for VLC systems. The responsivity of silicon-based PDs within the VL range can be considered linear. Fig.1.9 presents the responsivities of three silicon-based PDs from Thorlabs. Saturation of PDs may occur when the received optical power exceeds a certain level. The linear range of normal PDs reaches up to a few mW. The saturation may cause a non-linear distortion of the received signal. However, the saturation effect can be neglected in VLC systems. When the path loss of the optical signal is taken into consideration, the optical power radiated by the transmitter has to exceed more than the radiant power constrained by eye-safety requirements to cause saturation at the PD [32]. In addition, signal clipping due to saturation can be avoided by means of the commonly employed automatic gain control (AGC).

The incident light intensity at the receiver also obeys Lambertian cosine law. Thus, the intensity of the received light is proportional to the cosine of the incident angle. PDs have viewing angles which are called field-of-view (FOV). The FOV of PDs is normally expressed in half-angle, i.e., the angle between the surface

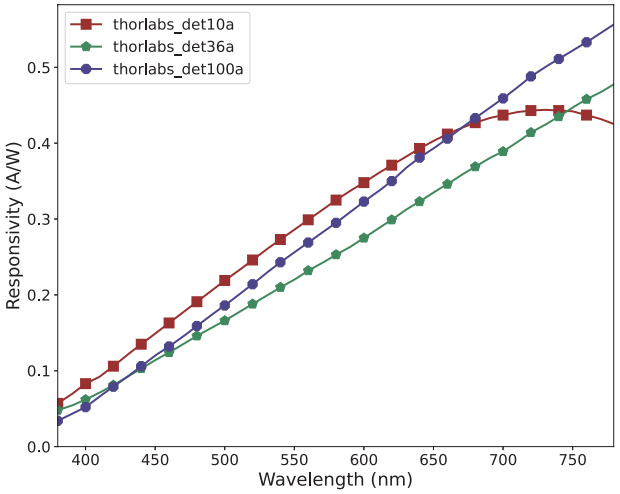

Figure 1.9: Responsivity of silicon-based PDs in visible light range

normal and the maximum detection angle. Light rays with an incident angle larger than the FOV are not detected by PDs. The FOV of traditional PDs is normally wide [34]. PDs with a wide FOV are able to detect light rays from a wide range. However, this also causes reception of a large amount of ambient light and other interference.

As VLC receivers need to detect modulated optical intensity radiant from transmitters, the modulation bandwidth of the PD is also of importance. The bandwidth of PDs depends on the active area. PDs need to keep a small area in order to increase the modulation bandwidth. The typical active area of PDs is 1 mm^2. Electrical modulation bandwidths of more than 100 MHz have been reported [32].

In order to select the portion of interest in the optical spectrum, an optical filter is applied in the **optical system** at the receiver side. The optical filter can also attenuate the ambient light. PDs receive light rays from multiple directions as they have wide FOV. The optical power carried by the light rays with a large incident angle is too small. Although increasing the active area of PDs can also increase the received power, it is expensive and will decrease the electrical modulation bandwidth of PDs. Thus, the viable solution is to apply collimator lens and optical concentrators. The collimator lens amplifies the signal and aligns the impinging light for optimum detection [32]. Optical concentrators increase the received power by increasing the effective area [5].

When the receiver collects enough amount of optical power from the VLC channel, a **demodulator** is applied to covert the signal back to the information bits. Normally, the electrical signal is first pre-amplified by means of a trans-impedance amplifier (TIA). The TIA converts an input electrical current to an output voltage.

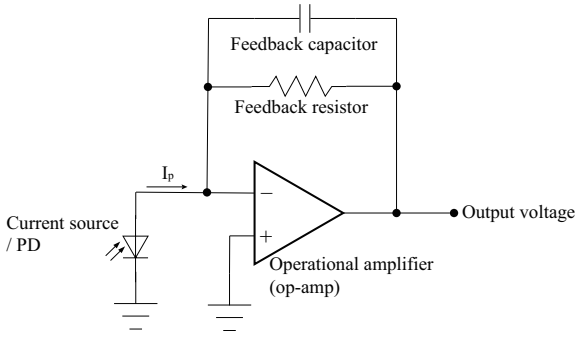

Figure 1.10: Circuit diagram of a typical TIA

The circuit diagram of a simple TIA is shown in Fig.1.10. The PD is operating in the reverse bias mode, i.e. the voltage applied across the anode to the cathode is negative. When the PD is impinged by the light, a reverse current flow I_p which is proportional to the light intensity is generated. The input offset voltage of the operational amplifier (op-amp) due to the photodiode is very low in this self-biased photovoltaic mode. The advantage of this reverse-bias mode is that the electrical current and voltage change linearly with the optical power. The current to voltage gain is based on the feedback resistance, i.e.,

$$\frac{V_{out}}{I_{in}} = -R_f, \tag{1.5}$$

where V_{out} is the output voltage of the TIA, $I_{in} = I_p$ is the electrical current generated by the PD, and R_f is the resistance of the feedback resistor. The feedback capacitor is used to compensate for the instability (oscillation) caused by the parasitic capacitance of the input and the internal capacitance of the op-amp. The value of the feedback capacitor has to be carefully chosen as a capacitor with a too large value will reduce the bandwidth of the amplifier and oscillation may occur if the value is too small. The electrically amplified signal, i.e., the output voltage from the TIA, is transformed to the digital signal by a DSP with an analog-to-digital converter (ADC). Based on the modulation scheme used in the transmitter, the DSP demodulates the digital signal using the corresponding demodulation method. As we have already mentioned in the subsection 1.1.1, single-carrier modulation schemes require complex equalization at the receiver in order to eliminate the ISI. The ISI in OFDM modulated signals, however, can be mitigated by removing the CP in each symbol. The demodulation of OFDM signals requires fast-Fourier transformation (FFT) which is a function embedded in modern DSP devices. With the FFT function, data carried by each subcarrier can be extracted.

1.1.3 The VLC channel

The **optical channel** is the most important component in a VLC system. The quality of the VLC system highly depends on the characterization of the optical channel. To characterize an optical channel, we first have to understand how the signal is transmitted via visible light. In traditional wireless communication systems, the information-bearing signal is modulated onto higher-frequency carrier waves (in the RF spectrum) by altering the amplitude, phase, or frequency of the carrier. These techniques are called amplitude, phase, and frequency modulation (AM, PM, and FM). Unlike traditional RF-based wireless technologies which use AM, PM, and FM, a VLC system tends to use a low-cost intensity modulation (IM) scheme. The main difference between IM and other modulation technologies is that the desired waveform of the signal is directly represented by the instantaneous transmitted power of the light. From section 1.1.1 we have known that the modulator in the transmitter drives the LED light source using modulated electrical signals. It is straightforward to use IM for LED light sources as the radiant optical power of the light is proportional to the electrical current which has been modulated using OOK, PPM, or OFDM. At the receiver side, coherent detection which has been widely used for AM, PM, and FM modulated signals are not suitable for IM modulated signals. Coherent detection extracts the information of the original signal by multiplying the signal received in a single electromagnetic mode with a locally generated carrier wave. The mixed-signal passes through a low-pass filter and the result contains the phase and amplitude information of the original signal. However, it is extremely difficult to collect appreciable signal power in a single electromagnetic mode in low-cost VLC systems [5]. Thus, direct detection (DD) is the most viable scheme which produces the electrical current proportional to the received optical power. Compared with modulation schemes used in RF technologies, IM/DD has the following advantages:

1. In contrast to coherent receivers which detects amplitude, phase, and frequency information of the signal, the IM-based optical sensors, i.e. PDs, have simple structures and good linearity, and they are also inexpensive [35].

2. The spatial variation of magnitude and phase, which is called “multipath fading” is not presented in IM/DD systems as the wavelength of VL is much smaller than the typical area of a PD [5, 15].

The relationship between the input and the output optical signal in an IM/DD channel can be described by the channel impulse response. The impulse response of a channel is the reaction of the channel as a function of time when the input of the channel is an impulse function. An impulse function contains all frequencies in the frequency domain. Thus, the impulse response can be used to characterize the channel as it defines the response of the channel for all frequencies.

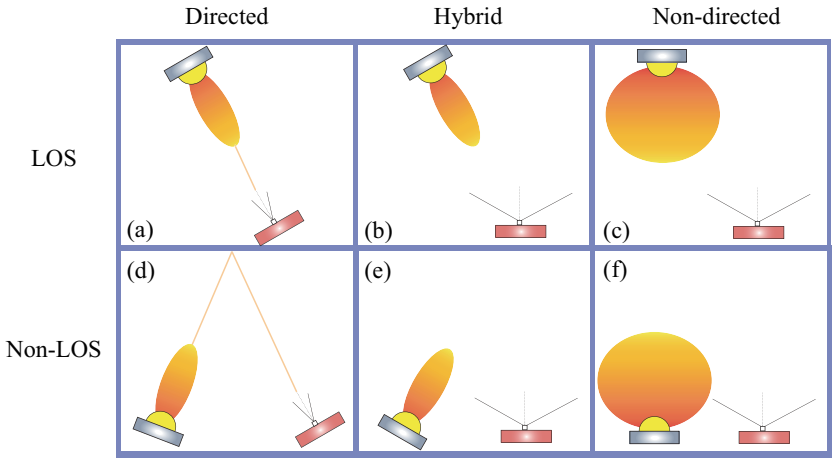

Figure 1.11: Typical configurations of VLC links

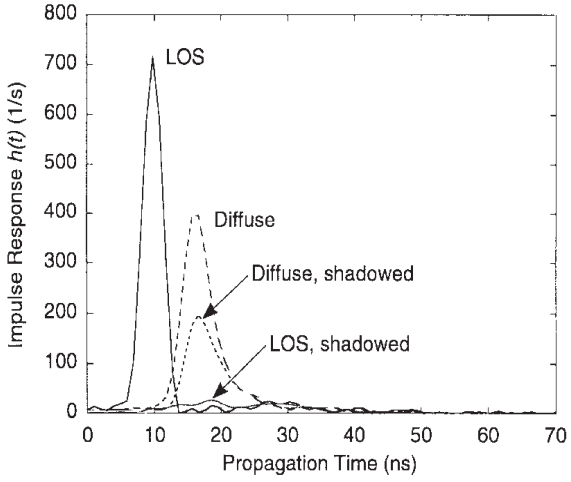

Figure 1.12: CIRs of non-directed-LOS and non-directed non-LOS (diffuse) infrared communication links. Measurements were performed in a 5.5 m×7.5 m room having a 3.5-m-high ceiling. Shadowing was effected by a person standing next to receiver. Detector area was 1 cm^2 [5]

The impulse response of a VLC channel can be defined as the received optical intensity as a function of time when the transmitted optical intensity is a unit-area Dirac delta function [36]. The received optical intensity contains the intensity of light rays received from all detectable directions. As LEDs and PDs both obey the Lambertian cosine law, the amount of the received optical power depends on the Lambertian pattern and the orientations of the transmitter and the receiver. In [5], six link configurations are classified according to the degree of directionality of transmitters and receivers and the existence of line-of-sight (LOS) (Fig.1.11). The LOS path is a direct path from the transmitter to the receiver. Link configurations in Fig.1.11(a)-(c) all contain uninterrupted LOS paths. In contrast to LOS link configurations, the receiver of a non-LOS link configuration receives all light rays via reflections. Link configurations in Fig.1.11(d)-(f) are non-LOS link configurations. The optical intensity received from non-LOS paths is normally smaller than that received from a LOS path due to the absorption by reflecting surfaces and the increasing length of the transmission path. Depending on the application of the VLC channel, the orientation of the transmitter and the receiver may also be directed and non-directed. The degree of directionality of a VLC transmitter or a VLC receiver describes its semi-angle or FOV. A directional VLC transmitter (receiver) uses LEDs (PDs) with a very small semi-angle (FOV). Directed VLC links as shown in Fig.1.11(a) and (d) normally use transmitters with narrow-beam and receivers with narrow FOV. Therefore, both the transmitter and the receiver have to aim to establish a link. In such configurations, there is a light ray radiant from the surface normal of the transmitter (i.e. 90°) and arrives the receiver also from the direction perpendicular to the surface. This directed light ray has the largest optical intensity according to the Lambertian cosine law. It should be noticed that the directed light ray may cause eye-safety issues and the transmitted optical power has to be limited. On the other side, non-directed links shown in Fig.1.11(c) and (f) employ wide-angle transmitters and receivers. There is no need for the directed light ray, i.e. the transmitter and the receiver do not have to aim at each other. This makes non-directed links easy to be used in general applications. Hybrid configurations shown in Fig.1.11(b) and (e) combine transmitters and receivers having different degrees of directionality. Other link configurations can be seen as combinations of the aforementioned link configurations. For example, a multi-spot diffuse link configuration uses multiple narrow-beam LEDs and several narrow-FOV PDs to establish multiple directed non-LOS links [37]. Different link configurations result in different channel impulse responses (CIR). An example of CIRs of a non-directed LOS and a non-directed non-LOS infrared communication link (often mentioned as a diffuse link) is shown in Fig.1.12 [5]. Infrared communication links have similar characteristics as VLC links since both infrared and visible light rays cannot penetrate opaque objects and are reflected from glossy and non-glossy surfaces. The LOS configuration has a high peak and

a small tail, while the diffuse configuration has a relatively wide and small peak and a long tail. The temporal spread of CIRs is caused by multipath reflections from walls. Fig.1.12 also presents CIRs of the LOS and the diffuse infrared link in shadowing conditions. The shadowing of a LOS link means that a person or an object stands between the transmitter and the receiver such that the LOS path is obstructed. A shadowed non-LOS link often refers to a link with a person or an object standing near the transmitter or the receiver such that the shortest light path from the transmitter to the receiver is obstructed. The shadowing effect is not significant for the diffuse infrared link. However, the CIR of the LOS infrared link is significantly degraded due to the shadowing. From CIRs of two infrared links, we can know that LOS configurations normally have better performance but are vulnerable to shadowing. Diffuse configurations have more robust CIRs. The usage of link configurations depends on the requirements of the application.

1.2 VLC-based optical attocell networks

Optical attocell networks are a promising indoor solution for the coming fifth-generation (5G) wireless systems. An optical attocell network is based on VLC communication. Users in the optical attocell network are grouped into multiple attocells with a radius ranging from one to several meters and communicate with the nearest LED lamps using VLC. The LED lamps in the optical attocell network are connected to the Internet via a gateway. An optical attocell network can provide extra data capacity without interfering with the possible existing RF-based wireless networks. A few applications can complement current wireless networks with optical attocell networks: 1) special applications in electromagnetic-sensitive environments such as hospitals, airplanes, and the underground mining industry [38]; 2) optical attocell networks together with light-as-a-service (LaaS) can be a key part of the emerging smart cities, smart homes, and Internet-of-things (IoT) [39].; 3) optical attocell networks are more secure than incumbent wireless technologies as the radiation of the VLC signals is naturally confined within a room. Despite the attractive advantages, optical attocell networks based on VLC also have some drawbacks. Due to the limitation of the LED modulation bandwidth, data rates supported by VLC-based optical attocell networks are limited. Another disadvantage is the dimming problem. Pulse-width-modulation (PWM) is commonly used to dim the LED lamp. The brightness perceived by human eyes is controlled by the percentage of the "off" period in the total duty cycle. As the VLC signal cannot be sent during the "off" period, it is difficult to provide high-speed VLC data transmission while the lamp is dimmed [28].

Using VLC for indoor wireless networks has been widely discussed. Since 2009 the Institute of Electrical and Electronics Engineers (IEEE) has been working on VLC-based networks and has standardized the use of VLC for wireless

personal area networks (WPAN) in [6]. Three topologies for the medium access control (MAC) layer are supported in a visible-light communication personal area network (VPAN): peer-to-peer, star, and broadcast. Fig.1.13 illustrates these MAC topologies. Peer-to-peer topology implies communication between two VLC devices. Star topology supports bi-directional communication links between one source and multiple destinations. Broadcast topology is different from the aforementioned two topologies. The source simply transmits signals to all destinations. The communication is uni-directional. Based on these MAC topologies, different network topologies have been proposed for indoor VLC-based networks [28]. Single-cell-per-user topology shown in Fig.1.14(a) is based on the peer-to-peer topology. A cell is an area served by a base station (BS) which is a LED lamp. In each cell, peer-to-peer communication between the BS and the single user is supported. All resources, i.e. time, frequency, and wavelength, can be used by the single user in the cell. The single-cell-per-user topology is practical for applications in airplanes, trains, or buses where reading lamps on top of each seat are mounted. Single-cell-per-room topology shown in Fig.1.14(b) is based on the star and the broadcast topology. All users in a room are served by a single BS. Resources must be shared by all users. The single-cell-per-room topology is only applicable for small rooms, since the data throughput available for each user decreases when the number of users increases, and the link quality for users in the corner is extremely poor. Cellular topology shown in Fig.1.14(c) uses multiple cells to cover a room. More than one user can be served in a cell. If handover is applied, network connectivity will not be interrupted when users are roaming between cells. Cellular topology is considered the most applicable topology for VLC-based indoor networks. In subsection 1.2.1, we explain the advantages of using the cellular topology for VLC-based networks which are called optical attocell networks in the rest of this dissertation. Subsection 1.2.2 introduces the structure of typical attocell networks. Challenges of optical attocell networks are discussed in subsection 1.2.3.

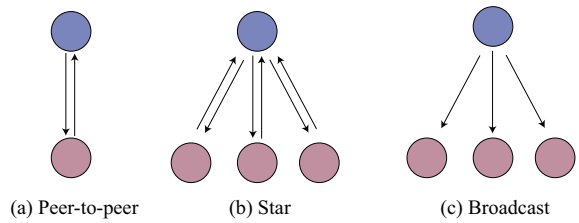

Figure 1.13: MAC topologies supported for VPAN in IEEE 15.7 standardization [6]

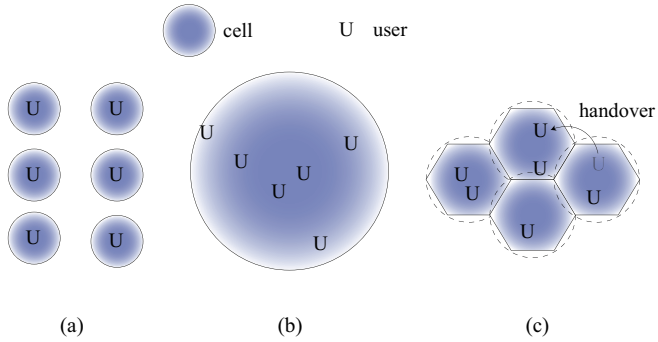

Figure 1.14: Network topologies: (a) single-cell-per-user; (b) single-cell-per-room; (c) cellular; darkness of the color indicates the quality of the signal

1.2.1 Cellular networks

Cellular technologies have been applied in wireless communication for a few decades. The total service area of a cellular network is divided into cells. Users in a cell are served by a BS which is normally located in the cell center. The shape of a cell is normally hexagonal as hexagons are a good approximation of circles and can fill a certain area without gaps. The available electrical spectrum is divided into multiple groups. Adjacent cells use frequencies in different groups to avoid interference. Cells with a certain spatial distance can re-use the same group of frequencies. Using cellular technologies has many desirable advantages compared to using a single large transmitter:

1. Users and BSs use less power than in networks with a single large transmitter since the distance between users and BSs is decreased.

2. Larger coverage area can be realized as cells can be added indefinitely.

3. The frequency re-use strategy increases the capacity of the network.

Depending on the size of cell coverage area, cellular networks can use macrocells, microcells, picocells, and femtocells. A macrocell has the widest coverage area ranging from one to several kilometers. The BS of a macrocell requires very high transmission power (typically tens of watts) to serve users in a large area. The cost for site lease, additional electricity and the backhaul for macrocell BSs is extremely high. Reducing cell sizes has been proven to reduce the cost and increase the network capacity by 1000-fold. The enormous gain obtained from smaller cell sizes arises from efficient spatial reuse of the spectrum, or alternatively, a higher area spectral efficiency (ASE), i.e., the sum data rate per unit bandwidth per unit area [40].

A small-cell concept has no conflict with the existing macrocellular networks. Heterogeneous networks which use combinations of cells with different sizes have been proposed to offer wireless coverage from the outdoor environment to office buildings and homes. Optical attocell networks which use attocells with a radius ranging from one to several meters can be a part of heterogeneous networks. BSs in optical attocell networks operating in the optical spectrum do not interfere with existing RF-based macrocellular networks [32]. Thus, using optical attocell networks is a good solution to address the last-meter bottleneck of current mobile networks. VLC-based optical attocell networks directly use existing LED lamps as BSs. This type of network can be simply deployed indoor as the cell size is quite small. BSs in VLC-based optical attocell networks are sometimes called access points (APs). We use BS and AP interchangeable in the rest of this dissertation when referring to the wireless device that connects users in an optical attocell to other wireless devices and the Internet.

1.2.2 The structure of optical attocell networks

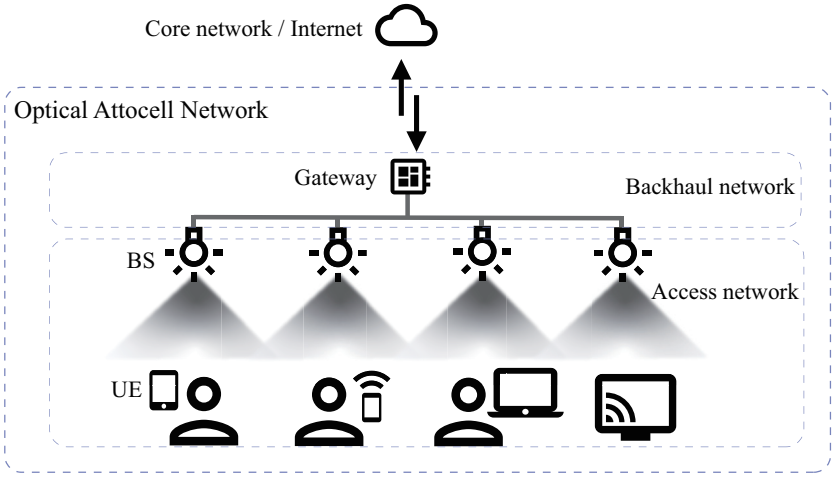

Figure 1.15: Illustration of the structure of optical attocell networks

An optical attocell network is composed of two parts: an **access network** and a **backhaul network**. Fig.1.15 illustrates the structure of the optical attocell network. The main components of optical attocell networks are VLC base stations (BSs) and user equipment (UE). LED lamps used for illumination can be configured as VLC BSs by adding VLC control units. UEs are mobile or desktop devices which require seamless wireless communication in an indoor environment, for example, a living room, an office, or a conference hall. BSs transmit data to UEs via VLC links. The transmission links from BSs to UEs are categorized as down-

links. The uplink transmission from UEs to BSs is also wireless. Optical wireless technologies are considered for the uplink transmission for two reasons: 1) they do not cause interference with RF-based networks and 2) they are power-efficient which is suitable for mobile devices. As mobile and desktop devices are not used for illumination, IR is generally considered for uplink data transmission. Communication links between BSs and UEs form an **access network**. The access network consists of access links in multiple attocells. Each attocell is served by one central BS. These attocells are spatially separated as lighting fixtures are deployed to generate uniform illumination in a room. Depending on the indoor illumination requirements, the existing lighting infrastructures could be densely deployed. The balance of lighting fixtures being BSs and those that provide only illumination is determined by the requirement of the network, but potentially all lighting fixtures can be BSs [32]. Similar to other cellular networks, access links in one cell share the resources (time, frequency, and wavelength), and these resources can be reused by access links in attocells with a certain distance. The spatial reuse strategy is determined by the requirement of the network. Dense reuse of the resources can achieve high data density, i.e. data rate per square meter (b/s/m^2), however, may cause very large interference in adjacent cells [32].

In order to connect UEs to the Internet as well as to realize the communication between UEs in different cells, a **backhaul network** is required. An important component of the backhaul network is the gateway which connects the backhaul network to the core network, i.e. the Internet. The gateway has a central control unit and routing/switching functions. A separate device, for example, a VLC router, can be used as a VLC gateway. It is also possible to add the control unit and routing functions in one of the VLC BSs, such that one of the BSs functions as a gateway. Communication links between the gateway and other BSs are backhaul links. There have been many technologies proposed for establishing backhaul links in optical attocell networks. The original idea of using wired backhaul links was proposed by Komine and Nakagawa in [41]. Power-line communication (PLC) was proposed to transmit backhaul data over power cables. Similar to optical IM/DD, the transmitted signals are added to the cyclic waveform of the alternating current (AC). PLC utilizes the existing power cables for communication. Lighting fixtures which have been connected to electricity power lines are also connected to a PLC modem and can communicate through the PLC backhaul links. A disadvantage that may prevent the usage of PLC is that battery-driven lamps cannot be wired-connected to the PLC-based backhaul network. Power-over-Ethernet (PoE) has been proposed for integrating the power supply and the backhaul transmission over Ethernet cables [42]. A PoE system consists of the power supply which is called the power sourcing equipment (PSE), the powered loads which are called the powered devices, and the standard twist-paired Ethernet cables to connect the PSE and the powered devices [43]. The power is supplied

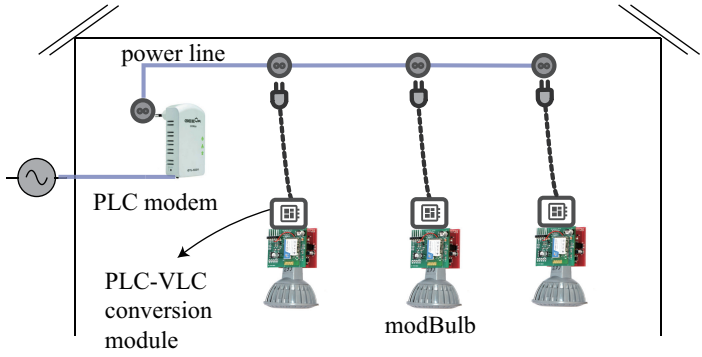

(a) PLC backhauling

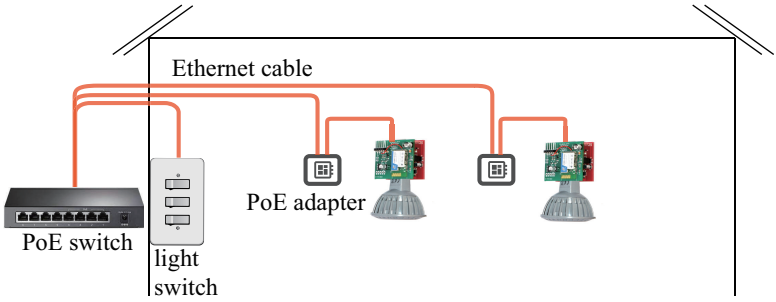

(b) PoE backhauling

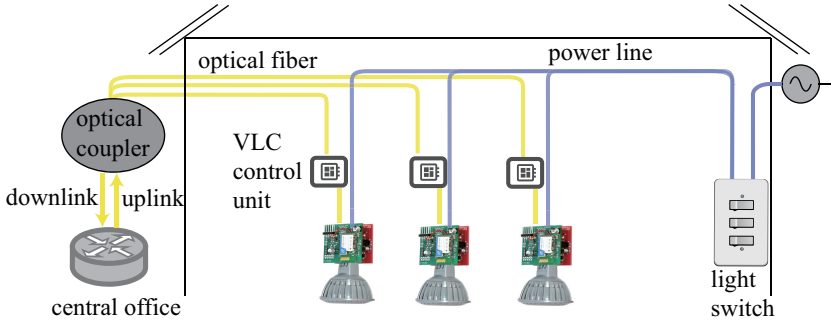

(c) Optical fiber backhauling

Figure 1.16: Wired backhaul network solutions for optical attocell networks: (a) power-line communication (PLC); (b) power-over-Ethernet (PoE); (c) optical fiber; BSs are modular light bulbs (modBulb) for VLC [7]

by the PSE and distributed via Ethernet cables. No extra AC power adapter is required for the powered devices. One advantage of using PoE for backhauling in optical attocell networks is that LEDs require a constant current input to operate. Hence, to mimic the same functionality as PoE, where all the drivers are located centrally – this current control would have to be done centrally too [44]. Using optical fibers for backhauling in optical attocell networks is also considered in [45]. Compared to PoE and PLC, optical fibers do not support simultaneous power supply and data transmission. Power cables are still required for supplying electricity to LED lamps. The major advantage of using optical fibers for the backhaul network in optical attocell networks is that fiber links support huge data rates. Backhaul networks using PLC, PoE, and optical fibers are illustrated in Fig.1.16. LED lamps can be plugged into sockets or controlled by a wall switch. PLC and PoE use a central controller (a modem or a switch) to integrate and split power and data. The optical fiber backhaul solution may need an extra optical coupler to split downlink and uplink data. It is important that every LED lamp must be connected to and controlled by a VLC control unit/ a PLC-VLC conversion module/ a PoE adapter in order to function as a VLC BS.

1.2.3 Challenges of optical attocell networks

VLC-based optical attocell networks utilize the existing lighting fixtures for wireless data communication. The move from point-to-point VLC links to optical attocell networks poses several challenges. The first challenge faced by optical wireless links is that IR and visible light cannot penetrate opaque objects like human bodies and furniture. IR and visible light are absorbed by dark objects, diffusely reflected by light-colored objects, and directionally reflected from shiny surfaces [5]. The access downlink (using VLC) and uplink (using IR-based OWC) are sometimes unintentionally blocked by people roaming in the room. The blockage of light rays, normally called the shadowing effect, will cause performance degradation. The degradation is caused by the absence of the dominant component and the presence of multiple reflection components. The shadowing effect of the LOS and the diffuse configuration has been shown in Fig.1.12. The absence of the LOS component decreases the total received optical power and consequently decreases the signal-to-noise ratio (SNR) of the link. The shadowing effect also causes performance degradation in non-LOS configurations. When the shortest light path from the transmitter to the receiver is obstructed, the total received power is slightly reduced. Both LOS and non-LOS configurations receive multiple copies of the signals from reflected paths. If the link is shadowed, light rays will be reflected by the obstructing object and walls or other furniture. Eventually, the receiver detects more reflected copies with larger delays. Inter-symbol interference (ISI) caused by large delay spread may cause further penalties in SNR

and consequently reduce the capacity of the link.

The second challenge comes from the limited modulation bandwidth of VLC using intensity modulation. In optical attocell networks, the total available modulation bandwidth is reused by attocells. The reuse distance has to be carefully chosen in order to avoid large co-channel interference (CCI). CCI is experienced in many wireless networks. Unlike wired communication, wireless communication technologies using RF and visible light do not use wires to guide the direction of the signal propagation. In an ideal situation without matter between the sender and the receiver, the wireless transmission has the characteristics shown in Fig.1.17. When the distance between the sender and the receiver is within the transmission range, the receiver detects the signal with a very low error rate. A reliable transmission can be guaranteed in the transmission range. When the distance between the sender and the receiver increases, detection of the signal is possible. The power transmitted by the sender is large enough to differ from background noise. However, the error rate is too high to establish reliable communication within the detection range. The receiver goes in the interference range when the distance further increases. The signal cannot be detected by the receiver as the received power from the intended sender is too small. Interfering power from other senders becomes larger and disturbs the communication link.

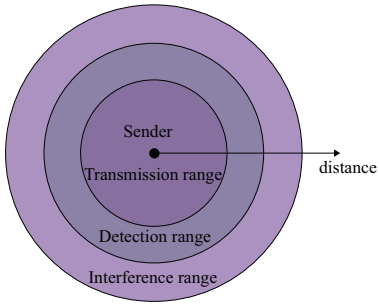

Figure 1.17: Characteristic of wireless transmission: transmission range, detection range, interference range [8]

In optical attocell networks, UEs traverse three ranges when they are roaming in the room. These lead to several problems in optical attocell networks: 1) frequency planning in different cells is required in order to avoid CCI; 2) handover is required when UEs are roaming from one cell to another, frequency planning should also consider the frequent changes of the number of UEs. Resource schedulers are then required to adaptively allocate frequency and other resources (power, time, wavelength) in order to avoid CCI and improve the spectral efficiency of the network. A centralized control mechanism such as resource schedulers within the controller of a software-defined network (SDN) is also a viable solution [39, 46].

1.3 The new backhaul solution

The backhaul network is an essential component in the optical attocell network. The data collected from and transmitted to the access network aggregates in the backhaul network. A non-reliable backhaul network may become the bottleneck of the optical attocell network. In this dissertation, we are going to present our work on designing a reliable backhaul network for optical attocell networks.

Wired backhaul networks introduced in subsection 1.2.2 with unlimited capacity are assumed in many research articles. However, wired backhaul solutions have some issues and their capacity is limited in real applications. The first issue is the extra cost for installation. The optical fiber backhauling requires extra optical fiber wirings connected to LED lamps. Although the PoE backhauling does not add extra wirings, the existing power wirings connected to lighting fixtures have to be replaced with twist-pair Ethernet cables. High complexity and cost for installation/replacement are inevitable. Furthermore, additional hardware cost for the control module for every LED lamp (i.e. the PLC-VLC conversion module, the PoE adapter) also prevents the application in scenarios which require a huge number of VLC BSs, for example, large conference hall or huge buildings. Secondly, as PLC uses power lines which are unshielded and untwisted, these wirings turn into unintentional antennas and cause radio interference with existing users in the same frequency band [47]. Interference and noises from household appliances also exist and degrade the performance of the PLC backhaul links [48].

Wireless backhaul solutions are independent of wiring infrastructure. Therefore, the high cost for installation and replacement can be avoided. In [38], a backhaul approach using millimeter-wave (mmWave) was proposed. A major problem is that the bio-effects on human bodies caused by non-ionizing mmWave radiation deserve consideration and further study [49]. Security is also an issue when using mmWave as the mmWave signal can go through walls. A new backhaul solution, wireless backhaul using VLC, was proposed in [50]. Using VLC for wireless backhauling is straightforward as no extra cost for installing wirings and extra control units are needed. The existing VLC control units used for access data transmission can be directly used to control backhaul data transmission. VLC-based backhauling only requires extra LED and PD chips which are called auxiliary transceivers. Installation and maintenance of VLC backhauling are simple and cost-efficient since only low-cost LED and PD chips are needed to be added or replaced.

The VLC backhauling proposed in [50] was based on directed LOS links between auxiliary transceivers on adjacent BSs. The LOS configuration has good performance in ideal cases. In an ideal environment with an enclosed space created by a suspended ceiling under the actual ceiling, the LOS backhaul links can transmit data without interfering with the access links. In general environments without suspended ceilings, interference should be considered. In addition, the

shadowing effect dramatically degrades the performance of LOS links as shown in Fig.1.12 and discussed in [5]. In many interior lighting designs, lamps are embedded in the ceiling without enclosed space between lamps. Lamps may be also mounted on different heights or separated by walls. The LOS link configuration cannot be directly applied in such scenarios. A more general VLC backhauling solution is needed to fill the gap.

1.4 Outline and research contributions

In this section, the key topics in this doctoral dissertation are highlighted. To summarize, a novel VLC-based backhaul network using non-LOS configuration is simulated and analyzed. To design a robust VLC-based backhaul network for optical attocell networks, we first analyze the performance of different non-LOS links and the performance of optical attocell networks using non-LOS links. Optical attocell networks using VLC-based backhaul networks face challenges. As we have discussed in subsection 1.2.3, VLC links are subject to the shadowing effect as visible light connot penetrate opaque objects. In addition, efficient frequency-planning schemes are necessary in order to avoid large CCI. We propose strategies to address those challenges and a new issue faced by VLC backhauling, i.e. the misalignment effect. The general outline of the dissertation is shown in Fig.1.18. In Chapter 2, we analyze the performance of different VLC link configurations. The interference of VLC backhaul links in the optical attocell network is discussed in Chapter 3. The impact caused by misaligned backhaul transceivers is presented in Appendix A. In Chapter 4, we focus on the shadowing effect and present a cross-layer recovery scheme. The misalignment effect is analyzed in Chapter 5. The detection and mitigation strategies are discussed in this chapter. We discuss every chapter in a separate paragraph.

In order to apply VLC-based backhaul networks in more general cases, we propose to use non-LOS configurations to establish backhaul links. There are different kinds of non-LOS configurations as shown in Fig.1.11. It has been shown in research that non-LOS configurations with purely diffuse reflections suffer from multipath effects. The multipath effects degrade the performance of purely diffuse non-LOS channels by decreasing the direct-current (DC) gain and increasing the delay spread of the signal. The DC gain is the magnitude of channel impulse response at DC, i.e. the zero-frequency component in the frequency domain. A channel with a high DC gain can achieve better SNR with a fixed transmitted power. The delay spread is another important measure of channel performance. As we have mentioned in subsection 1.2.3, delay spread will cause ISI, which needs to be mitigated by adding CP in OFDM signals. Adding a long CP will cause large penalties in the SNR and consequently degrades the channel performance. In order to overcome these drawbacks, we propose to use **non-LOS configurations**

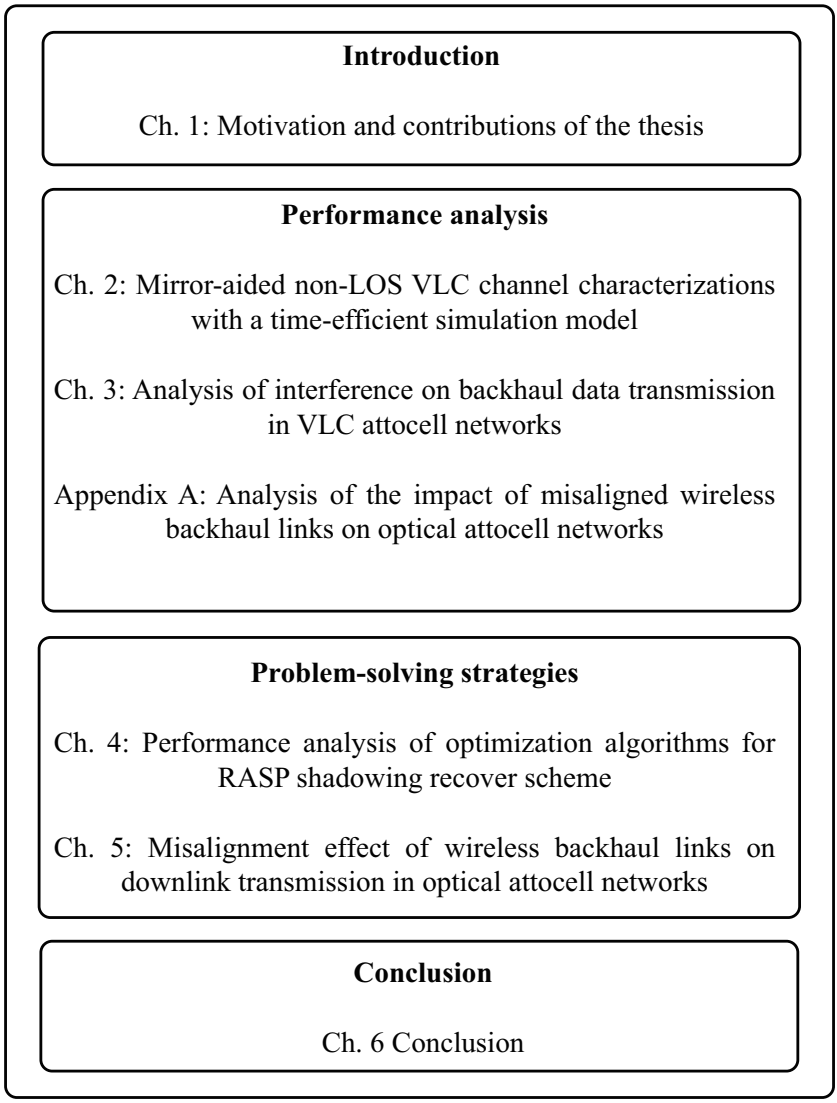

Figure 1.18: Outline of this doctoral dissertation

aided by mirrors. Compared to purely diffuse reflections, specular reflections from glossy surfaces like mirrors are directional. Reflected light rays from mirrors are concentrated. To assess the performance of VLC links using the mirror-aided non-LOS configuration, a simulation model is required. Existing simulation models were either inaccurate or time-consuming. Many simulation models were not suitable for VLC links with large optical spectrums as the spectral information is not considered. In addition, multi-bounce specular reflections have not been taken into account. The new simulation model presented in Chapter 2 is **a time-efficient model** for simulating VLC links. The simulation model takes into account the spectral information of VLC links. Both specular reflections and diffuse reflections (from the non-glossy surface) can be simulated. Based on the results obtained by this simulation model, we found that mirror-aided non-LOS links achieve good performance since the first-bounce specular reflection from mirrors provides larger DC gain and smaller delay spread.

The mirror-aided non-LOS configuration uses LEDs oriented towards mirrors (placed on the floor or table) to provide backhaul data transmission. Using this VLC backhauling in optical attocell networks will cause interference between access and backhaul links. As a UE is normally placed on the floor (or about one meter above the floor) and oriented upwards to receive the access data from the nearest BS, the access data link may interfere with the backhaul links from the same BS and neighboring BSs. Based on the results and discussion in Chapter 2, using directed receivers oriented towards mirrors can achieve larger data rates than using downward-oriented receivers. The directed backhaul receiver not only detects the target signal from the neighboring BS via the mirror which the receiver is oriented towards, it may also detect interfering signals from other BSs. In order to minimize the interference, the FOV of the backhaul receivers has to be small. In the meanwhile, the FOV can not be configured extremely small as the backhaul receivers have to be able to detect the target signal in the case when they are not perfectly aligned to the mirrors. Based on the analysis and the **calculation of FOV** used for backhaul receivers, we investigate the interference in optical attocell networks using mirror-aided non-LOS backhaul links in Chapter 3. We assess the overall network performance in terms of the aggregate data rate of the optical attocell network. The aggregate data rate is the sum of the end-to-end data rate of all UEs in the network. The end-to-end data rate is determined by the signal-to-interference-plus-noise ratio (SINR) of the link. The interference is affected by multiple factors. Larger transmitted optical power improves the performance of a link but also creates larger interference to other links. The sizes of viewing angles of LEDs also affect the interference of access and backhaul links. We compare the performance of optical attocell networks using different backhaul links: LOS backhaul links with directed oriented LED-PD pairs; hybrid mirror-aided non-LOS backhaul links with downward-oriented LEDs and directed PDs; mirror-aided non-

LOS backhaul links with LED-PD pairs which are both oriented towards mirrors. To ensure a fair comparison, the transmitted power is configured according to the illumination and eye-safety requirements. Simulation results show that the performance of mirror-died non-LOS backhaul links is affected by interference when all links reuse the whole electrical spectrum. **A simple static frequency planning** is discussed in Chapter 3. The static frequency planning divides the whole electrical spectrum into multiple parts and allocates different portions of the electrical spectrum to access and backhaul links in one cell. This frequency planning method improves the performance of networks using the directed mirror-aided non-LOS backhaul links.

As the LOS configuration and the directed mirror-aided non-LOS configuration both require the directed path, the alignment is important for these backhaul link configurations. In Chapter 3, the FOV configuration has taken into account the misalignment. In Appendix A, we further analyze the performance degradation in optical attocell networks caused by misaligned backhaul links. From the results presented in Chapter 3, we found that mirror-aided non-LOS backhaul links can achieve better performance by using frequency planning in misaligned cases. Thus, the performance of misaligned mirror-aided non-LOS backhaul links using different frequency planning schemes is also analyzed. Simulation results show that optical attocell networks using mirror-aided non-LOS backhaul links are always in the interference-limited regime regardless of the misalignment angle. This means that using a proper frequency planning scheme can improve the performance of misaligned mirror-aided non-LOS backhaul links by reducing interference.

Based on the performance analysis in Chapter 2, 3, and Appendix A, we design strategies to solve the major problem in optical attocell networks using mirror-aided backhauling: the shadowing effect and the misalignment effect. The shadowing effect is the major challenge of general optical attocell networks. As mirror-aided non-LOS backhaul links also use LEDs orienting towards the floor, people roaming in the room also causes temporal link blockages. Previous shadowing-mitigation strategies only considered the physical (PHY) layer and the medium access control (MAC) layer. Network layer functions such as routing algorithm and load assignment were not taken into account. In Chapter 4, we propose **a cross-layer resilience scheme RASP** to mitigate shadowing effects in optical attocell networks using mirror-aided non-LOS VLC backhauling, where R stands for routing, A stands for load assignment, S stands for subcarrier selection, and P stands for power allocation. The RASP scheme is a cross-layer routing and resource allocation scheme by configuring four control variables: the routing control variable, the load control variable, the subcarrier control variable, and the power control variable. These control variables are determined by control policies such as routing algorithms and frequency allocation schemes. The optimal combina-

tion of control policies is explored by using an optimization method. We consider neighbor-searching algorithms in Chapter 4 since a set of control policies used for the RASP scheme can be seen as a possible solution and solutions with only one difference of the option in the set can be seen as neighbors of the set. We investigate the performance of three optimization schemes: partial enumeration, hill-climbing, and Tabu-search. We found that Tabu-search can find a better solution if the size of neighbors is large. However, a larger neighbor size also increases the searching time. In order to reduce the searching time while maintaining the performance, **a Tabu-search method using decomposed neighbor sets** is proposed. This method significantly reduces the searching time and has a larger probability (about 50%) to get zero throughput loss when shadowing occurs.

Misalignment effects are specific for optical attocell networks using directed backhaul link configurations. The received power is maximized when the transmitter and the receiver of a backhaul link are perfectly aligned, i.e. oriented towards the mirror. The SINR of the backhaul link is decreased when the transmitter or the receiver is misaligned. In order to mitigate the misalignment effect, we propose **a redundant transmission strategy and an adaptive strategy** in Chapter 5. The redundant transmission strategy uses neighboring backhaul transmitters to send redundant data. This redundant transmission strategy is based on frequency planning schemes which assign different portions of the electrical spectrum to every three neighboring transmitters. In these frequency planning schemes, a backhaul transmitter uses a portion of the electrical spectrum other than its neighbors. With the redundant transmission strategy, a backhaul transmitter can also use the electrical spectrum assigned to its neighbors to send redundant data to the receiver of the neighboring link without interfering with other backhaul links. This strategy becomes beneficial when the misalignment angle becomes larger than a certain threshold. The adaptive strategy improves the performance by adaptively choosing proper methods for different misalignment angles. Both strategies require information on the misalignment angle. In order to detect the misalignment angle, **a HELLO/ACK method** is also proposed and presented in this chapter.

In this doctoral dissertation, we present our contributions to robust VLC-based backhaul networks. This dissertation is composed of a number of publications that were realized within the scope of this PhD and have been published in academic journals or are currently under review. Each chapter presents such a publication as-is. The publications provide a consistent overview of the work performed. The publications often contain a Future Work Section, which do not necessarily encompass work performed in the rest of the dissertation. The complete list of publications that resulted from this work is presented in Section 1.5.

1.5 Publications

The research results obtained during this PhD research have been published in scientific journals and presented at a series of international conferences. The following list provides an overview of the publications.

1.5.1 Publications in international journals (listed in the Science Citation Index [1])

1. **Y. Wu**, P. Audenaert, D. Colle, M. Pickavet, "Mirror-Aided Non-LOS VLC Channel Characterizations with A Time-Efficient Simulation Model", Published in Photonic Network Communications (PNET), 38: p.151-166, 2019.

2. **Y. Wu**, D. Colle, M. Pickavet, "Analysis of Interference on Backhaul Data Transmission in VLC Attocell Networks", Published in Photonic Network Communications (PNET), 41(2): p.189-201, 2021.

3. **Y. Wu**, D. Colle, M. Pickavet, "Performance Analysis of Optimization Algorithms for RASP Shadowing Recover Scheme", Published in IEEE Transaction on Network and Service Management (TNSM), 18(3): p.2789-2799, Sep. 2021.

4. **Y. Wu**, D. Colle, M. Pickavet, "Misalignment Effect of Wireless Backhaul Links on Downlink Transmission in Optical Attocell Networks", Submitted to Journal of Optical Communications and Networking (JOCN), May 2021.

1.5.2 Publications in international conferences (listed in the Science Citation Index [2])

1. **Y. Wu**, D. Colle, M. Pickavet, "A Cross-Layer Heuristic Algorithm for Addressing Shadowing Problem in Optical Attocell Networks", Published in Proceedings of International Conference on the Design of Reliable Communication Networks (DRCN), p.156-159, 2020, Milan, Italy.[3]

[1] The publications listed are recognized as 'A1 publications', according to the following definition used by Ghent University: A1 publications are articles listed in the Science Citation Index Expanded, the Social Science Citation Index or the Arts and Humanities Citation Index of the ISI Web of Science, restricted to contributions listed as article, review, letter, note or proceedings paper.

[2] The publications listed are recognized as 'P1 publications', according to the following definition used by Ghent University: P1 publications are proceedings listed in the Conference Proceedings Citation Index - Science or Conference Proceedings Citation Index - Social Science and Humanities of the ISI Web of Science, restricted to contributions listed as article, review, letter, note or proceedings paper, except for publications that are classified as A1.

[3] This paper won the Excellent Paper Award of The 16th IEEE International Conference on the Design of Reliable Communication Networks

2. **Y. Wu**, D. Colle, M. Pickavet, “Analysis of the Impact of Misaligned Wireless Backhaul Links on Optical Attocell Networks”, Published in Proceedings of International Conference on Transparent Optical Networks (ICTON), p.1-6, 2020, Bari, Italy.

References

[1] U. S. Government Publishing Office. *The United States Frequency Allocation Chart*. Technical report, 2016.

[2] PureLiFi. *A world's First*, 2016.

[3] S. Dutta Gupta and Avinash Agarwal. *Light emitting diodes for agriculture: Smart lighting*. Light Emitting Diodes for Agriculture: Smart Lighting, (January 2018):1–334, 2017.

[4] Martin Aubé, Johanne Roby, and Miroslav Kocifaj. *Evaluating Potential Spectral Impacts of Various Artificial Lights on Melatonin Suppression, Photosynthesis, and Star Visibility*. PLoS ONE, 8(7), 2013.

[5] J.M. Kahn and J.R. Barry. *Wireless Infrared Communications*. Proceedings of the IEEE, 85(2):265–298, 1997.

[6] IEEE. *IEEE Standard for Local and metropolitan area networks — Part 15.7 : Short-Range Wireless Optical Communication Using Visible Light*. 2011.

[7] Kasun Hewage, Ambuj Varshney, Abdalah Hilmia, and Thiemo Voigt. *modBulb: A modular light bulb for visible light communication*. Proceedings of the Annual International Conference on Mobile Computing and Networking, MOBICOM, 03-07-October-2016:13–18, 2016.

[8] Jochen Schiller. *Mobile Communications*. Addison-Weley, 2 edition, 2003.

[9] Dilukshan Karunatilaka, Fahad Zafar, Vineetha Kalavally, and Rajendran Parthiban. *LED Based Indoor Visible Light Communications: State of the Art*. IEEE Communications Surveys and Tutorials, 17(3):1649–1678, 2015.

[10] Sridhar Rajagopal, Richard D. Roberts, and Sang Kyu Lim. *IEEE 802.15.7 visible light communication: Modulation schemes and dimming support*. IEEE Communications Magazine, 50(3):72–82, 2012.

[11] David L Begley and Special Initiatives. *Free-Space Laser Communications: A Historical Perspective*. 1:391–392, 1980.

[12] F R Gfeller and U Bapst. *Wireless in-House Data Communication Via Diffuse Infrared Radiation*. Proceedings of the IEEE, 67(11):1474–1486, 1979.

[13] Y. Tanaka, S. Haruyama, and M. Nakagawa. *Wireless optical trasnsmissions with white colored LED for wireless home links*. IEEE International Symposium on Personal, Indoor and Mobile Radio Communications, PIMRC, 2:1325–1329, 2000.

[14] Y Tanaka, T Komine, S Haruyama, and M Nakagawa. *Indoor visible communication utilizing plural white LEDs as lighting*. In 12th IEEE Int. Symp. Personal, Indoor and Mobile Radio Communications, volume 2, pages 81–85, 2001.

[15] Harald Burchardt, Nikola Serafimovski, Dobroslav Tsonev, Stefan Videv, and H Haas. *VLC : Beyond Point-to-Point Communication*. IEEE Communications Magazine, 52(July):98–105, 2014.

[16] Markets and Markets. *Free Space Optics (FSO) and Visible Light Communication (VLC)/Light Fidelity (Li-Fi) Market with COVID-19 Impact Analysis by Component (LED, Photodetector, Microcontroller, Software), Transmission Type, Application, Geography - Global Forecast to 2025*. Technical report, 2020.

[17] V Jungnickel, M Uysal, N Serafimovski, T Baykas, E Ciaramella, Z Ghassemlooy, R Green, H Haas, P A Haigh, V P Gil Jimenez, F Miramirkhani, and M Wolf. *A European View on the Next Generation Optical Wireless Communication Standard*. IEEE Conference on Standards for Communications and Networking (CSCN), pages 106–111, 2015.

[18] Dandan Zhu and Colin J. Humphreys. *Solid-State Lighting Based on Light Emitting Diode Technology*. In Optics in Our Time, pages 87–118. 2016.

[19] Abdullah Sevincer, Aashish Bhattarai Member, and Mehmet Bilgi Member. *LIGHTNETs : Smart LIGHTing and Mobile Optical Wireless NETworks – A Survey*. IEEE Communications Surveys and Tutorials, 15(4):1620–1641, 2013.

[20] Jinsung Byun, Insung Hong, Byoungjoo Lee, and Sehyun Park. *Intelligent household LED lighting system considering energy efficiency and user satisfaction*. IEEE Transactions on Consumer Electronics, 59(1):70–76, 2013.

[21] Julia M. Phillips, Michael E. Coltrin, Mary H. Crawford, Arthur J. Fischer, Michael R. Krames, Regina Mueller-Mach, Gerd O. Mueller, Yoshi Ohno, Lauren E.S. Rohwer, Jerry A. Simmons, and Jeffrey Y. Tsao. *Research challenges to ultra-efficient inorganic solid-state lighting*. Laser and Photonics Reviews, 1(4):307–333, 2007.

[22] A. Neumann, J. J. Wierer, W. Davis, Y. Ohno, S. R. J. Brueck, and J.Y. Tsao. *Four-color laser white illuminant demonstrating high color-rendering quality*. Optics Express, 19(S4):A982, 2011.

[23] Sevket U. Yuruker, Enes Tamdogan, and Mehmet Arik. *An Experimental and Computational Study on Efficiency of White LED Packages with a Thermocaloric Approach*. IEEE Transactions on Components, Packaging and Manufacturing Technology, 7(2):201–207, 2017.

[24] E. Fred Schubert. *Light-Emitting Diodes*. Cambridge University Press, 2nd edition, 2006.

[25] Yanrong Pei, Shaoxin Zhu, Hua Yang, Lixia Zhao, Xiaoyan Yi, Junxi Wang, and Jinmin Li. *LED Modulation Characteristics in a Visible-Light Communication System*. Optics and Photonics Journal, 3(2011):139–142, 2013.

[26] Ricardo X.G. Ferreira, Enyuan Xie, Jonathan J.D. McKendry, Sujan Rajbhandari, Hyunchae Chun, Grahame Faulkner, Scott Watson, Anthony E. Kelly, Erdan Gu, Richard V. Penty, Ian H. White, Dominic C. O'Brien, and Martin D. Dawson. *High Bandwidth GaN-Based Micro-LEDs for Multi-Gb/s Visible Light Communications*. IEEE Photonics Technology Letters, 28(19):2023–2026, 2016.

[27] Pengfei Tian, Xiaoyan Liu, Suyu Yi, Yuxin Huang, Shuailong Zhang, Xiaolin Zhou, Laigui Hu, Lirong Zheng, and Ran Liu. *High-speed underwater optical wireless communication using a blue GaN-based micro-LED*. Optics Express, 25(2):1193, 2017.

[28] Hany Elgala, Raed Mesleh, and H. Haas. *Indoor optical wireless communication: Potential and state-of-the-art*. IEEE Communications Magazine, 49(9):56–62, 2011.

[29] Tao Jiang, Da Chen, Chunxing Ni, and Daiming Qu. *OQAM/FBMC for Future Wireless Communications*. 2018.

[30] Jean Walrand and Pravin Varaiya. *High-Performance Communication Networks*. 2000.

[31] J. Armstrong and A.J. Lowery. *Power efficient optical OFDM*. Electronics Letters, 42(6):370–372, 2006.

[32] S. Dimitrov and H. Haas. *Principles of LED Light Communications: Towards Networked LiFi*. Cambridge University Press, 2015.

[33] Pengfei Luo, Min Zhang, Zabih Ghassemlooy, Hoa Le Minh, Hsin Mu Tsai, Xuan Tang, Lih Chieh Png, and Dahai Han. *Experimental Demonstration of*

RGB LED-Based Optical Camera Communications. IEEE Photonics Journal, 7(5):1–12, 2015.

[34] Zhaocheng Wang, Qi Wang, Wei Huang, and Zhengyuan XU. *Visible Light Communications: Modulation and Signal Processing*. John Wiley and Sons, 2017.

[35] Y.B. Gianchandani, O. Tabata, and H.P. Zappe. *Comprehensive Microsystems*. Elsevier, 2 edition, 2008.

[36] J. R. Barry, J.M. Kahn, William J. Krause, Edward A. Lee, and David G. Messerschmitt. *Simulation of Multipath Impulse Response for Indoor Wireless Optical Channels*. IEEE Journal on Selected Areas in Communications, 11(3):367–379, 1993.

[37] G. Yun and M. Kavehrad. *Indoor infrared wireless communications using spot diffusing and fly-eye receivers*. Canadian Journal of Electrical and Computer Engineering, 18(4):151–157, 1993.

[38] Lifang Feng, Rose Qingyang Hu, Jianping Wang, Peng Xu, and Yi Qian. *Applying VLC in 5G Networks: Architectures and Key Technologies*. IEEE network, 30(6):77–83, 2016.

[39] Harald Haas. *LiFi is a paradigm-shifting 5G technology*. Reviews in Physics, 3(October 2017):26–31, 2018.

[40] Vikram Chandrasekhar, Jeffrey G. Andrews, and Alan Gatherer. *Femtocell networks: A survey*. IEEE Communications Magazine, 46(9):59–67, 2008.

[41] Toshihiko Komine and Masao Nakagawa. *Integrated System of White LED Visible Light Communication and Power Line Communication*. IEEE Transactions on Consumer Electronics, 49(1):71–79, 2003.

[42] Hany Elgala, Raed Mesleh, and H. Haas. *Indoor broadcasting via white LEDs and OFDM*. IEEE Transactions on Consumer Electronics, 55(3):1127–1134, 2009.

[43] IEEE. *IEEE Standard for Information technology - Part 3: Carrier Sense Multiple Access with Collision Detection (CSMA/CD) Access Method and Physical Layer Specifications - Amendment: Data Terminal Equipment (DTE) Power via Media Dependent Interface (MDI)*. IEEE Spectrum, 12(4):98–98, 2003.

[44] James Johnston, Garry Banks, and Matt Stewart. *Beyond Power over Ethernet: the development of Digital Energy Networks for Buildings*. Technical Report April, 2012.

[45] Yiguang Wang, Nan Chi, Yuanquan Wang, Li Tao, and Jianyang Shi. *Network Architecture of a High-Speed Visible Light Communication Local Area Network*. IEEE Photonics Technology Letters, 27(2):197–200, 2015.

[46] Anna Tzanakaki, Markos Anastasopoulos, Ignacio Berberana, Dimitris Syrivelis, Paris Flegkas, Thanasis Korakis, Daniel Camps Mur, Ilker Demirkol, Jesus Gutierrez, Eckhard Grass, Qing Wei, Emmanouil Pateromichelakis, Nikola Vucic, Albrecht Fehske, Michael Grieger, Michael Eiselt, Jens Bartelt, Gerhard Fettweis, George Lyberopoulos, Eleni Theodoropoulou, and Dimitra Simeonidou. *Wireless-optical network convergence: Enabling the 5G architecture to support operational and end-user services*. IEEE Communications Magazine, 55(10):184–192, 2017.

[47] B. Adebisi, J. Stott, and B. Honary. *Experimental study of the interference caused by PLC transmission on HF bands*. In IET International Conference on Ionospheric Radio Systems and Techniques, 2006.

[48] Jianming Liu, Bingzhen Zhao, Liang Geng, Zhou Yuan, and Yirong Wang. *Communication performance of broadband PLC technologies for smart grid*. In IEEE International Symposium on Power Line Communications and Its Applications, 2011.

[49] Ting Wu, Theodore S. Rappaport, and Christopher M. Collins. *Safe for generations to come: Considerations of safety for millimeter waves in wireless communications*. IEEE Microwave Magazine, 16(2):65–84, 2015.

[50] Hossein Kazemi, Majid Safari, and H. Haas. *A Wireless Backhaul Solution Using Visible Light Communication for Indoor Li-Fi Attocell Networks*. In IEEE ICC 2017 Optical Networks and Systems Symposium, 2017.

[51] Hossein Kazemi, Majid Safari, and Harald Haas. *A Wireless Optical Backhaul Solution for Optical Attocell Networks*. IEEE Transactions on Wireless Communications, 18(2):807–823, 2019.

2

Mirror-Aided Non-LOS VLC Channel Characterizations with A Time-Efficient Simulation Model

Before developing a backhaul network based on mirror-aided non-LOS VLC links, we first need to assess the performance of the VLC channel. Therefore, a proper simulation model is required to assess the channel performance. The simulation model presented in this chapter, the iterative VLC simulation model, is the tool we designed to assess the performance of VLC links including the mirror-aided non-LOS configuration. The link configurations which achieve good overall performance are then used in the analysis in the following chapters.

* * *

Y. Wu, P. Audenaert, M. Pickavet, D. Colle

Published in Photonic Network Communications, 2019, Vol. 38, pp. 151-166.

Abstract *The emerging cost-efficient visible light communication (VLC)-based indoor wireless network requires an economical solution for backhaul transmission. Non-line-of-sight (non-LOS) VLC links are generally applicable candidates to set up a backhaul network without rearrangement of existing lighting fixtures. Here, we describe non-LOS channels aided by the first-order specular reflection from mirrors, which can be used to overcome the multipath effect of purely diffuse*

non-LOS channels. Characterizations of purely diffuse and mirror-aided non-LOS channels are conducted with a time-efficient simulation model based on an iterative algorithm. Any bounce of reflections combined with specular and diffuse reflections can be simulated using the proposed iterative VLC model in polynomial time. Simulation results show that mirror-aided non-LOS channels outperform purely diffuse non-LOS links regardless of the link configuration. The effect of concentration and directionality of non-LOS VLC channels are also shown and discussed.

2.1 Introduction

Visible light communication (VLC) is an emerging technology to address the bandwidth bottleneck of the radio frequency (RF) spectrum. A VLC-based indoor wireless network uses existing light-emitting-diode (LED) lamps for simultaneous illumination and data transmission. The prospect of ubiquitous VLC applications owing to the wide usage of LEDs for indoor lighting as well as the potential of reliable gigabit transmission makes VLC a promising technique for seamless and high-speed indoor wireless data transmission. A VLC-based indoor wireless network uses LED lamps as access points (APs), each of which provides access transmission within a small cell which is commonly referred to as an attocell. Despite the growing scientific interest in access links of VLC attocell networks [1–4], i.e. data transmission from LED modules of APs to user devices, an underlying assumption in those studies is that all APs are wired connected to the Internet. Various wired backhaul approaches have been proposed to be integrated with the VLC-based network, which are shown in Fig.2.1(a). Power line communication (PLC) uses the existing electric power grid for the backhaul data transmission [5, 6]. The main issue is the high interference and the non-white noise [7]. Power-over-Ethernet (PoE) has been proposed for integrating the power supply and the high-speed backhaul transmission in Ethernet cables at the expense of high cost for replacing the existing power wiring [8]. A VLC-based backhaul solution for relay transmission was proposed in [9], where only one gateway employed with six auxiliary LEDs is connected to the Internet via wire. Each auxiliary LED is responsible for the line-of-sight (LOS) link-based backhaul transmission with one auxiliary photodiode (PD) of the AP of an adjacent hexagonal cell. An example of downstream traffic from the gateway to APs is shown in Fig.2.1(b). More auxiliary transceivers are required for bidirectional backhaul transmission. Despite the fact that LOS backhaul links are able to support large channel capacity, the arrangement of auxiliary VLC transceivers largely depends on the geometry of cells. Misplacement of auxiliary transceivers could introduce large interference. In addition, the heights of APs have to be carefully adjusted in order to maintain the LOS between each pair of auxiliary transceivers. Thus, the design of

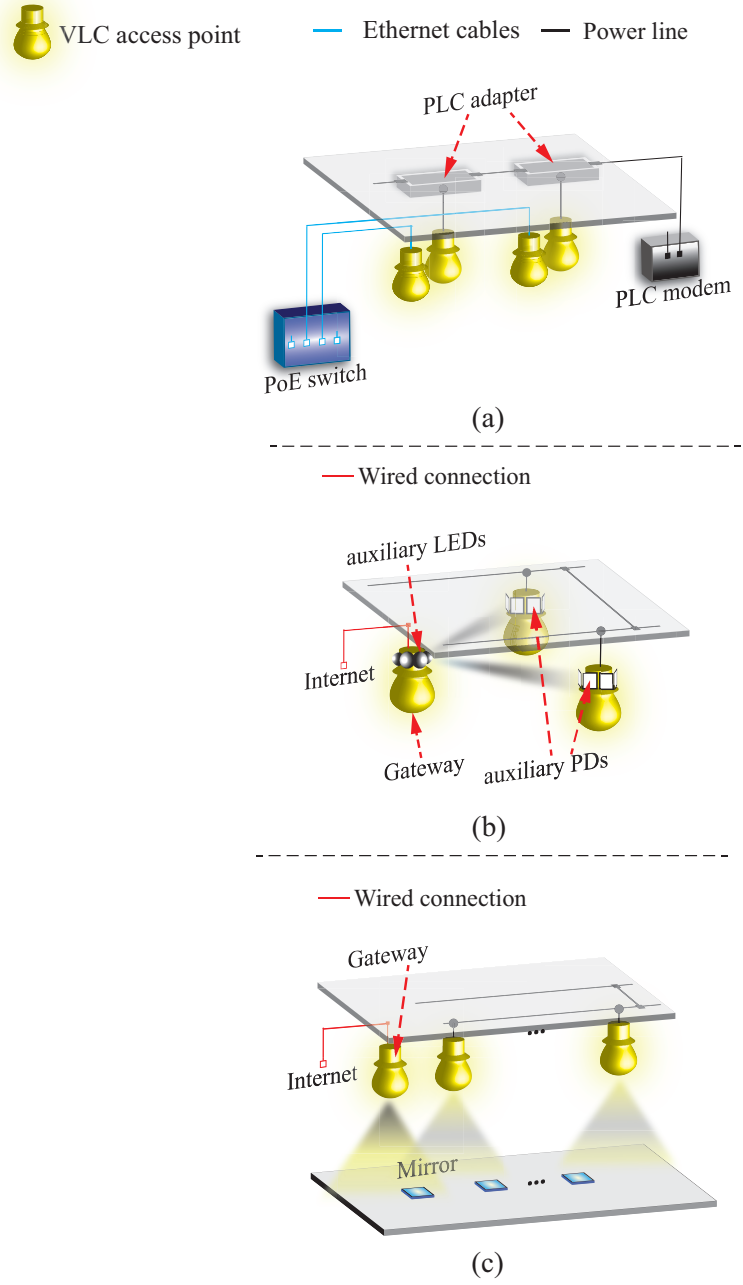

Figure 2.1: Backhaul configurations: (a) Wired backhaul links with PoE or PLC; (b) LOS-based wireless backhaul links; (c) Mirror-aided non-LOS wireless backhaul links

the LOS link-based wireless backhaul network has a low level of generality. In many realistic environments where a series of ceiling lamps are used for indoor illumination, non-LOS VLC links are more generally applicable. In order to mitigate multipath effects caused by diffuse reflections from interior objects and walls, we propose here a mirror-aided non-LOS VLC link-based backhaul network as shown in Fig.2.1 (c). The mirror placed on the floor is used to provide a concentrated and directed first-bounce specularly reflected path from the transmitting AP to the receiving AP such that the channel impulse response is dominated by a specular component. The mirror-aided non-LOS link-based backhaul network necessitates neither replacement of the existing wiring nor strict requirements on the placement of VLC APs. The sizes and positions of mirrors can be easily adjusted according to the application. An added-value of the proposed backhaul solution is that dynamic channel allocation schemes can be easily performed to satisfy different bandwidth requirements on access and backhaul links, as each LED of the VLC AP can be used for simultaneous access and backhaul transmission by allocating different orthogonal frequency division multiplexing (OFDM) subcarriers. Mirror-aided non-LOS links can be foreseen as a low cost and high-performance backhaul solution for the indoor VLC-based wireless network, as the rearrangement of existing lighting fixtures is not required.

Despite fixed positions of lighting fixtures, orientations and concentrations of LED modules and PD modules of each VLC AP can be configured to achieve better channel performance. In order to design a robust backhaul network, extensive research on mirror-aided non-LOS VLC channel characteristics is essential. However, characterization of mirror-aided non-LOS VLC channels cannot be obtained with current simulation models in a reasonable time. Analytical methods presented in [10–12] and methods based on Monte-Carlo ray-tracing algorithm [13–15] cannot provide accurate results, as they reduce the time complexity of the simulation at the expense of accuracy. Near-accurate Infrared (IR) channel characterization can be obtained using a well-known recursive computation method [16, 17]. Based on the recursive method, authors in [18] presented a VLC channel simulation model by adding wavelength-dependent parameters. However, time-complexity is extremely large when increasing the resolution of wavelengths and the accuracy of the results has to be lowered in order to reduce the time-complexity. An iterative method was proposed for IR channel characterization [17, 19]. Optimization is needed to apply this method for VLC channel modeling. In addition to the accuracy requirement, the characterization of mirror-aided non-LOS VLC channels should take into account multi-bounce specular reflections. Unfortunately, current iterative methods only model purely diffuse reflections but ignore specular reflections. In order to investigate the performance of mirror-aided non-LOS VLC channels, we present a new iterative model for characterizing wavelength-dependent VLC channels in rooms with Lambertian surfaces and ideal mirrors.

Multi-bounce channel impulse responses can be simulated in polynomial time. Simulations are undertaken to investigate the performance of purely diffuse and mirror-aided non-LOS VLC channels as well as the impact of different link configurations on the channel performance. Results show that mirror-aided non-LOS channels outperform purely diffuse non-LOS links regardless of the link configuration. Guidelines for achieving reliable high-speed data transmission using the proposed mirror-aided non-LOS channels are also given. The paper is organized in the following way. The following section introduces theories for analyzing multipath VLC channels. The third section describes the computer implementation of the iterative algorithm. Simulation results and discussions are presented in the fourth section.

2.2 Theoretical approaches

Intensity-modulation and direct detection (IM/DD) is the most viable technique used in VLC systems, as the main advantage of IM/DD is its simplicity and low-cost [20]. The waveform of an intensity-modulated signal is represented by the instantaneous radiant power of the LED. PDs are commonly used to detect changes in optical intensity. Light rays radiant from the LED are reflected from walls of the room and surfaces of interior objects. The reflected portion of the optical power depends on the reflectivity of the material at each wavelength. In addition to light rays originating from the transmitter of the concerning VLC channel, a receiver could also receive light radiant from other luminous objects. These luminous objects are considered noise and interfering sources and their contribution to the total received power can be either filtered or mitigated by using multiplexing schemes. In this section, we introduce the method we use to model the simulation environment and multi-bounce reflections. The numerical approach presented in this section is used to iteratively calculate VLC channel impulse responses taking into account different reflecting properties of materials.

2.2.1 Modeling of the environment

The simulation environment of indoor VLC channels is a room with optional interior objects (such as bookcases, desks, and people). We encapsulate the room and all objects into axis-aligned bounding boxes. Each bounding box is a rectangular six-sided box having its surfaces oriented in such a way that normal vectors of all surfaces are parallel with axes of the 3-dimensional Cartesian coordinate system. Surfaces oriented towards the positive and the negative direction of the z-axis are defined as the floor and the ceiling of the box, respectively. The other surfaces are defined as sidewalls of the box. The largest box is an empty room with six internal surfaces shown in Fig.2.2(a) as B_1. Interior objects B_2 and B_3 are modeled as

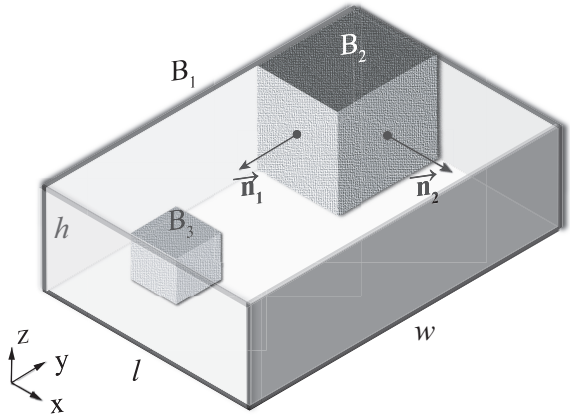

(a)

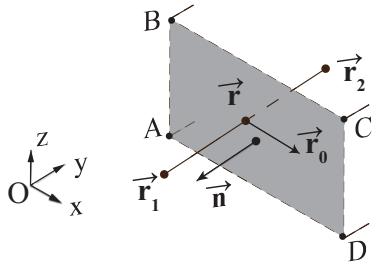

(b)

Figure 2.2: (a) Geometry of an L-shaped room modeled with a room (B_1), a wall-box (B_2), and an object-box (B_3); (b) A path between two points denoted by $\vec{\mathbf{r_1}}$ and $\vec{\mathbf{r_2}}$ obstructed by a plane at the point $\vec{\mathbf{r}}$

boxes with external surfaces. As the ceiling, the floor, and two sidewalls of B_2 are overlapping with the floor, the ceiling, and two walls of B_1, respectively, the simulation environment can be seen as an L-shaped room. All points inside B_2 are obstructed by the two remaining surfaces (surfaces having orientations $\overrightarrow{\mathbf{n_1}}$ and $\overrightarrow{\mathbf{n_2}}$).

The LOS path of a light ray is modeled as a line segment bounded by two points representing locations of the light source and the receiver. The LOS path between two points can be obstructed by opaque objects between them. Luminous objects, i.e. other lighting fixtures, are also considered opaque objects. Fig.2.2(b) illustrates the geometry of an obstructed LOS path. The LOS path is obstructed when the line segment intersects at least one surface. The boundary of each surface is defined by vertices (points A, B, C, and D) of the surface. When the surface is a rectangle and all points have positive coordinates, the boundary can be defined by an initial point (point A) and a terminal point (point C), which are vertices located at the minimum and the maximum Euclidean distance from the origin $\mathbf{O} = (\mathbf{0}, \mathbf{0}, \mathbf{0})$, respectively. The coordinate of a point on a surface is represented by a vector $\vec{\mathbf{r}}$ and can be calculated by solving the plane equation of the surface:

$$\vec{\mathbf{n}} \cdot (\vec{\mathbf{r}} - \overrightarrow{\mathbf{r_0}}) = 0, \tag{2.1}$$

where $\vec{\mathbf{n}}$ is the normal vector of the surface and $\overrightarrow{\mathbf{r_0}}$ is the coordinate of an arbitrary point on the surface. A LOS path is represented by a line equation:

$$\vec{\mathbf{r}} = \overrightarrow{\mathbf{r_1}} + (\overrightarrow{\mathbf{r_2}} - \overrightarrow{\mathbf{r_1}})t, \quad 0 \leq t \leq 1, \tag{2.2}$$

where $\overrightarrow{\mathbf{r_1}}$ and $\overrightarrow{\mathbf{r_2}}$ are vectors representing locations of the sender and the receiver, respectively, and t is a scaling factor. As the LOS path is a line segment connecting two points, the range of t is limited to $0 \leq t \leq 1$, such that $\vec{\mathbf{r}}$ is on the line segment between $\overrightarrow{\mathbf{r_1}}$ and $\overrightarrow{\mathbf{r_2}}$. The coordinate of the point of intersection $\vec{\mathbf{r}}$ can be solved by Eq.(2.1) and Eq.(2.2). The LOS path is unobstructed by a surface if no intersecting point is found or the point exceeds the surface's boundary. We use a function $V(\vec{\mathbf{r_s}}, \vec{\mathbf{r_r}})$ to describe the visibility of the LOS path from a sender s to a receiver r, where $\vec{\mathbf{r_s}}$ and $\vec{\mathbf{r_r}}$ are vectors representing coordinates of s and r, respectively. When the path does not intersect with any surface in the room $V(\vec{\mathbf{r_s}}, \vec{\mathbf{r_r}}) = 1$, and $V(\vec{\mathbf{r_s}}, \vec{\mathbf{r_r}}) = 0$ when the path is obstructed by at least one surface. As the visibility does not change when s and r are swapped, $V(\vec{\mathbf{r_s}}, \vec{\mathbf{r_r}}) = V(\vec{\mathbf{r_r}}, \vec{\mathbf{r_s}})$.

2.2.2 VLC channel impulse response

An IM/DD channel can be modeled as a baseband linear system:

$$Y(t) = X(t) * h(t), \tag{2.3}$$

where $*$ denotes convolution, $X(t)$ and $Y(t)$ are waveforms of the transmitted and received signal represented by optical power, respectively, and $h(t)$ is the channel

impulse response. As light rays are reflected by surfaces in an indoor environment, the received signal consists of a large number of copies of the transmitted signal carried by light rays reflected by a different number of surfaces. The magnitude of each received copy is the optical power carried by the light ray. The delay is the traveling time of the light ray from the sender to the receiver. When the transmitted signal $X(t)$ is a unit-area Dirac delta function $\delta(t)$, the impulse response of the VLC channel is the superposition of all received copies of the signal. Each copy is a delayed and scaled version of $\delta(t)$. We categorize the copies according to the total number of reflections before reaching the receiver, which is denoted by k. The impulse response is

$$h(t) \approx \sum_{k=0}^{K} h^{(k)}(t), \tag{2.4}$$

where $h^{(k)}(t)$ is the superposition of received signals from light rays reflected k times and K is the maximum number of reflections. When K approaching infinity, $h(t)$ approaches the actual impulse response .

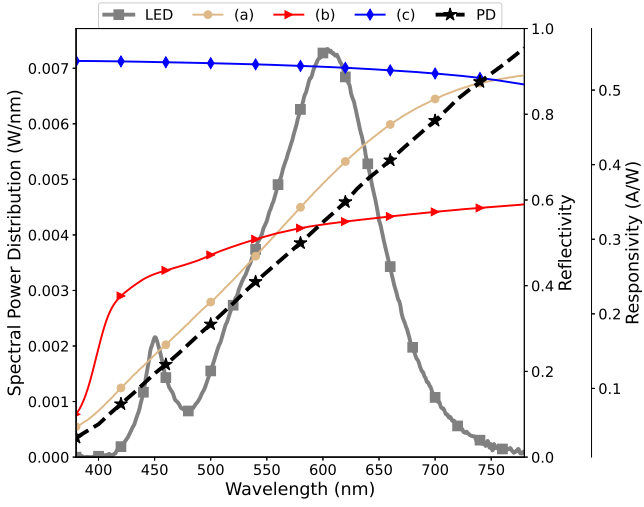

Figure 2.3: SPD of LED, responsivity of PD and reflectivity of (a) pine wood at incident angle 10°*, (b) white rubberized coating at incident angle* 10°*, (c) aluminum at normal incidence angle* 0°

In one of the most well-known simulation models for optical wireless channels, the transmitted optical power and the reflectivity of materials are assumed constant across the near monochromatic spectrum of IR [16]. However, visible LEDs generate white light by superposing the radiant power in different color re-

gions. The spectrum of a white LED is not a uniform distribution across all wavelengths, but rather with large peaks occurring in different regions. In addition, the reflectivity of materials and the responsivity of the PD are not constant across the visible range of the electromagnetic spectrum. Thus, the optical power reflected by multiple surfaces and received by the PD is wavelength-dependent. In order to characterize VLC channels taking into account their spectral properties, we model the transmitted signal as a function of wavelength:$X(t, \lambda) = \Phi_n(\lambda)\delta(t)$. Here, λ is the wavelength in nm, and $\Phi_n(\lambda) = \Phi(\lambda)/P_s$ is the normalized spectral power distribution (SPD) in $\mathrm{W} \cdot \mathrm{nm}^{-1}$, where $\Phi(\lambda)$ is the SPD of the LED sender and $P_s = \int_{390nm}^{700nm} \Phi(\lambda)d\lambda$ is the total transmitted power of the LED. Fig.2.3 shows the normalized SPD of a white Cree BR30 LED lamp, the responsivity of a Thorlabs PD, and the reflectivity of three materials. The spectral characteristic of the LED is obtained from Lamp SPD Database [21]. Over 2400 spectra of natural and artificial materials are available in the ASTER spectral library [22].

For computer simulation, $\delta(t)$ is represented by sending 1 W optical power in the first time slot. The transmitted power is represented by a 2-dimensional array $X[t][\lambda]$:

$$X[t][\lambda] = \Phi_n[\lambda]\delta[t]. \tag{2.5}$$

$X[t][\lambda]$ represents the optical power transmitted at the wavelength sample λ during the time slot from t to $t + \Delta t$, where Δt is the temporal resolution in ns. The received signal $Y^{(k)}[t][\lambda]$ is the superposition of optical power at the wavelength λ and the time slot t of light rays reflected k times. The k-bounce impulse response $h^{(k)}(t)$ is calculated by integrating the received signals $Y^{(k)}[t][\lambda]$ over the visible light spectrum.

2.2.3 Lambert's cosine law and line-of-sight (LOS) path

A receiver only detects light rays with incident angles smaller than its field-of-view (FOV). Assuming that the optical power received throughout the active area of the element is constant, the receiver collects the total power of light rays reaching its active area. The received power consists of multiple reflected components and a possibly existing LOS component. The geometry of a LOS path between a point light source s and a receiver r is illustrated in Fig.2.4(a). The optical power received by r is

$$P_r = \frac{A_r}{D^2} I_s \cos(\theta) \mathrm{rect}(\frac{\theta}{\Theta}), \tag{2.6}$$

where $\mathrm{rect}(\cdot)$ is a rectangular function:

$$\mathrm{rect}(x) = \begin{cases} 1, & |x| \leq 1 \\ 0, & |x| > 1 \end{cases} \tag{2.7}$$

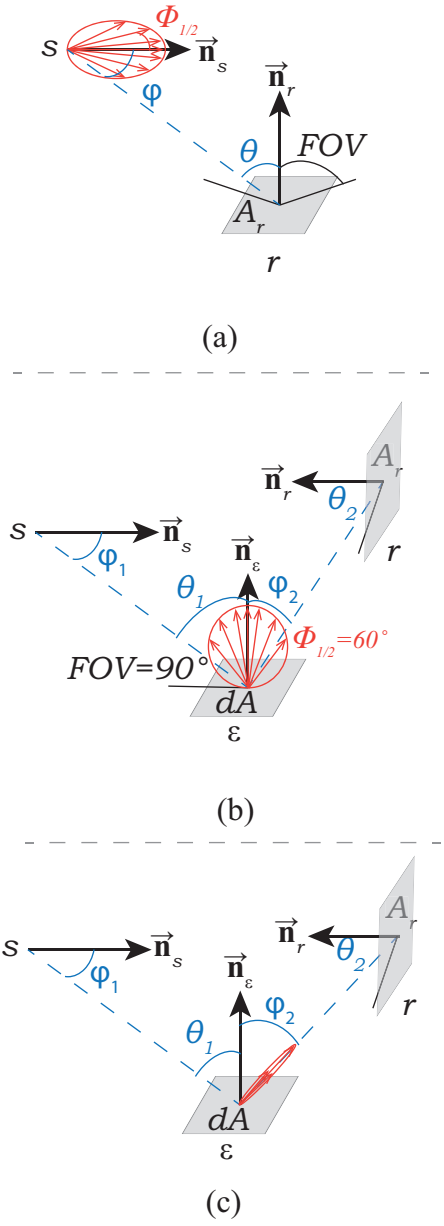

Figure 2.4: Geometry of (a) a LOS path from a point light source s to a receiver r, (b) a diffusely reflected path from s to r which is reflected off a Lambertian surface with $m = 1$ at a point ε, (c) a specularly reflected path from s to r which is reflected off an ideal mirror at a point ε; blue dash lines denote LOS paths while red vectors denote possible directions and lengths of the vectors denote radiant intensity of light rays

I_s is the radiant intensity from the light source s, Θ is the field-of-view (FOV) of r, A_r is the active area of r, and D is the Euclidean distance between s and r:

$$D = \|\vec{\mathbf{r_r}} - \vec{\mathbf{r_s}}\|. \tag{2.8}$$

where $\vec{\mathbf{r_s}}$, $\vec{\mathbf{r_r}}$ represent coordinates of s and r, respectively. The incident angle θ is measured with respect to the orientation of r denoted by the unit-length normal vector $\vec{\mathbf{n_r}}$ of its active area, which can be calculated by

$$\cos(\theta) = \frac{(\vec{\mathbf{r_s}} - \vec{\mathbf{r_r}}) \cdot \vec{\mathbf{n_r}}}{D}. \tag{2.9}$$

The radiant intensity I_s can be obtained by a generalized Lambert pattern if s is a diffuse radiator (for instance, a LED) obeying Lambert's cosine law [23]. The radiant intensity from a Lambertian surface in the direction with the radiant angle of ϕ is

$$I_s(\phi) = \frac{m+1}{2\pi} P_s \cos^m(\phi) \text{rect}(\frac{\phi}{\pi/2}), \tag{2.10}$$

where ϕ is the radiant angle with respect to the orientation of s denoted by a unit-length vector $\vec{\mathbf{n_s}}$ which can be calculated by

$$\cos(\phi) = \frac{(\vec{\mathbf{r_r}} - \vec{\mathbf{r_s}}) \cdot \vec{\mathbf{n_s}}}{D}. \tag{2.11}$$

Here, P_s is the total radiant power from s, the Lambertian order $m = -\frac{\ln(2)}{\ln(\cos(\Phi_{1/2}))}$ is an index describing the concentration of s, where $\Phi_{1/2}$ is the semi angle at half intensity of s and normally given by LED manufacturers, and the rectangular function is used to ensure a non-negative intensity. We use $g^{df}_{s,r}$ to denote the path loss of a LOS path from a Lambertian sender (i.e. a diffuse radiator) s to a receiver r, i.e. the proportion of P_r to P_s:

$$g^{df}_{s,r} = \frac{(m+1)A_r}{2\pi D^2} \cos^m(\phi) \cos(\theta) \text{rect}(\frac{\phi}{\pi/2}) \text{rect}(\frac{\theta}{\Theta}) \tag{2.12}$$

The LOS component of the received signal, i.e. the temporal and spectral distribution of the optical power received from the LOS path from s to r is calculated by

$$DF(s,r): \quad Y^{df}_{s,r}[t][\lambda] = g^{df}_{s,r} V(\vec{\mathbf{r_s}}, \vec{\mathbf{r_r}}) X_s[t - \tau_{s,r}][\lambda], \tag{2.13}$$

where $\tau_{s,r}$ is the delay of the LOS path:

$$\tau_{s,r} = \frac{D}{c}, \tag{2.14}$$

where c is the speed of light. In order to simplify the notation for further discussions, we use $DF(s,r)$ to denote Eq.(2.13).

2.2.4 Modeling of diffuse reflections

A reflected path can be modeled as having an incident LOS path and a radiant LOS path. The radiant pattern at the reflecting point depends on the material of the reflecting surface. Most rough surfaces are considered Lambertian surfaces and exhibit diffuse reflections. Light rays are reflected in all directions from a reflecting point on a Lambertian surface regardless of the angle of incidence. The radiant intensity can be calculated with Eq.(2.10). Fig.2.4(b) illustrates a diffusely reflected path from a light source s to a receiver r. The path from s to ε is called the incident LOS path, and the path from ε to r is the radiant LOS path. The reflecting point is assumed an ideal Lambertian surface with $m = 1$. The optical power is received by an infinitesimal area dA around the reflecting point with FOV $\Theta = \pi/2$. The proportion of the radiant power to the received power is defined by the reflectivity of the material.

Multi-bounce received power of a light ray can be obtained by recursively calculating optical power received by each LOS path [16]. However, there are total N^k light rays for the k-th bounce and thereby in total $N^k(k+1)$ calculations of $DF(s,r)$ are required for each k-bounce impulse response, where N is the number of reflecting points. The computational effort of the recursive method increases exponentially with k. In order to reduce the complexity of calculations without loss of accuracy for a large number of reflections, we calculate the optical power received via diffusely reflected paths iteratively by modeling each reflecting point in the environment as having multiple levels of *active* senders and receivers. The k-th sender and the k-th receiver of a reflecting point ε are denoted by $\varepsilon^{s(k)}$ and $\varepsilon^{r(k)}$, respectively. Similarly, the PD receiver R is modeled as having multiple levels of receivers denoted by $R^{(k)}$. The LED sender S has only one active sender transmitting the signal $X[t][\lambda]$ and is denoted by $S^{(-1)}$. The k-th receiver of every reflecting point receives optical power from all $(k-1)$-th senders. The k-th sender then radiants the power to all $(k+1)$-th receivers. As the LED and reflecting points are assumed perfect Lambertian surfaces, the radiant power from the k-th sender is independent of the direction and the intensity of the light ray from each incident LOS path. Thus, impulse responses with a total number of K bounces can be calculated with $(K+1)$ iterations from 0 to K. There is only one sender in the 0-th iteration. Thus, $(N+1)$ calculations of $DF(s,r)$ are required to calculate the optical power received by the 0-th receivers of reflecting points and the PD, i.e. $\varepsilon_i^{r(0)}, i = 0, 1, \cdots, N-1$, and $R^{(0)}$. For each additional iteration, N^2 calculations are required to calculate the power radiant from N senders. The time complexity increases linearly.

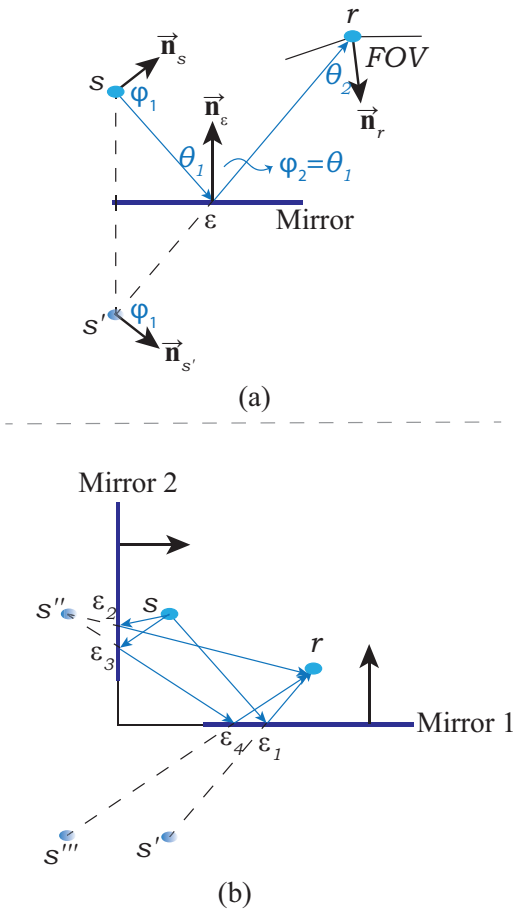

Figure 2.5: (a) Geometry of a specularly reflected path (mirror-obstructed LOS path) from s to r; s' denotes the mirror image of s, ε denotes the reflecting point; (b) Multi-bounce specular reflections caused by multiple mirror images of s

2.2.5 Modeling of specular reflections

Glossy surfaces like mirrors exhibit directed and concentrated specular reflections. The radiant intensity from a point on a mirror drops dramatically when the angle between ϕ_2 and θ_1 increases as shown in Fig.2.4(c), where θ_1 is the incident angle of the incident LOS path and ϕ_2 is the radiant angle of the radiant LOS path. It is extremely difficult to iteratively calculate the multipath impulse responses taking into account specular reflections, as the direction and the intensity of the light ray from each radiant LOS path depends on the corresponding incident LOS path. Nonetheless, we can model a specularly reflected path as a LOS path which is "obstructed" by an ideal mirror using the method described in section 2.2.1. The specular reflection from a perfect mirror is equivalent to a LOS path from the mirror image of s (denoted by s') to r which is "obstructed" by the mirror at the intersecting point ε as illustrated in Fig.2.5(a). We assume that all mirrors exhibit perfect specular reflections such that the radiant angle of the radiant path equals the incident angle of the incident path. The path loss of the *mirror-obstructed* LOS path from s' to r can be calculated with $DF(s', r)$ multiplied with the reflectivity of the mirror. The reflectivity ρ is wavelength-dependent and incident-angle-dependent. The refracted and reflected portion of the light ray is described by the Fresnel equation. Schlick's approximation is a generally used method to approximate the Fresnel equation expressing the reflection of light on a well-oriented facet with less than 1% error [24], which is formulated as

$$\rho(\theta, \lambda) \approx \rho_0(\lambda) + (1 - \rho_0(\lambda))(1 - \cos(\theta))^5, \tag{2.15}$$

where θ is the incident angle and $\rho_0(\lambda)$ is the reflectivity of the material at wavelength λ at normal incidence. We use a function $V^m(\overrightarrow{\mathbf{r_s}}, \overrightarrow{\mathbf{r_r}})$ to denote the visibility of the mirror-obstructed LOS path. In contrast to the definition of $V(\overrightarrow{\mathbf{r_s}}, \overrightarrow{\mathbf{r_r}})$ in section 2.2.1, $V^m(\overrightarrow{\mathbf{r_{s'}}}, \overrightarrow{\mathbf{r_r}}) = 1$ when the path is obstructed by a mirror, and $V^m(\overrightarrow{\mathbf{r_{s'}}}, \overrightarrow{\mathbf{r_r}}) = 0$ when r cannot "see" the mirror image s'.

The temporal and spectral distribution of the power received by a mirror-obstructed LOS path is calculated by

$$SP(s, r) : Y^{sp}_{s,r}[t][\lambda] = g^{sp}_{s,r}[\lambda] V(\overrightarrow{\mathbf{r_s}}, \overrightarrow{\mathbf{r_{\varepsilon_m}}}) V(\overrightarrow{\mathbf{r_r}}, \overrightarrow{\mathbf{r_{\varepsilon_m}}}) X_s[t - \tau_{s',r}][\lambda], \tag{2.16}$$

where ε_m denotes the reflecting point on the mirror and $g^{sp}_{s,r}[\lambda] = g^{df}_{s',r} \rho_{s,r}[\lambda] V^m(\overrightarrow{\mathbf{r_{s'}}}, \overrightarrow{\mathbf{r_r}})$ is the path loss of the mirror-obstructed LOS path. Similarly, we use $SP(s, r)$ to denote Eq.(2.16).

The reflecting point on the mirror is considered *passive*. Thus, each k-th receiver detects specularly reflected light rays from $(k-2)$-th senders when there is only one mirror. Multipath impulse responses of mirror-aided non-LOS channels can be iteratively calculated. When multiple mirrors having different orientations are placed as shown in Fig.2.5(b), there will be multiple mirror-obstructed LOS

paths and thereby multiple reflecting points. The total received power can be calculated by superposing $Y_{s,r}^{sp}[t][\lambda]$ obtained from all mirror images. In a specific case where two mirrors are oriented towards opposite directions, infinite numbers of images will be generated. The time complexity increases with the number of mirror images. In order to simplify the simulation, we assume that all mirrors are placed at the same height with the same orientation, such that each diffusely reflecting point as well as the LED sender S only has one mirror image. A complete study of the combinations of diffuse reflections and specular highlights on glossy surfaces is beyond the scope of this study, but it will be considered in future work.

2.3 Implementation

Based on the theoretical approaches described in the previous section, we implement a simulation model to iteratively calculate the impulse response of the VLC channel. A major advantage of the iterative method is that the overhead for calculating impulse responses of VLC channels originating from the same sender in the same environment to different receivers is significantly reduced. The iterative algorithm consists of an environment initialization phase, an iterative computation phase, and the final phase for calculating the impulse response.

2.3.1 Environment initialization

As we have discussed in section 2.2.4 and 2.2.5, the k-bounce impulse response can be calculated by superposing optical power received from all reflecting points. Instead of taking an infinite number of points into account, we divide diffuse surfaces into a grid of differential elements. Each differential element has an active area of $dA = \Delta d^2$, where Δd is the spatial resolution. The location (i.e. coordinate) of each differential element as well as locations active senders and receivers of the element are assumed to be the central point of the element. Although the iterative calculation of k-bounce impulse responses requires a large number of calculations of $DF(s,r)$ and $SP(s,r)$, it can be seen from Eq.(2.12) and Eq.(2.14) that values of $g_{s,r}^{df}$ and $\tau_{s,r}$ are independent of the number of reflections. In addition, visibility functions $V(\vec{\mathbf{r_s}}, \vec{\mathbf{r_r}})$ and $V^m(\vec{\mathbf{r_{s'}}}, \vec{\mathbf{r_r}})$ as well as the incident angle-dependent reflectivity only depend on the properties of the environment, i.e. the layout of boxes and reflectivity of surfaces. Thus, we construct lookup tables for $g_{s,r}^{df}$, $\tau_{s,r}$, $V(\vec{\mathbf{r_s}}, \vec{\mathbf{r_r}})$, and $\rho_{s,r}[\lambda]$ of all LOS paths between two differential elements in the environment initialization phase. When there are mirrors in the environment, additional lookup tables for $g_{s',r}^{sp}$ and $\tau_{s',r}$ will be constructed. The size of each lookup table is N_ε^2, where N_ε is the total number of differential elements.

Constructing the lookup table for $g_{s,r}^{df}$ requires N_ε^2 calculations of Eq.(2.12). Each calculation consists of several multiplications and summations. We can fur-

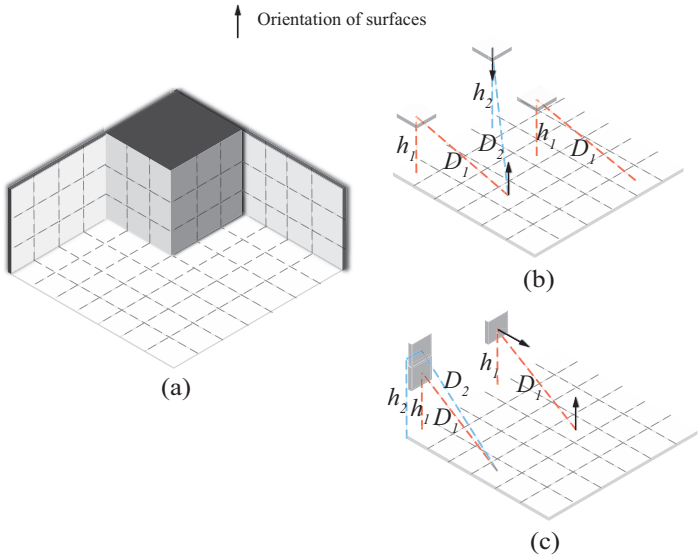

Figure 2.6: (a) Differential elements aligned on a Cartesian grid; (b) Elements on two surfaces having opposite orientations; (c) Elements on two intersecting surfaces having perpendicular orientations

ther reduce the number of calculations for a specific case where all differential elements are aligned on a Cartesian grid where each cell is a unit square having the area of $dA = \Delta d^2$ as shown in Fig.2.6(a). Since the radiant intensity from a light source is non-negative, $g_{s,r}^{df}$ is only meaningful when the radiant angle $\phi \leq \pi/2$. We can categorize Lambertian surfaces with meaningful $g_{s,r}^{df}$ according to the orientation of one surface relative to the orientation of the other:

- two surfaces having opposite orientations as shown in Fig.2.6(b);
- two surfaces having perpendicular (i.e. orthogonal) orientations as shown in Fig.2.6(c).

As all differential elements have the same values of m, dA, and Θ, $g_{s,r}^{df}$ is a function of $\vec{\mathbf{r_s}}$, $\vec{\mathbf{r_r}}$, $\vec{\mathbf{n_s}}$, and $\vec{\mathbf{n_r}}$. When two surfaces have opposite orientations and vertical distance of h as shown in Fig.2.6(b), $g_{s,r}^{df}$ becomes a function of the relative distance D between r and the projection of s. For each value of h, there are at maximum $(N_{max})^2$ unique values of D, where $N_{max} = L_{max}/\Delta d$, with L_{max} is the maximum side-length of the largest box. For a pair of surfaces having perpendicular orientations, there are N_{max} unique values of h as shown in Fig.2.6(c), thereby N_m^3 unique values of $g_{s,r}^{df}$. The total number of calculations is reduced to $N_{op}N_{max}^2 + N_{max}^3$. This optimized method is appropriate for simulations when N_ε is very large.

2.3.2 Iterative calculations and impulse responses

In order to obtain the kth bounce impulse response, the signal received by $R^{(k)}$ is calculated. The signal $Y_{R^{(k)}}[t][\lambda]$ is the temporal and spectral distribution of the optical power received from all $(k-1)$th senders. We use $\mathcal{S}^{(k)}$ and $\mathcal{R}^{(k)}$ to denote sets of kth senders and kth receivers, respectively. The iterative algorithm is illustrated in Algorithm 1. The size of the array $X_S[t][\lambda]$ is $(T \times W)$, where $W = (700nm - 390nm)/\Delta\lambda$ is the number of wavelengths, $T = Kt_{max}/\Delta t$ is the number of time slots, (where the temporal resolution $\Delta t = \Delta d/(c\sqrt{2})$ is chosen to be the minimum delay, which is the traveling time of a light ray between central points of two adjacent elements having perpendicular orientations) and $t_{max} = (\sqrt{L_x^2 + L_y^2 + L_z^2})/c$ is the maximum travelling time of a light ray along the diagonal of the largest box (where L_x, L_y, and L_z are side-lengths of the largest box along x, y, and z axes, respectively). The k-bounce impulse response is calculated with Eq.(2.4), where $Y_R^{(k)}[t] = \sum_{\lambda=390nm}^{700nm} Y_R^{(k)}[t][\lambda]\Delta\lambda$.

It can be seen from Algorithm 1 that calculations of transmitted signals from active senders of differential elements are independent of R. Impulse responses of channels between S and another receiver (i.e. a PD in a different location with different orientation) can be simulated in the same manner by changing the parameters of R in step (6) and (24). Intermediate results $X_{s(k)}[t][\lambda]$ are stored on the hard disk in order to reduce the overhead for calculating the impulse response of multiple channels. We programmed the simulation model in Python 3.5 using open-source packages for calculations and plotting figures. All tables are stored in the form of HDF5 data files on the hard disk. The simulation time and the size of disk files scale with the total number of elements and the maximum number of reflections. We ran simulations on 24-core 64-bit PCs with 24 GB RAM. The simulation of an empty room with a size of $5\,\mathrm{m} \times 5\,\mathrm{m} \times 3\,\mathrm{m}$, Δd =0.2 m, $\Delta\lambda$ =10 nm and $K = 7$ took $\sim$6 min for constructing lookup tables for LOS paths, $\sim$1 min for the first iteration and $\sim$90 min for each additional iteration. When the simulation environment and the sender are fixed, the value of $X_{s(k)}[t][\lambda]$ is not changed and can be used to calculate the power received by different receivers. Improving the spatial resolution will lead to large memory consumption and eventually a large amount of simulation time. Authors in [17] found that spatial resolutions of more than five divisions per meter, i.e. with Δd smaller than 0.2 m, do not significantly improve the accuracy.

2.4 Simulation results

INITIALIZE $X_S[t][\lambda]$ with Eq.(2.5)
for k in $[-1, K-1]$ **do**
    $\mathcal{S}^{(k)} = \{S \text{ if } k == -1 \text{ else } \emptyset\} \cup \{\varepsilon_i^{s(k)}, i \in [0, N_\varepsilon - 1]\}$ ▷ A set of kth senders
end for
for k in $[0, K]$ **do**
    $\mathcal{R}^{(k)} = \{R^{(k)}\} \cup \{\varepsilon_i^{r(k)}, i \in [0, N_\varepsilon - 1] \text{ if } k < K \text{ else } \emptyset\}$ ▷ A set of kth receivers
end for
for k in $[0, K]$ **do** ▷ The kth iteration
    for r in $\mathcal{R}^{(k)}$ **do**
        for s in $\mathcal{S}^{(k-1)}$ **do** ▷ Signals received from LOS paths
            if r and s on different elements **then**
                Calculate $Y_{s,r}^{df}[t][\lambda]$ with $DF(s, r)$
                Calculate $\rho_{s,r}[\lambda]$ with Eq.(2.15)
            end if
        end for
        if there are mirrors **then**
            for s in $\mathcal{S}^{(k-2)}$ **do** ▷ Signals received from mirror-obstructed LOS paths
                Calculate $Y_{s,r}^{sp}[t][\lambda]$ with $SP(s, r)$
                Calculate $\rho_{s',r}[\lambda]$ with Eq.(2.15)
            end for
        else
            $Y_{s,r}^{sp}[t][\lambda] = 0 \quad \forall s \in \mathcal{S}^{(k-2)}$
        end if
        if $r \neq R$ **then**
            for $s(k)$ in $\mathcal{S}^{(k)}$ **do** ▷ Transmitted signals for next iteration
                if r and $s(k)$ on the same element **then**
                    $X_{s(k)}[t][\lambda] = \sum_{s \in \mathcal{S}^{(k-1)}} Y_{s,r}^{df}[t][\lambda]\rho_{s,r}[\lambda] + \sum_{s \in \mathcal{S}^{(k-2)}} Y_{s,r}^{sp}[t][\lambda]\rho_{s',r}[\lambda]$
                end if
            end for
        else ▷ Signals received by $R^{(k)}$
            $Y_r[t][\lambda] = \sum_{s \in \mathcal{S}^{(k-1)}} Y_{s,r}^{df}[t][\lambda] + \sum_{s \in \mathcal{S}^{(k-2)}} Y_{s,r}^{sp}[t][\lambda]$
        end if
    end for
end for

algorithm 1: Iterative calculations

	Environment 1	**Environment 2**	**Environment 3**
Box (Room)	$\vec{\mathbf{r}} = (0, 0, 0)$ l=5 m w=5 m h=3 m	$\vec{\mathbf{r}} = (0, 0, 0)$ l=5 m w=5 m h=3 m	$\vec{\mathbf{r}} = (0, 0, 0)$ l=5 m w=5 m h=3 m
Mirror		$\vec{\mathbf{r}} = (3.2, 2.4, 0)$ l=0.2 m w=0.2 m h=0 m	$\vec{\mathbf{r}} = (0, 0, 0)$ l=5 m w=5 m h=0 m

Table 2.1: Simulation environments

	Room		Mirror	
	wavelength dependent	constant	wavelength dependent	constant
ceiling	white rubberized coating	0.52	-	-
floor	pine wood	0.58	aluminum coating	0.91
walls	white rubberized coating	0.52	-	-

Table 2.2: Materials and reflectivity of surfaces

	Sender	Receiver
Configuration A	$\overrightarrow{\mathbf{r_S}} = (l/2, w/2, h-0.5)$	$\overrightarrow{\mathbf{r_R}} = (l/2+1.5, w/2, h-0.5)$
	$\theta_S = 180°$	$\theta_R = 180°$
	$\phi_S = 0°$	$\phi_R = 0°$
	$\Phi_{1/2} = 30°, 60°$	$\Theta = 10°, 20°, ...70°$
Configuration B	$\overrightarrow{\mathbf{r_S}} = (l/2, w/2, h-0.5)$	$\overrightarrow{\mathbf{r_R}} = (l/2+1.5, w/2, h-0.5)$
	$\theta_S = 180°$	$\theta_R = 163°$
	$\phi_S = 0°$	$\phi_R = 180°$
	$\Phi_{1/2} = 30°, 60°$	$\Theta = 10°, 20°, ...70°$
Configuration C	$\overrightarrow{\mathbf{r_S}} = (l/2, w/2, h-0.5)$	$\overrightarrow{\mathbf{r_R}} = (l/2+1.5, w/2, h-0.5)$
	$\theta_S = 163°$	$\theta_R = 180°$
	$\phi_S = 0°$	$\phi_R = 0°$
	$\Phi_{1/2} = 30°, 60°$	$\Theta = 10°, 20°, ...70°$
Configuration D	$\overrightarrow{\mathbf{r_S}} = (l/2, w/2, h-0.5)$	$\overrightarrow{\mathbf{r_R}} = (l/2+1.5, w/2, h-0.5)$
	$\theta_S = 163°$	$\theta_R = 163°$
	$\phi_S = 0°$	$\phi_R = 180°$
	$\Phi_{1/2} = 30°, 60°$	$\Theta = 10°, 20°, ...70°$

Table 2.3: Link configurations

Channel characterizations of purely diffuse and mirror-aided non-LOS channels are discussed in this section. We model three environments as shown in Table 2.1. The location of each box denoted by $\vec{\mathbf{r}}$ is the coordinate of the point located at the minimum distance from the origin and l, w and h denote the side-length of a box along the x-, y-, z-axis, respectively. Environment 1 is designed for simulating purely diffuse non-LOS VLC links, while Environment 2 and 3 are used to simulate mirror-aided non-LOS channels. The placement of the mirror depends on the locations and orientations of the intended sender and receiver of the mirror-aided non-LOS link in order to provide the first-order specular reflection from the LED sender to the receiver. Ideally, one specularly reflecting point is sufficient to establish a mirror-aided non-LOS link. However, the size of a mirror is not infinitesimal and the receiver detects higher-order specular reflections which consist of light rays from differential elements to the receiver reflected by the mirror. Thus, we use a small mirror having the same size as one differential element to simulate an ideal case when the receiver only detects the specular reflection from the sender in Environment 2. The impact of the size of the mirror on channel performance is investigated with an extreme case as Environment 3 where the whole floor is covered by a large mirror such that there aren't any diffuse reflections from the floor and all remaining reflecting points (differential elements) are mirrored.

The materials of surfaces of each box in Table 2.1 are presented in Table 2.2. The wavelength-dependent reflectivity of each material has been shown in Fig.2.3.

In Environment 2 and 3, the floor of the room is covered with a surface which mimics an ideal mirror. Mirrors are assumed to have very thin glass coated with aluminum such that it only exhibits perfect specular reflections on the aluminum coating. In addition to the wavelength-dependent environments, we also simulate environments with constant reflectivity using the same method as in [18], where the reflectivity is a weighted average value across the visible light spectrum:

$$\overline{\rho}(\lambda) = \frac{\int_{390nm}^{700nm} \Phi_n(\lambda)\rho(\lambda)d\lambda}{\int_{390nm}^{700nm} \Phi_n(\lambda)d\lambda} = \int_{390nm}^{700nm} \Phi_n(\lambda)\rho(\lambda)d\lambda, \tag{2.17}$$

This averaging ensures that the first-order reflected power from each surface is the same as that in the wavelength-dependent environments.

As we have discussed in previous sections, impulse responses of indoor VLC links depend on positions and orientations of the sender and the receiver, as well as intervening reflectors (the environment). The effect of positions of the sender and the receiver on channel impulse responses have been discussed in literature [25, 26]. As LEDs of the transmitting AP can be configured to have different orientations and beam-widths and the receiving AP can apply angle-diversity PDs with different viewing angles, it is also worth investigating the effect of configurations on non-LOS VLC links. Therefore, we simulate four non-LOS VLC link configurations as shown in Table 2.3. Orientations of senders and receivers are represented by unit-length vectors defined by zenith angles θ_S and θ_R, azimuth angles ϕ_S and ϕ_R. The zenith angle ranging from 0° to 180° is the angle of a vector measured from the $+z$ axis. A vector on the XOY plane has the zenith angle of 90°. The azimuth angle is a signed angle of the projection of a vector onto the XOY plane with respect to the $+x$ axis. The sign of the angle is so defined that the $+y$ axis has the azimuth angle of -90°. Four link configurations can be categorized according to the orientations of senders and receivers. Senders in configuration C and D are oriented towards a point ε_c on the floor, where ε_c is the first-order specularly reflecting point of mirror-aided non-LOS links. Receivers in configuration B and D are oriented towards ε_c. Senders and receivers in other configurations are oriented directly downwards.

2.4.1 Multipath effect on non-LOS VLC links

Impulse responses of non-LOS channels in three environments as described in table 2.1 are shown in 2.7, 2.8 and 2.9. The location of the small mirror and the orientation as well as the FOV Θ of the receiver are configured such that the receiver is able to detect the first-order specular reflection in Environment 2. Impulse responses $h(t)$ are normalized with a factor $10^{-9}/\Delta t$ which correspond to the optical power received per unit time. The total optical power detected by the receiver of the purely diffuse non-LOS link is $988.6\,\mathrm{nW}$. The first-order component carries

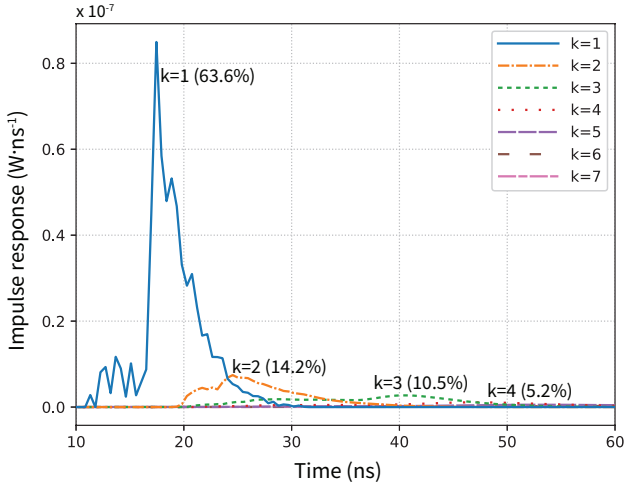

Figure 2.7: Multipath impulse responses of one link with configuration A (both senders and receivers are oriented directly downwards) in Environment 1 (purely diffuse); $\Phi_{1/2} = 60°$, $\Theta = 70°$, $\Delta d = 0.2m$, $\Delta\lambda = 20nm$, $K = 7$

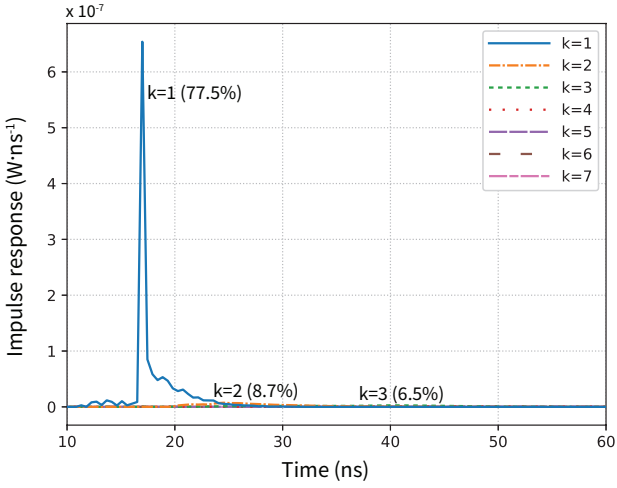

Figure 2.8: Multipath impulse responses of one link with configuration A (both senders and receivers are oriented directly downwards) in Environment 2 (mirror-aided, small); $\Phi_{1/2} = 60°$, $\Theta = 70°$, $\Delta d = 0.2m$, $\Delta\lambda = 20nm$, $K = 7$

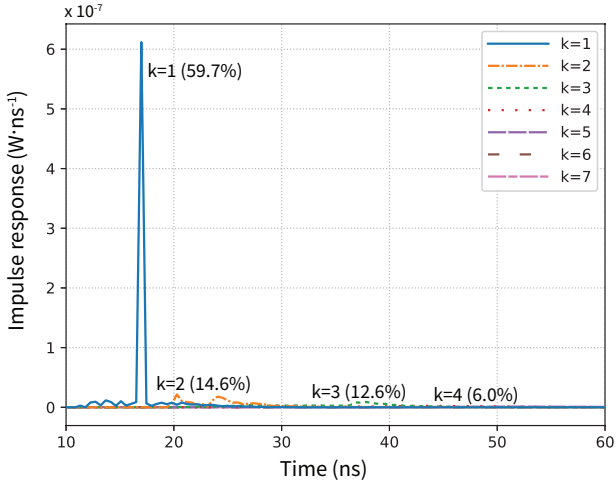

Figure 2.9: Multipath impulse responses of one link with configuration A (both senders and receivers are oriented directly downwards) in Environment 3 (mirror-aided, large); $\Phi_{1/2} = 60^{\circ}$, $\Theta = 70^{\circ}$, $\Delta d = 0.2m$, $\Delta\lambda = 20nm$, $K = 7$,

63.6% of the total optical power. The second-order and the third-order components are still significant and broaden the impulse response as shown in Fig.2.7. The receiver of the mirror-aided non-LOS link with a small mirror receives in total $1.6\,\mu$W optical power. It can be seen in Fig.2.8 that the first-order component dominates the impulse response. Received power after 40 ns is no longer significant as the third order and higher-order components contain relatively low power compared to low-order components. When the size of the mirror increases, the total received power is reduced to $1.3\,\mu$W. The second-order and higher-order components become significant as shown in Fig.2.9. It is clearly shown that impulse responses of mirror-aided non-LOS links have higher peak values and narrower pulses than the impulse response of the purely diffuse non-LOS link. It can be seen that increasing the size of the mirror reduces the peak value of the first bounce ($k = 1$) and increases higher-order received power. The difference in the first-bounce received power is due to the lack of first-order diffuse reflections from the floor which is covered by a mirror in Environment 3. As the specular reflection is directional, the receiver in Environment 3 can only detect one first-order specular reflection from the large mirror on the floor, while one first-order specular reflection and multiple first-order diffuse reflections can be detected by the receiver in Environment 2. Thus, further increasing mirror size cannot improve the total received power when the mirror size is large enough to provide the desired first-order specular reflection. This also explains why the first-order impulse response

in Fig.2.9 is narrower than that that in Fig.2.8. When the number of reflections increases, the receiver in Environment 3 receives more power from higher-order specular reflections. Small peaks in the second-order and the third-order components are likely due to the fact that highly reflective walls reflect a large amount of power.

2.4.2 Wavelength dependency of VLC links

In order to highlight the wavelength dependency of VLC links, we compare VLC links simulated with the proposed iterative model and the model presented in [18] taking into account the responsivity of PD. Similar to the averaged reflectivity obtained with Eq.(2.17), the wavelength-independent responsivity is the weighted average value of the responsivity shown in Fig.2.3, which is $0.296\,\mathrm{A}\cdot\mathrm{W}^{-1}$ calculated with Eq.(2.17). Instead of directly comparing simulated impulse responses, two channel parameters — the DC gain and the root-mean-square (RMS) delay spread — derived from channel impulse responses of two models are compared. The DC gain $H0$ is the channel magnitude response $|H[f]|$ at zero frequency, i.e. $|H[0]|$. In order to highlight the impact of the total number of reflections K on the simulated results, we calculate the channel DC gain $H0^{(K)}$ when 0 to K bounces are taken into account:

$$H0^{(K)} = \left| \sum_{t=0}^{N_t-1} \sum_{k=0}^{K} h_{PD}^{(k)}[t]\Delta t \right| = \left| \sum_{t=0}^{N_t-1} \sum_{k=0}^{K} Y_R^{(k)}[t][\lambda] R_{PD}[\lambda] \right|, \tag{2.18}$$

where N_t is the number of sampled values of the discrete impulse response, $Y_R^{(k)}[t][\lambda]$ denotes the total received optical power at the wavelength λ during the time slot t and $R_{PD}[\lambda]$ is the wavelength-dependent responsivity of the PD in $\mathrm{A}\cdot\mathrm{W}^{-1}$. We use $h_{PD}(t)$ to distinguish electrical impulse responses from impulse responses calculated directly by the optical power, i.e. $h(t)$. The channel DC gain determines the achievable signal-to-noise ratio (SNR) for a fixed transmitted power. The RMS delay spread, denoted by τ_{RMS}, is an important measure of inter-symbol interference (ISI), which is a major problem in the design of a robust wireless communication channel. The RMS delay spread τ_{RMS} of a channel can be calculated using the impulse response [10]:

$$\tau_{RMS} = \sqrt{\frac{\int_{-\infty}^{\infty} (t-\mu)^2 h_{PD}^2(t)dt}{\int_{-\infty}^{\infty} h_{PD}^2(t)dt}}, \tag{2.19}$$

where μ is the mean delay spread which is calculated by

$$\mu = \frac{\int_{-\infty}^{\infty} t^2 h_{PD}^2(t)dt}{\int_{-\infty}^{\infty} h_{PD}^2(t)dt}. \tag{2.20}$$

Similar to the channel DC gain $H0^{(K)}$, the RMS delay spread with different numbers of total reflections $\tau_{RMS}^{(K)}$ are calculated. Approximate results of $\tau_{RMS}^{(K)}$ can be obtained by replacing integrals with finite summations and substituting $h_{PD}(t) = \sum_{k=0}^{K} h_{PD}^{(k)}[t]$. The values $H0^{(K)}$ and $\tau_{RMS}^{(K)}$ of all links listed in Table 2.3 (which are simulated in all environments as listed in Table 2.1) are calculated.

The accuracy of the DC gain and the RMS delay spread is important for VLC channel characterizations. Thus, it is essential to compare the calculated results of $H0^{(K)}$ and $\tau_{RMS}^{(K)}$ obtained from different simulation models. To highlight the error caused by increasing K, we show differences in the results represented by a calculation error ratio ξ. The calculation error ratio of the DC gain is

$$\xi_{H0^{(K)}} = \left| 1 - \frac{H0_{const}^{(K)}}{H0_{wv}^{(K)}} \right|, \quad H0_{wv}^{(K)} \neq 0, \tag{2.21}$$

where $H0_{wv}^{(K)}$ and $H0_{const}^{(K)}$ are DC gains calculated from impulse responses simulated in the wavelength-dependent environments and environments with constant reflectivity, respectively. Similarly, $\xi_{\tau_{RMS}^{(K)}}$ can be calculated with Eq.(2.21) substituting $H0_{wv}^{(K)}$ and $H0_{const}^{(K)}$ with $\tau_{wv}^{(K)}$ and $\tau_{const}^{(K)}$, respectively. Mean values and corresponding confidence intervals (95%) of $\xi_{H0^{(K)}}$ and $\xi_{\tau_{RMS}^{(K)}}$ are presented in Fig.2.10. It can be seen that the calculation error rates of the DC gain and the RMS delay spread increase with the number of total reflections K. The calculation error ratio of the RMS delay spread increases from 3% to 8.8% when K increases from 1 to 5. The same trend can be seen in the calculation error ratio of the DC gain, which increases from 3.4% to 4.6% when K increases from 1 to 5. Although a limited number of links is compared, it is shown by confidence intervals that the use of the model with averaged reflectivity and responsivity increases the calculation error with the total number of reflections for most simulation scenarios. Thus, the wavelength dependency of VLC links must be considered in order to obtain accurate results. In addition, it is obvious that the model assuming constant reflectivity and responsivity is inappropriate for simulations taking into account optical devices, for instance, optical filters and amplifiers, which have chromatic properties in the visible light spectrum.

2.4.3 Mirror-aided non-LOS VLC channel characterizations

The signal-to-noise ratio (SNR) is an important measure of the quality of a wireless channel. A higher SNR value implies the ability to achieve higher channel capacity without significant errors. In order to investigate the effect of link configurations on VLC channels, we analyze the SNR of VLC channels modulated with optical orthogonal frequency division multiplexing (O-OFDM), which is a promising modulation scheme for optical wireless channels [27]. Transmitted data

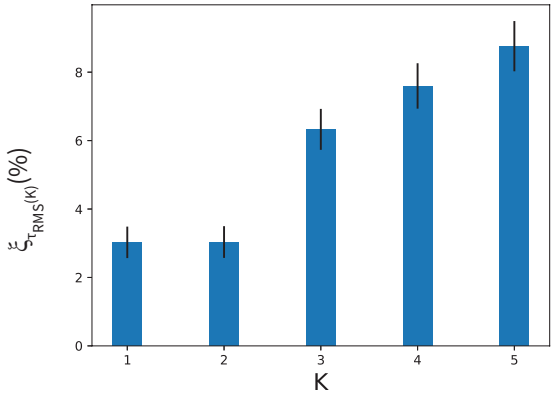

(a)

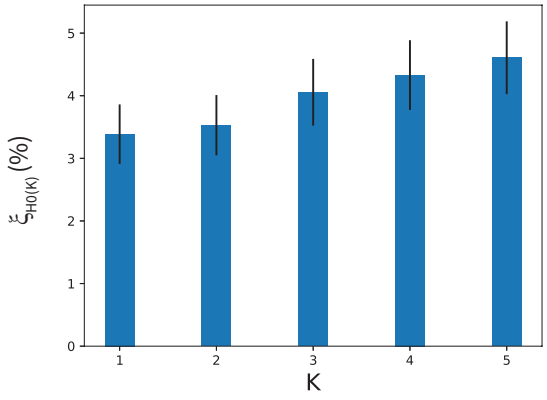

(b)

Figure 2.10: Mean values and confidence intervals of (a) the calculation error ratio of the DC gain $\xi_{H0(K)}$ and (b) the calculation error ratio of the RMS delay spread $\xi_{\tau_{RMS}^{(K)}}$

is quadrature amplitude modulated to represent the magnitude of the transmitted signal in the frequency domain. The time-domain signal is the inverse discrete Fourier transform of the modulated data symbols and is represented by optical power. In DCO-OFDM, DC-bias is added to ensure non-negative optical intensity. The transmitted time-domain signal can be represented by the superposition of time-domain signals transmitted in all subcarriers $X_n(t), n = 0, 1, ..., N_c - 1$, added by the DC-bias X_{DC}, where N_c is the number of subcarriers. The 0-th and $N_c/2$-th subcarriers are set to zero, where the $N_c/2$-th subcarrier is the Nyquist term. As the intensity-modulated signal must be real, Hermitian symmetry is required [4], i.e. $X_n = X^*_{N_c-n}$, where $[\cdot]^*$ is the complex conjugate operation. The DC-bias in DCO-OFDM can be utilized for illumination purposes, which is a suitable candidate for access downlinks and non-LOS backhaul links. In DCO-OFDM, the average transmitted optical power P_{opt} is the expected value of the transmitted signal $X_n(t)$, i.e. the DC bias X_{DC}. The total transmitted electrical power is $P_{elec} = \sum_{n=1}^{N_c-1} E[X_n^2(t)]$, where $E[\cdot]$ denotes the expectation operator. The relationship between P_{opt} and P_{elec} can be obtained by $a = P_{opt}/\sqrt{P_{elec}}$ [4], where a is a unit-less bias factor. We assume that the electrical power are equally allocated on $N_c - 2$ subcarriers, i.e. the electrical power transmitted on n-th subcarrier is $P_{n,elec} = P_{elec}/(N_c - 2), n \neq 0, N_c/2$.

Inter-symbol interference (ISI) caused by large root-mean-square (RMS) delay spread, which denoted by τ_{RMS}, is a major problem in the design of a robust wireless communication channel. In order to avoid the ISI caused by the large RMS delay spread, we add a cyclic prefix (CP) to the transmitted time-domain signals. The length of CP is chosen such that the CP duration is longer than 4 times the RMS delay spread, i.e. $N_{cp} = \lceil 4\tau_{RMS}/T_s \rceil$, where $\lceil x \rceil$ is the least integer greater than or equal to x and T_s is the sampling rate which is chosen to be twice the signal bandwidth B. The RMS delay spread τ_{RMS} of a channel can be calculated using the impulse response [10]:

$$\tau_{RMS} = \sqrt{\frac{\int_{-\infty}^{\infty}(t-\mu)^2 h_{PD}^2(t)dt}{\int_{-\infty}^{\infty} h_{PD}^2(t)dt}}, \tag{2.22}$$

where μ is the mean delay spread which is calculated by

$$\mu = \frac{\int_{-\infty}^{\infty} t^2 h_{PD}^2(t)dt}{\int_{-\infty}^{\infty} h_{PD}^2(t)dt}. \tag{2.23}$$

Inserting CP causes loss in power efficiency and consequently causes SNR loss. We calculate the SNR of each channel taking into account the loss in power efficiency caused by τ_{RMS}:

$$SNR = 10\log_{10}\left(E\left[\frac{P_{n,elec}|H_n|^2}{\sigma_n^2}\right]\right) + 10\log_{10}\left(\frac{N_c - 2}{N_c - 2 + N_{cp}}\right), \tag{2.24}$$

Parameter	Symbol	Value
Transmitted optical power	P_{opt}	10 W
DC bias factor	a	3
Signal bandwidth	B	300 MHz
Number of subcarriers	N_c	64
Noise spectral density	N_0	$1 \times 10^{-21}\mathrm{A}^2 \cdot \mathrm{Hz}^{-1}$

Table 2.4: Channel parameters

where $|H_n|$ is the channel magnitude response on the n-th subcarrier, $\sigma_n^2 = N_0 B/N_c$ is the noise power on the n-th subcarrier, and N_0 is the power spectral density of the additive white Gaussian noise. The SNR is represented in dB. Parameters of OFDM channels are presented in Table 2.4.

In order to highlight the effect of transceivers' concentrations and link configurations on the channel performance, we present the SNR of the received signal over each VLC channel normalized to the required SNR to achieve the bit error rate (BER) of 10^{-6} when using uncoded four-quadrature amplitude modulation (4-QAM) and 64-QAM. The required BER $= 10^{-6}$ is below the 7% hard-decision forward error correction (FEC) limit of 3.8×10^{-3} [28]. The relationship between SNR and BER in additive white Gaussian channel is $BER \approx \frac{4}{\log_2 M}(1 - \frac{1}{\sqrt{M}}) \sum_{i=1}^{\sqrt{M}/2} Q(2(i-1)\sqrt{3\gamma \log_2 M/(M-1)})$ [29], where $Q(x)$ is the tail probability distribution function, M is the QAM size and $\gamma = E_b/N_0 = \frac{P_S}{P_N}\frac{R_b}{B}$ is the SNR per bit, where R_b is the net data rate of OFDM signal exclusive CP and FEC overhead, and P_S and P_N represent received signal power and noise power, respectively. The ratio between P_S and P_N is the SNR. The net bit rate can be calculated with $R_b = \frac{2BN_d \log_2 M}{N_c}$, where N_d is the number of data subcarriers. The net bit rates using uncoded 4-QAM and 64-QAM are 581.25 Mbps and 1.74 Gbps, respectively. The calculation of gross bit rates must take into account the overhead caused by additional CP samples and FEC codes.

SNRs of different link configurations are shown in Fig.2.11. It can be seen that increasing Θ can improve the performance of purely diffuse non-LOS channels, while no significant performance enhancement to mirror-aided non-LOS channels when Θ is large enough to receive the first-order specularly reflected signal, which corresponds to $\Theta \geq 17^\circ$ with Configuration A and C and $\Theta \geq 0^\circ$ with the others. As there are no specular reflections in Environment 1, increasing Θ can slightly strengthen the received optical power. However, in Environment 2 and 3, the first-order specular component dominates the channel impulse response. Furthermore, large Θ could lead to performance degradation of some diffuse non-LOS channels. This is likely due to the penalty caused by the long CP duration.

It is clearly shown that purely diffuse non-LOS channels with the given channel

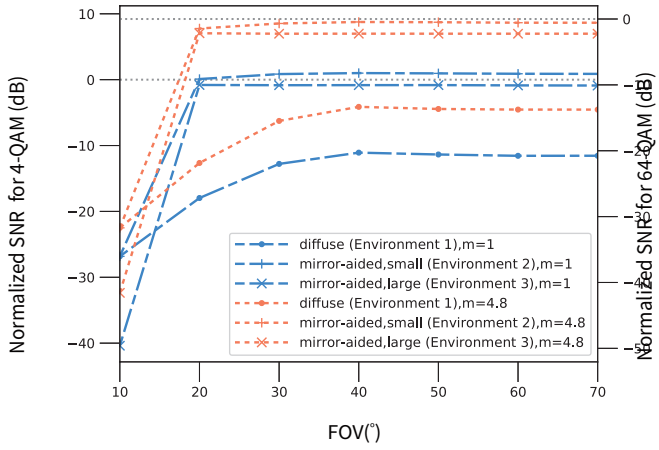

(a) Configuration A

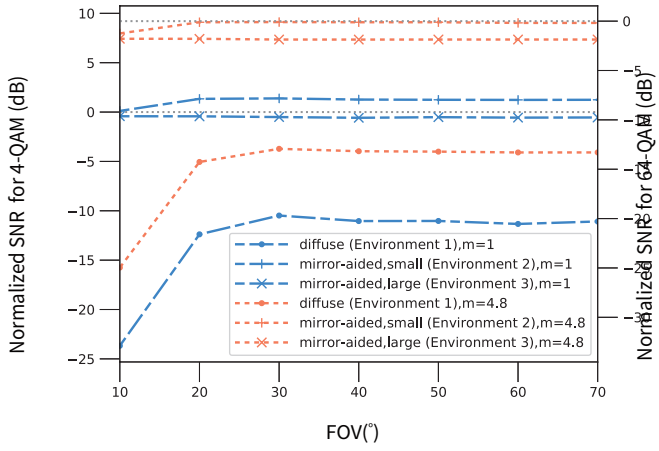

(b) Configuration B

Figure 2.11: SNR of non-LOS VLC channels with different link configurations normalized to the required SNR using uncoded 4-QAM and 64-QAM with the BER requirement of 10^{-6}; (a) S and R oriented directly downwards; (b) S oriented downwards, R oriented towards the mirror.

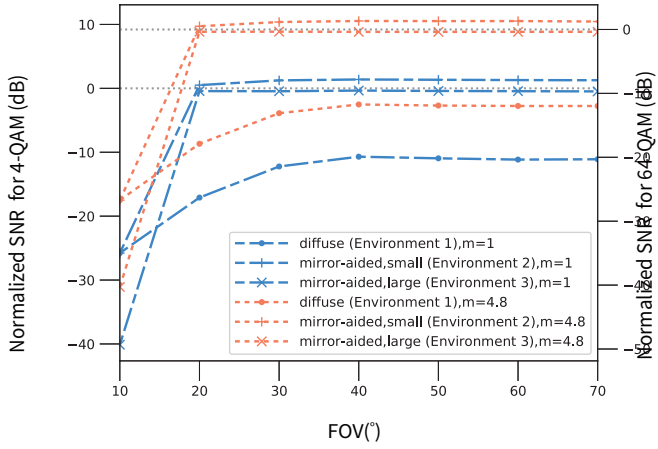

(c) Configuration C

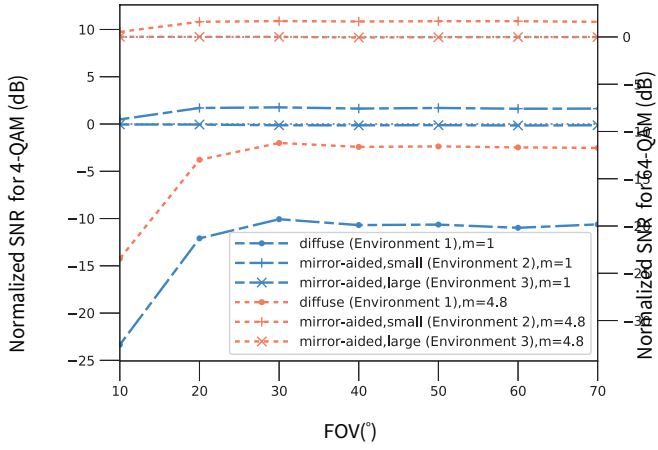

(d) Configuration D

Figure 2.11: (continued) SNR of non-LOS VLC channels with different link configurations normalized to the required SNR using uncoded 4-QAM and 64-QAM with the BER requirement of 10^{-6}; (c) S oriented towards the mirror, R oriented downwards; (d) S and R oriented towards the mirror.

parameters cannot guarantee reliable transmission with a bit rate of $581.25\,\mathrm{Mbps}$, i.e. 4-QAM. Channels in Environment 2 and 3 have larger SNRs than channels in Environment 1, as the received optical power rises when adding first-order specular reflections. Mirror-aided non-LOS channels in Environment 2 can support the reliable transmission with 4-QAM. However, when the floor is covered by a large mirror, i.e. in Environment 3, concentrate light pattern ($m = 4.8$, i.e. $\Phi_{1/2} = 30°$) is required to provide sufficient SNR. In addition, mirror-aided non-LOS channels with Configuration A and B cannot guarantee reliable transmission with 64-QAM. By using more directed receivers (Configuration C and D) and transmitters with small semi-angle, mirror-aided non-LOS channels in Environment 2 are able to guarantee reliable transmission with 64-QAM. Generally, the following requirements are needed to achieve reliable transmission with a large data rate: directed receivers (using Configuration C and D), small mirror size (Environment 2), and more concentrated senders.

2.5 Conclusion

The aim of this research is to investigate the performance of purely diffuse and mirror-aided non-LOS VLC channels, which are promising candidates for the backhaul transmission of indoor VLC networks. To the best of our knowledge, the proposed non-LOS link-based backhaul solution as well as the effect of link configurations on mirror-aided non-LOS links have not been researched before. Simulations of mirror-aided non-LOS links are undertaken by a time-efficient model based on an iterative method. Multi-bounce channel impulse responses taking into account both diffuse and specular reflections can be obtained with this iterative model in a reasonable time. Simulations of different link configurations are undertaken to assess the performance of non-LOS channels. Simulation results show that adding the first-order specular reflection to non-LOS channels increases the SNR by at least $10\,\mathrm{dB}$, while further increasing the mirror size cannot lead to better channel performance. It is also shown that link configurations have a large impact on the channel performance. In our simulation, mirror-aided non-LOS channels with directed receivers and concentrated transmitting light patterns can guarantee reliable data transmission with a data rate of $1.74\,\mathrm{Gbps}$. Thus, the proposed mirror-aided non-LOS VLC channels have the potential to support high-speed backhaul data transmission. The interference caused by other active VLC APs is not covered in this study, but will be considered in future work.

References

[1] Y Tanaka, T Komine, S Haruyama, and M Nakagawa. *Indoor visible communication utilizing plural white LEDs as lighting*. In 12th IEEE Int. Symp. Personal, Indoor and Mobile Radio Communications, volume 2, pages 81–85, 2001.

[2] Toshihiko Komine and Masao Nakagawa. *Fundamental analysis for visible-light communication system using LED lights*. IEEE Transactions on Consumer Electronics, 50(1):100–107, 2004.

[3] Jelena Grubor, Sebastian Randel, Klaus Dieter Langer, and Joachim W. Walewski. *Broadband information broadcasting using LED-based interior lighting*. Journal of Lightwave Technology, 26(24):3883–3892, 2008.

[4] Cheng Chen, Muhammad Ijaz, Dobroslav Tsonev, and H. Haas. *Analysis of downlink transmission in DCO-OFDM-based optical attocell networks*. In 2014 IEEE Global Communications Conference, GLOBECOM 2014, pages 2072–2077, 2014.

[5] Toshihiko Komine and Masao Nakagawa. *Integrated System of White LED Visible Light Communication and Power Line Communication*. IEEE Transactions on Consumer Electronics, 49(1):71–79, 2003.

[6] P Hu, P H Pathak, A K Das, Z Yang, and P Mohapatra. *PLiFi: Hybrid WiFi-VLC networking using power lines*. In 3rd ACM Workshop on Visible Light Communication Systems, VLCS 2016, volume 03-07-Octo, pages 31–36, 2016.

[7] Dilukshan Karunatilaka, Fahad Zafar, Vineetha Kalavally, and Rajendran Parthiban. *LED Based Indoor Visible Light Communications: State of the Art*. IEEE Communications Surveys and Tutorials, 17(3):1649–1678, 2015.

[8] Yiguang Wang, Nan Chi, Yuanquan Wang, Li Tao, and Jianyang Shi. *Network Architecture of a High-Speed Visible Light Communication Local Area Network*. IEEE Photonics Technology Letters, 27(2):197–200, 2015.

[9] Hossein Kazemi, Majid Safari, and H. Haas. *A Wireless Backhaul Solution Using Visible Light Communication for Indoor Li-Fi Attocell Networks*. In IEEE ICC 2017 Optical Networks and Systems Symposium, 2017.

[10] Jeffrey B. Carruthers and J.M. Kahn. *Modeling of Nondirected Wireless Infrared Channels*. IEEE TRANSACTIONS ON COMMUNICATIONS, 45(10):1260–1268, 1997.

[11] Cheng Chen, Dushyantha Basnayaka, and H. Haas. *Non-line-of-sight channel impulse response characterisation in visible light communications*. 2016 IEEE International Conference on Communications, ICC 2016, 2016.

[12] V Jungnickel, V Pohl, S Nönnig, and C von Helmolt. *A physical model of the wireless infrared communication channel*. IEEE Journal on Selected Areas in Communications, 20(3):631–640, 2002.

[13] F.J. Lopez-Hernandez, R. Perez-Jimenez, and A. Santamaria. *Ray-tracing algorithms for fast calculation of the channel impulse response on diffuse IR wireless indoor channels*. Optical Engineering, 39:2775–2780, 2000.

[14] Elham Sarbazi, Murat Uysal, Mohamed Abdallah, and Khalid Qaraqe. *Indoor channel modelling and characterization for visible light communications*. International Conference on Transparent Optical Networks, pages 1–4, 2014.

[15] Farshad Miramirkhani and Murat Uysal. *Channel Modeling and Characterization for Visible Light Communications*. IEEE Photonics Journal, 7(6), 2015.

[16] J. R. Barry, J.M. Kahn, William J. Krause, Edward A. Lee, and David G. Messerschmitt. *Simulation of Multipath Impulse Response for Indoor Wireless Optical Channels*. IEEE Journal on Selected Areas in Communications, 11(3):367–379, 1993.

[17] Jeffrey B. Carruthers and Prasanna Kannan. *Iterative site-based modeling for wireless infrared channels*. IEEE Transactions on Antennas and Propagation, 50(5):759–765, 2002.

[18] Kwonhyung Lee, Hyuncheol Park, and John R. Barry. *Indoor channel characteristics for visible light communications*. IEEE Communications Letters, 15(2):217–219, 2011.

[19] F.J. Lopez-Hernandez and M.J. Betancor. *DUSTIN: Algorithm for calculation of impulse response on IR wireless indoor channels*. Electronics Letters, 33(21):1804–1806, 1997.

[20] Mohammad Ali Khalighi and Murat Uysal. *Survey on Free Space Optical Communication: A Communication Theory Perspective*. IEEE Communications Surveys and Tutorials, 16(4):2231–2258, 2014.

[21] Martin Aubé, Johanne Roby, and Miroslav Kocifaj. *Evaluating Potential Spectral Impacts of Various Artificial Lights on Melatonin Suppression, Photosynthesis, and Star Visibility*. PLoS ONE, 8(7), 2013.

[22] A. M. Baldridge, S. J. Hook, C. I. Grove, and G. Rivera. *The ASTER spectral library version 2.0*. Remote Sensing of Environment, 113(4):711–715, 2009.

[23] F R Gfeller and U Bapst. *Wireless in-House Data Communication Via Diffuse Infrared Radiation*. Proceedings of the IEEE, 67(11):1474–1486, 1979.

[24] Christophe Schlick. *An Inexpensive BRDF Model for Physically-based Rendering*, 1994.

[25] Sivabalan Arumugam and Joseph John. *Effect of transmitter positions on received power and bandwidth in diffuse indoor optical wireless systems*. Optical and Quantum Electronics, 39(1):1–14, 2007.

[26] Álvaro De-La-Llana-Calvo, José Lázaro-Galilea, Alfredo Gardel-Vicente, David Rodríguez-Navarro, Ignacio Bravo-Muñoz, Georgios Tsirigotis, and Juan Iglesias-Miguel. *Modeling the Effect of Optical Signal Multipath*. Sensors, 17(9):2038, 2017.

[27] J. Armstrong. *OFDM for optical communications*. Journal of Lightwave Technology, 27(3):189–204, 2009.

[28] Itu-T Study Group. *ITU-T Rec. G.975.1 (02/2004) Forward error correction for high bit-rate DWDM submarine systems*. Technical report, 2005.

[29] Jianhua Lu. *M-PSK and M-QAM BER computation using signal-space concepts*. IEEE Transactions on Communications, 1999.

3

Analysis of Interference on Backhaul Data Transmission in VLC Attocell Networks

In the previous chapter we have investigated the performance of VLC channels using the mirror-aided non-LOS configuration. Point-to-point VLC links without interference have been considered in the simulation. Applying mirror-aided VLC backhaul links in an optical attocell network will introduce interference to access links. Furthermore, mirror-aided VLC backhaul links may also interfere with each other. The analysis of the interference is presented in this chapter. As the simulation of a number of VLC links is very time-consuming, we only consider the first-order specular reflecting component taking into account the conclusion of the previous chapter. The small-mirror scenario is considered in the analysis in this and following chapters, as the power received by the first-order specular reflection dominates the total received power in this scenario and the delay spread is smaller compared to other scenarios.

* * *

Y. Wu, M. Pickavet, D. Colle

Published in Photonic Network Communications, 2021, Vol. 41(2), pp. 189-201.

Abstract *Visible light communication (VLC) is a promising technology that addresses the bandwidth bottleneck of radio-frequency based indoor wireless networks. Optical attocell networks using VLC backhaul links have been proposed. Line-of-sight (LOS) and mirror-aided non-LOS links can be used for backhaul transmission. As the visible light spectrum is used for both access downlink and bidirectional backhaul transmission, co-channel interference is a major issue. In this paper, we analyze the performance of optical attocell networks using VLC backhaul links taking into account illumination and eye safety requirements. Based on the signal-to-interference-plus-noise ratio (SINR) of different backhaul links, the bandwidth allocation ratio when using an in-band frequency reused scheme is discussed. Finally, aggregate data rates of networks using different VLC backhaul configurations are compared. Results show that LOS backhaul configuration can achieve nearly optimal network performance while mirror-aided non-LOS backhaul configuration is more robust against misalignment.*

3.1 Introduction

Due to the increasing number of mobile devices and the growing demand on data traffic for indoor activities such as virtual reality and high-definition video streaming, radio-frequency (RF) based indoor wireless networks are experiencing a spectrum crisis. Visible light communication (VLC) using off-the-shelf light-emitting-diodes (LEDs) and photodiodes (PDs) as front-end devices is an emerging technology to address the bandwidth bottleneck of RF technologies [1]. A VLC system uses intensity modulation and direct detection (IM/DD) which represents the transmitted signal as high-frequency fluctuation in the radiant intensity. Thus, VLC supports simultaneous illumination and data transmission. As LED lamps are ubiquitous and IM/DD technology is simple and low-cost, a VLC-based optical attocell network is a cost-efficient solution that complements the spectrum shortage of current wireless home networks [2–5].

In a VLC-based optical attocell network, each LED lamp is a base station (BS) which covers mobile devices in a small cell with a radius ranging from one to several meters. An access network is composed of communication links amongst user equipment (UE) and BSs. Access downlinks from BSs to UEs are based on VLC, while uplinks normally use infrared to carry information. BSs communicate with each other through a backhaul network. The backhaul network is connected to the Internet through a gateway which can be one of the VLC BSs. Although there is growing interest in access downlink transmission in recent years [6–8], the capacity of backhaul links is not considered in those studies. There is a number of backhaul solutions proposed for optical attocell networks. Wired approaches such as power-line communication (PLC) and power-over-Ethernet (PoE) which provide simultaneous power supply and data transmission have been considered

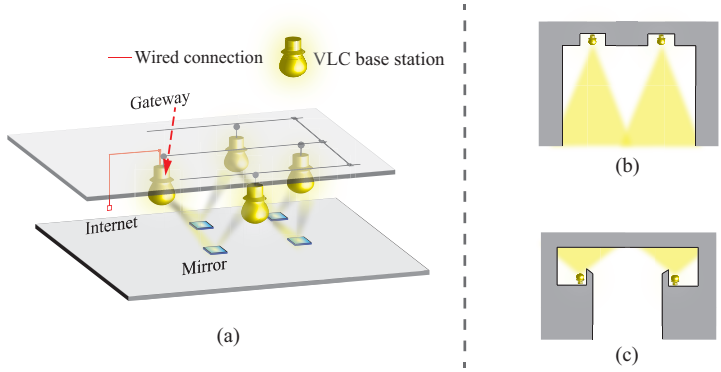

Figure 3.1: (a) Mirror-aided non-LOS VLC link-based backhaul network; (b)Illumination design with embedded ceiling lamps; (c) Illumination design with diffuse lighting system

in [9, 10]. These wired backhaul solutions require installing additional control devices like modems or replacing current power cables. Thus, the cost for installation and maintenance could be extremely high. In addition, PLC is vulnerable to RF interference and disturbance on power lines, as unshielded wirings may turn to unintended antennas [11]. Data rates of PLC devices are reduced due to noises and appliance interference [12]. A backhaul approach using millimeter-wave (mmWave) has been considered in [13]. Although the mmWave-based backhaul network has the potential for high-speed data transmission, the bio-effects on human bodies caused by non-ionizing mmWave radiation deserve consideration and further study [14]. Security is also an issue when using mmWave as the mmWave signal can go through walls. In [15], a VLC link-based backhaul solution using line-of-sight (LOS) links between auxiliary LEDs and PDs has been proposed. The downlink performance of a two-tier optical attocell network using LOS VLC backhaul links has been analyzed in [16]. It has been shown that LOS VLC backhaul links attain good performance especially when the frequency band is fully reused. However, a significant drawback of the LOS VLC backhaul solution is the strict LOS requirement. Imperfect alignment or obstruction may cause performance degradation due to signal power reduction and larger interference from neighboring transmitters. As there are different interior lighting design strategies, the LOS condition may not be fulfilled in some applications where lamps are placed at different heights or separated by walls. In order to improve the generality of VLC backhaul links, we propose to use mirror-aided non-LOS VLC backhaul links as an alternative solution. A network based on mirror-aided non-LOS backhaul links is illustrated in Fig.3.1(a). Mirrors or glossy floor tiles are used to provide specular reflections. The advantage of this backhaul solution is that non-LOS configuration can be used in indoor applications where the LOS con-

dition may not be fulfilled, for instance, interior illumination design like embedded lamps and diffuse lighting shown in Fig.3.1(b) and (c), respectively. Specular reflections are directional and the reflectivity of glossy surfaces and mirrors is higher than that of diffuse surfaces. Thus, the quality of mirror-aided non-LOS links is better than that of normal diffuse non-LOS links [17]. The position of mirrors is determined by the locations and orientations of LED lamps. In order to mitigate multi-path effects, small mirrors are preferred [17]. When mirrors are placed on the floor, obstructions caused by surroundings and moving people could temporarily degrade the performance of non-LOS links. This can be solved in higher layers (network layer) by using adjacent BSs as relays.

Similar to the access network, co-channel interference is a major issue that affects the performance of the backhaul network. Interference of an optical attocell network using LOS-VLC backhaul links has been analyzed in [16]. Two frequency reused schemes, fully reused (FR) and in-band (IB) methods, have been discussed. However, the analysis of co-channel interference only considered downlink transmission, i.e. transmission from the gateway to UEs. In this paper, we analyze the performance of the proposed backhaul solution in a two-tier optical attocell network. In the analysis, a shortest-path routing algorithm is used such that the backhaul network has a tree structure. The interference caused by backhaul uplink transmission, i.e., backhaul data sent from tier-2 to tier-1 BSs and from tier-1 BSs to the gateway, is also taken into account. The channel performance is assessed in terms of signal-to-interference-plus-noise ratio (SINR). DC-biased optical orthogonal frequency division multiplexing (DCO-OFDM) is considered due to its low complexity of equalization and high spectral efficiency [18]. Network aggregate data rates using different VLC backhaul solutions are calculated and compared.

3.2 Physical layer channel model

In a VLC system, data transmitted by the LED is modulated using IM. The PD of the receiving device converts the optical power to the electrical signal. The channel model described in the following subsection can be used to simulate the gain of LOS and mirror-aided non-LOS VLC links. Multi-bounce reflections are neglected as the LOS component and the first-bounce specular reflection component dominate impulse responses of LOS links and mirror-aided non-LOS links, respectively [18] [17]. Despite the simplicity and cost-efficiency of IM/DD, the channel capacity is limited by the modulation bandwidth of LEDs. In addition to the channel model, the modulation scheme used for IM/DD signal has to be considered. Optical OFDM is a viable modulation scheme for VLC systems due to its high spectral efficiency. High peak-to-average-power-ratio of optical OFDM modulated signal, which is the major issue of using OFDM in RF systems, provides a higher electrical signal-to-noise ratio (SNR) for VLC systems when the average

transmitted optical power is limited by illumination requirements. Amongst optical OFDM schemes proposed for IM/DD VLC systems, DCO-OFDM which has higher spectral efficiency and lower complexity is considered in this work. We assume that all LEDs are Lambertian point sources and operate within the linear dynamic range such that non-linear distortions are avoided. Thermal noise and shot noise at the receiver are modeled as additive white Gaussian noises (AWGN).

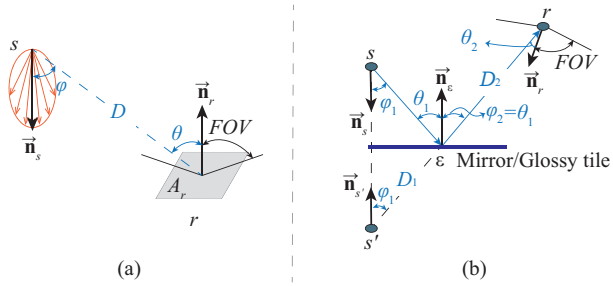

Figure 3.2: Geometry of (a) a LOS path from a Lambertian sender s to a receiver r, $\vec{n}_s$ and $\vec{n}_r$ represent orientations of the sender and the receiver, respectively, the red lobe represents the emission pattern of the sender; (b) a mirror-obstructed LOS path from a virtual sender s' (the mirror image of a sender s) to a receiver r

3.2.1 Light propagation model

Fig.3.2 (a) illustrates the geometry of a LOS VLC link from a Lambertian sender s (LED) to the PD of a receiver r. The emission pattern of a LED can be described by a Lambert order $m = -\ln 2/\ln(\cos(\Phi_{1/2}))$, where $\Phi_{1/2}$ is the semi-angle at half-intensity of the LED emission pattern. The gain of the LOS path $G_{s,r}$ is the ratio of the received optical power to the transmitted optical power. This can be calculated with a normalized Lambertian pattern [19]

$$G_{s,r} = \frac{(m+1)A_r}{2\pi D^2}\cos^m(\phi)\cos(\theta)\text{rect}(\frac{\theta}{\Theta}), \tag{3.1}$$

where ϕ and θ are angles of LOS paths measured from orientations of the sender s and the receiver r, respectively, D is the Euclidean distance from s to r, A_r is the active area of the PD, Θ is the field-of-view (FOV) of the PD. The rectangular function rect(x) is 1 if $|x| \leq 1$, and 0 otherwise.

A non-LOS link implies that $G_{s,r}$ between the transmitting BS_s and the receiving BS_r is 0. The non-LOS channel has lower gains than a channel with a dominant LOS component when all light rays are diffusely reflected from Lambertian surfaces [20]. Nonetheless, specular reflections from glossy surfaces or mirrors are directional. In order to improve the channel performance, we propose

to add a dominant first-bounce specularly reflected component to the non-LOS channel impulse response. This can be done by polishing the floor or replacing some tiles on the floor with glossy tiles or mirrors. In order to simplify the simulation, specular reflections from glossy surfaces are emulated by placing perfect mirrors on the floor. We assume that all mirrors are ideal such that each incident ray is perfectly reflected towards the direction defined by the law of reflection. In order to simplify calculations of gains of mirror-aided non-LOS links, we model the specular reflection as a *mirror-obstructed LOS path* as shown in Fig.3.2 (b). The calculation of the gain of the mirror-obstructed LOS path $G_{s',r}$ is similar to Eq.(3.1) by substituting ϕ with ϕ_1, θ with θ_2, and D with $(D_1 + D_2)$. The final result should be multiplied by the reflectivity of the mirror. Here, s' is the mirror image of the sender s. The condition of such a mirror-aided non-LOS link is that there isn't obstruction between the sender and the mirror and between the mirror and the receiver. In addition, the receiver's FOV must be large enough to "see" the reflecting point ε. In order to simplify notations, we use G^{LOS} to denote the gain of a LOS path and $G^{ma-nLOS}$ to denote the gain of a mirror-obstructed LOS path, i.e. a mirror-aided non-LOS path.

3.2.2 Optical OFDM

Unlike RF technologies, Intensity-modulated OFDM signals transmitted in VLC channels must be real and non-negative. Data symbols are quadrature amplitude modulated (QAM) to represent the magnitude of the transmitted signal in the frequency domain. The time-domain signal is the inverse discrete Fourier transform of the modulated data symbols and is represented by optical power transmitted by LEDs. Modulated data symbols of all subcarriers in the frequency domain are denoted by $X_n, n = 0, 1, \cdots, N-1$, where N is the number of OFDM subcarriers. The 0-th and $(N/2)$-th subcarriers are set to zero, where the $(N/2)$-th subcarrier is the Nyquist term. Hermitian symmetry $X_n = X^*_{N-n}$ is necessary to ensure real time-domain signals, where $[\cdot]^*$ denotes the complex conjugate operation. In DCO-OFDM, DC-bias is added to the modulated signal and all negative values are clipped to ensure non-negative optical intensity. The clipping noise can be neglected when choosing an appropriate biased factor a. The biased factor can be expressed as the relationship between the average transmitted optical power $P_{t,opt}$ and the total transmitted electrical power $P_{t,elec}$ with $a = P_{t,opt}/\sqrt{P_{t,elec}}$. The total transmitted electrical power can be obtained by $P_{t,elec} = \sum_{n=1}^{N-1} \mathrm{E}[x_n^2(t)]$, where $x_n(t)$ is the time-domain signal of the n-th subcarrier at time sample t, $\mathrm{E}[\cdot]$ denotes the expectation operation. The average transmitted optical power $P_{t,opt}$ is the mean value of the time-domain signal after adding the DC bias x_{DC} and therefore $P_{t,opt} = x_{DC}$ [21].

3.3 Optical Attocell Network Based on VLC Backhaul

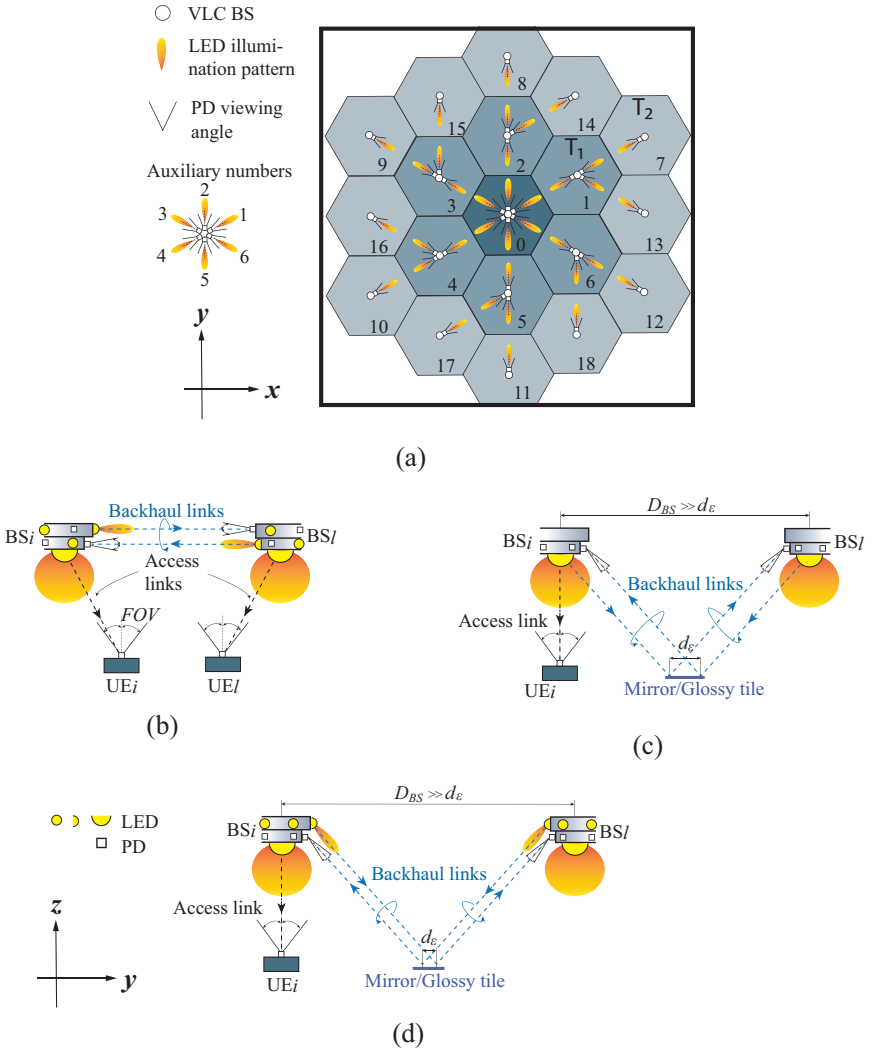

Figure 3.3: (a) Layout of the optical attocell network with cell radius $R = 2$ m and horizontal orientation of auxiliary transceivers; (b) LOS (multi) configuration; (c) ma-nLOS (single) configuration; (d) ma-nLOS (multi) configuration

An optical attocell network is composed of an access network and a backhaul network. In order to guarantee access downlink transmission, each BS has been equipped with a group of VLC senders, i.e. visible-light LEDs. The access uplink

transmission is separated from the downlink by operating in the infrared spectrum. Thus, infrared PDs embedded in BSs are used to receive data transmitted by UEs. In a VLC-based backhaul network, extra visible-light LEDs and PDs are required for backhaul transmission. Notice that the cost for replacing lamps with extra LED and PD chips is much lower than that for replacing cables. Thus, VLC-based backhaul network is cost-efficient compared with wired backhaul approaches.

3.3.1 Cellular system

Hexagonal cells are considered in this paper as hexagons are proper approximations of circles and cover the whole floor without overlapping. Fig.3.3(a) illustrates the layout of a two-tier hexagonal cellular network with 19 cells. The length and width of the room are both $8R$, where R is the cell radius. Every BS is located in the center of one cell. All BSs are placed at the same height of $2.85\,\mathrm{m}$. Each BS has six auxiliary PDs for receiving backhaul data and uses downward-oriented LEDs or six auxiliary LEDs for backhaul transmission depending on the backhaul configuration. The horizontal projection of orientation of auxiliary transceivers, i.e. auxiliary LEDs and PDs, is also presented in Fig.3.3(a). Each auxiliary transceiver is numbered based on its horizontal orientation. We denote LEDs of BS_i as i-s$j, j \in [0, 1, ..., 6]$, where s0 denotes downward-oriented LEDs. Similarly, auxiliary PDs of BS_i are denoted by i-r$j, j \in [1, ..., 6]$. The actual orientation of auxiliary transceivers depends on the backhaul link configuration and will be discussed later. Assuming that BS_0 is the gateway, every BS is connected to the gateway directly or via multiple hops. Every intermediate BS decodes the received backhaul signal and forwards it to the next-hop BSs. In order to simplify the analysis, we assume a simple shortest-path routing scheme. Dijkstra algorithm is used for finding shortest paths as it is more time-efficient compared with other shortest-path routing algorithms like Bellman–Ford algorithm. The gateway communicates with its neighboring BSs, which are called tier-1 BSs $\mathcal{T}_1 = \{\mathrm{BS}_i, i \in [1, 2, ..., 6]\}$. Each tier-1 BS is responsible for backhaul data transmission with the gateway and two neighboring tier-2 BSs $\mathcal{T}_2 = \{\mathrm{BS}_i, i \in [7, 8, ..., 18]\}$. Fig.3.3(a) shows the auxiliary transceivers used for backhaul communication based on the routing scheme. To simplify our analysis we consider that only downward-oriented LEDs and auxiliary LEDs shown in the figure are transmitting power. In more practical scenarios other transceivers could be used for different routing strategies or addressing shadowing problems.

3.3.2 VLC backhaul configuration

The LOS backhaul link configuration introduced in [16] uses horizontally placed auxiliary LEDs and PDs to ensure a direct LOS path. These auxiliary transceivers are embedded in the VLC light bulbs. Each auxiliary LED-PD pair enables uni-

directional backhaul transmission from the LED transmitter to the PD receiver. In order to ensure bidirectional backhaul data transmission, each backhaul link requires two auxiliary LED-PD pairs having opposite transmitting directions. We assume full-duplex backhaul transmission. The self-interference between auxiliary LEDs and PDs mounted on the same BS is neglected due to the following reasons: 1) Auxiliary LEDs have a directive illumination pattern and the direct LOS path from the auxiliary LED to the auxiliary PD mounted on the same BS can be physically blocked [22]; 2) Multipath interference due to reflections via walls is not significant compared to the dominant intended LOS and mirror-aided non-LOS signal [17, 23]; 3) Multipath interference from ceiling reflection could be higher than other reflected components as lamps are assumed to be mounted on the ceiling. In this case, self-interference cancellation can be applied to retrieve the desired signal.

In some indoor scenarios, for instance, recessed/embedded downlights or tray ceiling, there is no direct LOS path between two adjacent LED bulbs. As the quality of LOS link configuration depends on the LOS condition, obstructed LOS path and misaligned auxiliary transceivers will cause significant performance degradation. In order to address this issue, specular reflection can be used to replace a LOS path. Reflection from glossy surfaces and mirrors is directional and the reflectivity of practical mirrors is higher than diffuse surfaces. As discussed in [17], adding the first-order specular reflection to non-LOS channels increases the SNR by at least 10 dB. Thus, the quality of mirror-aided non-LOS links is better than that of normal diffuse non-LOS links. In addition, mirror-aided non-LOS links using small mirrors are robust against multipath effect [17]. The shortest specular reflection path between two adjacent BSs is the path reflected by a mirror placed on the ceiling, i.e. mirrors oriented downwards, as upwards oriented lamps are normally placed close to the ceiling in order to illuminate a large area. The usage of this kind of configuration is limited as the specular reflection from the ceiling could also be obstructed if the interior design is not possible for ensuring the LOS condition. Thus, we only discuss backhaul links using upward-oriented mirrors. Mirrors can be placed on the floor or on tables. Although some specularly reflected paths could be (temporarily) obstructed by pedestrian or interior objects, this can be resolved by upper layers (for instance, by using routing protocols and hand-off schemes). For simplicity, we assume an empty room with mirrors on the floor. Mirrors are placed at the reflecting points, which are center points of edges of each hexagon as shown in the figure. The size of mirrors can be very small as long as the reflecting point is covered. Auxiliary PDs are oriented towards the corresponding reflecting points to maximize the received power. Downward-oriented LEDs, which are used for illumination and access transmission, can also be used to send backhaul signals to auxiliary PDs via specular reflections. However, different frequency bands should be allocated to different links in order to avoid interference.

This configuration is low-cost but not spectral efficient. A second configuration is to use narrow-beam auxiliary LEDs oriented towards mirrors for backhaul transmission. This backhaul configuration benefits from the high channel gain of the direct mirror-aided non-LOS path. Although the infrared backhaul channel provides better performance as discussed in [16], direct radiation by infrared LEDs causes larger damage to human eyes than LEDs working in the visible range. This is due to the fact that the damage from infrared LEDs cannot be reduced by the natural aversion reflex of eyes as human eyes cannot perceive light at infrared range [24]. Thus, visible LEDs are used as auxiliary transmitters in our work. In the following discussion, LOS configuration and mirror-aided non-LOS configuration using auxiliary LEDs are denoted by *LOS (multi)* and *ma-nLOS (multi)*, and mirror-aided non-LOS configuration using downward-oriented LEDs for backhaul transmission is denoted by *ma-nLOS (single)*. Three link configurations are illustrated in Fig.3.3(b), (c), and (d). Notice that in reality, the distances between LED and PD chips in the same BS are much smaller (a few centimeters) compared to the distance between two BSs. Thus, the distance between two reflecting points on the mirror d_ϵ shown in Fig.3.3(c) and (d) is much smaller than the distance between two BSs D_{BS}. Without loss of generality, we assume that all LEDs and PDs of the same BS are located at the same point.

In order to avoid interference and multipath effect, the FOV of auxiliary PDs should be small. However, the relative orientation of auxiliary PDs with respect to mirrors/auxiliary LEDs determines the received power as seen in Eq.(3.1). In case of installation errors, auxiliary transceivers of some BSs may rotate against the vertical axis with a certain angle. Misaligned auxiliary PDs need enough viewing angle to receive the LOS signal or the signal from the one-bounce specular reflection. The configuration of FOV depends on the layout of lamps as shown in Fig.3.4. The vector $\overrightarrow{\mathbf{n_r}}$ and $\overrightarrow{\mathbf{n}'_\mathbf{r}}$ denote orientation of perfectly aligned auxiliary PD and misaligned auxiliary PD, respectively. The maximum horizontal misalignment angle $\Delta\theta_{max}$ =30°, as the auxiliary PD with $\Delta\theta_{max}$ >30° can be assigned to another LED (of a neighboring BS). We consider the boundary cases when $\Delta\theta_{max}$ =30° in Fig.3.4. Auxiliary transceivers of LOS (multi) configuration shown in Fig.3.4(a) are placed horizontally. The misaligned auxiliary PD of BS_2 has to be able to see the auxiliary LED of its target BS_0. The minimum FOV is equal to the maximum horizontal misalignment angle, i.e. $\Theta^b_{min} = \Delta\theta_{max}$. Similarly, the maximum horizontal misalignment angle of ma-nLOS (multi) backhaul transceivers is also 30° as shown in Fig.3.4(b). The misaligned auxiliary PD of BS_2 has to be able to receive the one-bounce specular reflection from the reflecting point on the mirror. Based on the geometry of mirrors and BSs, the minimum FOV is $\Theta^b_{min} = 2\text{arcsin}(\frac{\frac{\sqrt{3}R}{2}\sin\frac{\Delta\theta_{max}}{2}}{\sqrt{H^2+(\frac{\sqrt{3}R}{2})^2}})$.

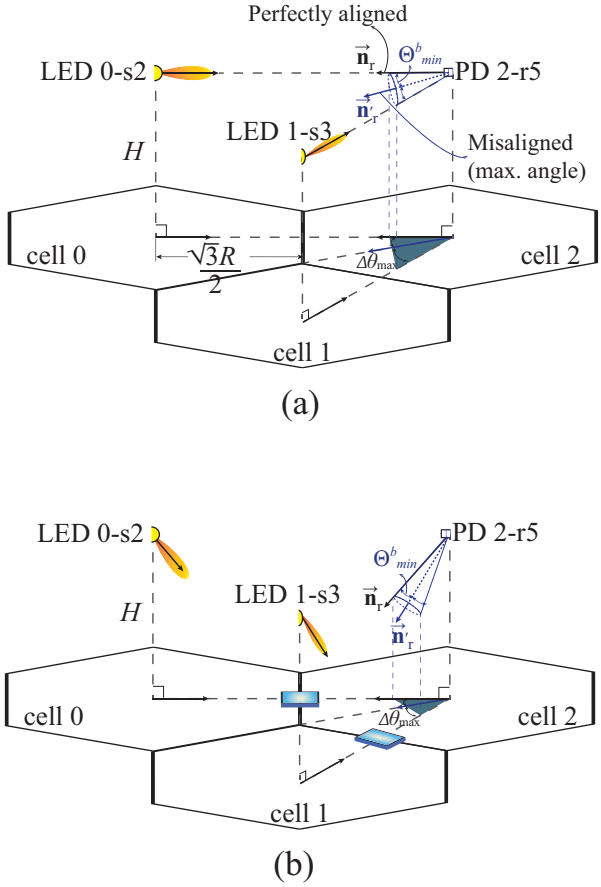

Figure 3.4: Examples of misalignment of (a) LOS (multi) backhaul configuration and (b) ma-nLOS (multi) backhaul configuration

3.4 Performance Analysis

As visible light spectrum is used for access downlink and bidirectional backhaul links, the co-channel interference between access and backhaul links will be analyzed. The primary purpose of LED lamps is illumination. Thus, the transmitted power must take the illumination requirements into account. The aggregate data rate of the optical attocell network using different backhaul configurations will be compared.

3.4.1 Illuminance requirements

In order to provide uniform illumination, wide-beam LEDs are normally used for indoor lighting. We assume that the semi-angle of downward-oriented LEDs $\Phi^a = 60°$. The primary purpose of these LEDs is illumination. Their transmitted power P^a is determined by the illumination requirement. Recommended light levels for offices vary with activities [25]. Without loss of generality, we configure the transmitted power of downward-oriented LEDs providing average illuminance of $500\,\mathrm{lx}$ at desk height ($0.8\,\mathrm{m}$). In LOS (multi) backhaul configuration and ma-nLOS (multi) backhaul configuration, the primary purpose of the narrow-beam auxiliary LEDs is backhaul transmission. When auxiliary LEDs are added for backhaul transmission, the average illuminance should be limited under $750\,\mathrm{lx}$, which is the maximum value required for activities in offices. In addition to the average illuminance requirement, eye-safety issues due to the concentrated illumination pattern must be considered. Although LEDs working in visible-light range are used for safety reasons as discussed in 3.3.2, direct and reflected light from narrow-beam visible LEDs may cause visual discomfort. Thus, a vertical eye illuminance threshold should be taken into account. Illuminance larger than this threshold may cause visual discomfort. There are large discrepancies among the existing and newly defined thresholds, which range from $875\,\mathrm{lx}$ to $3000\,\mathrm{lx}$ [26]. In this paper, we limit the transmitted power of auxiliary LEDs such that the maximum vertical illuminance on human eyes (assuming at height of $1.5\,\mathrm{m}$) is $2000\,\mathrm{lx}$. The maximum value of vertical illuminance on human eyes is measured at the point where the human can directly see the reflected light rays from mirrors. The illuminance values vary with transmitted power and the concentration of the light beam. The admission region of the ratio between transmitted power of downward-oriented LEDs and auxiliary LEDs $k = P^b_{opt}/P^a_{opt}$ and the semi-angle of auxiliary LEDs Φ^b can be found by drawing contour lines of maximum average illuminance and vertical illuminance threshold. Fig.3.5 (a) and (b) show admission regions for LOS (multi) backhaul configuration and ma-nLOS (multi) backhaul configuration, respectively. Choosing the values of Φ^b and k within these regions can fulfill the average illuminance requirement (less than $750\,\mathrm{lx}$) and the vertical discomfort illuminance threshold (under $2000\,\mathrm{lx}$). In Fig.3.5 (a) it is shown that the vertical illuminance never exceeds $2000\,\mathrm{lx}$ and the average illuminance is larger than $750\,\mathrm{lx}$ when Φ^b becomes large. It can be seen in Fig.3.5 (b) that P^b_{opt} of the ma-nLOS (multi) backhaul configuration has a more strict limitation due to specular reflected light rays. When Φ^b is small, the concentrated light beam of auxiliary LEDs leads to very large vertical illuminance on human eyes, thereby limiting the transmitted power of auxiliary LEDs. Increasing Φ^b allows larger transmitted power under the condition of vertical illuminance threshold. Unlike the decreasing trend of the contour line of average illuminance versus Φ^b in Fig.3.5 (a), the $750\,\mathrm{lx}$) line of ma-nLOS (multi) configuration slightly decreases versus Φ^b. This

is likely due to the fact that auxiliary LEDs pointing towards mirrors on the floor has a larger influence on average illuminance than horizontally placed auxiliary LEDs. Increasing Φ^b may reduce the maximum illuminance on the floor while increasing the minimum illuminance, which leads to near-constant contour lines of average illuminance versus Φ^b. Regardless of the backhaul configuration, increasing k always leads to larger average and vertical illuminance when the value of Φ^b is fixed.

3.4.2 SINR analysis of VLC backhaul

Assuming all BSs are transmitting backhaul and access signals simultaneously, VLC backhaul links will interfere with access downlink transmission. Two frequency reused schemes, fully reused (FR) and in-band (IB) methods, have been discussed in [16]. With the FR method access and backhaul links share the whole spectrum, while two orthogonal bands are used to transmit access and backhaul data with the IB method. SINR of access and backhaul links depends on the backhaul configuration and the frequency reuse scheme.

3.4.2.1 Ma-nLOS (single) backhaul

The purpose of downward-oriented LEDs is to provide illuminance and access downlink transmission. When ma-nLOS (single) backhaul configuration is used, they are also used to send backhaul data. However, PDs of UEs detect access and backhaul signals sent from the same BS via the same LOS path. Similarly, auxiliary PDs also receive the power of access and backhaul signal sent from the same BS via the same mirror-obstructed LOS path. If the access link and backhaul link use the same spectrum and an equal amount of optical power is transmitted on both links, PDs detect very large interference came from the same path as the intended signal. Increasing the transmitted power of one link leads to a lower SINR of the other link. In order to guarantee the performance, different orthogonal bands should be used to transmit access and backhaul data, i.e. IB method should be used. Thus, the SINR on the n-th subcarrier of an access link between a BS and a UE targeted to this BS is calculated as

$$\gamma_n^{\text{a-IB}} = \eta \frac{P_{elec,n}^a R_{PD}^2 |G^{LOS}|^2}{\sigma_n^2 + \sum_{i \in \mathcal{I}_a} P_{elec,n}^a R_{PD}^2 |G_{i\text{-}s0}^{LOS}|^2}, \tag{3.2}$$

where R_{PD} is the responsivity of PD in A/W, $\sigma_n = N_0 B/N$ is the noise power on the n-th subcarrier, N_0 is the power spectral density (PSD) of AWGN channels, and B is the bandwidth of OFDM signal, G_s^{LOS} denotes the channel gain of the LOS path from a LED denoted by s to the PD of the UE, the subscript is omitted for the path of the calculated access link, P_{elec}^a denotes the transmitted electrical power for access data, which can be calculated by the optical power P_{opt}^a using

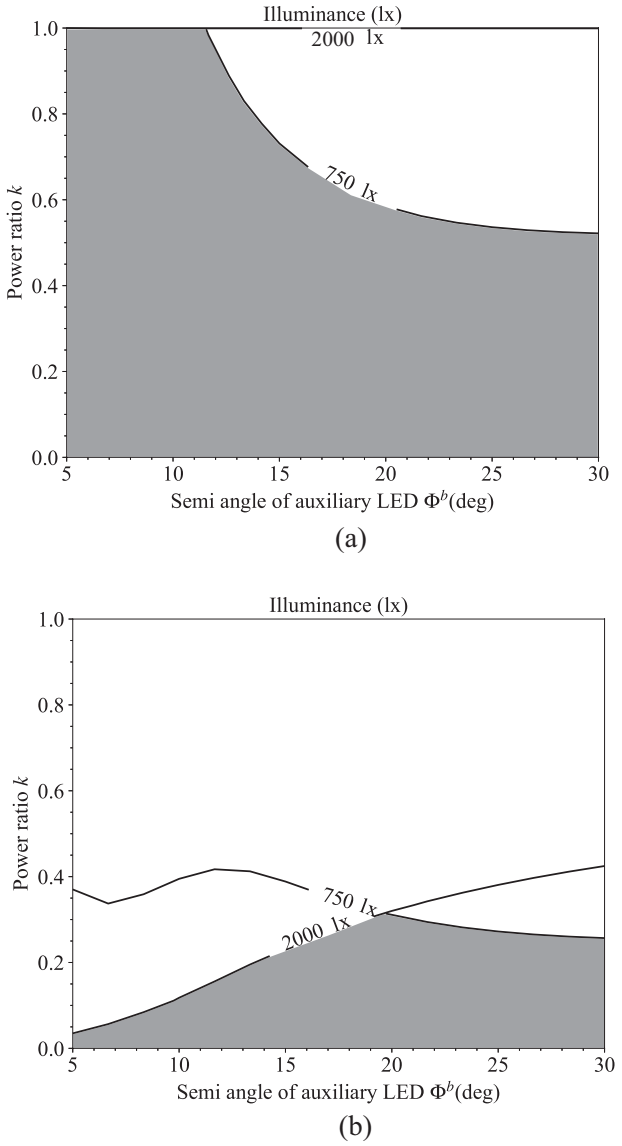

*Figure 3.5: Contour lines of the average illuminance requirement (*750 lx*) and the vertical illuminance threshold (*2000 lx*) for (a) LOS (multi) backhaul and (b) ma-nLOS (multi) backhaul; shadowed areas are admission regions of power ratio k and semi-angle Φ^b*

the relationship in section 3.2.2. Here, we assume that electrical power is equally allocated on all modulated subcarriers, such that $P^a_{elec,n} = P^a_{elec}/(N-2)$. The second term in the denominator of the equation is the total electric power received from interfering sources. The interference set $\mathcal{I}_a$ consists of all BSs except for the tagged BS. The factor η indicates the bandwidth efficiency loss caused by adding cyclic prefix (CP) at the end of each OFDM frame. Adding CP to OFDM frames can overcome inter-symbol interference (ISI) with simple equalization. The length of CP is chosen such that the CP duration is longer than 4 times the root-mean-square (RMS) delay spread of the channel, i.e. $T_{cp} = N_{cp}T_s = \lceil 4\tau_{RMS}f_s \rceil \cdot T_s$, where $\lceil x \rceil$ is the least integer greater than or equal to x, f_s is the sampling rate which is twice the signal bandwidth B, $T_s = 1/f_s$ is the sampling period, and τ_{RMS} is the RMS delay spread which is calculated using the simulated channel impulse response. Therefore the efficiency loss factor is calculated by

$$\eta = \frac{N-2}{N-2+N_{cp}} = \frac{N-2}{N-2+\lceil 4\tau_{RMS}f_s \rceil}. \tag{3.3}$$

The IB method used in [15] divides the spectrum into two orthogonal bands and allocates them to access and backhaul transmission. All backhaul links share the same orthogonal band. However, backhaul data sent to different BSs interfere with each other when downward-oriented LEDs are used for backhaul transmission. As shown in Fig.3.3(a), the gateway sends backhaul signal to six neighboring tier-1 BSs, each tier-1 BS sends backhaul downlink data to two tier-2 BS and uplink data to the gateway, and each tier-2 BS sends backhaul uplink data to the corresponding tier-1 BS. As auxiliary PDs are oriented towards different horizontal directions as shown in Fig.3.3(a), interference from simultaneously transmitting backhaul links of their orienting BSs should be minimized. Thus, we divide the whole electric spectrum into six orthogonal bands which correspond to the maximum number of simultaneously transmitting backhaul links of one BS (the gateway). For simplicity, we allocate six orthogonal bands according to the number of auxiliary PD illustrated in Fig.3.3(a), i.e. an auxiliary PD i-rj of BS$_i$ only detects interference signal intended to be sent to the auxiliary PD l-rj of BS$_l$. The SINR on the n-th subcarrier of a backhaul link between a downward-oriented LED and its targeted auxiliary PD is calculated as

$$\gamma_n^{b\text{-IB}} = \eta \frac{P^b_{elec,n} R^2_{PD} |G^{ma\text{-}nLOS}|^2}{\sigma_n^2 + \sum_{i \in \mathcal{I}_b} P^b_{elec,n} R^2_{PD} |G^{ma\text{-}nLOS}_{i\text{-}s0}|^2} \tag{3.4}$$

Similarly, $G_s^{ma-nLOS}$ denotes the channel gain of the mirror-aided non-LOS path from the LED sender denoted by s to the receiving auxiliary PD, the subscript is omitted for the path of the calculated backhaul link, P^b_{elec} denotes the transmitted electrical power for backhaul data. As downward-oriented LEDs are used for both access and backhaul data transmission, $P^b_{elec} = P^a_{elec}$. The interference set $\mathcal{I}_b$ con-

sists of BSs transmitting backhaul data to an auxiliary PD with the same number of the targeted PD.

3.4.2.2 Ma-nLOS (multi) backhaul

When additional auxiliary LEDs are used for backhaul transmission, backhaul data is transmitted via mirror-obstructed LOS paths. If IB method is used, the SINR on the n-th subcarrier of access links is calculated as Eq.(3.2). The calculation of SINR of backhaul links is similar to Eq.(3.4). However, the interference set $\mathcal{I}_b$ for the ma-nLOS (multi) using the IB method becomes auxiliary LEDs with the same number as the tagged auxiliary LED. P^b_{elec} is calculated by P^b_{opt} based on the illumination and eye safety requirements. As access and backhaul data is transmitted via different paths, FR method can be used. The SINR on the n-th subcarrier of access links using FR method is

$$\begin{aligned}\gamma_n^{a\text{-FR}} &= \eta \frac{P^a_{elec,n} R^2_{PD} |G^{LOS}|^2}{\sigma_n^2 + I}, \\ I &= \sum_{i \in \mathcal{I}_a} P^a_{elec,n} R^2_{PD} |G^{LOS}_{i\text{-}s0}|^2 \\ &+ \sum_{i \in \mathcal{I}_b} \sum_{j \in \mathcal{A}_i} P^b_{elec,n} R^2_{PD} |G^{LOS}_{i\text{-}sj}|^2,\end{aligned} \tag{3.5}$$

where G_s^{LOS} denotes the channel gain of the LOS path from a downward-oriented LED or an auxiliary LED to the PD of the UE. The main difference between Eq.(3.2) and Eq.(3.5) is the total received interfering power. The interference set $\mathcal{I}_a$ of Eq.(3.5) consists of all BSs except for the tagged BS. The set $\mathcal{I}_b$ consists of all BSs and $\mathcal{A}_i$ consists of all power-transmitting auxiliary LEDs of BS$_i$ (based on the routing scheme shown in Fig.3.3(a)). The SINR on the n-th subcarrier of backhaul links can be calculated by

$$\begin{aligned}\gamma_n^{b\text{-FR}} &= \eta \frac{P^b_{elec,n} R^2_{PD} |G^{ma\text{-}nLOS}|^2}{\sigma_n^2 + I}, \\ I &= \sum_{i \in \mathcal{I}_a} P^a_{elec,n} R^2_{PD} |G^{ma\text{-}nLOS}_{i\text{-}s0}|^2 \\ &+ \sum_{i \in \mathcal{I}_b} \sum_{j \in \hat{\mathcal{A}}_i} P^b_{elec,n} R^2_{PD} |G^{ma\text{-}nLOS}_{i\text{-}sj}|^2\end{aligned} \tag{3.6}$$

where $G_s^{ma\text{-}nLOS}$ denotes the channel gain of the mirror-aided non-LOS path from a downward-oriented LED or an auxiliary LED to the auxiliary PD. Here, $\mathcal{I}_a$ and $\mathcal{I}_b$ in I both consist of all BSs. The set $\hat{\mathcal{A}}_i$ is a sub-set of $\mathcal{A}_i$ which excludes the targeted auxiliary LED.

3.4.2.3 LOS (multi) backhaul

Similar to ma-nLOS (multi) backhaul, FR and IB methods can be used for LOS backhaul configuration. SINR of access links can be calculated using the same equations presented in 3.4.2.1 and 3.4.2.2. Calculations of SINR of backhaul links are similar to that in the previous subsection. However, the channel gain of mirror-aided non-LOS paths should be replaced by that of LOS paths. As all BSs are placed at the same height, some LOS paths could be obstructed by BSs between them. Thus, there is no interference detected from these paths.

3.4.3 Channel performance

In this section, we assess the performance of backhaul configurations in terms of the aggregate data rate of the network. The aggregate data rate is the sum of the data rates provided to all UEs in the network. The achievable data rate of a link is calculated using Shannon theorem $R = b\log_2(1+\gamma)$, where b is the bandwidth allocated to the link, γ is the SINR of the link. The end-to-end data rates of UEs in tier-1 and tier-2 cells are limited by backhaul data rates. If the IB method is used, data rates of UEs in the gateway cell are affected by bandwidth allocation ratio $\delta = B_a/B$, where B_a is the bandwidth allocated to access links. When multiple UEs are located in a cell, all UEs equally share the spectrum B_a. The sum of the data rates of these UEs achieves the maximum value when all UEs are located at a point with the maximum SINR, where is the center of the cell. It is clear that the maximum sum rate is equal to the achievable data rate of a single UE located at the cell center.

Due to asymmetric spatial distribution of SINR of access links in cells of tier-2 BSs, the BSs in $\mathcal{T}_2$ are divided into two groups, which are $\mathcal{T}_{2^a} = \{BS_i, i \in [7, 8, .., 12]\}$ and $\mathcal{T}_{2^b} = \{BS_i, i \in [13, 14, .., 18]\}$, respectively. In order to calculate the aggregate data rate, we need to determine the bandwidth allocation ratio for different backhaul configurations using the IB method. As backhaul links cannot become bottleneck for data transmission to UEs, the data rate of each backhaul downlink $R^{b\text{-IB}}_{\mathcal{T}_i}, i \in [1, 2^a, 2^b]$ should be large enough to provide access data transmission to all downstream UEs, i.e. $R^{a\text{-IB}}_{\mathcal{T}_i}, i \in [1, 2^a, 2^b]$. Based on the inequality $R^{b\text{-IB}}_{\mathcal{T}_1} \geq R^{a\text{-IB}}_{\mathcal{T}_1} + R^{a\text{-IB}}_{\mathcal{T}_{2^a}} + R^{a\text{-IB}}_{\mathcal{T}_{2^b}}$, the upper-bound of bandwidth allocation ratio of the gateway is calculated as in Eq.(3.7), where $\gamma^{b\text{-IB}}_{n,\mathcal{T}_i}$ denotes the SINR on n-th subcarrier of the backhaul link to $\mathcal{T}_i, i \in [1, 2^a, 2^b]$ BSs, $\gamma^{a\text{-IB}}_{n,\mathcal{T}_i}$ is the SINR on n-th subcarrier of the access link to UEs in $\mathcal{T}_i, i \in [0, 1, 2^a, 2^b]$ cells. Notice that $\gamma^{a\text{-IB}}_{n,\mathcal{T}_i}$ is calculated at the center point of the cell. The factor $\frac{1}{6}$ comes from six orthogonal bands used for backhaul data transmission to different neighboring BSs as discussed in section 3.4.2.1. As one tier-1 BS only serves two tier-2 BSs, $\delta_{\mathcal{T}_1}$ of tier-1 BSs is larger than that of the gateway. In a network using static frequency allocation, δ is fixed for every BS. In order to guarantee the access data transmis-

sion to all UEs, δ should be the bandwidth allocation ratio of the gateway cell, i.e. $\delta = \delta_{\mathcal{T}_0}$. Due to the illumination and eye safety requirements, the range of the optical power allowed to transmit backhaul data using auxiliary LEDs depends on the semi-angle of auxiliary LEDs as shown in Fig.3.5. By taking different values of Φ_b and k, we observe that the maximum value of delta is obtained at the maximum value of k when Φ_b is fixed. We show the maximum values of δ with different values of semi-angle Φ^b in Fig.3.6. The ratio δ of the ma-nLOS (single) backhaul configuration is very small and does not vary with Φ^b. In ma-nLOS (multi) backhaul configuration, δ drops dramatically when Φ^b exceeds 10°. When Φ^b is larger than 20°, almost all bandwidth has to be allocated to backhaul links. The bandwidth ratio for LOS (multi) backhaul configuration is larger than that for the ma-nLOS (multi) backhaul except for $\Phi^b = 10^\circ$. We observe that the maximum value of δ is obtained at maximum value of k shown in Fig.3.5. Thus, at $\Phi^b = 10^\circ$, ma-nLOS (multi) backhaul configuration is more power-efficient and achieves better performance than LOS (multi) backhaul configuration.

$$\delta_{\mathcal{T}_0} = \frac{\frac{1}{6}\log_2(1+\gamma_{n,\mathcal{T}_1}^{b\text{-IB}})}{\frac{1}{6}\log_2(1+\gamma_{n,\mathcal{T}_1}^{b\text{-IB}}) + \log_2(1+\gamma_{n,\mathcal{T}_1}^{a\text{-IB}}) + \log_2(1+\gamma_{n,\mathcal{T}_{2^a}}^{a\text{-IB}}) + \log_2(1+\gamma_{n,\mathcal{T}_{2^b}}^{a\text{-IB}})}, \tag{3.7}$$

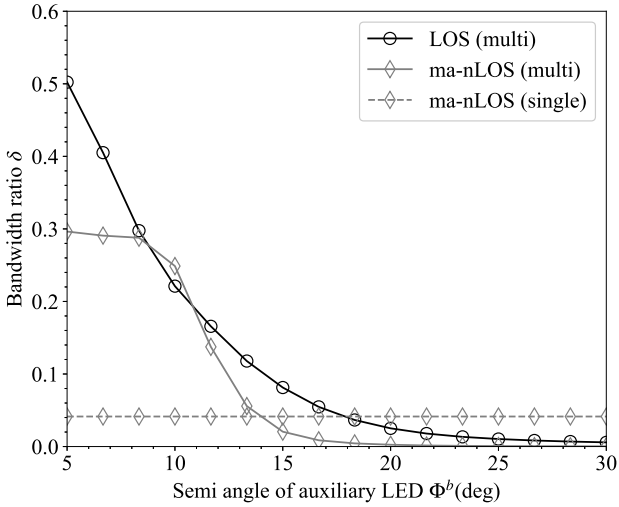

Figure 3.6: Bandwidth allocation ratio δ of three backhaul configurations with different backhaul semi-angle Φ^b; horizontal misalignment angle $\Delta\theta = 0^\circ$; heights of UEs are $1.15\,\mathrm{m}$

Parameter	Symbol	Value
Number of subcarriers	N	1024
Bandwidth	B	20 MHz
Noise PSD	N_0	1×10^{-21} A^2/Hz
PD detecting area	A_r	1 cm^2
PD responsitivity	R_{PD}	0.5 A/W
Reflectivity of mirrors	ρ_m	0.9

Table 3.1: Simulation parameters

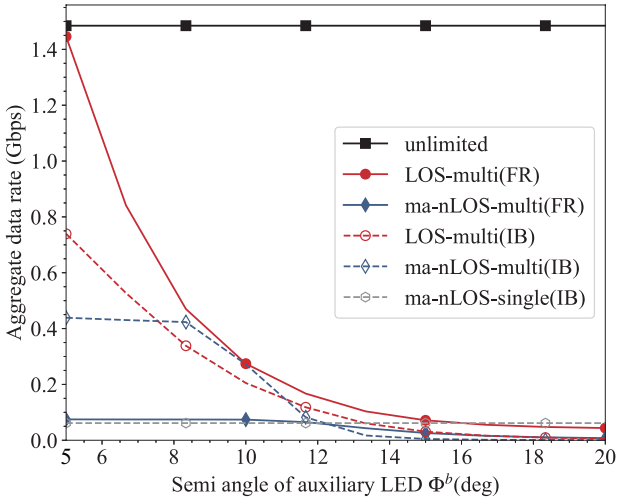

Figure 3.7: Aggregate data rates of optical attocell networks using different backhaul configurations; horizontal misalignment angle $\Delta\theta$ =0°; heights of UEs are 1.15 m

Using δ values calculated in Fig.3.5, the aggregate data rate of the network using IB method is $R = R_{\mathcal{T}_0}^{a\text{-IB}} + 6(R_{\mathcal{T}_1}^{a\text{-IB}} + R_{\mathcal{T}_{2^a}}^{a\text{-IB}} + R_{\mathcal{T}_{2^b}}^{a\text{-IB}})$, where $R_{\mathcal{T}_i}^{a\text{-IB}} = \xi\delta B\log_2(1+\gamma_{\mathcal{T}_i}^{a\text{-IB}})$, $\xi = (N-2)/(2N)$ is the bandwidth utilization factor of DCO-OFDM. Similarly, the aggregate data rates of the network using FR method are calculated by replacing $R_{\mathcal{T}_i}^{a\text{-IB}}$ with $R_{\mathcal{T}_i}^{a\text{-FR}}$, where $R_{\mathcal{T}_i}^{a\text{-FR}} = \xi B\log_2(1+\gamma_{\mathcal{T}_i}^{a\text{-FR}})$. For comparison, the aggregate data rate of a network using backhaul links with unlimited capacity is also calculated. The mirrors used in our simulations are assumed aluminium-coated mirrors. Without loss of generality, the reflectivity of mirrors is obtained by taking the average of $\Phi_e(\lambda)\rho(\lambda)/\Phi_e(\lambda)$ over the visible light spectrum, where $\Phi_e(\lambda)$ is the spectral density of a commercial blue LED with yellow phosphor at wavelength λ and $\rho(\lambda)$ is the reflectivity of aluminium-

coated mirrors at λ. Parameters are shown in table 3.1. Results of aggregate data rates are shown in Fig.3.7. The network using backhaul with unlimited capacity achieves maximum $1.45\,\mathrm{Gbps}$. The network using ma-nLOS (single) backhaul configuration using IB method only achieves $0.07\,\mathrm{Gbps}$. For the rest backhaul configurations which use auxiliary LEDs for backhaul transmission, it is clearly shown that the performance highly depends on the FOV of auxiliary LEDs. The aggregate data rate drops when Φ^b increases. LOS (multi) backhaul configuration with FR method outperforms other backhaul configurations. It can achieve almost the same performance as backhaul with unlimited capacity when Φ^b is very small. However, the performance degrades dramatically when increasing Φ^b. When the IB method is used, the performance of the LOS (multi) backhaul configuration degrades due to low spectral efficiency. The case of ma-nLOS (multi) backhaul is exactly the opposite: using the IB method can achieve better performance than using the FR method. When IB method is used and Φ^b is between 7° and 11°, this backhaul configuration performs as good as LOS (multi) backhaul configuration using the same frequency reuse scheme. When Φ^b $>13^\circ$ the ma-nLOS (single) configuration out performs ma-nLOS (multi) using IB method. If FR method is used for ma-nLOS (multi) backhaul, the network performance is the worse than the ma-nLOS (single) configuration when Φ^b is larger than 11°. The aggregate data rate of the network slightly increases by minimizing the semi-angle of auxiliary LEDs.

In the above analysis, horizontal misalignment angle $\Delta\theta$ $=0^\circ$ is assumed. This ideal case may not be guaranteed in some scenarios, for instance, one of the BSs rotates against the vertical axis due to installation errors or cleaning. We calculate network aggregate data rates in the above-mentioned misalignment scenario and show in Fig.3.8. We assume that the bandwidth allocation ratio δ calculated by Eq.(3.7) does not change. The data rate ratio $R_{mis}(\Delta\theta)/R(0)$ indicates the robustness of the backhaul configuration against misalignment. Here, $R(0)$ is the aggregate data rate when all auxiliary transceivers are perfectly aligned ($\Delta\theta$ $=0^\circ$), and $R_{mis}(\Delta\theta)$ is the aggregate data rate when rotating auxiliary transceivers (both PDs and LEDs) of the misaligned BS with horizontal misalignment angle $\Delta\theta$. Auxiliary transceivers of other BSs remain the same orientation. The positive value of $\Delta\theta$ means rotating auxiliary transceivers (both PDs and LEDs) of the misaligned BS anti-clockwise. It is shown in Fig.3.8 that the LOS (multi) configuration is vulnerable to misalignment than the ma-nLOS (multi) configuration regardless of the frequency reuse scheme. The data rate ratio $R_{mis}(\Delta\theta)/R(0)$ of networks using the LOS (multi) configuration suddenly drops when $\Delta\theta$ of auxiliary transceivers of BS_0 is greater than $\pm 13^\circ$ as shown in Fig.3.8 (a). This is likely due to the fact that the SINR of LOS backhaul links dramatically decreases due to misalignment and backhaul links become the bottleneck when $\Delta\theta > \pm 13^\circ$. When the horizontal misalignment angle $\Delta\theta$ of BS_0 is very large, for instance,

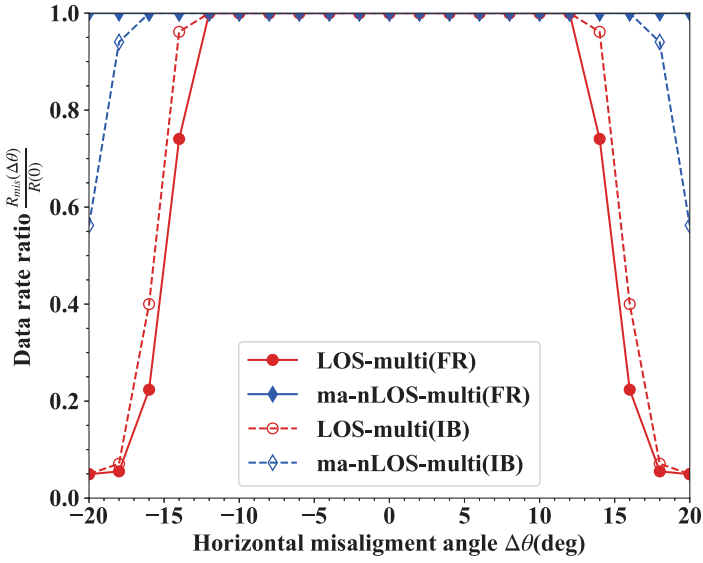

(a) Misaligned BS0

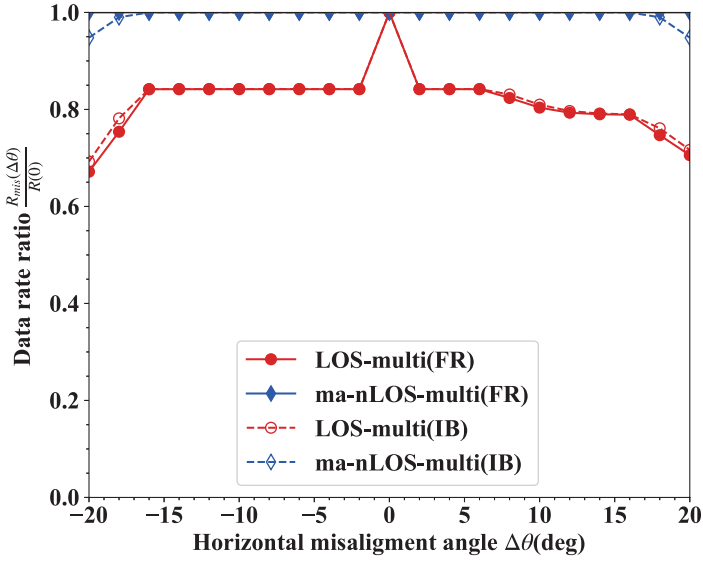

(b) Misaligned BS1

Figure 3.8: Data rate ratio $R_{mis}(\Delta\theta)/R(0)$ of networks using two backhaul configurations when rotating auxiliary transceivers of (a) BS_0 (gateway) and (b) BS_1 ($\mathcal{T}_1$) against the vertical axis; Φ^b=5°; heights of UEs are 1.15 m.

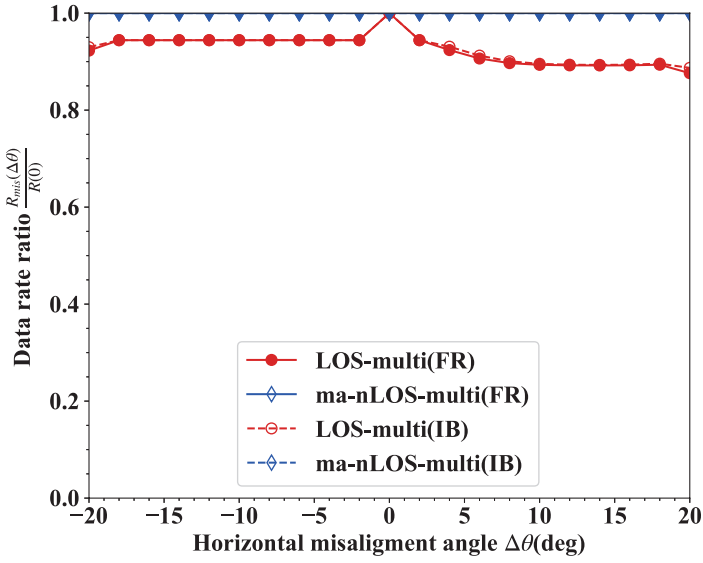

(c) Misaligned BS7

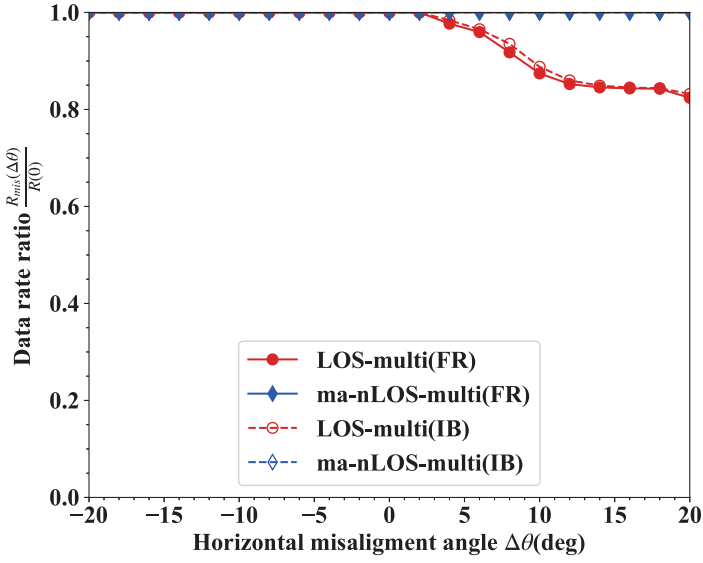

(d) Misaligned BS14

Figure 3.8: (continued) Data rate ratio $R_{mis}(\Delta\theta)/R(0)$ of networks using two backhaul configurations when rotating auxiliary transceivers of (c) BS$_7$ ($\mathcal{T}_{2^a}$) and (d) BS$_{14}$ ($\mathcal{T}_{2^b}$) against the vertical axis; Φ^b=5°; heights of UEs are 1.15 m.

$\Delta\theta = \pm 20°$, networks using ma-nLOS (multi) and IB method can achieve higher aggregate rates ($0.25\,\mathrm{Gbps}$) than other configurations (lower than $0.1\,\mathrm{Gbps}$). A misaligned tier-1 or tier-2 BS has almost no effect on ma-nLOS (multi) configuration. It is also shown that $R_{mis}(\Delta\theta)/R(0)$ is symmetric around $\Delta\theta = 0°$ when BS_0 is misaligned. However, it is not the case for other misaligned BSs shown in Fig.3.8 (b), (c), and (d). This is caused by the unsymmetrical placement of auxiliary transceivers of tier-1 BSs. The simulation results reveal that mirror-aided non-LOS configurations are more suitable for indoor applications having higher requirements of stability.

3.5 Conclusion

The purpose of this study is to analyze the performance of optical attocell networks using VLC backhaul links taking into account illumination and eye safety requirements. A LOS backhaul configuration (LOS (multi)) and two mirror-aided non-LOS configurations (ma-nLOS (single) and ma-nLOS (multi)) are analyzed and compared. The transmitted power of auxiliary LEDs should be limited due to indoor illumination requirements and eye safety issues. The ma-nLOS (multi) configuration has a more strict limitation on the auxiliary transmitted power. Bandwidth allocation ratio for networks using IB frequency reused scheme is calculated. The ma-nLOS (multi) configuration requires larger bandwidth for backhaul transmission than the LOS (multi) configuration in order to avoid throughput bottleneck. Aggregate data rates of optical attocell networks using different backhaul configurations are compared. An FR frequency reuse scheme is also considered. It is shown that LOS (multi) configuration using the FR scheme outperforms other backhaul configurations. The ma-nLOS (multi) configuration using the IB method can achieve almost as good performance as the LOS (multi) configuration using the same frequency reuse strategy. Results also reveal backhaul configurations using auxiliary LEDs need narrow-beam auxiliary transmitters to guarantee the performance of the network. Finally, performance comparison of backhaul links using a gateway with misaligned auxiliary transceivers shows that the LOS (multi) configuration is more vulnerable to misalignment.

References

[1] Harald Burchardt, Nikola Serafimovski, Dobroslav Tsonev, Stefan Videv, and H. Haas. *VLC : Beyond Point-to-Point Communication*. IEEE Communications Magazine, 52(7):98–105, 2014.

[2] Abdullah Sevincer, Aashish Bhattarai Member, and Mehmet Bilgi Member. *LIGHTNETs : Smart LIGHTing and Mobile Optical Wireless NETworks – A Survey*. IEEE Communications Surveys & Tutorials, 15(4):1620–1641, 2013.

[3] Deva K Borah, Anthony C Boucouvalas, Christopher C Davis, Steve Hranilovic, and Konstantinos Yiannopoulos. *A review of communication-oriented optical wireless systems*. EURASIP Journal on Wireless Communications and Networking, (1):1–28, 2012.

[4] V Jungnickel, M Uysal, N Serafimovski, T Baykas, E Ciaramella, Z Ghassemlooy, R Green, H. Haas, P A Haigh, V P Gil Jimenez, F Miramirkhani, and M Wolf. *A European View on the Next Generation Optical Wireless Communication Standard*. In IEEE Conference on Standards for Communications and Networking (CSCN), pages 106–111, 2015.

[5] Hany Elgala, Raed Mesleh, and H. Haas. *Indoor optical wireless communication: Potential and state-of-the-art*. IEEE Communications Magazine, 49(9):56–62, 2011.

[6] Hossein Kazemi and H. Haas. *Downlink cooperation with fractional frequency reuse in DCO-OFDMA optical attocell networks*. In IEEE International Conference on Communications, 2016.

[7] Cheng Chen, Dushyantha A. Basnayaka, and H. Haas. *Downlink performance of optical attocell networks*. Journal of Lightwave Technology, 34(1):137–156, 2016.

[8] Irina Stefan, Harald Burchardt, and H. Haas. *Area spectral efficiency performance comparison between VLC and RF femtocell networks*. IEEE International Conference on Communications, pages 3825–3829, 2013.

[9] Toshihiko Komine and Masao Nakagawa. *Integrated System of White LED Visible Light Communication and Power Line Communication*. IEEE Transactions on Consumer Electronics, 49(1):71–79, 2003.

[10] Yiguang Wang, Nan Chi, Yuanquan Wang, Li Tao, and Jianyang Shi. *Network Architecture of a High-Speed Visible Light Communication Local Area Network*. IEEE Photonics Technology Letters, 27(2):197–200, 2015.

[11] Dilukshan Karunatilaka, Fahad Zafar, Vineetha Kalavally, and Rajendran Parthiban. *LED Based Indoor Visible Light Communications: State of the Art*. IEEE Communications Surveys & Tutorials, 17(3):1649–1678, 2015.

[12] Jianming Liu, Bingzhen Zhao, Liang Geng, Zhou Yuan, and Yirong Wang. *Communication performance of broadband PLC technologies for smart grid*. In IEEE International Symposium on Power Line Communications and Its Applications, 2011.

[13] Lifang Feng, Rose Qingyang Hu, Jianping Wang, Peng Xu, and Yi Qian. *Applying VLC in 5G Networks: Architectures and Key Technologies*. IEEE network, 30(6):77–83, 2016.

[14] Ting Wu, Theodore S. Rappaport, and Christopher M. Collins. *Safe for generations to come: Considerations of safety for millimeter waves in wireless communications*. IEEE Microwave Magazine, 16(2):65–84, 2015.

[15] Hossein Kazemi, Majid Safari, and H. Haas. *A Wireless Backhaul Solution Using Visible Light Communication for Indoor Li-Fi Attocell Networks*. In IEEE ICC 2017 Optical Networks and Systems Symposium, 2017.

[16] Hossein Kazemi, Majid Safari, and Harald Haas. *A Wireless Optical Backhaul Solution for Optical Attocell Networks*. IEEE Transactions on Wireless Communications, 18(2):807–823, 2019.

[17] Yuhui Wu, Pieter Audenaert, Mario Pickavet, and Didier Colle. *Mirror-aided non-LOS VLC channel characterizations with a time-efficient simulation model*. Photonic Network Communications, 38(38):151–166, 2019.

[18] Cheng Chen, Stefan Videv, Dobroslav Tsonev, and H. Haas. *Fractional Frequency Rreuse in DCO-OFDM-Based Optical Attocell Networks*. Journal of Lightwave Technology, 33(19):3986–4000, 2015.

[19] F R Gfeller and U Bapst. *Wireless in-House Data Communication Via Diffuse Infrared Radiation*. Proceedings of the IEEE, 67(11):1474–1486, 1979.

[20] J.M. Kahn and J.R. Barry. *Wireless Infrared Communications*. Proceedings of the IEEE, 85(2):265–298, 1997.

[21] J. Armstrong and B. J C Schmidt. *Comparison of asymmetrically clipped optical OFDM and DC-biased optical OFDM in AWGN*. IEEE Communications Letters, 12(5):343–345, 2008.

[22] Hongming Yang and Ashish Pandharipande. *Full-duplex relay VLC in LED lighting linear system topology*. In Industrial Electronics Conference, pages 6075–6080. IEEE, 2013.

[23] Omer Narmanlioglu, Refik Caglar Kizilirmak, Farshad Miramirkhani, and Murat Uysal. *Cooperative visible light communications with full-duplex relaying*. IEEE Photonics Journal, 9(3):1–11, 2017.

[24] Radiation Safety Office. *Laser Safety Mannual*. 2007.

[25] European Committee for Standardization. *Light and lighting - Lighting of work places - Part 1 : Indoor work*. 2002.

[26] Jae Yong Suk. *Luminance and vertical eye illuminance thresholds for occupants' visual comfort in daylit office environments*. Building and Environment, 148:107–115, 2019.

4

Performance Analysis of Optimization Algorithms for RASP Shadowing Recover Scheme

One of the major problems of the optical attocell networks is the shadowing effect. Pedestrians will cause temporal blockage of the VLC-based access and backhaul links. A shadowing recover scheme, RASP, is presented in this chapter. The RASP is a cross-layer recover scheme which optimizes the routing and the resource allocation in order to minimize the throughput loss in shadowed scenarios.

From the results obtained from the previous chapter, we found that the directional mirror-aided non-LOS backhaul links can achieve the best network performance when using an in-band mode, i.e. different frequency bands are used to transmit access and backhaul data. This link configuration is then considered in this and the following chapters. The RASP method also considers using the in-band mode in the resource allocation scheme.

* * *

Y. Wu, M. Pickavet, D. Colle

Published in IEEE Transaction on Network and Service Management, 2021, 18(3): p.2789-2799.

Abstract *Optical attocell networks based on visible light communication*

(VLC) are cost-efficient solutions which complement the spectrum shortage of radio-frequency(RF)-based indoor wireless networks. However, communication using visible light is vulnerable to the shadowing effect caused by random pedestrians as visible light cannot penetrate opaque objects. A cross-layer resilience scheme RASP (routing, load assignment, subcarrier selection, power allocation) is proposed to address the shadowing effect. Network performance using different combinations of cross-layer control policies, i.e. algorithms and allocation methods, is evaluated and compared by RASP. An optimization algorithm is used to find the optimal/near-optimal combination of RASP control policies. In order to find the proper optimization algorithm for RASP, we investigate and compare the performance of different algorithms, including partial enumeration and neighbor-searching algorithms like hill-climbing and Tabu-search. An improved Tabu-search algorithm is proposed to reduce the time complexity.

4.1 Introduction

Recent years have witnessed growing demand for bandwidth for indoor wireless services such as high-definition video streaming and video conferencing. Although wireless technologies based on radio-frequency (RF) have been well investigated and widely used for indoor data transmission, the available RF spectrum has become more and more crowded due to the increased bandwidth requirement. Visible light communication (VLC) has been drawing scientific interest as it supports simultaneous illumination and wireless access data transmission to user equipment (UE) such as smartphones and laptops. VLC transmitters are visible light-emitting-diodes (LEDs). The transmitted signal is represented by high-frequency fluctuation in the radiant intensity. VLC receivers are low-cost photodiodes (PDs) which convert radiant intensity to electrical current. As visible LEDs work in the visible light spectrum, VLC can complement RF-based wireless technologies without interference. An optical attocell network using LED lamps for data transmission is shown in Fig.4.1(a). Every LED lamp is a base station (BS) and transmits the modulated signal to UEs in an attocell whose radius ranges from one to several meters. Communication links between BSs and UEs form an access network. The access network is connected to the Internet via a backhaul network. The backhaul network connects all BSs to a gateway. The gateway can be either an extra equipment or one of the BSs. There have been many solutions proposed for the backhaul network. Wired solutions like power line communication (PLC) and Power-over-Ethernet (PoE) use the existing electric power grid or integrate power supply and high-speed backhaul transmission in Ethernet cables [1, 2]. These wired solutions require a high cost for installation and may experience large interference with domestic appliances [3]. Wi-Fi is not considered as an option for backhauling due to the following reasons: 1) there is limited RF spectrum avail-

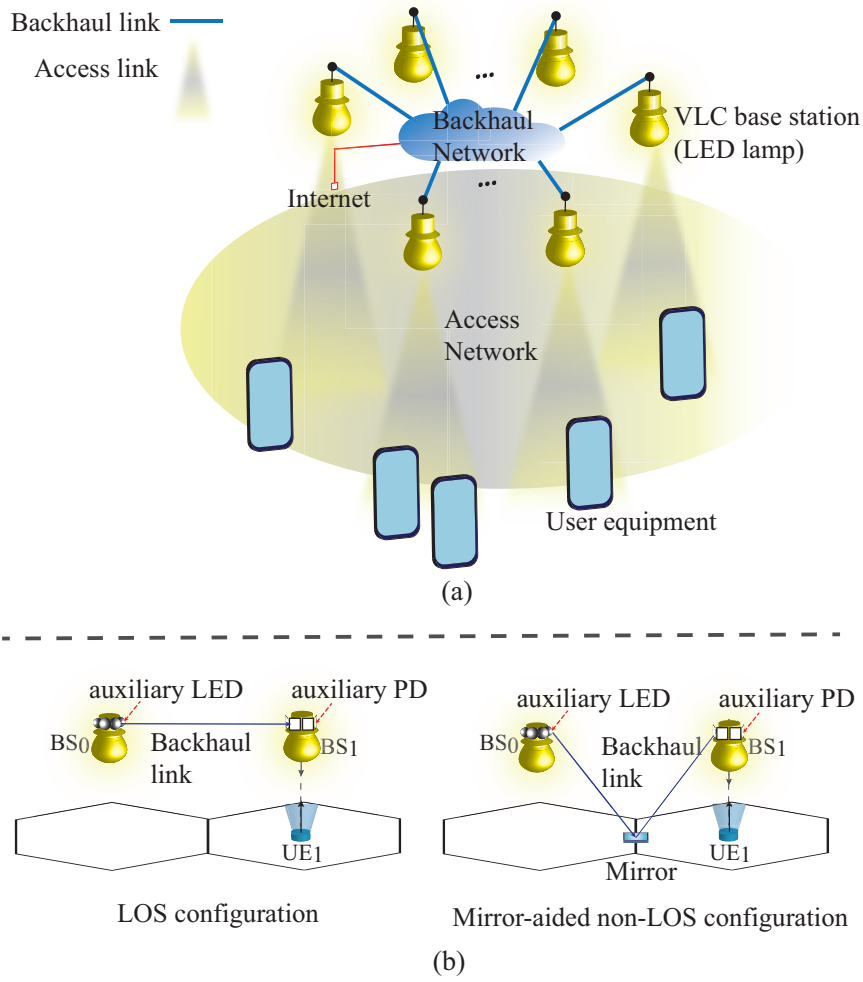

Figure 4.1: (a) Optical attocell network and (b) wireless backhaul link configurations (hexagons represent cells)

able for backhauling in optical attocell networks; 2) backhaul links using Wi-Fi also interfere with existing indoor WiFi networks and the interference cancellation have to be done in both WiFi and VLC networks. Wireless backhaul technologies using line-of-sight (LOS) and mirror-aided non-LOS link configurations as shown in Fig.4.1(b) can be easily installed and configured without changing the existing power grid [4, 5]. Both wireless backhaul link configurations require auxiliary transceivers. Auxiliary transceivers used in mirror-aided non-LOS link configuration are oriented toward mirrors or glossy tiles on the floor while communicating auxiliary transceivers used in LOS configuration are directly oriented toward each other. LOS configuration has a more strict alignment requirement to maintain every direct LOS transmission path and therefore more vulnerable to misalignment [6]. Mirror-aided non-LOS link configuration can be an alternative solution when LOS configuration is not applicable, for example, when lamps are placed at different heights or separated by walls.

One drawback of using VLC links for backhaul transmission is that VLC links suffer from the shadowing effect. As visible light cannot penetrate opaque objects like furniture and human bodies, VLC links could be physically blocked. Due to the lack of the dominant LOS or the first-bounce specular reflection component, impulse responses and channel gains of LOS and mirror-aided non-LOS links are significantly degraded [7]. Roaming people and other indoor activities (such as moving furniture) may cause shadows on receivers such that VLC links are blocked. This shadowing effect can happen on access links and mirror-aided non-LOS backhaul links where LEDs are oriented toward the floor. But it can also happen on LOS backhaul links due to some activities on the ceiling, for example, cleaning or repairing. Link failures caused by the shadowing effect must be recovered to ensure the quality of many activities like video-conferencing and teleworking. Network reliability can be improved by network recovery or resilience schemes. A multispot-diffuse multiple-input-multiple-output (MSD-MIMO) scheme was proposed to recover infrared(IR)-based optical wireless networks [9]. The impact of the shadowing effect is minimized by increasing the transmitting power of unobstructed multispot-diffuse links. Authors in [10] proposed a resilience scheme using adaptive equalization and multiple LEDs to send redundant information. The above research uses redundancy to address the shadowing problem. Larger transmitted power is required when shadowing occurs. We proposed a cross-layer resilience scheme *RASP* to address the shadowing effect, where R stands for routing, A stands for load assignment, S stands for subcarrier selection, and P stands for power allocation [11]. RASP is more power-efficient than the aforementioned schemes as total transmitted power is not increased by network recovery. As measures against all possible link failures are not practical as described in [12], shadowing scenarios with single-link failure are considered in order to verify the feasibility of the RASP scheme. Multiple-link failure scenar-

ios and discussion of shared-risk link groups will be investigated in future work. Performance of RASP using a simple enumeration method which searches the optimal/near-optimal solution in small solution space has been evaluated in [11]. Random subcarrier allocation was used and the performance of the RASP scheme was affected by the randomness of subcarrier allocation. In order to avoid the randomness of subcarrier allocation, cyclic subcarrier allocation with different chunk lengths of subcarriers is considered in this work. In addition, the enumeration method may not be suitable for networks on a large scale as the solution space is limited. To find the optimal/near-optimal solution in a larger solution space, we investigate the performance of different optimization algorithms. The simple enumeration method is compared with two neighbor-searching algorithms, hill-climbing (HC) and Tabu-search (TS). An improved TS algorithm is proposed to reduce the searching time of traditional TS while maintaining performance. The paper is organized in the following way. The following section introduces optical attocell networks and VLC channels. The third section describes the RASP resilience scheme, control policies used in the simulation, and simulation results showing the performance of RASP. Comparisons of optimization algorithms are presented in the fourth section.

4.2 Optical Attocell Networks

Optical attocell networks using VLC-based wireless backhaul links are considered in this paper. In an optical network using mirror-aided non-LOS backhaul links, access LEDs and backhaul LEDs are oriented toward the floor and have the same probability to be shadowed by random pedestrians. In order to investigate the performance of the shadowing recover scheme RASP in networks with all links having the same shadowing probability, we consider mirror-aided non-LOS links as backhaul links in our simulations. In this section, the geometry of optical attocell networks and channel characteristics of VLC links are introduced.

4.2.1 Network Model

An optical attocell network consists of multiple hexagonal cells with a radius ranging from one to several meters. Hexagons are a good approximation of circles and multiple hexagons can fill a certain area without gaps. Each optical attocell is served by a VLC BS, which is a LED lamp. Each BS locates in the center of one cell and provides simultaneous illumination and data transmission to UEs within the cell. Access downlinks from BSs to UEs are VLC links as visible LEDs are used for illumination. Access uplinks, however, can be IR-based optical wireless links, as there is no illumination requirement for mobile devices. Once an access link between a BS and a UE is shadowed, the affected UE will be assigned to the

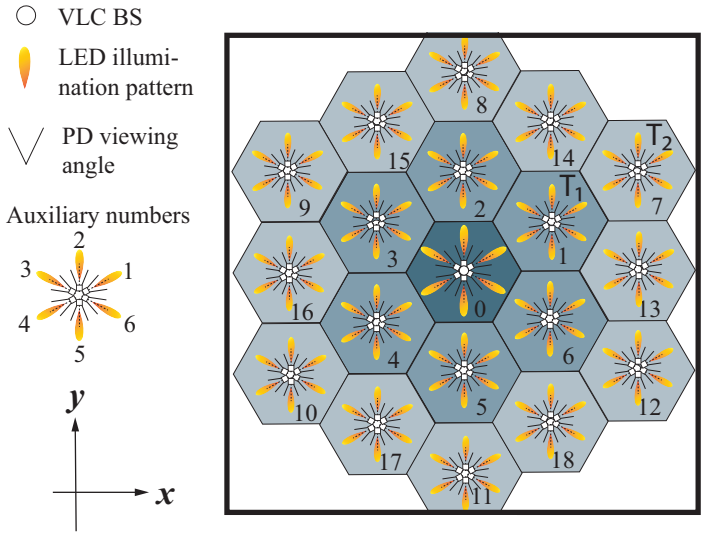

Figure 4.2: Layout of a two-tier optical attocell network

nearest BS. We assume the central BS BS_0 is the gateway which is wired connected to the Internet. BSs are grouped according to hop counts from the gateway when no shadowing occurs as shown in Fig.4.2. Tier-1 BS set denoted as T_1 consists of six neighboring BSs of the gateway BS_1 to BS_6. Tier-2 BS set T_2 consists of BSs BS_7 to BS_{18}, etc.. BSs communicate with all neighboring BSs via mirror-aided non-LOS backhaul links. Each BS has six auxiliary transceivers numbered from 1 to 6 for backhaul transmission. Every BS can be a relay BS which forwards data packets received from one of its neighbors to another neighboring BS according to the routing algorithm. VLC-based backhaul communication between neighboring BSs is simple and cost-efficient as only a few LED and PD chips are required. Communication links form a mesh-type network, which can be seen as the general topology of optical attocell networks using VLC-based backhaul links. Decode-and-forward scheme is used for the relay process. Backhaul links using IR can achieve better performance as discussed in [5]. However, direct radiation by IR-LEDs causes larger damage to human eyes than LEDs working in the visible range as the damage from IR-LEDs cannot be reduced by the natural aversion reflex of eyes [13]. Thus, mirror-aided non-LOS backhaul links are also VLC links.

In an optical attocell network, the gateway is responsible for exchanging data between the Internet and UEs. If BSs work in a distributed manner, i.e., BSs only exchange their information (forwarding table, buffer size, etc.) with neighboring BSs, the gateway cannot know the channel state information of all BSs and may

not be able to control the ingress and egress data flow of the whole network. When assuming channel state information is known by all BSs, it is straightforward to use a central controller at the gateway side which collects information of all BSs and sends control information after processing current network information. A software-defined network (SDN) controller is a viable candidate for configuring and controlling optical attocell networks. The major advantage of using SDN controllers is that SDN offers centralized control and an overview of the whole network. Communication between the SDN controller and BSs can be realized by the Openflow protocol. Openflow messages can be used to handle network traffic and exchange network statistics. Many open-source SDN controllers which support Openflow protocol and enable network virtualization are promising for controlling optical attocell networks in a centralized manner. Given data rates requested by UEs, the central controller determines forwarding rules based on a routing algorithm. When the forwarding information is determined, the central controller assigns loads and allocates resources for each link according to the channel state information (received intensity level, interference level, etc.). The available resource for VLC channels includes electrical bandwidth, electrical power, and optical wavelengths, etc.

4.2.2 Visible Light Communication Channel

As LEDs are incoherent light sources, it is difficult to collect amplitude and phase information in light emitted by LEDs. Intensity modulation and direct detection (IM/DD) is widely used in VLC as it is cost-efficient. By using IM/DD, the transmitted signal is represented by high-frequency fluctuation in radiant intensity. PDs convert the detected light intensity into electrical current. LOS link configuration is illustrated in Fig.4.3(a). The gain of a direct LOS link is denoted by G_{LOS} and can be calculated using positions and orientations of the sender and receiver [8]. Channel modeling and calculation of channel gains of mirror-aided non-LOS links have been discussed in [4]. Mirror-aided non-LOS links take advantage of first-bounce specular reflections. The first-bounce specular reflecting path can be seen as a LOS path from the mirror image of the sender to the receiver passing through a mirror, which is illustrated in Fig.4.3(b). Thus, the gain of the first-bounce specular reflecting path $G_{\text{ma-nLOS}}$ can be calculated using the gain G_{LOS} of LOS link from the mirror image of the sender to the receiver multiplied by the reflectivity of the mirror.

As VLC technology uses intensity modulation, electrical bandwidth is limited by LEDs' modulation bandwidth. In this work, we consider blue LEDs with yellow phosphor as VLC transmitters and white-light luminaires. Each BS is able to use the total available bandwidth $W = 20$MHz. Optical orthogonal frequency division multiplexing (OFDM) is a viable modulation scheme for VLC systems

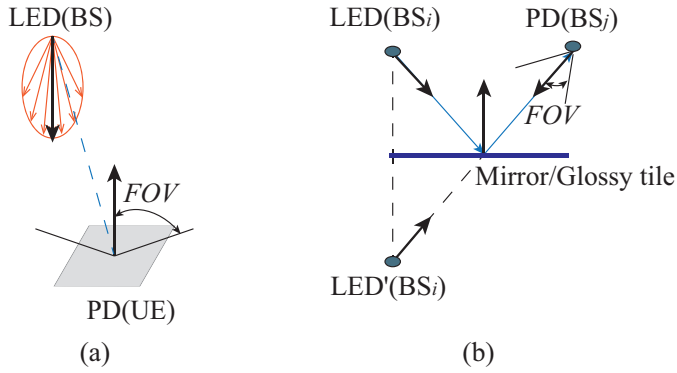

Figure 4.3: Vertical geometry of (a) a LOS link and (b) a mirror-aided non-LOS link; FOV is the filed-of-view of PDs

due to its high spectral efficiency. Data symbols are quadrature amplitude modulated (QAM) to represent the magnitude of the transmitted signal in the frequency domain. Amongst optical OFDM schemes proposed for IM/DD VLC systems, direct current optical OFDM (DCO-OFDM) which has higher spectral efficiency and lower complexity is considered in this work. As light intensity must be non-negative, DC-bias is added to the modulated OFDM signal and the remaining negative value is clipped. Based on DCO-OFDM, total bandwidth is divided into K_{sc} subcarriers and K_d subcarriers are used for carrying data, where $K_d = K_{sc} - 2$. As the transmitted signal of optical OFDM should be real, half of the data-carry subcarriers are used to transmit complex conjugate of the other half [14]. The actual number of subcarriers available to carry data is $K_d/2$. Depending on data rate requests and inter-link interference, each link can use part of or all $K_d/2$ subcarriers to send data.

Total electrical power P_{elec} is evenly distributed across all data-carry subcarriers, i.e. $p_k = P_{elec}/K_d$. Electrical power P_{elec} is calculated by transmitting optical power P_{opt} and DC-bias factor α using the relationship $\alpha = P_{opt}/\sqrt{P_{elec}}$. Transmitting optical power P_{opt} is determined by illumination and eye safety requirements. Average illuminance recommended for offices varies with activities is listed in [15]. As auxiliary LEDs are more concentrated, their transmitting power should be constrained to avoid the visual discomfort of human eyes. There are large discrepancies among the existing and newly defined thresholds of visual discomfort, which range from $875\,\mathrm{lx}$ to $3000\,\mathrm{lx}$ [16]. In our simulations, we configure the transmitting optical power as the largest value that fulfills the average illuminance requirement (less than $750\,\mathrm{lx}$) and the vertical discomfort illuminance threshold (under $2000\,\mathrm{lx}$).

4.3 Resilience Scheme

As the wavelength of visible light is very short, visible light cannot penetrate opaque objects. When the LOS path or the first-bounce specular reflection component is obstructed by pedestrians, PDs can only receive a multi-bounce reflected signal, which has extremely low channel gain and high delay spread. Thus, the performance of shadowed VLC links is degraded due to the lack of LOS or first-bounce specular reflection component. Without loss of generality, we assume that a VLC link is completely blocked by pedestrians, and transmission of the shadowed link is broken. In order to guarantee network reliability, a resilience scheme has to be applied to improve overall network performance when shadowing occurs. The purpose of the resilience scheme is to maximize the aggregate end-to-end throughput such that affected UEs (affected due to directly shadowed access links or shadowed upstream backhaul links) can get enough data rates while guaranteeing the throughput of unaffected UEs.

4.3.1 Control Variables

To design a resilience scheme, we firstly model the optical attocell networks with nodes (BSs and UEs) and edges (links). We use $\mathbf{B}$ to denote a set of all BS nodes and $\mathbf{U}$ to denote a set of all UE nodes. Requested data is represented by a set of data commodities denoted by $\mathbf{C}$. In the set $\mathbf{C}$ each data commodity c contains a source node $s(c) \in \mathbf{B} \cup \mathbf{U}$, a destination node $d(c) \in \mathbf{B} \cup \mathbf{U}$, and requested throughput $T(c) \geq 0$ Mbps. A set $\mathbf{L}$ consists of all backhaul links and access links in the network. A backhaul link has a start node $s(l) \in \mathbf{B}$ and an end node $e(l) \in \mathbf{B}$. An access downlink has a start node $s(l) \in \mathbf{B}$ and an end node $e(l) \in \mathbf{U}$. The access uplinks from UEs to downward-oriented LED are IR links and all other links use visible light (VL). When an active link is shadowed, routes across this link will be affected and need to be reassigned. Once routes are changed, loads, i.e. data rates carried by each link, are changed. In consequence resources available for each link, i.e. the number of subcarriers and power transmitted on these subcarriers as discussed in the previous section, must be reallocated. Therefore, the resilience scheme for addressing the shadowing effect should be a cross-layer scheme.

According to the routing algorithm, there could be one to multiple routes for data commodity c. Routes assigned to data commodity c are denoted by a vector $\vec{r}^{c}$. The i-th route is denoted as $r^{c(i)}$ and $0 \leq i \leq N_c - 1$. Here, $N_c = |\vec{r}^{c}|$ is the number of routes assigned to data commodity c, where $||$ denotes set cardinality. Each element $r^{c(i)}$ is a set of control variables $r_l^{c(i)} = \{0, 1\}$. The control variable $r_l^{c(i)}$ describes the routing policy, where $r_l^{c(i)} = 1$ means that link l is chosen to send data commodity c via the i-th route, and $r_l^{c(i)} = 0$ otherwise.

When there are multiple routes assigned to one data commodity c, the re-

quested throughput $T(c)$ should be allocated to different routes according to a load assignment method. Similar to the routing policy, load control variables $a^{c(i)} \leq 1$ are used. This control variable denotes the ratio of the requested throughput carried by a certain route. The load assigned to the i-th route of data commodity c is $a^{c(i)}T(c)$. The constraint for load assignment is

$$\sum_{i=0}^{N^c-1} a^{c(i)} = 1, \forall c \in \mathbf{C} \tag{4.1}$$

Thus, for each data commodity c, the load assignment policy is described by a vector $\vec{a}^c = [a^{c(0)}, a^{c(1)}, \cdots]$.

Communication channels can use different resources (e.g. time, bandwidth) to avoid interference and maximize channel capacity. In order to exploit the impact of the interference amongst links of different BSs, we consider full-duplex VLC channels, i.e. all links can operate at the same time slot. Self-interference between auxiliary LEDs and PDs mounted on the same BS is neglected due to the following reasons: (1) Auxiliary LEDs have directive illumination pattern and the direct LOS path from the auxiliary LED to the auxiliary PD mounted on the same BS can be physically blocked [17]; (2) Multipath interference due to reflections via walls is not significant compared to the dominant intended LOS and mirror-aided non-LOS signal [4, 18]; (3) Self-interference cancellation can be applied to retrieve the desired signal. Channel resource like electrical bandwidth and optical wavelength is allocated based on frequency division multiple access (FDMA) and wavelength division multiple access (WDMA) schemes. Although multiple LEDs with different wavelengths (e.g. red-green-blue LEDs) have been used to increase the capacity of VLC links, it is not considered in our work. The reason is that the primary purpose of the indoor VLC transmission system is illumination. Chromaticity, quality, and brightness of the light should follow indoor lighting standards. Changing the radiant intensity of different wavelengths may affect the quality of the light in terms of the Color Rendering Index (CRI) [19]. This violates the primary purpose of using VLC. Thus, all visible LEDS are working in the same wavelength and the resource allocation scheme considered in this work is OFDMA which allocates different OFDM subcarriers to VLC links. OFDMA subcarrier selection policy is described using a vector $\vec{w}^l$ where $K_d/2 = |\vec{w}^l|$ is the number of subcarriers carrying real data. The element in $\vec{w}^l$ is the subcarrier control variable $w_k^l = \{0, 1\}$, where $w_k^l = 1$ means that the k-th subcarrier is allocated to link l. For each BS, one subcarrier can only be assigned to one link at a time. We have following constraint:

$$\sum_{\forall l \in \{l:s(l)=b\}} w_k^l \leq 1, \forall b \in \mathbf{B} \tag{4.2}$$

The transmitted power of one LED is constrained by illumination and eye

safety requirements. As each link is allowed to use a certain amount of subcarriers, not all subcarriers of this link should be allocated power. The amount of power allocated on different subcarriers has to be optimized to avoid interference to other links. The transmitted power allocated on different subcarriers of each link is determined by a power allocation scheme. A constraint

$$\sum_{k=0}^{K_{sc}-1} p_k^l \leq P_{elec}^l, \forall l \in \mathbf{L} \tag{4.3}$$

should be met, where p_k^l is the amount of electrical power allocated on the k-th subcarrier of link l and P_{elec}^l is the total electrical power available for a LED transmitter of link l. Similar with the subcarrier selection policy, a vector $\vec{p}^l$ with $K_d/2 = |\vec{p}^l|$ can be used and p_k^l represents the k-th element of $\vec{p}^l$. Based on the illumination and eye safety requirements discussed in 4.2.2, we assume that all downward-oriented LEDs (access LEDs) transmit the same optical power and the transmitted optical power of auxiliary LEDs (backhaul LEDs) as 10% of access LEDs. The electrical power P_{elec}^l of different links can be calculated using the transmitted optical power.

4.3.2 RASP Method

RASP method is a cross-layer routing and resource allocation scheme by configuring four control variables: routing control variable $r_l^{c(i)}$, load control variable $a^{c(i)}$, subcarrier control variable w_k^l, and power control variable p_k^l. Control policies denoted by R (routing policy), A (load assignment policy), S (subcarrier allocation policy), and P (power allocation policy) control each of these control variables respectively. The purpose of the RASP method is to find the optimal or near-optimal combination of control policies by evaluating the overall network performance when choosing different combinations of control policies. Options of different control policies considered in our simulations are described in this subsection. Notice that, control policies are not restricted to the following options and could be any method depending on the requirements of the application. Options of each control policy are denoted by integer numbers.

4.3.2.1 **Routing Policy** (R)

Each UE is assigned to exactly one BS, which is the nearest BS. We assume that all edges (links) have the same cost=1. Every neighboring BSs are connected and the optical attocell network is a mesh-type network. Many routing algorithms have been proposed for packet routing in mesh networks. Routing algorithms based on shortest paths (i.e. minimum hop counts) can be used to avoid long transmission delays when the size of the network increases.

Option 1: Shortest Path Routing R=1

If the shortest path routing is chosen, the Dijkstra routing algorithm is applied to find the path with minimum hop-count for a data commodity c. If there are multiple shortest paths, the routing algorithm randomly chooses one, i.e. $\max(N_c) = 1, \forall c \in \mathbf{C}$.

Option 2: K-Shortest Path Routing R=2

If the traffic is congested in some links, it is better to choose longer paths with light-loaded or unused links. As traditional transmission control protocol (TCP) can use packet numbers to reorder the incoming packets, it is possible to send packets via paths with different hops. With this option, the K-shortest path routing algorithm is performed. Yen's K-shortest path routing algorithm is used to discover the first K shortest paths. In the following simulations, $K = 2$ shortest-path routing is used for option R=2.

4.3.2.2 Load Assignment Policy (A)

Due to inter-link interference, the capacity of links is not known before assigning channel resources and power. The load assignment scheme is designed based on known information, i.e. network topology and routing information.

Option 1: Fair Assignment A=1

The simplest load assignment method is to evenly distribute data amongst all paths to the UE, i.e. $a^{c(i)} = 1/N_c$.

Option 2: Weighted-Fair Assignment A=2

As link capacities are limited, the fair assignment may not be suitable if too many loads are assigned on some bottleneck links. The weighted-fair load assignment method allocates the load based on the weights of links along each route. The weight of a link l which is denoted by f_l is the reciprocal of the total number of routes with $r_l^{\mu(i)} = 1, \mu \in \mathbf{C}$, such that the more routes going through a link, the lower the weight. The weight of a route $f^{c(i)}$ is the minimum value of f_l of links along this route. The load assignment control variable is $a^{c(i)} = \frac{f^{c(i)}}{\sum_{i=0}^{N_c-1} f^{c(i)}}$.

4.3.2.3 Subcarrier Allocation Policy (S)

The capacity of a link has to be adjusted according to the assigned load. Based on Shannon's theorem, the link capacity is proportional to the bandwidth. Therefore, the number of subcarriers required by each link is estimated by the sum of loads on this link $T_l = \sum_{c \in \mathbf{C}} \sum_{i=0}^{N_c-1} r_l^{c(i)} a^{c(i)} T(c)$. The actual number of subcarriers is

limited by the number of available subcarriers $K_d/2$ of a BS. For each BS $b \in \mathbf{B}$, the number of subcarriers allocated to link l with $e(l) = b$ is

$$k_l = \frac{T_l}{\sum_{m\in\{m:e(m)=b\}} T_m} \frac{K_d}{2}$$

.

Option 1: Blockwise Subcarrier Allocation S=1

Every link is assigned a consecutive sequence of subcarriers. The number of the subcarrier chunk is fixed as 5 in our simulations. As shown in Fig.4.2, LEDs are numbered according to their orientations. Subcarrier chunks are assigned to transmitting links in a cyclic manner as shown in Fig.4.4. Blockwise subcarrier allocation is popular in applications where channel state information is not available [20].

Option 2: Interleaved Subcarrier Allocation S=2

Interleaved subcarrier allocation is a special case of blockwise allocation. The number of subcarriers in a chunk is reduced to 1 as shown in Fig.4.4. Interleaved allocation method has lower device requirement than blockwise subcarrier allocation [21].

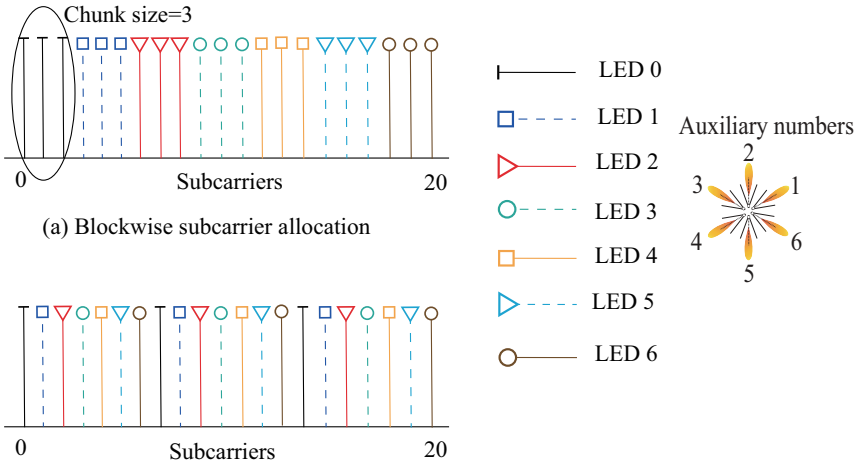

(a) Blockwise subcarrier allocation

(b) Interleaved subcarrier allocation

Figure 4.4: Illustration of (a) blockwise subcarrier allocation and (b) interleaved subcarrier allocation schemes for a BS with seven active LED transmitters, each link from a LED transmitter is represented by a different color

4.3.2.4 Power Allocation Policy (P)

For all $K_d/2$ subcarriers carrying the real data, half of the electrical power should be allocated to them, the other half of electrical power is allocated to their complex conjugates. Before applying the following power allocation policy, the central controller equally allocates total transmitting power to all subcarriers carrying the real data, i.e. $p_k^l = P_{elec}^l/K_d$. The controller then calculates the SINR, the major interfering source of each subcarrier of each link, and the actual link capacity based on current control policies.

Option 1: Adaptive Power Allocation P=1

If one or more links are overloaded, i.e. the actual link capacity is less than the assigned load, the power is re-allocated based on the major interfering source information. We generate a matrix of *risky tags* $rt_{s,r,k}$, where the transmitter of link s is a possible interfering source of the receiver of link r, and k is the index of the subcarrier. If s is the major interfering source of r on the k-th subcarrier, i.e. the transmitter of link s causes the largest interference to the receiver of the link r on the k-th subcarrier, $rt_{s,r,k}$ is set to be 1, and 0 otherwise. Re-allocating power on subcarriers of a link s with $rt_{s,r,k} = 0$ has less impact on the overall performance. A water-filling algorithm is used to re-allocate power that maximizes the link capacity taking into account the total power constraint [22]. The total amount of power is the sum of previously allocated power on subcarriers with $rt_{s,r,k} = 0$. When applying the water-filling algorithm, current SINR information is used.

Option 2: Adaptive Power Allocation with Relaxation P=2

The difference between two adaptive power allocation options P=1 and P=2 are the number of subcarriers that need to be reallocated. Based on the link capacities and load assignment information, a matrix of *relax tags* $xt_{s,r,k}$ is generated to denote the relaxation of a link. $xt_{s,r,k} = 1$ only if $rt_{s,r,k} = 1$ and the ratio between the capacity of s and the load assigned to s is larger than a predefined relaxing ratio ϵ. In addition to power on subcarriers with $rt_{s,r,k} = 0$, power on subcarriers with $xt_{s,r,k} = 1$ are also reallocated using water-filling algorithm.

4.3.3 Simulations of Performance of RASP Scheme

Performance of RASP scheme is assessed by simulations with mesh-type optical attocell networks as shown in Fig.4.2. In our simulations, all data commodities have the same priority and the overall performance is to be optimized. For different applications, data commodities or links may have different priorities and the optimization purpose could be different. Priorities of control variables for different data commodities and links can be described by weight matrices. RASP options

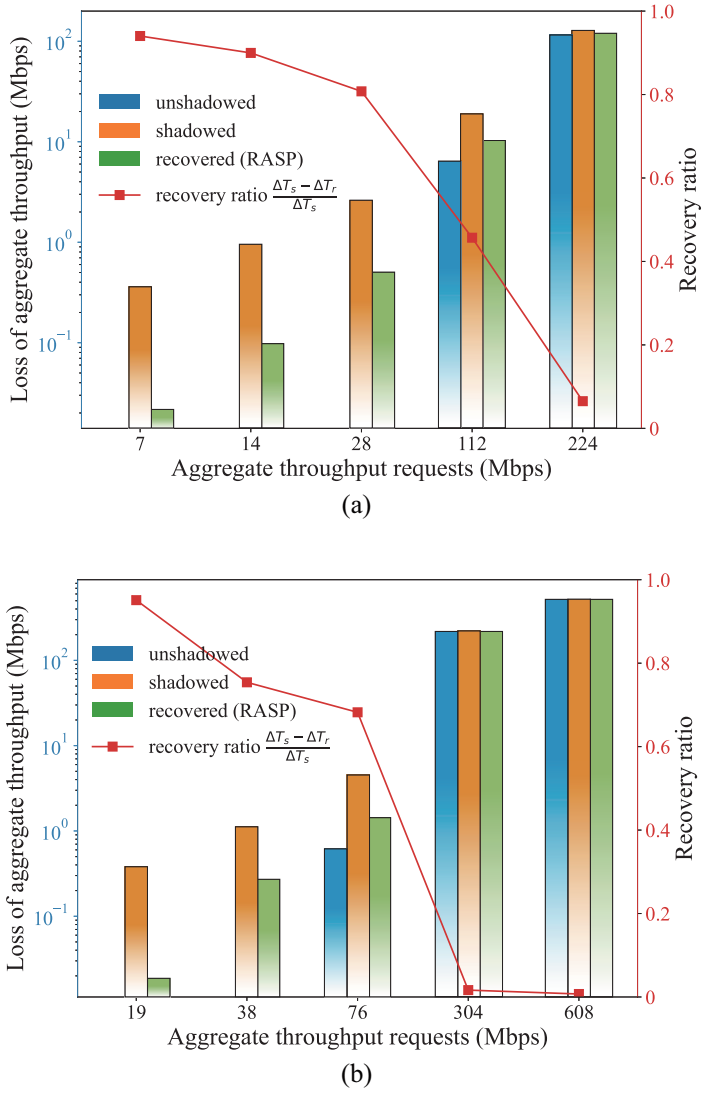

Figure 4.5: Performance of RASP scheme of (a) one-tier network and (b) two-tier network; left axis shows loss of aggregate throughput of unshadowed, shadowed and recovered networks; right axis shows the percentage of throughput loss recovered by RASP

must take into account weight matrices to ensure optimum performance. We consider an extreme case where each cell has a UE located in the cell center which continuously requires a fixed amount of data. The requested data rate of each UE is chosen from a set {1, 2, 4, 16, 32} Mbps/UE, which corresponds to aggregate throughput requests of {7, 14, 28, 112, 224} Mbps. Network related parameters are set as following: cell radius is $2\,\mathrm{m}$; heights of BSs and UEs are $3\,\mathrm{m}$ and $1\,\mathrm{m}$, respectively. Other simulation parameters are shown in table 4.1. In each simulation, one random signal link is shadowed and the loss of aggregate throughput ΔT before shadowing, after shadowing, and recovered from shadowing is calculated. When the network is not congested, there is no loss of aggregate throughput ΔT before shadowing. However, ΔT before shadowing increases when aggregate throughput requests exceed network capacity. The throughput loss ΔT represents the amount of traffic that cannot be provided by the network compared with aggregate throughput requests and is calculated by

$$\Delta T = \sum_{c \in \mathbf{C}} T(c) - \sum_{c \in \mathbf{C}} \hat{T}(c) \tag{4.4}$$

where $T(c)$ is the requested data rate of commodity c and $\hat{T}(c)$ is the actual end-to-end data rate of c. The actual end-to-end data rate $\hat{T}(c)$ is calculated by

$$\hat{T}(c) = \sum_{i=0}^{N_c - 1} \min(a^{c(i)} T(c), \min_{\forall l \in \{l : r_l^{c(i)} = 1, \forall l \in \mathbf{L}\}} T_l(c(i))) \tag{4.5}$$

where $T_l(c(i))$ is the portion of the capacity of link l available for the i-th route of commodity c and $T(c)$ is the requested throughput of commodity c. The capacity portion $T_l(c(i))$ is calculated based on the requested load:

$$T_l(c(i)) = \frac{r_l^{c(i)} a^{c(i)} T(c)}{\sum_{\forall \mu \in \mathbf{C}} \sum_{j=0}^{N_\mu - 1} r_l^{\mu(j)} a^{\mu(j)} T(\mu)} T_l \tag{4.6}$$

where C_l is the capacity of link l. Link capacity can be calculated using Shannon's theorem $T_l = \sum_{k=1}^{K_{sc}} W_k \log_2(1 + \gamma_k^l)$, where $W_k = W/K_{sc}$ is the bandwidth of each subcarrier, and $\gamma_k^l = \frac{w_k^l p_k^l |G_k^l|^2}{\sigma_k^2 + I_k^l}$ is the signal-to-interference-plus-noise ratio (SINR) on the k-th subcarrier, G_k^l is the channel gain of the k-th subcarrier of link l, $\sigma_k^2 = N_0 W/K_{sc}$ is the noise power on the k-th subcarrier and N_0 is the power spectral density of the additive white Gaussian noise. I_k^l is the total interference power on the k-th subcarrier of link l, which is the sum of power received by the end node of l, i.e. $I_k^l = \sum_{m \in \{m : e(m) != e(l), \forall m \in \mathbf{L}\}} w_k^m p_k^m |G_k^m|^2$. The SINR calculation is taking into account the bit-error-rate requirement $BER = 10^{-6}$. The channel gain $|G_k^l|$ of LOS links and mirror-aided non-LOS links is calculated based on the method in section 4.2.2. To highlight the recovery performance of

Parameter	Symbol	Value
Number of subcarriers	N	1024
Bandwidth	B	$20\,\mathrm{MHz}$
Noise PSD	N_0	$1 \times 10^{-21}\ \mathrm{A}^2/\mathrm{Hz}$
PD detecting area	A_r	$1\,\mathrm{cm}^2$
PD responsitivity	R_{PD}	$0.5\,\mathrm{A/W}$
Reflectivity of mirrors	ρ_m	0.9

Table 4.1: Simulation parameters

RASP, the recovery ratio is calculated. The recovery ratio is the percentage of recovered throughput loss to the throughput loss caused by shadowing. Recovery ratio is calculated by $(\Delta T_s - \Delta T_r)/\Delta T_s$, where ΔT_s and ΔT_r represent throughput loss of shadowed and recovered networks, respectively. Average results are taken by 200 simulations and shown in Fig.4.5. It can be seen that for both one-tier and two-tier networks, more than 90% of throughput loss can be recovered when the aggregate requested data rate is 7 Mbps. The recovery performance degrades when the aggregate throughput requests increase. This is likely due to the fact that the aggregate throughput requests almost exceed network capacity. Due to the limited modulation bandwidth of LEDs, the data rate of the central gateway is limited. As all downlink data is distributed from the central gateway, traffic congestion occurs at the gateway. If aggregate throughput requests, i.e. sum data rates requested by users, exceed the data rate that the gateway can provide, optimization cannot further improve the network performance.

4.4 Optimization Methods And Simulations

The purpose of the RASP method is to find the optimal or near-optimal combination of control policies when shadowing occurs. An optimization algorithm is required to explore combinations of control policies. In this section, we introduce neighbor-searching optimization methods and compare their performance in mesh-type optical attocell networks. For simplicity, we assume that there is no internal data traffic, i.e. UEs in the network only require data from the Internet via the gateway.

4.4.1 Neighbor-Searching Algorithms

It can be seen from 4.3.1 that each data commodity c has independent control vectors ($\vec{r}^c$ and $\vec{a}^c$) and each link l has an independent control vector ($\vec{p}^l$). Although the control vector $\vec{w}^l$ for links of one BS is not independent due to the constraint Eq.(4.2), a set of $\vec{w}^l, \forall l \in \{l : s(l) = b_i\}, b_i \in \mathbf{B}$ is independent of another set of

$\vec{w}^l, \forall l \in \{l : s(l) = b_j\}, b_j \in \mathbf{B}, b_i \neq b_j$ as every BS reuses the whole spectrum. Thus, independent control policies can be applied to different data commodities c and links l. Let $C = |\mathbf{C}|$, $L = |\mathbf{L}|$, $B = |\mathbf{B}|$ be numbers of data commodities, links, and BSs, respectively. In addition, let N_{R}, N_{A}, N_{S}, and N_{P} be numbers of options of R, A, S, P control policies, respectively. Based on the previous section, values of $N_{\mathrm{R}} = N_{\mathrm{A}} = N_{\mathrm{S}} = N_{\mathrm{P}} = 2$ in our simulations. The number of all possible combinations of control policies is $N_{\mathrm{R}}^C N_{\mathrm{A}}^C N_{\mathrm{S}}^B N_{\mathrm{P}}^L = 2^{2C+B+L}$.

In 4.3.3, the method used to find the optimal (near-optimal) performance metric is a simple partial enumeration (PE) method. All data commodities were assumed to apply the same routing and load assignment policies and all links were assumed to apply the same subcarrier allocation and power allocation policies. A limited number of possible combinations of control policies, i.e. $N_{\mathrm{R}} N_{\mathrm{A}} N_{\mathrm{S}} N_{\mathrm{P}}$ combinations, were enumerated. Enumerating all possible combinations where independent control policies are applied to different data commodities and links requires a brute-force method. However, the number of combinations with independent control policies is large even for a small size network, for example, a one-tier ring-type network (a network with central gateway and six one-tier BSs as shown in Fig.4.2) has 2^{16} combinations if there is only one data commodity in the network and this number increases exponentially with the number of data commodities. It is necessary to use an efficient optimization algorithm to find the optimal/near-optimal solution in such a large solution space. We can notice from 4.3.2 that every option is denoted by an integer number. In order to distinguish different control policies, the abbreviation of the control policy where an option belongs to is added to the notation of the option as a prefix. For example, shortest-path routing is denoted as R1 and weighted-fair load assignment is denoted as A2. One combination, which is also called one solution, is a set of $2C + B + L$ options with the form $\{\mathrm{R}j_0, \mathrm{R}j_1, ..., \mathrm{R}j_{C-1}, \mathrm{A}j_C, ..., \mathrm{A}j_{2C-1}, \mathrm{S}j_{2C}, ..., \mathrm{S}j_{2C+B-1}, \mathrm{P}j_{2C+B}, ..., \mathrm{P}j_{2C+B+L-1}\}$. Here, j_i denotes the integer number of the option chosen for i-th element in the set. Neighbors of a solution are solutions with only one difference of the option in the set. To find the optimal/near-optimal solution from the solution space, neighbor-searching algorithms like hill-climbing (HC) and Tabu-search (TS) can be used. HC is an iterative algorithm which begins with a given or an arbitrary solution and finds the best solution amongst its neighborhood (or a subset of its neighbors). The best solution amongst neighbors will be the initial solution of the next iteration. The searching process will keep going until no further improvement can be found. This is also called steepest-ascent HC, as the algorithm always moves in the direction with the largest gradient. Assuming $\mathbf{S}$ is the set of all solutions, $\mathbf{N}(s)$ is the neighbor-set of a solution s, and $f(\cdot)$ is the cost function. The cost function in our simulation is Eq.(4.4) which is used to calculate the throughput loss of the current solution. The pseudo-code of using steepest-ascent HC to solve a minimization problem is shown in Algorithm 2. The

maximization problem can also apply this algorithm by multiplying the objective function by -1. The initial solution is randomly chosen from the solution space. The stop condition can be defined as exceeding a limited number of iterations or meeting the goal of the cost.

It can be seen that HC may get stuck in local optima as the algorithm breaks if none of the neighbors is better than the current best solution. TS can be used to overcome this problem by relaxing the searching rules. In each iteration, a solution with a cost worse than the current best solution can be accepted in order to overcome local optima. Sometimes solutions with costs equal to the best solutions may be found in consecutive iterations and the algorithm may get stuck in a plateau region. To avoid getting stuck in the plateau region, a partial reset strategy is used to force the algorithm to search new regions. With the partial reset strategy, a new solution s' is chosen from the reset set of the solution found by the current iteration, which is denoted by $\mathbf{R}(s)$ where s denotes the solution. Solutions in the reset set $\mathbf{R}(s)$ have one different option than the current solution s from each of the control policies R, A, S, and P. In addition, a tabu-list is introduced to avoid going back to explored solutions. The tabu-list is a short-term memory set of moves made in recent iterations. When the size of tabu-list exceeds a value N_{tabu}, the oldest move will be popped. Generally, moves in the tabu-list are not allowed to make until they are removed from the list. An aspiration rule allows making a move in the tabu-list if the cost of the new solution is better than that of the current best solution. The algorithm of a basic TS is shown in Algorithm 3, where TL denotes tabu-list and $move(s, n)$ denotes the move from solution s to solution n.

4.4.2 Comparison of Optimization Methods

The performance of different optimization methods is compared by simulations. Similar as 4.3.3, each cell has a UE located in the cell center which requires a fixed amount of data. Three different data requests are compared: light data request with 4 Mbps/UE, moderate data request with 16 Mbps/UE, and heavy data request with 32 Mbps/UE. UEs are numbered with the cell number, i.e. UE_1 is located in the cell center of cell 1 and originally assigned to BS_1. In this simulation access link in cell 0, i.e. the link from BS_0 to UE_0, is shadowed. The performance of the network is assessed by loss of throughput ΔT. Equation 4.4 is used as cost function in the simulation.

Fig.4.6 shows the comparison of throughput loss ΔT when using different optimization algorithms. Stop conditions of HC and TS are exceeding 20 iterations or found of zero throughput loss ΔT. Length of tabu-list is one-fourth of the maximum iteration, i.e., 5. The number in the bracket indicates the maximum number of neighbors that the optimization method can search, i.e. HC(1) means that $|N(s)| = 1$ and only one neighbor can be visited in one iteration and HC(all)

1: INITIALIZE random $s \in \mathbf{S}$, $best = s$, $best\_cost = f(s)$
2: **while** not $stop\_condition$ **do**
3: $best\_cost\_in\_neighbor = \infty$
4: **for** $n \in \mathbf{N}(s)$ **do**
5: **if** $f(n) < best\_cost\_in\_neighbor$ **then**
6: $best\_cost\_in\_neighbor = f(n)$
7: $best\_in\_neighbor = n$
8: **end if**
9: **end for**
10: **if** $best\_cost\_in\_neighbor < best\_cost$ **then**
11: $s = best\_in\_neighbor$
12: $best = best\_in\_neighbor$
13: $best\_cost = best\_cost\_in\_neighbor$
14: **else**
15: break
16: **end if**
17: **end while**
18: Return $best$ and $best\_cost$

algorithm 2: Steepest-Ascent HC

means that all neighbors can be visited. It can be seen that the neighbor size of the algorithm has a significant impact on the performance. When the size of the neighbor set is large, the optimization algorithm has a larger probability to find the best solution in neighbors. Table 4.2 shows the maximum number of solutions that have been visited in the simulation. Although TS can achieve better performance than PE when searching all neighbors, the maximum number of visited solutions of TS is about 30 times that of PE. Assuming that the time for visiting one solution is the same for all algorithms, which is about 80 ms in our simulations, it is obvious that a large number of visited solutions indicates a longer searching time. Differences between results of PE, TS with all neighbors, and HC with all neighbors are highlighted. It is shown that TS with a large neighbor size outperforms other optimization methods. This is likely due to the fact that TS has a larger solution space than PE and uses relaxing rules to avoid stuck in local optima. In addition, TS has the ability to overcome the plateau effect. An example of solutions found by each iteration of TS and HC is shown in Fig.4.7. It can be seen that HC stops at the beginning of the plateau region as no improvement is found. TS with a partial reset strategy is able to search new regions even if the new solution is worse than the current best solution. Thus, TS has the potential to find a better solution than HC at the cost of a longer searching time. It is also noticed that moderate and heavy data requests (aggregate throughput of 112 Mbps and 224 Mbps) may exceed the network capacity in the shadowing scenario. Throughput losses in

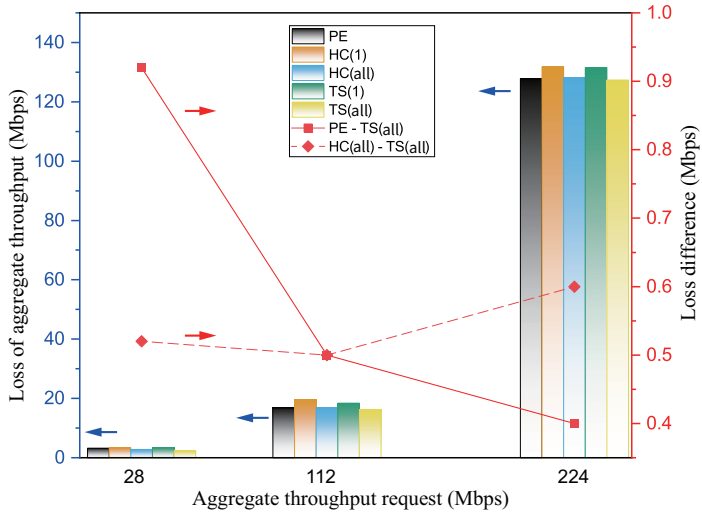

Figure 4.6: Loss of aggregate throughput versus aggregate throughput of one-tier optical attocell networks; PE−TS(all) and HC(all)−TS(all) denote the difference of ΔT of PE and TS(all) and that of HC(all) and TS(all), respectively; maximum iteration is 20

```
1: INITIALIZE random s ∈ S, best = s, best_cost = f(s), TL = ∅
2: while not stop_condition do
3:     best_cost_in_neighbor = ∞
4:     for n ∈ N(s) do
5:         if move(s, n) ∈ TL then
6:             if f(n) < best_cost then                          ▷ aspiration rule
7:                 best_cost = f(n)
8:                 best = n
9:                 if f(n) < best_cost_in_neighbor then
10:                    best_cost_in_neighbor = f(n)
11:                    best_in_neighbor = n
12:                end if
13:            end if
14:        else
15:            if f(n) < best_cost_in_neighbor then
16:                best_cost_in_neighbor = f(n)
17:                best_in_neighbor = n
18:            end if
19:        end if
20:    end for
21:    move(s, best_in_neighbor) → TL
22:    s = best_in_neighbor
23:    if s < best_cost then
24:        best = s
25:        best_cost = best_cost_in_neighbor
26:    else if s = best_cost then                                ▷ plateau
27:        choose random s′ ∈ R(s)                               ▷ partial reset
28:        s = s′
29:    end if
30:    if len(TL) > N_tabu then
31:        pop TL
32:    end if
33: end while
34: Return best and best_cost
```

algorithm 3: Basic TS

PE	HC(1)	HC(all)	TS(1)	TS(all)
16	2	126	20	467

Table 4.2: Maximum number of visited solutions

the moderate request scenario and heavy request scenario are larger than 20 Mbps and 120 Mbps, respectively. Thus, only light data requests (lower than aggregate throughput of 28 Mbps) are considered in later simulations.

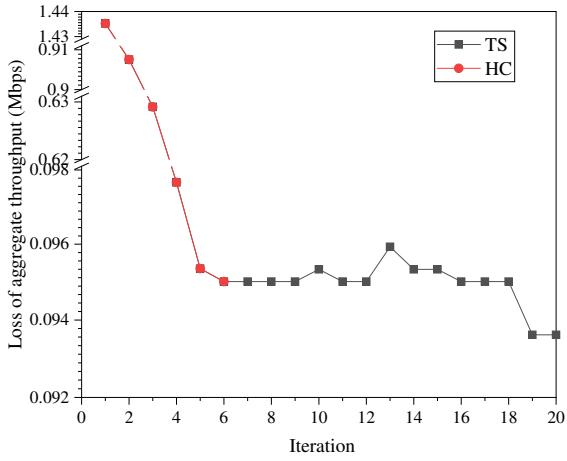

Figure 4.7: Solutions found by each iteration with HC and TS in a one-tier network with data request with 1.8 Mbps/UE, maximum iteration is 20

4.4.3 An Improved TS Algorithm

From previous simulation results, we know that neighbor size has a large impact on performance. However, a large neighbor size leads to a longer searching time. We notice that each solution can be represented with the form $\{\{\mathrm{R}j_0, \mathrm{R}j_1, ..., \mathrm{R}j_{C-1}\}, \{\mathrm{A}j_C, ..., \mathrm{A}j_{2C-1}\}, \{\mathrm{S}j_{2C}, ..., \mathrm{S}j_{2C+B-1}\}, \{\mathrm{P}j_{2C+B}, ..., \mathrm{P}j_{2C+B+L-1}\}\}$, which is a set composed by four subsets representing options of R, A, S, and P control policies, respectively. Therefore, the TS algorithm can be further improved by decomposing neighbors into four subsets according to RASP control policies. Each neighbor-subset consists of solutions having different options in one of the four subsets. For instance, solutions in neighbor-subset $\mathbf{N}_R(s)$ have same options $\{\{\mathrm{A}j_C, ..., \mathrm{A}j_{2C-1}\}, \{\mathrm{S}j_{2C}, ..., \mathrm{S}j_{2C+B-1}\}, \{\mathrm{P}j_{2C+B}, ..., \mathrm{P}j_{2C+B+L-1}\}\}$ as s and one different option in $\{\{\mathrm{R}j_0, \mathrm{R}j_1, ..., \mathrm{R}j_{C-1}\}\}$. In each iteration, a random

solution from each subset is chosen and evaluated. The subset of the solution having the best cost is considered as the subset with a higher potential to achieve the best performance. Therefore, this subset is chosen as the neighbor set to be visited in the current iteration. This improved TS algorithm adds a process (described in Algorithm 4) to find the neighbor set $\hat{\mathbf{N}}$ and this set $\hat{\mathbf{N}}$ replaces $\mathbf{N}$ in line 4 of Algorithm 3. In addition, the reset set $\mathbf{R}(s)$ does not include $\hat{\mathbf{N}}$ such that the algorithm is able to search other neighbor-subsets if plateau occurs. This decomposition method avoids moving to subsets whose solutions are less attractive. The number of visited solutions will be significantly reduced as only solutions in one subset are visited in each iteration.

```
1: ...
2: while not stop_condition do                          ▷ line 2 in Algorithm 3
3:     best_sub = None
4:     best_cost_in_sub = ∞
5:     for N_sub(s) in {N_R(s), N_A(s), N_S(s), N_P(s)} do
6:         random n_sub ∈ N_sub(s)
7:         if f(n_sub) < best_cost_in_sub then
8:             best_sub = N_sub(s)
9:             best_cost_in_sub = f(n_sub)
10:        end if
11:    end for
12:    N̂(s) = best_sub
13:    best_cost_in_neighbor = ∞                        ▷ line 3 in Algorithm 3
14:    for n ∈ N̂(s) do
15:    ...
16: end while
```

algorithm 4: Finding neighbor set for improved TS (TS-decomposition)

In order to compare the performance of basic TS and the improved TS which is called TS-decomposition, we simulate one-tier and two-tier optical attocell networks with one random shadowed link and calculate the cumulative distribution function (CDF) of the loss of aggregate throughput ΔT. Results are shown in Fig.4.8. Light requested data rate is assumed, i.e. 4 Mbps/UE. From Fig.4.8(a) we can see that the difference of CDF between two TS algorithms and PE is small. Two TS algorithms do not get throughput loss larger than 3 Mbps. TS-decomposition achieves better performance than TS with less number of visited solutions, i.e. less searching time. Comparing the performance of two-tier networks as shown in Fig.4.8(b), it can be seen that two TS algorithms can achieve much better performance than PE. TS is more time-consuming than TS-decomposition and the performance of TS is worse than that of TS-decomposition. Although TS-decomposition requires a longer searching time than PE, it has a larger probability

(about 50%) to get zero throughput loss. It can be seen that TS-decomposition has a better trade-off between performance and searching time.

4.5 Conclusion

The performance of optical attocell networks degrades due to random shadowing caused by pedestrians. A cross-layer resilience scheme RASP is proposed to address the shadowing effect in optical attocell networks. Simulation results show that RASP can achieve more than 90% recovery ratio in networks with light data requests. Three optimization algorithms, PE, HC, and TS, used for the RASP scheme are investigated and compared. TS achieves the best performance at the expense of a large number of solutions to search. In order to reduce the searching time, we proposed to improve TS by decomposing neighbors into four subsets according to RASP. Simulation results show that the TS-decomposition algorithm achieves better performance than both PE and TS. TS-decomposition has a better trade-off between performance and searching time as the number of visited solutions of TS is significantly reduced by decomposing neighbors.

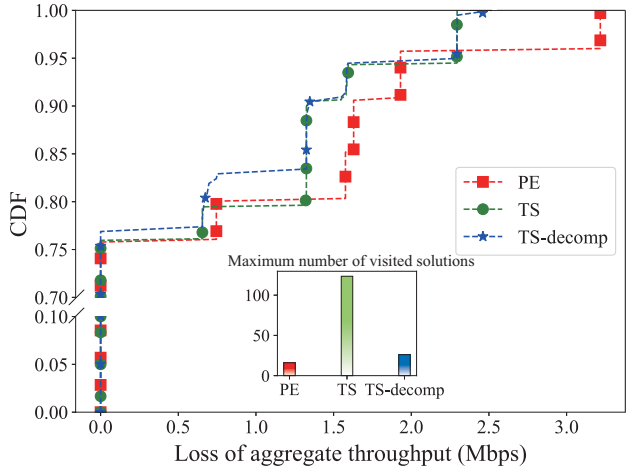

(a)

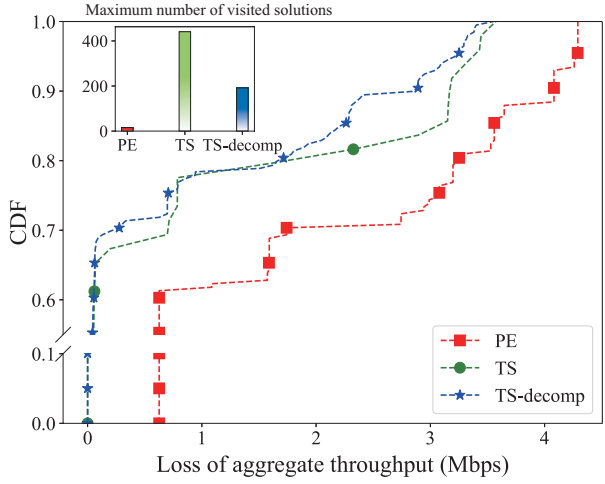

(b)

Figure 4.8: CDF of loss of aggregate throughput in (a) one-tier networks and (b) two-tier networks with one random shadowed link; each cell has one central UE continuously requesting data rates of 4 Mbps; maximum number of visited solutions are shown in insets

References

[1] Toshihiko Komine and Masao Nakagawa. *Integrated System of White LED Visible Light Communication and Power Line Communication*. IEEE Transactions on Consumer Electronics, 49(1):71–79, 2003.

[2] Yiguang Wang, Nan Chi, Yuanquan Wang, Li Tao, and Jianyang Shi. *Network Architecture of a High-Speed Visible Light Communication Local Area Network*. IEEE Photonics Technology Letters, 27(2):197–200, 2015.

[3] Dilukshan Karunatilaka, Fahad Zafar, Vineetha Kalavally, and Rajendran Parthiban. *LED Based Indoor Visible Light Communications: State of the Art*. IEEE Communications Surveys & Tutorials, 17(3):1649–1678, 2015.

[4] Yuhui Wu, Pieter Audenaert, Mario Pickavet, and Didier Colle. *Mirror-aided non-LOS VLC channel characterizations with a time-efficient simulation model*. Photonic Network Communications, 38(38):151–166, 2019.

[5] Hossein Kazemi, Majid Safari, and Harald Haas. *A Wireless Optical Backhaul Solution for Optical Attocell Networks*. IEEE Transactions on Wireless Communications, 2019.

[6] Yuhui Wu, Mario Pickavet, and Didier Colle. *Analysis of the Impact of Misaligned Wireless Backhaul Links on Optical Attocell Networks*. In International Conference on Transparent Optical Networks, 2020.

[7] J.M. Kahn and J.R. Barry. *Wireless Infrared Communications*. Proceedings of the IEEE, 85(2):265–298, 1997.

[8] F R Gfeller and U Bapst. *Wireless in-House Data Communication Via Diffuse Infrared Radiation*. Proceedings of the IEEE, 67(11):1474–1486, 1979.

[9] Svetla Jivkova, B A Hristov, Mohsen Kavehrad, and Abstract In. *Power-Efficient Multispot-Diffuse to Broad-Band Optical Wireless Communications*. IEEE Transactions on Vehicular Technology, 53(3):882–889, 2004.

[10] Toshihiko Komine, Jun Hwan Lee, Shinichiro Haruyama, and Masao Nakagawa. *Adaptive equalization system for visible light wireless communication*

utilizing multiple white led lighting equipment. IEEE Transactions on Wireless Communications, 8(6):2892–2900, 2009.

[11] Yuhui Wu, Mario Pickavet, and Didier Colle. *A Cross-Layer Heuristic Algorithm for Addressing Shadowing Problem in Optical Attocell Networks*. In International Conference on the Design of Reliable Communication Networks (DRCN), 2020.

[12] J.P. Vasseur, Mario Pickavet, and P. Demeester. *Network Recovery*. Elsevier Inc., San Francisco, 1 edition, 2004.

[13] Radiation Safety Office. *Laser Safety Mannual*. 2007.

[14] J. Armstrong and B. J C Schmidt. *Comparison of asymmetrically clipped optical OFDM and DC-biased optical OFDM in AWGN*. IEEE Communications Letters, 12(5):343–345, 2008.

[15] European Committee for Standardization. *Light and lighting - Lighting of work places - Part 1 : Indoor work*. 2002.

[16] Jae Yong Suk. *Luminance and vertical eye illuminance thresholds for occupants' visual comfort in daylit office environments*. Building and Environment, 148:107–115, 2019.

[17] Hongming Yang and Ashish Pandharipande. *Full-duplex relay VLC in LED lighting linear system topology*. In Industrial Electronics Conference, pages 6075–6080. IEEE, 2013.

[18] Omer Narmanlioglu, Refik Caglar Kizilirmak, Farshad Miramirkhani, and Murat Uysal. *Cooperative visible light communications with full-duplex relaying*. IEEE Photonics Journal, 9(3):1–11, 2017.

[19] Dilukshan Karunatilaka, Vineetha Kalavally, and R. Parthiban. *Improving Lighting Quality and Capacity of OFDM-Based WDM-VLC Systems*. IEEE Photonics Technology Letters, 28(20):2149–2152, 2016.

[20] Antonia Maria Masucci, Elena Veronica Belmega, and Inbar Fijalkow. *Optimal blockwise subcarrier allocation policies in single-carrier FDMA uplink systems*. Eurasip Journal on Advances in Signal Processing, 2014(1):1–17, 2014.

[21] Yuan Fang, Li Tao, and Nan Chi. *Interleaved subcarrier allocation for DFT-spread OFDM to reduce PAPR*. Technical Digest - 2012 17th Opto-Electronics and Communications Conference, OECC 2012, (July):341–342, 2012.

[22] Andreas F.Molish. *Wireless Communications*. 2 edition, 2011.

5

Misalignment Effect of Wireless Backhaul Links on Downlink Transmission in Optical Attocell Networks

Another major problem of the optical attocell networks is the misalignment effect. The performance of the network is degraded when the directional mirror-aided non-LOS links are misaligned. In Appendix A we present the analysis of the impact caused by misaligned backhaul links. In this chapter, we present two methods to mitigate the misalignment effect: a redundant transmission strategy and an adaptive strategy.

* * *

Y. Wu, M. Pickavet, D. Colle

Submitted to Journal of Optical Communications and Networking (JOCN), May 2021.

Abstract *Optical attocell networks are based on visible light communication (VLC). Light-emitting-diodes (LEDs) lamps are used for both illumination and communication. Communication links between LED base stations (BSs) form a backhaul network. VLC-based backhaul links using auxiliary transceivers have*

been proposed. Due to the requirement of direct line-of-sight (LOS) and the first-bounce specular reflection of mirror-aided non-LOS, perfect alignment of auxiliary transceivers is important for VLC-based backhaul links. However, perfect alignment may not be guaranteed due to the limitation of the layout of BSs or installation mistakes. Network performance degrades due to the misalignment effect. In this article, we investigate the impact of misalignment and a method for detecting misalignment. A redundant transmission strategy and an adaptive strategy are proposed to mitigate the misalignment effect.

5.1 Introduction

Optical attocell networks based on visible light communication (VLC) have drawn scientific interest in the last few years. In optical attocell networks, LED lamps are base stations (BSs) which illuminate and transmit data simultaneously. User equipment (UE) receive downlink information from BSs using photodiodes (PDs). Transmission of uplink data from UEs to BSs is normally done by using infrared (IR) as UEs are not used for illumination purposes [2]. Communication links between UEs and BSs are called access links. Access links form an access network. Data transmitted in the access network is received from or forwarded to the Internet via a backhaul network. The backhaul network consists of backhaul links between BSs. A gateway, which can be one of the VLC BSs or an extra VLC device, connects the optical attocell network to the Internet. Normally, the gateway is wired connected to the Internet. Backhaul links between BSs can be wired or wireless. Many backhaul solutions for communication between BSs have been proposed. Wired backhaul technologies, such as power-line communication (PLC) and power-over-Ethernet (PoE), have been proposed as a backhaul solution. However, wired backhaul solutions require installing additional control devices like modems or replacing current power cables. The cost for installation and maintenance could be extremely high. In addition, PLC is vulnerable to radio-frequency (RF) interference and disturbance on power lines [1]. Wireless backhaul solutions based on VLC links have been proposed in [4, 5]. VLC backhaul links are viable solutions for backhaul transmission as optical attocell networks have already used VLC for access data transmission. A central controller can be used to configure and control all VLC links in the network. Fig.5.1 illustrates two VLC backhaul link configurations. Both link configurations use auxiliary LEDs and PDs for backhaul transmission. A pair of auxiliary LED and PD oriented towards the same direction is called an auxiliary transceiver. The number of auxiliary transceivers depends on the shape of the VLC attocells. Six auxiliary transceivers are used in one BS for communication in a network with hexagonal cells. VLC backhaul links using line-of-sight (LOS) configuration shown in Fig.5.1(a) can achieve good performance when perfectly aligned. LOS configuration benefits by high LOS channel

gain of concentrated LED transmitters. However, strict LOS condition is required by this configuration. Compared with LOS configuration, mirror-aided non-LOS link configuration shown in Fig.5.1(b) takes advantage of the first-bounce specular reflection from glossy floor tiles or small mirrors placed on the floor. Mirror-aided non-LOS configuration is a flexible link configuration which doesn't require the strict LOS condition between backhaul transceivers. This makes mirror-aided non-LOS configuration suitable for specific indoor applications where the LOS condition between BSs is not possible.

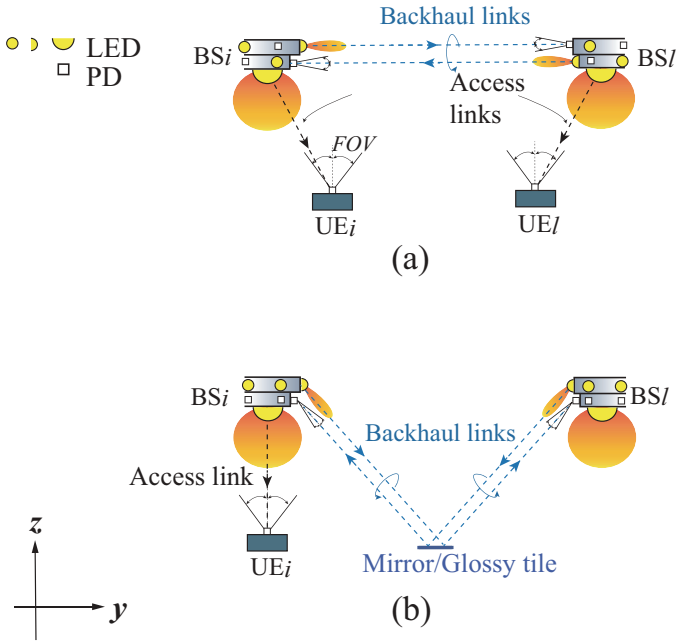

Figure 5.1: VLC backhaul link using (a) LOS link configuration; (b) mirror-aided non-LOS link configuration

VLC communication links use intensity modulation and direct detection (IM/DD) as it is simple and cost-efficient. By using the IM modulation scheme, signals are represented by high-frequency fluctuations in radiant intensity. PDs detect light intensity and convert the optical power to the electrical signal. As the amplitude of the electrical signal is represented by the instant optical intensity transmitted by LEDs, the electrical bandwidth available for a VLC link is limited by the modulation bandwidth of LEDs. By using different frequency reused schemes, multiple auxiliary LEDs can share the electrical bandwidth. In order to avoid interference, auxiliary LEDs have a very concentrated transmission pattern and auxiliary PDs normally use small field-of-view (FOV) [11]. If perfect alignment can not be guaranteed due to the limitation of the layout of BSs or installation mistakes,

the performance of misaligned backhaul links is degraded. The signal-to-noise ratio (SNR) of misaligned backhaul links rapidly decreases due to the decreasing signal power. In the meanwhile, the power received from interfering sources increases. In networks using mirror-aided non-LOS backhaul configuration, the impact of interfering sources is larger than that of noises [10]. The impact caused by interfering sources can be reduced by using frequency reuse schemes. Thus, we investigate mitigation schemes for the misalignment effect in networks with misaligned mirror-aided non-LOS backhaul links. A redundant transmission scheme is proposed to improve the performance of networks with a misaligned gateway. When all BSs in the network have random misaligned angles, an adaptive strategy is proposed. Simulations of random misaligned networks have been conducted to investigate the performance of the adaptive strategy.

5.2 Optical Attocell Networks

Optical attocell networks use VLC for access data transmission. Each LED lamp is a BS which covers an attocell with a radius ranging from one to several meters. UEs communicate with the nearest BS via access links. Access downlinks from BSs to UEs are based on VLC as data can be carried by visible light emitted from LED lamps. As UEs like laptops and smartphones are not used for illumination, IR is normally used for access uplink transmission. VLC is also used for backhaul transmission. Mirror-aided non-LOS backhaul links have the potential to support high-speed backhaul data transmission.

5.2.1 Cellular network

A two-tier ring type optical attocell network is shown in Fig.5.2(a). In this two-tier network, the central BS which is denoted as BS_0 is the gateway. With this ring-type network, we can easily categorize BSs into tier-1 BSs and tier-2 BSs. A set of tier-1 BSs is denoted as $\mathcal{T}_1$ and consists of neighboring BSs of the gateway, i.e. $\mathcal{T}_1 = \{\text{BS}_i, i \in [1,6]\}$. Tier-2 BSs $\mathcal{T}_2 = \{\text{BS}_i, i \in [7,18]\}$ are at least two hops away from the gateway. We assume an empty room with mirrors on the floor. Mirrors are placed on reflecting points, which are center points of edges of each hexagon as shown in the figure. The size of a mirror can be very small as long as the reflecting point is covered. In real applications, the number of UEs in each cell and the requested rate by each UE are both random. Each BS allocates part of its available electrical bandwidth for access downlink transmission to UEs in its cell. UEs share the whole access bandwidth and the data rates depend on the signal-to-noise-plus-interference ratio (SINR) γ of the access links and the allocated bandwidth B according to Shannon's theorem $C = B\log_2(1+\gamma)$. The sum of data rates of these UEs achieves the maximum value when all UEs are

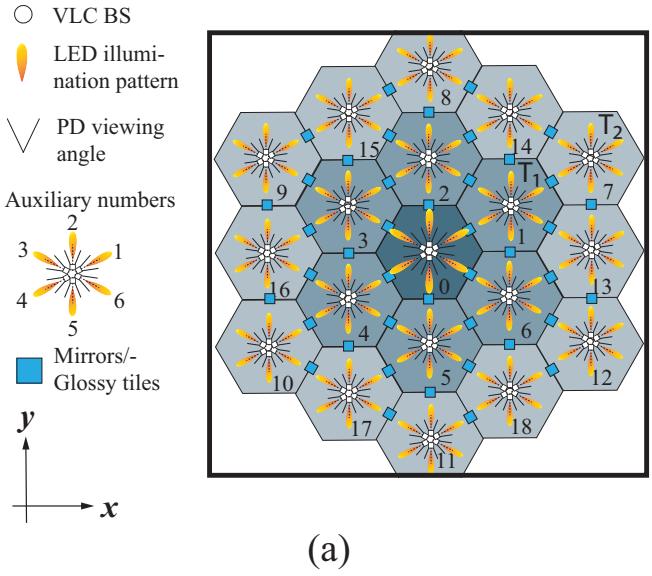

Figure 5.2: (a)Horizontal view of a two-tier cellular network; (b)Fixed shortest-path routing

located at a point with the maximum SINR, where is the center of the cell. It is clear that the maximum sum rate is equal to the achievable data rate of a single UE located at the cell center. Thus, we assume that there is only one UE located in the center of each cell. The end-to-end data rate for each UE is calculated. A simple fixed shortest-path routing is considered in our simulations. Assuming that there are no link failures, a routing scheme chooses the shortest path for packets sent from the gateway. Tier-1 BSs receive downlink data directly from the gateway and forward them to two neighboring tier-2 BSs. Decode-and-forward (DF) method is used in each relaying BS. Fig.5.2(b) illustrates the routing scheme. It can be seen that traffic flow is divided into several equal-length branches. This routing scheme ensures that each branch carries the same amount of traffic.

5.2.2 Illumination requirements

As the primary purpose of LED lamps is to provide uniform indoor illumination, it is necessary to investigate the transmitted power of LEDs under illumination requirements. Wide-beam LEDs with semi-angle of $\Phi = 60^\circ$ are normally used for indoor lighting. These wide-beam LEDs are oriented downwards and used for illumination and access downlink transmission. In aligned scenarios, auxiliary LEDs are oriented towards mirrors on the floor. These auxiliary LEDs are used for backhaul transmission. Narrow-beam LEDs are used to maximize transmission power and avoid interference. As the light beam emitted by auxiliary LEDs is more concentrated, eye-safety issues should be considered. Transmitted power of downward-oriented LEDs and auxiliary LEDs taking into account illumination and eye-safety requirements have been discussed in [11]. We configure the transmitted power such that the average indoor illuminance is under $750\,\mathrm{lx}$ which is the maximum value required for activities in offices [8]. Assuming that human eyes are at a height of $1.5\,\mathrm{m}$. Direct and reflected light from narrow-beam auxiliary LEDs may cause visual discomfort. The threshold for vertical illuminance has been examined by many experiments. The value ranges from $875\,\mathrm{lx}$ to $3000\,\mathrm{lx}$ [9]. In this work, the transmitted power of auxiliary LEDs is limited such that the maximum vertical illuminance measured at human eyes is under $2000\,\mathrm{lx}$.

5.2.3 Resource allocation

Mirror-aided non-LOS link configuration utilizes the first-bounce specular reflection from auxiliary LEDs to PDs. Every BS uses six auxiliary transceivers for bidirectional backhaul transmission. Full-duplex backhaul transmission is assumed, i.e. auxiliary transmitters and receivers of the same BS can work at the same time. Self-interference can be canceled using electrical or optical techniques and thus can be neglected [7].

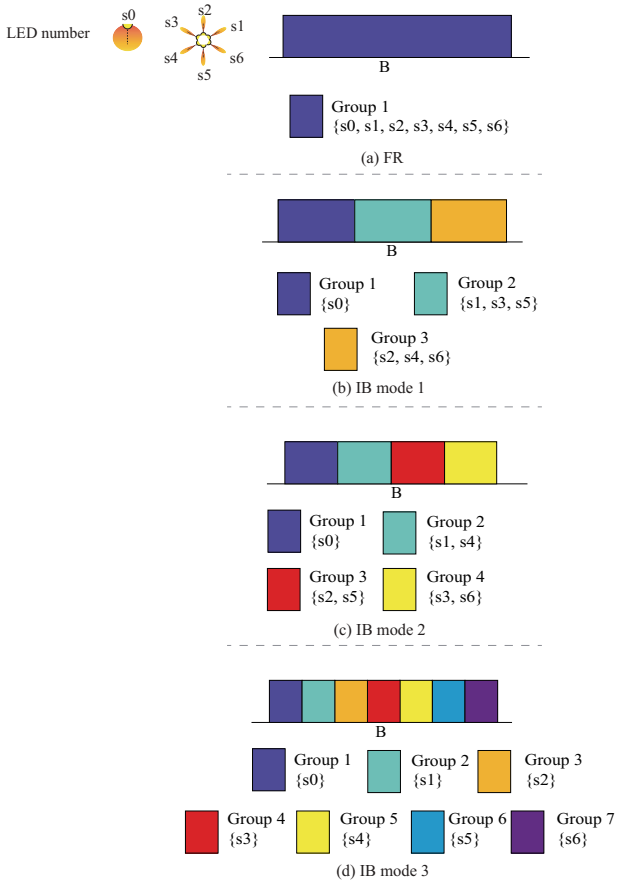

Figure 5.3: Illustration of bandwidth allocation of frequency reuse scheme (a) FR; (b) IB mode 1; (c) IB mode 2; (d) IB mode 3; B is the electrical bandwidth available for one BS

As IM/DD is used for VLC links, limited electrical bandwidth is available. We assume that every BS is able to use the whole electrical bandwidth. The bandwidth used by each LED transmitter of one BS depends on multiplexing and multiple access schemes. IM/DD-based VLC system normally uses orthogonal frequency division multiplexing (OFDM) to maximize spectral efficiency. The whole electrical bandwidth is divided into orthogonal subcarriers. VLC links are able to use different OFDM subcarriers to transmit signals. The total number of OFDM subcarriers is denoted by K. The number and fraction of OFDM subcarriers used by each link are determined by a frequency reuse scheme. We use interference set $\mathcal{I}_l$ to denote a set of links communicating on the same subcarriers as link l. Thus, the interference set $\mathcal{I}$ of each link is also determined by the frequency reuse scheme. We describe four frequency reuse schemes based on the allocation of subcarriers.

Fully reuse (FR) Every transmitter can reuse the whole electrical bandwidth. The interference set of a link from the j-th transmitter of a BS$_i$, which is denoted by i-sj, is $\mathcal{I}_{l:l(s)=i\text{-s}j} = \{m{:}m(s) = p\text{-s}n, \forall p \in [0, 18], \forall n \in [0, 6]\, l(s) \neq m(s)\}$. Here, $l(s)$ denotes the originating transmitter s of link l.

In-band (IB) mode 1 All downward-oriented transmitters for access data transmission use the same set of subcarriers. The rest subcarriers are divided into two groups: the first group consists of transmitters numbered with 1, 3, 5, and the second group consists of transmitters numbered with 2, 4, 6. Thus, each neighboring LEDs on a single base station use different bandwidth. The interference set of the link started from the transmitter i-sj is $\mathcal{I}_{l:l(s)=i\text{-s}j} = \{m{:}m(s) = p\text{-s}n, \forall p \in [0, 18], \forall n \in \{j, 1 + (j + 1) \bmod 6, 1 + (j + 3) \bmod 6\}, l(s) \neq m(s)\}$. Here, $x \bmod y$ denotes modulo operation and returns the remainder of the Euclidean division of x by y.

In-band (IB) mode 2 Similar with IB mode 1, IB mode 2 also allocates a set of subcarriers to all access-link transmitters. The rest subcarriers are divided into three groups such that every opposite transmitter-pair uses the same set of subcarriers. The interference set of the link started from the transmitter i-sj is $\mathcal{I}_{l:l(s)=i\text{-s}j} = \{m{:}m(s) = p\text{-s}n, \forall p \in [0, 18], \forall n \in \{j, 1 + (j + 2) \bmod 6\}, l(s) \neq m(s)\}$.

In-band (IB) mode 3 Each transmitter on a single BS uses individual subcarrier sets to avoid inter-link interference in the same cell. The interference set of the link started from the transmitter i-sj is $\mathcal{I}_{l:l(s)=i\text{-s}j} = \{m{:}m(s) = p\text{-s}j, \forall p \in [0, 18], p \neq m\}$.

Illustration of four frequency reuse schemes is shown in Fig.5.3. A simple FDM method configures all BSs with the same mode. Subcarriers are equally allocated to each group.

5.3 Misalignment in Cellular Networks

In previous research on optical attocell networks using VLC backhaul links, perfect alignment of auxiliary transceivers was assumed. Channel gain of a VLC link is proportional to cosines of angles between the transmitter and the receiver [3]:

$$G = \frac{m+1}{2\pi D^2} A_r \cos^m(\phi) \cos(\theta) \text{rect}(\frac{\theta}{\Theta}), \tag{5.1}$$

where ϕ and θ are angles of LOS paths measured from orientations of the transmitter and the receiver, respectively, D is the Euclidean distance from the transmitter and the receiver, $m = -\ln 2/\ln(\cos(\Phi_{1/2}))$ is Lambertian order of the transmitter, where $\Phi_{1/2}$ is the semi-angle at half-intensity of the LED emission pattern, A_r is the active area of the receiver PD, Θ is the field-of-view (FOV) of the PD. The rectangular function rect(x) is 1 if $|x| \leq 1$, and 0 otherwise. When both transmitter and receiver are aligned, i.e. $\phi = \theta = 0$, the received optical power is maximized. This ideal case may not be guaranteed in some scenarios, for instance, some BSs rotate against the vertical axis due to installation errors or cleaning. The horizontal rotation angle, i.e. horizontal misalignment angle, is denoted by $\Delta\theta$. The positive value of $\Delta\theta$ means rotation in the anti-clockwise direction. Every BS in the cellular network uses six auxiliary transceivers for backhaul transmission. When a BS is misaligned, all six auxiliary transceivers of this BS rotate with the same horizontal misalignment angle. This results in an increase of ϕ and θ of active backhaul links between this BS and its neighbors.

FOV of auxiliary PDs should be small in order to avoid multipath-effect and inter-cell interference. However, misaligned auxiliary PDs need enough viewing angle to receive the LOS signal or the signal from the first-bounce specular reflection. The configuration of FOV depends on the layout of lamps as shown in Fig.5.4. The vector $\overrightarrow{\mathbf{n_r}}$ and $\overrightarrow{\mathbf{n_r'}}$ denote orientation of perfectly aligned auxiliary PD and misaligned auxiliary PD, respectively. The maximum horizontal misalignment angle is $\Delta\theta_{max} = 30^\circ$, as the auxiliary PD with $\Delta\theta_{max} > 30^\circ$ can be assigned to another LED (of a neighboring BS). In Fig.5.4 we show a boundary case when the horizontal misalignment angle of BS_2 is $\Delta\theta = 30^\circ$. The misaligned auxiliary PD of BS_2 has to be able to receive the first-bounce specular reflection from the reflecting point on the mirror m_1. Based on the geometry of mirrors and BSs, the minimum FOV is $\Theta^b_{min} = 2\text{arcsin}(\frac{\frac{\sqrt{3}R}{2}\sin\frac{\Delta\theta_{max}}{2}}{\sqrt{H^2+(\frac{\sqrt{3}R}{2})^2}})$, where R is cell radius and H is the height of BSs [11].

5.3.1 Impact caused by misalignment

From Eq.(5.1) we know that the channel gain is reduced when ϕ and θ increase. Thus, the received power of the signal link is reduced when the transmitter and/or

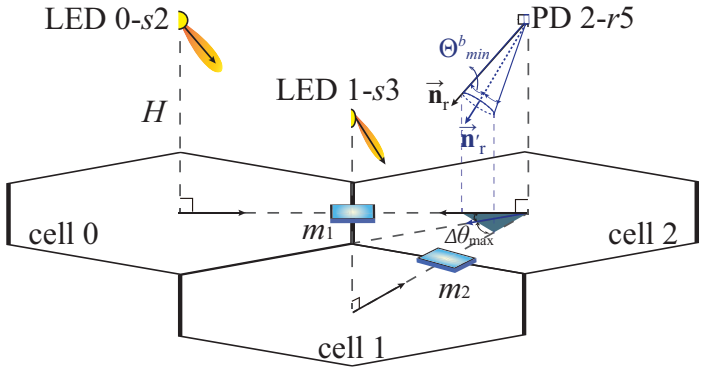

Figure 5.4: Examples of misalignment of ma-nLOS (multi) backhaul configuration; horizontal misalignment angle $\Delta\theta_{max}$ =30°

the receiver is misaligned. In the meantime, received power from interfering transmitters is increased. The SINR of the k-th subcarrier of a link is calculated by

$$\gamma_k = \frac{P_{\text{signal},k}}{\sigma_k^2 + P_{\text{intf},k}}, \tag{5.2}$$

where P_{signal}, k, P_{intf}, k, and σ_k^2 denote the received signal power, the interference power and the noise power of the k-th subcarrier, respectively. Here, $\sigma_k = N_0 B/K$ is the noise power on the k-th subcarrier, N_0 is the power spectral density (PSD) of additive white Gaussian noise (AWGN) channels and B is the bandwidth of the signal. Signal power $P_{\text{signal},k} = P_{elec,k} R_{PD}^2 |G|^2$ is the received power of the signal link, where R_{PD} is the responsivity of the PD and $P_{elec,k}$ is the transmitted electrical power of the k-th subcarrier. We assume that the total transmitted electrical power P_{elec} is evenly distributed on subcarriers assigned to the signal link. The transmitted electrical power P_{elec} is calculated based on the optical power P_{opt} and the modulation scheme. DC-bias (DC) optical OFDM which has higher spectral efficiency and lower complexity is considered in this work. Thus, the total transmitted electrical power P_{elec} with $\alpha = P_{opt}/\sqrt{P_{elec}}$, where α is the bias factor [6]. The interference power $P_{\text{intf},k} = \sum_{m \in \mathcal{I}} P_{elec,m,k} R_{PD}^2 |G_m|^2$ is the sum of power received by all interfering transmitters included in interference set $\mathcal{I}$ on the k-th subcarrier, where m denotes an interfering LED and G_m is the channel gain from m to the receiver. Transmitters in the interference set $\mathcal{I}$ depend on frequency division multiplexing. When transceivers are misaligned, the channel gain of the signal link G decreases, and channel gains of certain interfering

Parameter	Symbol	Value
Number of subcarriers	K	512
Bandwidth	B	$20\,\mathrm{MHz}$
Noise PSD	N_0	$1 \times 10^{-21}\ \mathrm{A}^2/\mathrm{Hz}$
PD detecting area	A_r	$1\,\mathrm{cm}^2$
PD responsitivity	R_{PD}	$0.5\,\mathrm{A/W}$
Reflectivity of mirrors	ρ_m	0.9

Table 5.1: Simulation parameters

links G_m increase. SINR of the VLC link between misaligned transceivers is decreased as both $P_{\text{signal},k}$ decreases and $P_{\text{intf},k}$ increases. The SINR of the backhaul link from BS_0 to BS_1 is shown in Fig.5.5. The horizontal misaligned angle varies from 0° to 30°. The value shown in the figure is the average of γ_k of all subcarriers allocated to link BS_0 to BS_1. Bandwidth allocation has been illustrated in Fig.5.3. In the simulation, cell radius is $2\,\mathrm{m}$. Heights of UEs and BSs of $1.15\,\mathrm{m}$ and $2.85\,\mathrm{m}$, respectively. Other simulation parameters are listed in table 5.1. We can see from Fig.5.5 that the SINR of the link from BS_0 to BS_1 decreases with increasing horizontal misaligned angle. Degradation of SINR depends on the IB mode. More than 3 dB SINR degradation can be seen in the link using IB mode 1.

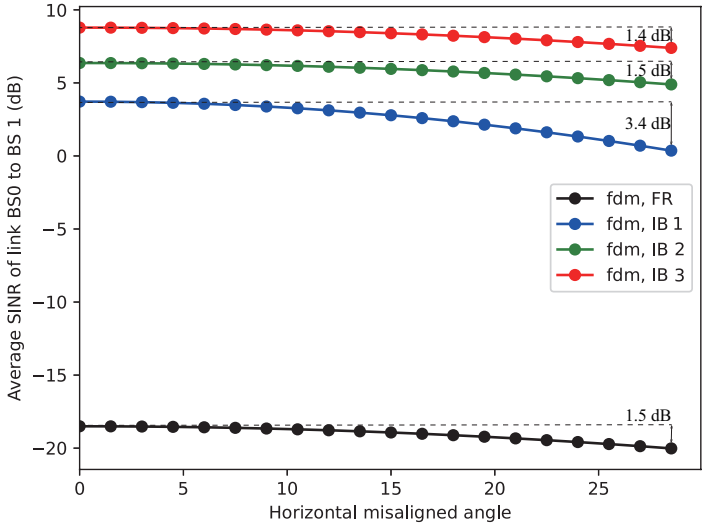

Figure 5.5: SINR of link BS0 to BS1 with different horizontal misalignment angles

5.3.2 Misalignment detection

Time slot	0	1	2	3	4	5	6	7	8	9	10	11	12
BS number	0	1	2, 7	3, 14	4, 8	5, 15	6, 9	13, 16	10	17	11	18	12

Table 5.2: Time slot allocation for HELLO/ACK processes

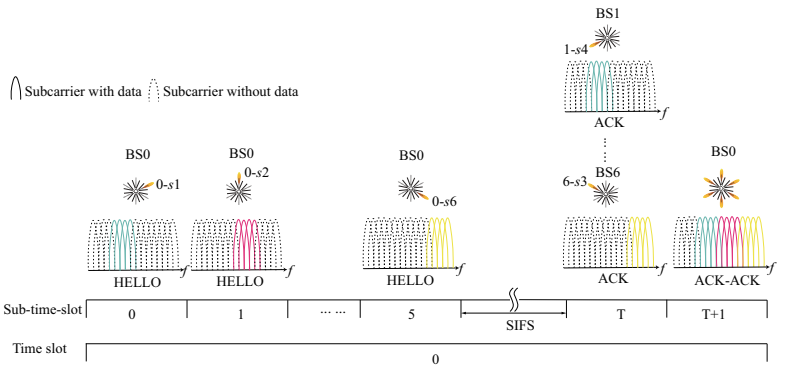

Figure 5.6: Frequency domain of HELLO messages and ACK messages in OMACK-based detection process with IB mode 2

In order to mitigate the impact caused by misalignment, we first have to detect the misalignment of auxiliary transceivers. When misalignment occurs, channel gains of misaligned links are changed. A misalignment detection method should be applied to determine whether the transmitter or the receiver is misaligned. In addition, the horizontal misaligned angle should be calculated for misalignment effect mitigation strategies. The misalignment detection is realized by a HELLO message protocol. To better explain the protocol, the following assumptions are made: 1) all BSs are perfectly aligned when installed; 2) every BS has a unique identity number (ID) which can be given by the manufacturer or programmed when installed. At time slot $T = 0$, a central controller which situates at the gateway starts the detection process. The detection process is begun with broadcasting HELLO messages to all neighbors, i.e. tier-1 BSs. The HELLO message contains the ID of the gateway, the number of the transmitting auxiliary transmitter, and the transmitted power on each subcarrier. The broadcasting, however, is done by six sub-times-slots. The gateway numbers its auxiliary transmitters in anti-clockwise order as shown in Fig.5.3 and every auxiliary transmitter uses the sub-time-slots and the allocated subcarriers to send the HELLO message. Neighboring BSs detect HELLO messages from different auxiliary transmitters in different sub-time-slots. By comparing the received power, neighboring BSs are able to determine the ID of the source BS, i.e. the gateway, and the number of their source auxiliary transmitters. BSs number their auxiliary transceivers based on the source auxiliary transmitters such that all BSs use the same way to number their auxiliary transceivers. An acknowledgment (ACK) of HELLO message which contains the ID of the receiving BS, the number of the receiving auxiliary receiver, and the calculated channel gain, is constructed by every receiving BS. After a short interframe space (SIFS) which can be a few sub-time-slots, BSs send the ACK messages to the gateway using OFDMA-based multicast ACK (OMACK) [12]. With the OMACK method, neighboring BSs only send data on subcarriers allocated to their source auxiliary transmitters. In the next sub-time-slot after receiving the ACK, the gateway sends an ACK-ACK to indicate the end of the HELLO/ACK process at time slot $T = 0$. The HELLO/ACK process and the frequency domain of HELLO messages and ACK messages are shown in Fig.5.6. Neighboring BSs repeat this HELLO/ACK process in the allocated time slots. Table 5.2 illustrates the allocation of time slots for HELLO/ACK process in two-tier networks shown in Fig.5.2. The allocated time slot for a BS can be calculated based on the first received HELLO message. When BS_j received the HELLO message from the auxiliary transmitter i-sn (The n-th transmitter of BS_i) in time slot $T = T_i$, the time slot for BS_j to perform its own HELLO/ACK process is $T_j = T_i + n$. A BS receives the HELLO message from different neighbors in the same or different time slots. It only performs its HELLO/ACK process at the earliest calculated time slot. The whole detection process is ended when all BSs finish their HELLO/ACK

process. After the detection process, every BS sends the channel gains of their backhaul links to the gateway. The central controller at the gateway collects the channel gains obtained at the installation phase. To detect misalignment, BSs can repeat this detection process every t seconds, where t is the misalignment detection window time. The detection window time should be large enough compared to the timing overhead of the detection process.

Calculation of horizontal misalignment angle is based on Eq.5.1. We denote the channel gain of an aligned link from BS$_i$ to BS$_j$ as G_{ij}. The gain calculated from each detection process is denoted as $G^{'}_{ij}$. From the previous section, we have known that $\phi = \theta = 0$ when all BS are perfectly aligned. The channel gains G_{ij} is detected when all BSs are installed and it is the channel gain of aligned cases. The ratio of $G^{'}_{ij}$ and G_{ij} is $\cos^m(\Delta\phi_i)\cos(\Delta\theta_j)$. Here, $\Delta\phi_i$ is the misalignment angle of auxiliary LEDs of BS$_i$ and $\Delta\theta_j$ is the misaligned angle of auxiliary PDs of BS$_j$. Notice that, misalignment angle of auxiliary transceivers in the same BS is the same, i.e. $\Delta\phi_i = \Delta\theta_i$. Thus, the ratio of $G^{'}_{ij}$ and G_{ij} can be also represented as $\cos^m(\Delta\phi_i)\cos(\Delta\phi_j)$. As both $G^{'}_{ij}$ and G_{ij} can be collected from the detection process, the value of $\Delta\phi_i$ can be calculated by solving simultaneous equations of ratios of $G^{'}_{ij}$ and G_{ij} of all links. Knowing the actual misalignment angle $\Delta\phi_i$, the horizontal misalignment angle can be then calculated based on the height of BSs and cell radius.

5.4 Mitigation Strategies for Different Misaligned Scenarios

From the previous section, we knew that misalignment causes decreasing signal power and increasing interference power. Due to the high Lambertian order m of auxiliary transmitters, misaligned transmitters have a larger impact on SINR than misaligned receivers. Thus, we focus on mitigation strategies for misaligned transmitters. As the center gateway transmits data to all UEs in the network, the impact caused by the misaligned gateway is of importance. A redundant transmission strategy is proposed to reduce the impact caused by the misaligned gateway. For a scenario where every BS has a random misaligned angle, an adaptive strategy is proposed based on the redundant transmission strategy and the FDM method described in 5.2.5.2.3.

5.4.1 Redundant transmission strategy

As described in 5.2.5.2.3, auxiliary transmitters can use different subcarriers to reduce interference from neighboring transmitters. We notice that every three neighboring auxiliary transmitters use different subcarriers in IB mode 2 and IB mode 3.

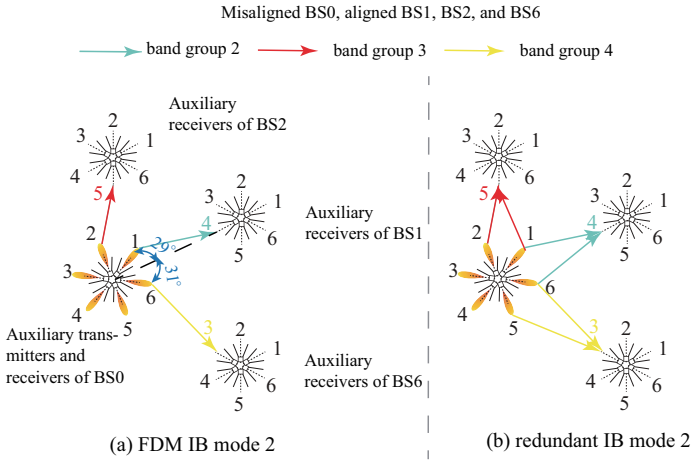

Figure 5.7: An example of redundant transmission using IB mode 2

If the j-th auxiliary transmitter uses the subcarriers assigned to the $(j-1)$mod 6-th auxiliary transmitter to send redundant data to the receiver, it will not cause extra interference to the link from $(j+1)$mod 6-th auxiliary transmitter. An example is shown in Fig.5.7. BS_0 is misaligned. All auxiliary transceivers associated with BS_0 rotate anti-clockwise against the vertical axis. BS_1, BS_2, and BS_6 are aligned. When FDM IB mode 2 is used, auxiliary transmitters 0-s1, 0-s2, and 0-s6 use subcarriers assigned to group 2, 3, and 4 to send data, respectively. As BS_0 is misaligned, optical power received by auxiliary receivers 1-r4, 2-r5, and 6-r3 is reduced. It can be seen that the angle between auxiliary transmitter 0-s6 and auxiliary receiver 1-r4 in this misaligned case is smaller than the angle when aligned (60°). As shown in Fig.5.7(b), transmitter 0-s6 can use subcarriers in group 2 to send the same data to 1-r4 at the same time as 0-s1. This redundant link will not cause extra interference to the original signal link (from 0-s1 to 1-r4). Similarly, other auxiliary transmitters can also send redundant information to auxiliary receivers with the smallest angle.

The performance of this redundant transmission strategy is shown in Fig.5.8. The FDM method is also simulated for comparison. In this simulation, only the gateway BS_0 is misaligned. Parameters in table 5.1 are used. Performance is assessed by aggregate data rates of UEs in the network, which is the sum of end-to-end data rates of all UEs. It can be seen that the performance of all FDM methods degrades with the increasing horizontal misalignment angle, while redundant transmission using both IB mode 2 and IB mode 3 has performance improvement with the increasing horizontal misalignment angle. FDM IB mode 1 outperforms other methods when $\Delta\theta$ <12°. When the horizontal misalignment angle $\Delta\theta$ >12°, redundant transmission using IB mode 2 has better performance.

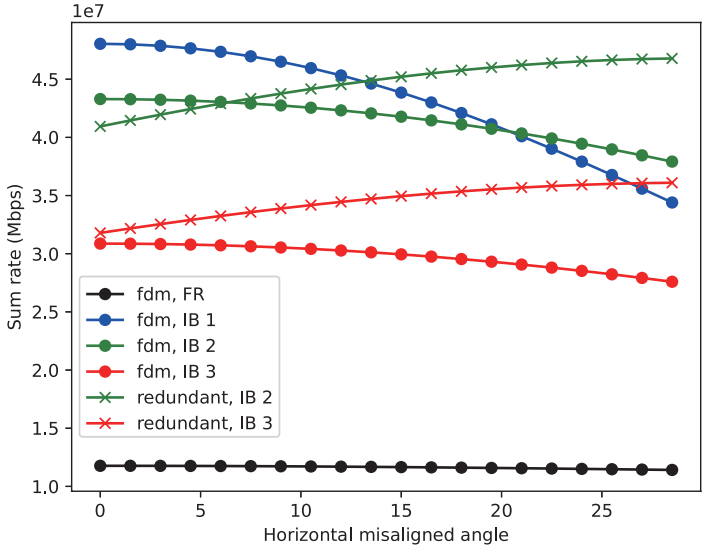

Figure 5.8: Aggregate data rate of networks using FDM and redundant transmission; R =2 m; heights of UEs and BSs are 1.15 m *and* 2.85 m*, respectively*

		Cell radius (m)					
		2	2.2	2.4	2.6	2.8	3
RHR	0.8	15°	18°	21°	21°	21°	22.5°
	0.85	12°	16.5°	18°	19.5°	19.5°	21°
	0.9	9°	13.5°	16.5°	16.5°	18°	19.5°
	0.95	6°	10.5°	13.5°	15°	16.5°	18°
	1	3°	7.5°	10.5°	12°	13.5°	15°

Table 5.3: Transition angle

This angle is called the transition angle. It is shown that the redundant transmission strategy can improve the network performance when the gateway is misaligned and the angle is larger than the transition angle. The value of the transition angle depends on cell radius and radius height ratio (RHR) which is the ratio of cell radius and the height between BSs and UEs. FDM IB mode 1 has the best performance when the misalignment angle is smaller than the transition angle, while redundant IB mode 2 outperforms other methods when the misalignment angle is larger than the transition angle. Simulated values of the transition angle in different networks are shown in table 5.3.

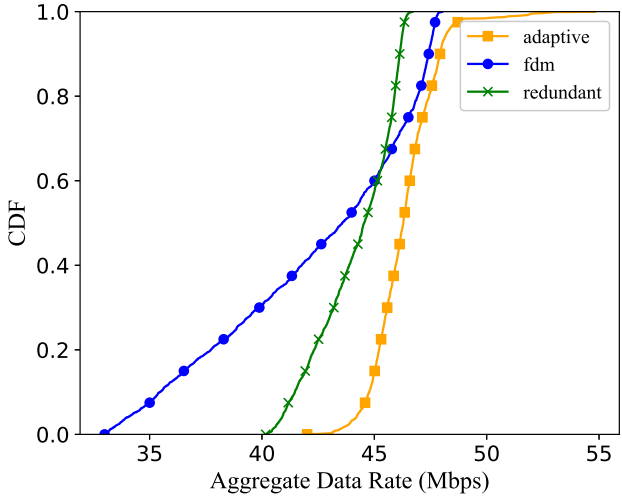

Figure 5.9: CDF of aggregate data rates of two-tier ring-type optical attocell network with random misalignment angles; R =2 m; heights of UEs and BSs are 1.15 m *and* 2.85 m*, respectively*

5.4.2 Adaptive strategy

In real applications, misalignment can happen on every BS. The performance of the redundant transmission strategy has to be assessed in networks when multiple BSs are misaligned. We consider a scenario that all BSs in the two-tier ring-type network are misaligned with random angles between $0°$ and $30°$. Networks using FDM IB mode 1 and the redundant transmission with IB mode 2 are simulated and aggregate data rates, i.e. sum rates of all UEs in the network, are compared. The third strategy is an adaptive strategy. BSs with the horizontal misalignment angle smaller than the transition angle uses FDM IB mode 1, while redundant transmission with IB mode 2 is required for BSs with horizontal misalignment angle larger than the transition angle. As IB mode 1 and IB mode 2 have different numbers of band groups, subcarriers used for access data transmission of IB mode 1 may overlap subcarriers used for backhaul transmission of IB mode 2. Auxiliary transmitters are oriented towards mirrors on the floor and could cause large interference to access links. In order to avoid the interference between access and backhaul links, all access links are only allowed to use subcarriers allocated for access transmission with IB mode 2. Aggregate data rates of networks using three strategies are simulated. More than thousands of simulations have been conducted for each strategy. Cumulative distribution function (CDF) of aggregate data rates are shown in Fig.5.9. From the result of the previous subsection, the performance

of FDM and the redundant transmission depends on the misalignment angle. As every BS has a random misalignment angle, the network cannot achieve the overall best performance if all BSs use the same strategy. The adaptive strategy configures the method used by each BS according to its misalignment angle. It can be seen that the adaptive strategy outperforms the other two strategies. It has more than 90% probability to get aggregate data rate larger than $45\,\mathrm{Mbps}$, while the other two strategies only get $\sim$35% probability.

5.5 Conclusions

Misalignment of VLC backhaul links causes performance degradation of optical attocell network. The impact of misalignment varies with the horizontal misalignment angle. In order to detect the horizontal misalignment angle of each misaligned BS, a HELLO/ACK method based on OMACK is proposed. With the knowledge of the horizontal misalignment angle, we propose a redundant transmission strategy to mitigate repercussions caused by a misaligned gateway. By comparing the performance of FDM and the redundant transmission strategy, we have found that the misalignment effect can be minimized by choosing different methods at different horizontal misalignment angles. The transition angle for choosing different methods has been simulated. In order to mitigate the misalignment effect in networks with multiple misaligned BSs, we propose an adaptive strategy. The performance of FDM, the redundant transmission strategy, and the adaptive strategy are assessed with simulations in networks with random misaligned BSs. The simulation results show that the adaptive strategy achieves more than 90% probability to get aggregate data rate larger than $45\,\mathrm{Mbps}$, while the other two strategies only get $\sim$35% probability.

References

[1] Dilukshan Karunatilaka, Fahad Zafar, Vineetha Kalavally, and Rajendran Parthiban. *LED Based Indoor Visible Light Communications: State of the Art*. IEEE Communications Surveys and Tutorials, 17(3):1649–1678, 2015.

[2] Harald Burchardt, Nikola Serafimovski, Dobroslav Tsonev, Stefan Videv, and H. Haas. *VLC : Beyond Point-to-Point Communication*. IEEE Communications Magazine, 52(7):98–105, 2014.

[3] J. R. Barry, J.M. Kahn, William J. Krause, Edward A. Lee, and David G. Messerschmitt. *Simulation of Multipath Impulse Response for Indoor Wireless Optical Channels*. IEEE Journal on Selected Areas in Communications, 11(3):367–379, 1993.

[4] Hossein Kazemi, Majid Safari, and Harald Haas. *A Wireless Optical Backhaul Solution for Optical Attocell Networks*. IEEE Transactions on Wireless Communications, 18(2):807–823, 2019.

[5] Yuhui Wu, Pieter Audenaert, Mario Pickavet, and Didier Colle. *Mirror-aided non-LOS VLC channel characterizations with a time-efficient simulation model*. Photonic Network Communications, 38(38):151–166, 2019.

[6] J. Armstrong and B. J C Schmidt. *Comparison of asymmetrically clipped optical OFDM and DC-biased optical OFDM in AWGN*. IEEE Communications Letters, 12(5):343–345, 2008.

[7] Hongming Yang and Ashish Pandharipande. *Full-duplex relay VLC in LED lighting linear system topology*. In Industrial Electronics Conference, pages 6075–6080. IEEE, 2013.

[8] European Committee for Standardization. *Light and lighting - Lighting of work places - Part 1 : Indoor work*. 2002.

[9] Jae Yong Suk. *Luminance and vertical eye illuminance thresholds for occupants' visual comfort in daylit office environments*. Building and Environment, 148:107–115, 2019.

[10] Yuhui Wu, Mario Pickavet, and Didier Colle. *Analysis of the Impact of Misaligned Wireless Backhaul Links on Optical Attocell Networks*. In International Conference on Transparent Optical Networks, 2020.

[11] Yuhui Wu, Mario Pickavet, and Didier Colle. *Analysis of interference on mirror-aided non-LOS backhaul data transmission in VLC attocell networks*. Photonic Network Communications, 41(2):189–201, 2021.

[12] Byung Seo Kim, Sung Won Kim, and Randy L. Ekl. *OFDMA-based reliable multicasting MAC protocol for WLANs*. IEEE Transactions on Vehicular Technology, 57(5):3136–3145, 2008.

6 Conclusion

The presented work on the mirror-aided non-LOS VLC-based backhaul network is a low-cost solution for optical attocell networks. Optical attocell networks are proposed to complement the bandwidth shortage of indoor wireless networks. The backhaul network is an essential component of the optical attocell networks, as data aggregate in the backhaul network. The LOS VLC-based backhaul network cannot be used in some scenarios where the LOS condition between lamps cannot be fulfilled. The presented mirror-aided non-LOS VLC-based backhaul network utilizes the specular reflection of the light from mirrors or glossy tiles on the floor/table. This fills the gap of the VLC-based backhaul networks as the LOS condition is not needed. In the next section, we outline the major contributions of this dissertation. Then, we conclude this work with some thoughts on the possibilities for future research.

6.1 Summary of the major contributions

The topic of this doctoral dissertation started from a simple concept: using light reflections to perform backhaul communication. The TED Global Talk "Wireless data from every light bulb" in 2011 showed the opportunity of using VLC links for indoor wireless communication [1]. A number of research articles and demonstrations also showed the possibility of point-to-point VLC links for high-speed data communication [2–7]. Using VLC links for backhaul data transmission is a straightforward idea: first, VLC links have the potential to provide a large amount

of data throughput; second, resource allocation and multiplexing of VLC-based access and backhaul links can be done centralized. A LOS-based VLC backhaul network was proposed in [8]. The LOS VLC link has been proven to support large data throughput [2, 7]. However, the LOS configuration requires LOS paths between horizontal backhaul links. In many indoor lighting designs, the LOS condition may not be fulfilled. For example, some recessed lamps are placed in holes of the ceiling and there is no LOS path between two recessed lamps. We notice that the non-LOS configuration can be used in such scenarios. Many research showed that the non-LOS configuration with pure diffuse reflections may not be able to support high data rates [9–11]. Specular reflections have never been considered in those research. We know from instinct that the specular reflection is more directional compared to the diffuse reflection. To investigate the performance of the non-LOS link configuration with specular reflections, we developed a simulation model in Chapter 2. Diffuse reflections and specular reflections with different numbers of bounces are computed and combined to obtain accurate results. The calculation of the final result is done iteratively. This method is much more time-efficient than the recursive model in [12], as the number of calculations for each additional bounce does not change and the total number of calculations increases linearly with the number of bounces. It is also important to be remarked that the proposed iterative model is the first iterative model which can model multi-bounce specular reflections of VLC links. This simulation model can be used to obtain accurate channel impulse responses of VLC links in different environments.

The iterative simulation model is used to assess the performance of different mirror-aided non-LOS channels in Chapter 2. We first investigate the link performance with different mirror sizes. We find that a small mirror that provides the first-bounce specular reflection can increase the total received power and increasing the mirror size cannot further improve the link performance. This indicates that the mirror-aided non-LOS link can use a very small mirror or glossy tile which covers the reflecting point of the first-bounce specular reflection. Then, we find that directed and hybrid mirror-aided non-LOS configurations perform much better than the non-directed configuration. This investigation can be used for choosing a proper configuration of the mirror-aided non-LOS link for specific applications. In addition, the FOV and the directionality of the receiver are important for link performance. In Chapter 2, we also compare the received power of each bounce. The simulation result shows that the mirror-aided non-LOS link in the small-mirror scenario receives over 70% power via the first-bounce specular reflection. This means that the first-bounce specular component is dominant in the total received power. This conclusion is then used in the later analysis in Chapter 3 and Appendix A.

Chapter 3 focuses on the interference between VLC-based access and backhaul links in a two-tier ring-type optical attocell network. We compare the network

performance with unlimited backhaul data rates and when using LOS and mirror-aided non-LOS backhaul link configurations. We first discuss the maximum transmitted power of LEDs taking into account illumination and eye-safety requirements. This is important for indoor optical attocell networks and must be considered when analyzing the performance of networks using VLC backhaul links. The results show that the semi-angle of auxiliary LEDs used for backhaul transmission has a large impact on the maximum transmitted power. From the simulation results in Chapter 3, we know that LOS backhaul links using auxiliary LEDs with semi-angle of 5° can achieve the best performance. The performance reaches the network performance with unlimited backhaul throughput when the semi-angle is small and degrades with the increasing semi-angle. The directed mirror-aided non-LOS backhaul links can achieve good performance when the interference between access and backhaul links can be reduced by frequency allocation schemes. From the results and discussion in Chapter 3 we know that both LOS and mirror-aided non-LOS backhaul link configurations can be used in a moderate-size network ($16\,\mathrm{m}\times16\,\mathrm{m}$).

Misalignment and shadowing effects are crucial to the performance of VLC links. Chapter 4 and Chapter 5 provide viable solutions to solve these two problems.

In the last part of Chapter 3, we find that a misaligned gateway has the largest impact on the overall network performance when there is only one misaligned BS in the network. This investigation brings a key message for designing strategies to mitigate the misalignment effect: improving the performance of networks with the misaligned gateway is of importance. In Appendix A we further investigate the misalignment effect caused by the misaligned gateway. The results show the possibility of using a proper frequency allocation scheme to improve the network performance in misaligned scenarios. Simulation results also give the best semi-angle of each frequency allocation scheme which can minimize the misalignment effect.

The strategy for mitigating the misalignment effect of mirror-aided non-LOS backhaul links is presented in Chapter 5. There are two strategies proposed in this chapter. The redundant transmission strategy can be used to improve the network performance when the gateway is misaligned. The performance of the redundant transmission strategy depends on the misalignment angle. There exists a transition angle for choosing the proposed redundant transmission strategy. This angle depends on the cell radius and the height of BSs. We give simulated values of the transition angles in different cases. Given the knowledge of the transition angle, an adaptive strategy is proposed for general misalignment scenarios, i.e. all BSs are randomly misaligned. Both strategies require the detection of misalignment angles. The protocol for detecting the misalignment angle of each BS in the network is proposed in Chapter 5. This protocol also helps the future design of mitigation

strategies.

Chapter 4 solves the shadowing effect in optical attocell networks using mirror-aided non-LOS backhaul links. The shadowing recovery strategy proposed in Chapter 4, the RASP, is a novel cross-layer strategy. This strategy takes advantage of the centralized controller which collects the information of the whole network and allocates resources for every BS. The RASP recovery scheme turns the shadowing recovery problem into an optimization problem. The optimal combination of control variables leads to the best recovery performance. Finding the optimal solution may not be possible in many shadowed cases. In Chapter 4, we try different searching algorithms and modify the Tabu search algorithm to improve its performance for solving the shadowing recovery problem. The RASP recovery scheme and the modified Tabu search algorithm make optical attocell networks using mirror-aided non-LOS backhaul links robust against the shadowing effect.

6.2 Future research

The work presented in this dissertation provides a general overview of designing a robust VLC-based backhaul network using the mirror-aided non-LOS configuration. The presented work starts with channel modeling and analysis and continues with solving two major problems: the shadowing effect and the misalignment effect. The methodology and the results presented in this dissertation will help future research on VLC-based optical attocell networks which are still evolving. Following research topics can be inspired and encouraged by the presented work.

6.2.1 Further applications of the simulation model

The iterative simulation model presented in Chapter 2 is pioneer work as it models VLC links in near-realistic application scenarios and greatly reduces the simulation time. Besides analyzing the performance of VLC-based backhaul links, this model can be used for many other technologies using VLC.

One of the most interesting VLC-based technologies is indoor positioning. Indoor positioning can be used in many applications, such as location in public places (shopping malls, airports, and train stations), tunnels, and industrial facilities [13]. Although the global positioning system (GPS) is widely used for outdoor positioning, it is unable to provide high precision in indoor environments as the GPS signals cannot penetrate through building walls. VLC is considered a viable technology for indoor positioning systems due to its high security and less interference with RF technologies. In addition, VLC-based systems are expected to provide better positioning accuracy than RF solutions [14]. Triangulation is the most popular algorithm for indoor positioning systems. With the triangulation algorithm, the location of the target is estimated with the help of the geometric properties of

the triangle. The measurement of distances is mathematically calculated using received signal strength (RSS), time of arrival, and/or time difference of arrival [14]. The simulation model presented in Chapter 2 can provide accurate results of the RSS and the delay of the signal. This makes the presented model suitable for simulations of VLC-based indoor positioning systems.

Another indoor scenario that can apply VLC is the internet-of-things (IoT). IoT enables data exchange between devices by using embedded sensors or software. VLC is also a viable technology for data communication between IoT devices due to its simplicity and low-cost [15]. Researchers in [16] suggest that using non-LOS VLC links for low-data rate IoT applications as the position and receiving angle of the receiver can be more flexible to improve communication mobility. Analysis of multiple order of reflections is important for non-LOS links. Future research on non-LOS VLC-based IoT applications can benefit from the simulation model presented in Chapter 2.

The application of the presented simulation model is not limited to the above-mentioned scenarios. Due to the increasing demand for indoor wireless data communication, the potential of VLC links, especially non-LOS VLC links, will be exploited and the time-efficient simulation model will be a powerful tool.

6.2.2 Universal standardization of VLC-based backhaul links

The work presented in this dissertation focuses on mirror-aided non-LOS backhaul links. Researchers also proposed to use LOS backhaul links in [8]. VLC-based backhaul links with other configurations can be suitable for some specific applications and may also be discussed in the future. A universal standardized can boost the cooperative research on VLC-based backhaul solutions.

The IEEE 802.15.7 task group has been working on the standardization of VLC links and a PHY-MAC standard for short-range VLC links has been completed [17]. This standard can be expanded to optical attocell networks using VLC for both access and backhaul data transmission. A PHY-MAC-Network layer specification for VLC-based backhaul solutions including the protocols for MAC and network layers can follow the approach in [18] and the previous standard.

6.2.3 Implementation and testing of recovery schemes

In this dissertation, we present two recovery schemes to address two major problems in optical attocell networks: the misalignment and the shadowing effects. The current research purpose is to discover feasible algorithms and methods. The performance of these recovery schemes is assessed by simulations. The proposed recovery schemes are written in Python and the actual processing time of the recovery schemes in real applications is not examined in our work. Future research can focus on the testing of the functionality and the actual processing delay. A

co-testing of two recovery schemes is also necessary as the misalignment and the shadowing effects co-exist in the optical attocell networks.

Testing for recovery schemes in optical attocell networks has not been discussed yet. Future research can follow frameworks for other testing purposes, for instance, the cloud recovery testing framework FATE (Failure Testing Service) and DESTINI (Declarative Testing Specifications) proposed in [19]. FATE gives non-similar failure scenarios higher priority to accelerate the testing for multiple failures. DESTINI is used to clearly, concisely, and precisely specify the expected behavior of the recovery scheme.

In addition to the functional testing, the examination of the delay in real-time applications is also important. The shadowing effect recovery scheme presented in Chapter 4 has already discussed the processing time of different algorithms and future tests can also take the discussion into account. In Chapter 5 we present the number of time slots required for the OMACK-based protocol for the detection of the misalignment angle. This work can also be considered in future testing.

Another important topic for future research is the implementation of these two recovery schemes. The misalignment effect recovery scheme requires the calculation with channel information. The shadowing effect recovery scheme is based on resource allocation and routing algorithm and an efficient searching algorithm is required for this recovery scheme. These calculations and algorithmic processes can be implemented with software programs and run by general central processing units (CPUs). However, the memory available for general-purpose CPUs is limited. As the calculations and algorithmic processes have to be done centralized in a central CPU, the processing time of the recovery schemes could be very large if the CPU encounters memory shortage and the performance of the recovery will be affected. A possible solution could be implemented with hardware, for example, programmable hardware like field programmable gate arrays (FPGAs). [20] implements a single source shortest-path routing algorithm on FPGA and achieves a speedup of up to 5 times over the CPU implementation. Searching algorithms can also be implemented on FPGA [21, 22].

6.2.4 Cooperative research with SDN

The recovery schemes proposed in Chapter 4 and Chapter 5 require collecting information on the whole network and allocating resources for all links. This centralized nature makes it suitable for software-defined networking (SDN) technology. With the SDN technology, each BS simply forwards the data and enforces the policy according to instructions received from the central controller [23]. The SDN technology provides the ability to dynamically configure the VLC-based optical attocell networks [24, 25].

Currently, OpenFlow protocol is generally considered for SDN technologies.

OpenFlow provides an open protocol to control the data flows for different switches and routers [26]. Adopting the OpenFlow protocol in wireless sensor networks is proposed in [27] and the usage of the OpenFlow in optical attocell networks has not been discussed yet. Future research can focus on the cooperative research of the OpenFlow protocol and recovery schemes for VLC links.

References

[1] Harald Haas. *Wireless data from every light bulb [video]*, 2011.

[2] A. M. Khalid, G. Cossu, R. Corsini, P. Choudhury, and E. Ciaramella. *1-Gb/s transmission over a phosphorescent white LED by using rate-adaptive discrete multitone modulation*. IEEE Photonics Journal, 4(5):1465–1473, 2012.

[3] Fang Ming Wu, Chun Ting Lin, Chia Chien Wei, Cheng Wei Chen, Zhen Yu Chen, and Hou Tzu Huang. *3.22-Gb/S Wdm Visible Light Communication of a Single Rgb Led Employing Carrier-Less Amplitude and Phase Modulation*. Optical Fiber Communication Conference, OFC 2013, pages 1–3, 2013.

[4] D Tsonev, H Chun, S Rajbhandari, J J D McKendry, S Videv, E Gu, M Haji, S Watson, A E Kelly, G Faulkner, M D Dawson, H. Haas, and D O'Brien. *A 3-Gb/s Single-LED OFDM-Based Wireless VLC Link Using a Gallium Nitride*. IEEE Photonics Technology Letters, 26(7):637–640, 2014.

[5] Dobroslav Tsonev, Stefan Videv, and H. Haas. *Towards a 100 Gb / s visible light wireless access network*. Optics Express, 23(2):369–374, 2015.

[6] Ricardo X.G. Ferreira, Enyuan Xie, Jonathan J.D. McKendry, Sujan Rajbhandari, Hyunchae Chun, Grahame Faulkner, Scott Watson, Anthony E. Kelly, Erdan Gu, Richard V. Penty, Ian H. White, Dominic C. O'Brien, and Martin D. Dawson. *High Bandwidth GaN-Based Micro-LEDs for Multi-Gb/s Visible Light Communications*. IEEE Photonics Technology Letters, 28(19):2023–2026, 2016.

[7] S. I. Slim, Ricardo Ferreira, Enyuan Xie, E Nyuan X Ie, Stefan Videv, S. Viola, S. Watson, N. Bamiedakis, R. V. Penty, I. H. White, Anthony Kelly, Erdan Gu, H. Haas, and Martin Dawson. *Towards 10 Gb / s orthogonal frequency division multiplexing-based visible light communication using a GaN violet micro-LED*. Photonics Research, 5(2):A35–A43, 2017.

[8] Hossein Kazemi, Majid Safari, and H. Haas. *A Wireless Backhaul Solution Using Visible Light Communication for Indoor Li-Fi Attocell Networks*. In IEEE ICC 2017 Optical Networks and Systems Symposium, 2017.

[9] J. R. Barry, J.M. Kahn, William J. Krause, Edward A. Lee, and David G. Messerschmitt. *Simulation of Multipath Impulse Response for Indoor Wireless Optical Channels*. IEEE Journal on Selected Areas in Communications, 11(3):367–379, 1993.

[10] J.M. Kahn and J.R. Barry. *Wireless Infrared Communications*. Proceedings of the IEEE, 85(2):265–298, 1997.

[11] S. Dimitrov, R. Mesleh, H. Haas, M. Cappitelli, M. Olbert, and E. Bassow. *Path Loss Simulation of an Infrared Optical Wireless System for Aircrafts*. Global Telecommunications Conference, 2009. GLOBECOM 2009. IEEE, pages 1–6, 2009.

[12] Kwonhyung Lee, Hyuncheol Park, and John R. Barry. *Indoor channel characteristics for visible light communications*. IEEE Communications Letters, 15(2):217–219, 2011.

[13] Neha Chaudhary, Luis Nero Alves, and Zabih Ghassemblooy. *Current trends on visible light positioning techniques*. 2nd West Asian Colloquium on Optical Wireless Communications, WACOWC 2019, pages 100–105, 2019.

[14] Fang Yang, Junnan Gao, and Yuanpeng Liu. *Indoor visible light positioning system based on cooperative localization*. Optical Engineering, 58(01):1, 2019.

[15] Chia-Wei Chen, Wei-Chung Wang, Jhao-Ting Wu, Hung-Yu Chen, Kevin Liang, Liang-Yu Wei, Yung Hsu, Chin-Wei Hsu, Chi-Wai Chow, Chien-Hung Yeh, Yang Liu, Hsiang-Chin Hsieh, and Yen-Ting Chen. *Visible light communications for the implementation of internet-of-things*. Optical Engineering, 55(6):060501, 2016.

[16] Yonghe Zhu, Chen Gong, Jianghua Luo, Zhengyuan Xu, and Weiqiang Xu. *SVM-assisted realization and demonstration of indoor 4 Mb/s non-line-of-sight visible light communication with second-order reflection*. IEEE Photonics Journal, 11(5):1–17, 2019.

[17] IEEE. *IEEE Standard for Local and metropolitan area networks — Part 15.7 : Short-Range Wireless Optical Communication Using Visible Light*. 2011.

[18] Sridhar Rajagopal, Sang-kyu Lim, Taehan Bae, Dae Ho Kim, Jaeseung Son, Ill Soon Jang, Doyoung Kim, Dong Won Han, Ying Li, Atsuya Yokoi, D K Jung, H S Shin, S B Park, K W Lee, Shadi Abu Surra, Farooq Khan, Tae Gyu Kang, and E T Won. *IEEE 802.15.7 VLC PHY/MAC Specification*. 2009.

[19] Haryadi S Gunawi, Thanh Do, Pallavi Joshi, Peter Alvaro, and Joseph M Hellerstein. *FATE and DESTINI: A Framework for Cloud Recovery Testing Haryadi*. In Proceedings of the 8th USENIX conference on Networked systems design and implementation, pages 238–252, 2011.

[20] Guoqing Lei, Yong Dou, Rongchun Li, and Fei Xia. *An FPGA Implementation for Solving the Large Single-Source-Shortest-Path Problem*. IEEE Transactions on Circuits and Systems II: Express Briefs, 63(5):473–477, 2016.

[21] Shin'ichi Wakabayashi, Yoshihiro Kimura, and Shinobu Nagayama. *FPGA implementation of Tabu search for the quadratic assignment problem*. Proceedings - 2006 IEEE International Conference on Field Programmable Technology, FPT 2006, pages 269–272, 2006.

[22] A. Messai, A. Mellit, A. Guessoum, and S. A. Kalogirou. *Maximum power point tracking using a GA optimized fuzzy logic controller and its FPGA implementation*. Solar Energy, 85(2):265–277, 2011.

[23] Ahmadreza Montazerolghaem. *Software-defined load-balanced data center: design, implementation and performance analysis*. Cluster Computing, 24(2):591–610, 2021.

[24] Dominic O'Brien, Lubin Zeng, Hoa Le-Minh, Grahame Faulkner, Olivier Bouchet, Sebastien Randel, Joachim Walewski, Jose A. Rabadan Borges, Klaus Dieter Langer, Jelena Grubor, Kyungwoo Lee, and Eun Tae Won. *Visible Light Communications: Theory and Applications*. 2009.

[25] Harald Haas. *LiFi is a paradigm-shifting 5G technology*. Reviews in Physics, 3(October 2017):26–31, 2018.

[26] Nick McKeown, Tom Anderson, Hari Balakrishnan, Guru Parulkar, Larry Peterson, Jennifer Rexford, Scott Shenker, and Jonathan Turner. *OpenFlow: Enabling innovation in campus networks*. ACM SIGCOMM Computer Communication Review, 38(2):69–74, 2008.

[27] Arif Mahmud and Rahim Rahmani. *Exploitation of OpenFlow in wireless sensor networks*. Proceedings of 2011 International Conference on Computer Science and Network Technology, ICCSNT 2011, 1:594–600, 2011.

A

Analysis of the Impact of Misaligned Wireless Backhaul Links on Optical Attocell Networks

From the results in chapter 3, we found that the directional mirror-aided non-LOS backhaul links can achieve better performance by using the in-band mode in aligned cases. In this Appendix, we present the performance of mirror-aided non-LOS backhaul links using different frequency allocation schemes in misaligned cases.

* * *

Y. Wu, M. Pickavet, D. Colle

Published in Proceedings of International Conference on Transparent Optical Networks, p.1-6, 2020.

Abstract *Wireless solutions based on visible light communication (VLC) have been proposed for backhaul transmission in optical attocell networks. Perfect alignment of auxiliary transceivers is important for wireless backhaul links due to the requirement of direct line-of-sight (LOS) and the first-bounce specular reflection of mirror-aided non-LOS. However, the perfect alignment may not be guaranteed due to the limitation of the layout of BSs or installation mistakes. In this article, we investigate the impact of misalignment on the overall network perfor-*

mance. Two VLC backhaul link configurations have been considered and compared. The performance of using different frequency reuse schemes and channel allocation schemes is compared.

A.1 Introduction

Optical attocell networks based on visible light communication (VLC) have drawn scientific interest in the last few years. Many backhaul solutions for connecting VLC base stations (BSs) to the Internet have been proposed. Wired backhaul technologies, such as power-line communication (PLC) and power-over-Ethernet (PoE), have been proposed as the backhaul solution. However, wired backhaul solutions require installing additional control devices like modems or replacing current power cables. The cost for installation and maintenance could be extremely high. Wireless backhaul solutions based on VLC links are proposed in [1, 2]. VLC backhaul links are viable solutions for optical attocell networks which have used VLC for access data transmission. One drawback of using VLC backhaul links is the impact caused by misaligned auxiliary transceivers, as misalignment violates the strict line-of-sight (LOS) condition of VLC backhaul links. In many indoor scenarios, perfect alignment may not be guaranteed due to the limitation of the layout of BSs or installation mistakes. Thus, it is necessary to investigate the misalignment impact on optical attocell networks. Three frequency reuse schemes are proposed. Static subcarrier allocation based on the frequency reuse scheme is considered. Simulation results of networks using two backhaul link configurations are presented and compared.

A.2 System Model

This section introduces VLC-based optical attocell networks considered in our work. Different link configurations and channel gain calculations are explained. Three frequency reused schemes: fully reused (FR), in-band (IB) mode 1, and IB mode 2. Allocation of subcarriers of optical orthogonal frequency division multiplexing (OFDM) is based on the chosen frequency reused scheme.

A.2.1 Visible Light Communication

A VLC communication system uses a visible light-emitting-diode (LED) to send an intensity-modulated (IM) signal which is high-frequency modulated on the light intensity. A photodiode (PD) receiver converts the received light to an electrical current and decodes the received signal. Optical OFDM, such as direct-current optical OFDM (DCO-OFDM), is commonly used for VLC systems due to its spectral

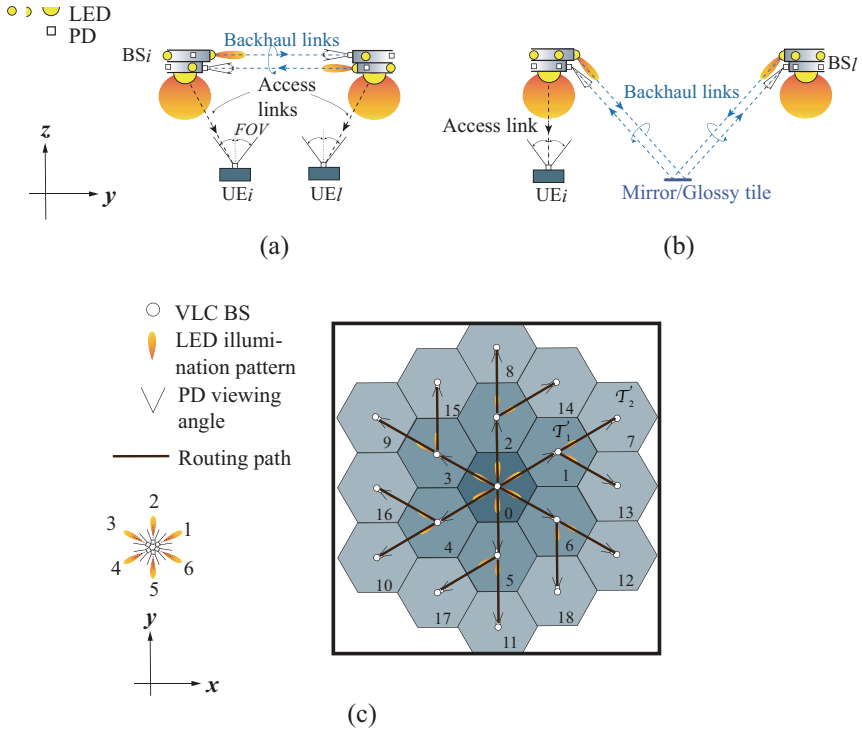

Figure A.1: (a) LOS link configuration; (b) Mirror-aided non-LOS link configuration; (c) Two-tier optical attocell network with central gateway

efficiency. As IM modulated signal must be real, the 0-th and $(K/2)$-th subcarriers are set to zero, where the $(K/2)$-th subcarrier is the Nyquist term, and K is the number of OFDM subcarriers. Transmitted electrical power P_{elec} is equally distributed among $K-2$ data-carrying subcarriers, i.e., $P_{elec,k} = P_{elec}/(K-2)$. In order to ensure non-negative optical intensity, DCO-OFDM adds DC-bias to the modulated signal and clips all negative values. The clipping noise can be neglected when choosing an appropriate biased factor a and we use $a = 3$ in the following calculation. The transmitted electrical power P_{elec} can be calculated based on the average transmitted optical power P_{opt} and the bias factor a based on the relationship $a = P_{opt}/\sqrt{P_{elec}}$. The optical power P_{opt} is the mean value of the time-domain signal after adding the DC bias [3]. Transmitted optical power P_{opt} is limited by illumination and eye safety requirements, which will be discussed in section A.3.1.

According to the orientation of the communicating LED-PD pair, VLC links are categorized into line-of-sight (LOS) and non-LOS link configurations. In [2], a mirror-aided non-LOS configuration is introduced, which improves the quality

of non-LOS links by adding first-bounce specular reflection. LOS and mirror-aided non-LOS configurations are illustrated in Fig.A.1(a) and (b), respectively. As LED lamps are Lambertian light sources, the received power of a LOS link can be calculated by Lambertian emission law. The LOS channel gain, which is the ratio of received power and transmitted power, is obtained by following equation [4]

$$G_{s,r} = \frac{(m+1)A_r}{2\pi D_{s,r}^2}\cos^m(\phi)\cos(\theta)\text{rect}(\frac{\theta}{\Theta}), \tag{A.1}$$

where ϕ and θ are angles of LOS paths measured from orientations of a sender s and a receiver r, respectively, $D_{s,r}$ is the Euclidean distance from s to r, A_r is the active area of the PD, Θ is the field-of-view (FOV) of the PD. A Lambert order $m = -\ln 2/\ln(\cos(\Phi_{1/2}))$ is used to describe LED's emission pattern, where $\Phi_{1/2}$ is the semi-angle at half-intensity of the LED emission pattern. The rectangular function rect(x) is 1 if $|x| \leq 1$, and 0 otherwise. Although the LOS component is missed in mirror-aided non-LOS configuration, this configuration takes advantage of the first-bounce specular reflection component. The mirror-aided non-LOS path can be seen as a "mirror-obstructed" LOS path [2]. The mirror-aided non-LOS channel gain can be calculated using Eq.(A.1) as the LOS channel. The gain of a mirror-aided non-LOS channel from a sender s to a receiver r is $\rho_m G_{s',r}$, where s' is the mirror image of s and ρ_m is the reflectivity of the mirror [2].

A.2.2 Optical Attocell Network

A VLC-based optical attocell network uses LED lamps as BSs. Each BS covers an attocell with a radius ranging from one to several meters. User equipment (UE) communicate with the nearest BS via VLC downlink and infrared (IR) uplink. A gateway, which can be one of the VLC BSs, connects the optical attocell network to the Internet. In this paper, we consider a two-tier ring-type optical attocell network as shown in Fig.A.1(c). The gateway is the central BS denoted as BS0. Other BSs are categorized into tier-1 BSs $\mathcal{T}_1$ and tier-2 BSs $\mathcal{T}_2$. Fixed routing is used in our work as shown in the figure. When the gateway receives data with the destination in a tier-2 cell (cell 7 to 18), it forwards this downlink information by using one of its neighboring tier-1 BSs (BS1 to BS6) as a relay. Uplink transmission in the direction from tier-2 BSs to the gateway is not considered in our work.

Communication links between BSs and the gateway form a backhaul network. VLC-based wireless backhaul network can use two different link configurations discussed in the previous section. Both backhaul link configurations require auxiliary LEDs and PDs as shown in Fig.A.1(a) and (b). When mirror-aided non-LOS backhaul links are used, small mirrors or small glossy floor tiles should be placed at the centers of every cell edge to provide first-bounce specular reflections.

A.2.3 Frequency Reuse Schemes

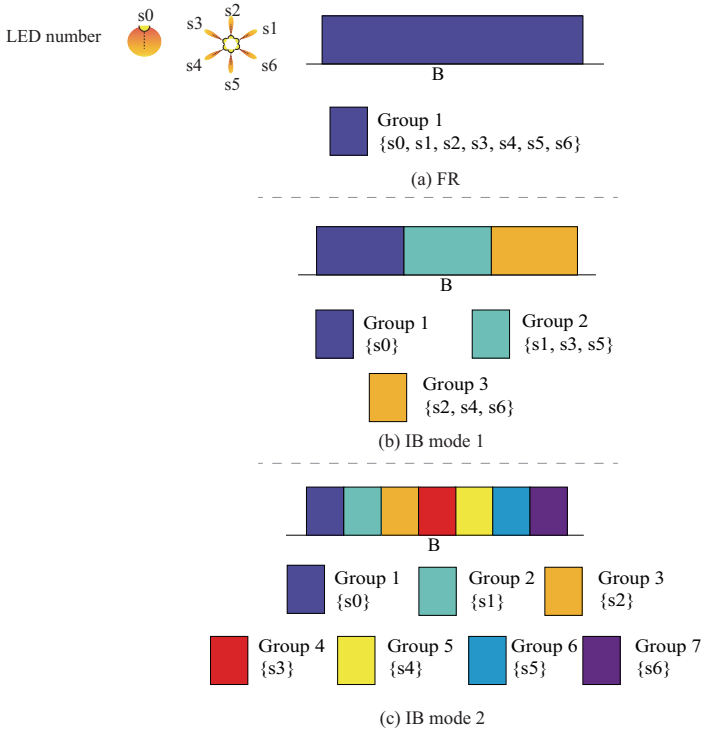

Figure A.2: Illustration of spectrum allocation of frequency reuse scheme (a) FR; (b) IB mode 1; (c) IB mode 2; B is the electrical bandwidth available for one BS

As DCO-OFDM is used to modulate the transmitted signal, different transmitters can use different OFDM subcarriers to send data. Receivers can convert the received signal on certain subcarriers using fast Fourier transform (FFT). Subcarriers are orthogonal to each other. Shannon-Hartley theorem can be applied individually on each subcarrier. VLC links using the same communicating subcarriers interfere with each other. The SINR on the k-th subcarrier of a link denoted by l is calculated by

$$\gamma_{l,k} = \eta \frac{P_{elec,l,k} R_{PD}^2 |G_l|^2}{\sigma_k^2 + \sum_{m \in \mathcal{I}_l} P_{elec,m,k} R_{PD}^2 |G_m|^2}, \tag{A.2}$$

where G_l is the channel gain of link l calculated with Eq.(A.1) or the extension equation $\rho_m G_{s',r}$ introduced in section A.2.1 for mirror-aided non-LOS channel, R_{PD} is the responsivity of PD in A/W, $\sigma_k = N_0 B/K$ is the noise power on the k-th subcarrier, N_0 is the power spectral density (PSD) of additive white Gaussian

noise (AWGN) channels, and B is the bandwidth of OFDM signal, G_l denotes the channel gain of the link l, $P_{elec,l,k}$ denotes the transmitted electrical power on the k-th subcarrier of link l. The efficiency loss factor $\eta = \frac{N-2}{N-2+N_{cp}}$ indicates the bandwidth efficiency loss caused by adding cyclic prefix (CP) at the end of each OFDM frame. Adding CP to OFDM frames can overcome inter-symbol interference (ISI) with simple equalization. We set $N_{cp} = 4$ in our calculations. The interference set $\mathcal{I}_l$ consists of links communicating on the same subcarriers as link l. In this work, we assume that every BS is able to use the whole electrical spectrum. The interference set of each link is determined by the frequency reuse scheme. We describe three frequency reuse schemes based on the allocation of subcarriers.

Fully reuse (FR) Every transmitter can reuse the whole spectrum. The interference set of a link from the j-th transmitter of a BSi, which is denoted by i-sj, is $\mathcal{I}_{l:l(s)=i\text{-s}j} = \{m{:}m(s) = p\text{-s}n, \forall p \in [0,18], \forall n \in [0,6]\, l(s) \neq m(s)\}$. Here, $l(s)$ denotes the originating transmitter s of link l.

In-band (IB) mode 1 All downward-oriented transmitters for access data transmission use the same set of subcarriers. The rest subcarriers are divided into two groups: the first group consists of transmitters numbered with 1, 3, 5, and the second group consists of transmitters numbered with 2, 4, 6. Thus, each neighboring LEDs on a single base station use different spectrum. The interference set is $\mathcal{I}_{l:l(s)=i\text{-s}j} = \{m{:}m(s) = p\text{-s}n, \forall p \in [0,18], \forall n \in \{j, 1+(j+1) \bmod 6, 1+(j+3) \bmod 6\}, l(s) \neq m(s)\}$. Here, $x \bmod y$ denotes modulo operation and returns the remainder of the Euclidean division of x by y.

In-band (IB) mode 2 Each transmitter on a single BS uses individual subcarrier sets to avoid inter-link interference in the same cell. The interference set is $\mathcal{I}_{l:l(s)=i\text{-s}j} = \{m{:}m(s) = p\text{-s}j, \forall p \in [0,18], p \neq m\}$.

An illustration of three frequency reuse schemes is shown in Fig.A.2. The number of subcarriers used by the access group, i.e. group 1 in both Fig.A.2(b) and Fig.A.2(c), is determined by a bandwidth allocation ratio δ. This ratio is calculated based on the requested rates of downlink traffic and will be discussed in section A.3.2. The remaining $(1-\delta)K$ subcarriers are evenly assigned to each backhaul group, i.e. group 2 and 3 in Fig.A.2(b) and group 2 to 7 in Fig.A.2(c).

A.3 Numeric Analysis

In order to assess the performance of networks with misaligned auxiliary transceivers using different frequency reuse schemes, we calculate the network average spectral

efficiency $\bar{\rho}$ in bit/s/Hz/cell. This is the average value of the end-to-end spectral efficiency of each downlink route from the gateway to the UE. The end-to-end spectral efficiency of one downlink route is the minimal value of the spectral efficiency of links along this route. If multiple routes share one link, the spectral efficiency is evenly allocated to each route. The spectral efficiency of one link is the mean of spectral efficiency on each allocated subcarrier which is calculated by $\rho_{l,k} = \delta_l \log_2(1 + \gamma_{l,k})$, where δ_l is the ratio of bandwidth (subcarriers) allocated to link l. When the FR method is used, $\delta_l = 1$ for all links. To obtain the spectral efficiency of each link, we have to determine the transmitted power and the bandwidth allocation ratio of each link.

A.3.1 Illumination And Eye Safety

Wide-beam LEDs are normally used for indoor lighting to provide uniform illumination. We assume that the semi-angle of downward-oriented LEDs $\Phi_a = 60°$. The primary purpose of these LEDs is illumination. Their transmitted power P^a_{opt} is determined by the illumination requirement. Auxiliary LEDs are used for backhaul data transmission. Increasing the transmitted power of auxiliary LEDs P^b_{opt} not only increases the average illuminance in the room but also increases the risk of causing visual discomfort on human eyes. This is because that narrow-beam visible LEDs used as auxiliary LEDs emit direct and reflected light. We configure the transmitted power such that average indoor illuminance is under $750\,\mathrm{lx}$, which is the maximum value required for activities in offices. Transmitted power of auxiliary LEDs is limited such that the maximum vertical illuminance on human eyes (assuming at height of $1.5\,\mathrm{m}$) is $2000\,\mathrm{lx}$. Discussion of illumination requirements on transmitted power is presented in a separate paper. In this work, transmitted power P^a_{opt} and P^b_{opt} is calculated based on the illumination and eye safety requirements and the semi-angle of auxiliary LEDs Φ_b. The calculated transmitted power is set to be the same for both link configurations and does not change with misalignment angles.

A.3.2 Bandwidth Allocation

When IB method is used, the fraction of subcarriers used for access data transmission is determined by bandwidth allocation ratio δ. As backhaul links cannot become the bottleneck for data transmission to UEs, the data rate of each backhaul downlink should be large enough to provide access data transmission to all downstream UEs. We use $\mathcal{DL}_l$ to denote the set of downstream access links of link l. Notice that all UEs equally share the spectrum δB when multiple UEs are located in a cell. The sum of the data rates of these UEs achieves the maximum value when all UEs are located at a point with the maximum SINR, i.e. in the center of the cell. The maximum sum rate is equal to the achievable data rate of a single

UE located at the cell center. Thus, we assume that every BS has one UE located at its cell center which uses the whole spectrum allocated to the access link. The bandwidth allocation ratio δ_l of one backhaul link l is

$$\delta_l = \frac{\frac{1}{b}\log_2(1+\gamma_l)}{\frac{1}{b}\log_2(1+\gamma_l) + \sum_{m\in\mathcal{DL}_l}\log_2(1+\gamma_m)}, \tag{A.3}$$

where γ_l is the average SINR of link l across all allocated subcarriers, b is the number of spectrum groups for backhaul links, $b = 2$ for IB mode 1 and $b = 6$ for IB mode 2. As a BS may have multiple backhaul links, the bandwidth allocation ratio δ_{BS} of one BS is the minimum value of δ_l of backhaul links of this BS. The ratio δ changes with misalignment angle as the SINR of each link changes. There are two options for configuration. The first option is global configuration. All BSs are configured with the same value of δ, which is the minimum value of δ_{BS} in the network. The second option configures each BS with its own calculated δ_{BS}. In the first option, the minimum value of δ is obtained by comparing all calculated results in the network, while every BS only needs to calculate its bandwidth allocation ratio in the second option.

A.4 Simulations and Results

The performance of networks with misaligned auxiliary transceivers using different frequency reuse schemes is assessed by computer simulations. In all misalignment scenarios, we assume that all auxiliary transmitters of BS0 rotate against the vertical axis with the same angle. From our simulations, we knew that misaligned BS0 may cause a larger impact on the overall performance than other BSs as the gateway BS0 sends downlink information to all BSs. In real applications, the configuration of Φ_b may depend on eye safety issues and the QoS requirement of backhaul links. Simulation results of networks using two link configurations are presented.

A.4.1 Average Spectral Efficiency

Due to the randomness of misalignment, the horizontal misalignment angle $\Delta\theta$ may vary within the range -30° to 30°. The negative value of angle means rotating auxiliary transceivers clock-wise. Notice that the angle of the orientation of one auxiliary transceiver with respect to its neighboring auxiliary transceiver is 60°. When horizontal misalignment angle exceeds $\pm 30^\circ$, the misaligned BS reassigns auxiliary LEDs for backhaul transmission. Although receiving PDs of tier-1 and tier-2 BSs are aligned in our simulations, we configure the FOV of receiving PDs to ensure successful backhaul data transmission in the misaligned case without loss of generality. In our simulations where the height of BSs is $2.85\,\mathrm{m}$, the height

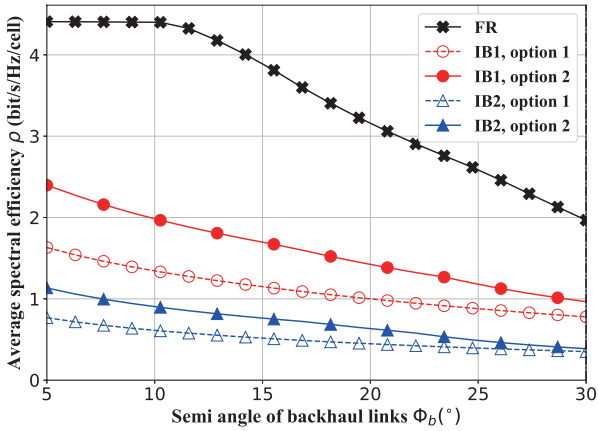

(a) LOS $\Delta\theta$ =0°

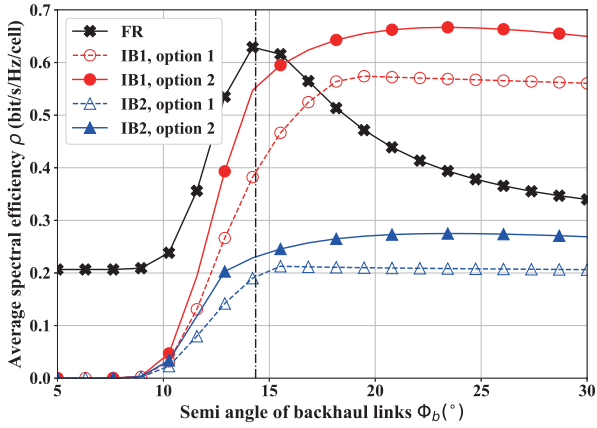

(b) LOS $\Delta\theta$ =27°

Figure A.3: Average spectral efficiency of networks using (a) LOS backhaul configuration with $\Delta\theta$ =0°; (b) LOS backhaul configuration with $\Delta\theta$ =27°.

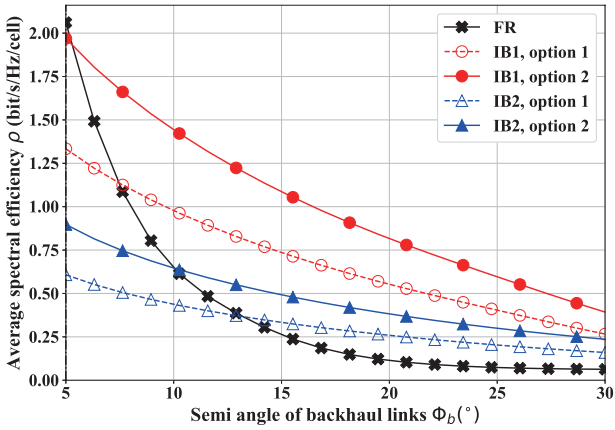

(c) Mirror-aided non-LOS $\Delta\theta$ =0°

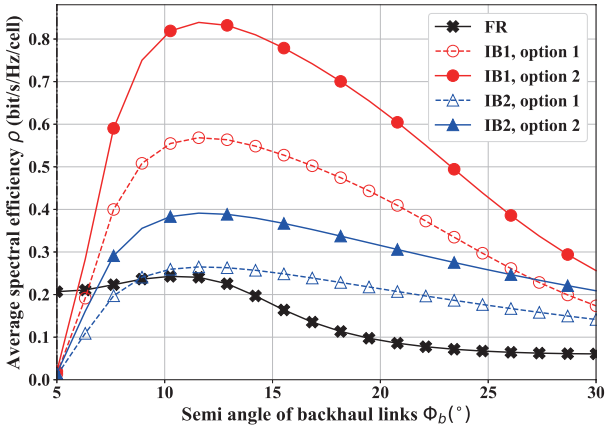

(d) Mirror-aided non-LOS $\Delta\theta$ =27°

Figure A.3: (continued) Average spectral efficiency of networks using (c) Mirror-aided non-LOS backhaul configuration with $\Delta\theta$ =0°; (d) Mirror-aided non-LOS backhaul configuration with $\Delta\theta$ =27°.

of UEs is $1.15\,\mathrm{m}$, and cell radius is $2\,\mathrm{m}$, FOVs of auxiliary PDs are 30° and 15.45° in LOS configuration and mirror-aided non-LOS configuration, respectively. The network average spectral efficiency (ASE) $\bar{\rho}$ of two link configurations with and without misalignment is shown in Fig.A.3. Due to the limit of space, we only show misalignment cases with large horizontal misalignment angles ($\Delta\theta$ =27°). It can be seen that misalignment causes significant performance degradation for both link configurations. However, the performance of different frequency reuse schemes depends on the horizontal misalignment angle $\Delta\theta$ and semi-angle of auxiliary LEDs Φ_b. By calculating the interference-to-noise ratio (INR) of each link, which is the ratio between the sum of interference and the noise, we found that the performance of different frequency reuse schemes depends on the regime of the network. When the average INR of networks without frequency reuse is smaller than 1, the optical attocell network is at the noise-limited regime. In this regime, using a frequency reuse scheme (two IB methods) cannot provide more gain as noise is dominant. When the average INR is larger than 1, the network is at the interference-limited regime. Using a frequency reuse scheme could provide better SINR on some links, thereby the network performance is improved. In Fig.A.3(b) we can see that there exists a transition point from noise-limited regime to interference-limited regime for LOS configuration, while networks using mirror-aided non-LOS configuration are always at interference-limited regime as shown in Fig.A.3(c) and (d). In addition, LOS configuration seems more vulnerable to misalignment for two reasons: 1) Comparing Fig.A.3(a) and (b), we can see that the maximum ASE that can be achieved by using LOS configuration significantly drops (maximum 4.4 bit/s/Hz/cell when aligned and maximum 0.67 bit/s/Hz/cell when misaligned). This is compared to mirror-aided non-LOS configuration whose maximum ASE drops from 2 bit/s/Hz/cell to 0.84 bit/s/Hz/cell (Fig.A.3(c) and (d)); 2) When the misalignment angle is large ($\Delta\theta$ =27°), using LOS configuration cannot achieve more than 0.7 bit/s/Hz/cell regardless the chosen semi-angle Φ_b, while using mirror-aided non-LOS configuration is able to get more than 0.8 bit/s/Hz/cell when Φ_b is between 10° to 15°.

A.4.2 Cumulative Distribution Function of ASE

In order to further compare the performance of using different frequency reuse schemes, we calculate the cumulative distribution function (CDF) of maximum ASE of each frequency reuse scheme obtained by simulating two-tier optical attocell networks in different regimes. Simulation results are shown in Fig.A.4. It can be seen from Fig.A.4(a) that FR outperforms other schemes when networks using LOS configuration in the noise-limited regime. By using FR scheme, networks have more than 50% probability to get maximum ASE $\bar{\rho}_{max} > 3$ bit/s/Hz/cell, while other schemes cannot provide $\bar{\rho}_{max}$ larger than 3 bit/s/Hz/cell. When net-

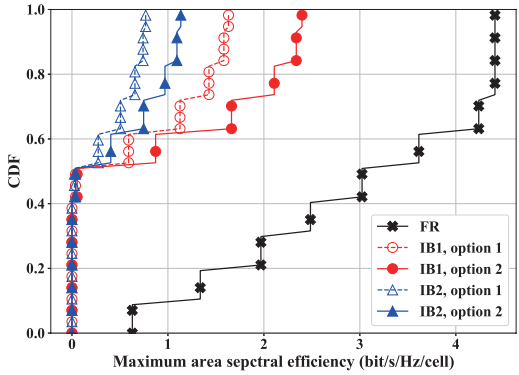

(a) LOS, noise-limited regime

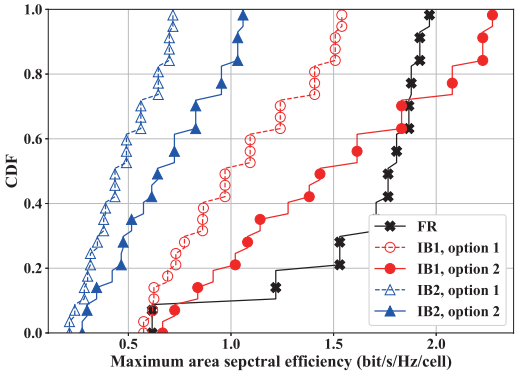

(b) LOS, interference-limited regime

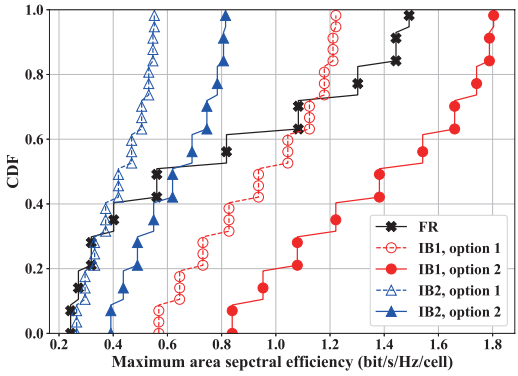

(c) Mirror-aided non-LOS, interference-limited regime

Figure A.4: CDF of maximum ASE of networks using (a) LOS backhaul configuration in the noise-limited regime; (b) LOS backhaul configuration in the interference-limited regime; (c) Mirror-aided non-LOS backhaul configuration in the interference-limited regime

works using LOS configuration are in the interference-limited regime as shown in Fig.A.4(b), IB mode 1 with option 2 can achieve better performance than FR. When networks use mirror-aided non-LOS backhaul configuration, networks are always in the interference-limited regime. Using the FR method could have a large probability to get poor performance as shown in Fig.A.4(c). For instance, networks using IB mode 1 with option 2 always have $\bar{\rho}_{max} > 0.8$ bit/s/Hz/cell, while networks using FR have near 50% probability to get $\bar{\rho}_{max} < 0.8$ bit/s/Hz/-cell. In addition, it is also shown that IB mode 1 with option 2 outperforms other IB methods regardless of the regime and backhaul configuration. In general, the FR method outperforms in the noise-limited regime, while IB mode 1 with option 2 has better performance when interference becomes larger. Given the same probability of horizontal misalignment angle, we calculated the expected values of the maximum ASE, i.e., $\mathrm{E}[\bar{\rho}_{max}]$ across all possible misalignment angles, where $\mathrm{E}[x]$ denotes the expectation of the variable x. The best Φ_b values that can achieve the maximum value of $\mathrm{E}[\bar{\rho}_{max}]$ are shown in Table 1. It can be seen that mirror-aided non-LOS configuration requires smaller Φ_b than LOS configuration to achieve the best overall performance.

Scheme and Option	LOS		Mirror-aided non-LOS	
	Φ_b	E$[\bar{\rho}_{max}]$ (bit/s/Hz/cell)	Φ_b	E$[\bar{\rho}_{max}]$ (bit/s/Hz/cell)
FR	13°	2.8	5°	0.9
IB 1, option 1	14°	0.9	8°	0.9
IB 1, option 2	13°	1.3	8°	1.3
IB 2. option 1	13°	0.4	8°	0.4
IB 2, option 2	12°	0.6	8°	0.6

Table A.1: Best auxiliary semi-angle to achieve the maximum of expected value of ASE

A.5 Conclusions

Two-tier optical attocell networks using different backhaul link configurations have different performance at misalignment scenarios. The impact of misalignment varies with horizontal misalignment angle and auxiliary semi-angle. By comparing the simulation results of two backhaul configurations and different frequency reuse schemes, we found that networks using LOS backhaul configuration transition from noise-limited regime to interference-limited regime when the misalignment angle and the semi-angle of auxiliary LEDs become larger. Networks using mirror-aided non-LOS backhaul configuration are always in the interference-limited regime. The FR scheme provides the best overall performance for networks in the noise-limited regime. Networks using the IB scheme can achieve better performance in the interference-limited regime. It is also found that LOS backhaul configuration is more vulnerable to misalignment than mirror-aided non-LOS configuration.

References

[1] H. Kazemi, M. Safari, and H. Haas, "A wireless optical backhaul solution for optical attocell networks", IEEE Transactions on Wireless Communications, vol. 18, pp. 807–823, 2019.

[2] Y. Wu, P. Audenaert, M. Pickavet, and D. Colle, "Mirror-aided non-LOS VLC channel characterizations with a time-efficient simulation model", Photonic Network Communications, vol. 38, pp. 151–166, 2019.

[3] J. Armstrong and B. J. C. Schmidt, "Comparison of asymmetrically clipped optical OFDM and DC-biased optical OFDM in AWGN", IEEE Communications Letters, vol. 12, pp. 343–345, 2008.

[4] J. R. Barry, J. M. Kahn, W. J. Krause, E. A. Lee, and D. G. Messerschmitt, "Simulation of multipath impulse response for indoor wireless optical channels", IEEE Journal on Selected Areas in Communications, vol. 11, pp. 367–379, 1993.

B

Physical Quantities and Units of Light

Many physical quantities of light are introduced in this book. We explain the units of these physical quantities in this appendix.

* * *

Quantity	Unit	Definition
Radiant energy	Joule (J)	The amount of energy transferred by electromagnetic waves
Radiant flux	Watt (W)	The amount of radiation per time unit
Radiant intensity	Watt per steradian (W/sr)	The radiant flux in a given direction per unit solid angle
Radiance	Watt per steradian per square meter ($W/sr/m^2$)	The radiant flux per unit solid angle per unit projected source area
Radiant exitance	Watt per square meter (W/m^2)	The radiant flux per unit area radiated by a surface
Irradiance	Watt per square meter (W/m^2)	The radiant flux per unit area received by a surface

Table B.1: Radiometric quantities and units

Quantity	Unit	Definition
Luminous flux	lumen (lm)	The luminous energy per unit time
Luminous intensity	candela=lumen per steradian (cd)	The luminous flux in a given direction per unit solid angle
Luminance	candela per square meter (cd/m^2)	The luminous flux per unit solid angle per unit projected source area
Luminous exitance	lumen per square meter (lm/m^2)	The luminous flux per unit area radiated by the surface
Illuminance	lux=lumen per square meter (lx)	The luminous flux per unit area received by the surface

Table B.2: Photometric quantities and units